

**ULTRAFAST ELECTRON DIFFRACTION:  
PULSED LASER DESORPTION ENABLES  
TIME-RESOLVED STRUCTURAL DETERMINATION  
OF THERMALLY LABILE CHROMOPHORES**

Thesis by

Andreas Gahlmann

In Partial Fulfillment of the Requirements for the  
Degree of

Doctor of Philosophy

CALIFORNIA INSTITUTE OF TECHNOLOGY

Pasadena, California

2011

(Defended April 27, 2011)

© 2011

Andreas Gahlmann

All Rights Reserved

Dedicated  
with love and gratitude  
to  
my wife  
and to  
my parents

## ACKNOWLEDGEMENTS

The number of people who have helped me reach this point in my education is very extensive and I would like to express my thankfulness to all of them. This work is the culmination of my scientific education as a student and I would like to acknowledge the individuals, who have become trusted mentors and colleagues for me.

First, I would like to thank my research advisor, Prof. Ahmed Zewail, for his continual support for me and for the research contained in this thesis. His unwavering commitment to this project, even in the face of considerable experimental challenges and seemingly endless equipment failures was truly motivating. He generously provided my research with sufficient funding to allow us to creatively explore directions that otherwise would remain untouched, but, in the end, would prove to produce the crucial breakthroughs that led to the successful realization of our goals. I always valued the occasions, when we would sit down together to discuss science, because his enthusiasm for our work was nothing short of infectious. It was an honor to work with him and learn from him. Many thanks also go to the members of my Ph.D. committee for overseeing my research over the years: Prof. Mitchio Okumura, Prof. Grant Jensen, Prof. Aron Kuppermann, and Prof. Peter Dervan.

The graduate students, post-docs, and staff scientists in the Zewail group were instrumental to the success of my studies and in my development as a scientist; to all of them I am grateful for the helpful comments and the insightful discussions. In particular, my immediate co-workers in the UED subgroup, Dr. Sang Tae Park, Dr. I-Ren Lee, Dr. Jonathan Feenstra, and Dr. Yonggang He deserve to be mentioned here. Their

contributions to the research presented in this thesis were indispensable and I have enjoyed sharing the moments of experimental breakthroughs with them. Also, De Ann Lewis and Maggie Sabanpan, the administrative assistants in the Zewail group, Agnes Tong, the chemistry option's graduate secretary, Mike Roy and Steve Olson, the machinists of the chemistry option, and the Caltech staff at large made this institution a wonderful place to do research.

To my good friends that I have met during my time at Caltech I owe special thanks for their collegial support. Patrick Theofanis has provided me with a much needed open ear during coffee breaks and, as a Southern California local, has infused me with his love of the ocean and taught me how to surf those waves. With Dr. David Flannigan I quickly found common ground in our love of cycling and together we spent a lot of quality time venturing deep into the beautiful and refreshingly quiet San Gabriel Mountains north of Caltech. Finally, Dr. Costas Anastassiou, who, although he had played against me on the rivaling basketball team in Switzerland, proved to be a key ally to me during my final years at Caltech. He provided me with the much needed perspective to finish my projects and simultaneously focus on my personal professional development. Without his unremitting insistence and encouragement, this thesis would probably not have been finished in time.

The excellent faculty and staff at the University of Portland deserve the credit for my initial science education that laid the foundation for me to complete this thesis research at a place like Caltech. In particular, Prof. Steven Mayer and Prof. Shannon Mayer kindled my interests in the physical sciences in these early years, when I was an undergraduate student in Portland, and they have remained pillars of support during my thesis research.

I would also like to thank Prof. W.E. Moerner, my future postdoctoral research advisor, for his receptiveness and his advice in developing a research plan for our joint efforts in the coming years.

Also, my parents-in-law, Tom and Elsa Barnett, and their entire family need to be mentioned here, because they have given me the home-away-from-home from the moment that I arrived on their doorstep ten years ago. While Tom, now a retired medical doctor, could always empathize with me being under the pressures of graduate school, he has always emphasized (and rightfully so) that my responsibilities are not just to my research, but also to my family.

To my parents, Heinrich and Verena Gahlmann, I am ever grateful for the wonderful upbringing they provided me with. As a child, I was always allowed and encouraged to engage in extracurricular activities that ended up covering quite a range of different instruments and athletic disciplines. I reached a point during my early high school years, when I recall telling my parents that I felt like I needed to give up some of my hobbies, because there simply were not enough hours in the day to fully pursue every one of them. Now, as a young father myself, I know that these privileges did not come for free, but instead required a tireless commitment from my parents every day. I strongly believe that these experiences helped me identify my passions and become the person that I am today. Realizing the sacrifices they made on my behalf, I can only hope that I can provide the same love and devotion for my children, as they grow up.

Finally, I would like to thank my wife, Jennifer, for her inexhaustible patience and her support for me as a student and as a young father. Her sacrifices of leaving her family as well as a wonderful work environment to accompany me to Caltech have been immense. Between me spending long hours at the lab and her having to work full-time to support our family, life truly became a juggling exercise. However, from the moment she stepped into my life, her love has provided the central support system for me to be able to complete my work with the care it deserved. For being this wonderful person in my life and for the gift to (very soon) raise two children with her, I love her more than she could ever know.

## ABSTRACT

The construction and utilization of the fourth-generation ultrafast electron diffraction apparatus, UED4, is the subject of this thesis. With UED4 and its novel and universal sample delivery method based on laser desorption, we were able to vaporize thermally labile molecular samples and determine their ground-state structures and the structures of their photochemical and photophysical reaction products. Each component part of the new UED4 apparatus is described, and the experimental and computational procedures used to extract structural information from the time-resolved diffraction patterns are presented.

Several molecules were studied in their ground states and photoinduced excited states or product states on the time scale of picoseconds and nanoseconds. With UED3, nitrobenzene was shown to undergo intramolecular rearrangement prior to NO loss in an ultrafast fragmentation reaction. In indole, the chromophore of the amino acid tryptophan, the involvement of a dark structure, formed on the picosecond time scale, was revealed in the nonradiative decay pathway of the initially excited state. By determining the ground state structures of the thermally labile nucleobases uracil and guanine, the first use of surface-assisted laser desorption in a pulsed electron diffraction experiment was reported using the newly developed UED4 apparatus. The determined structures of the photochemically generated species of the photochromic molecule 6-nitro-BIPS further demonstrated the capability of laser desorption electron diffraction to function as a time-resolved experiment. Finally, the fragmentation reaction of the amino acid tryptophan upon UV laser irradiation was studied with UED4. The ability to deliver increasingly large and conformationally heterogeneous molecules into the gas phase now provides new challenges and opportunities of both experimental and theoretical nature for the field of ultrafast electron diffraction.

## Table of Contents

<b>1</b>	<b>Introduction.....</b>	<b>1</b>
1.1	Historical Perspective.....	2
1.2	This Thesis .....	5
<b>2</b>	<b>Electron Diffraction Theory.....</b>	<b>7</b>
2.1	Atomic Scattering.....	8
2.2	Electron Scattering from Nuclei and Electrons.....	11
2.3	Molecular Scattering .....	13
2.4	Molecular Vibrations.....	17
2.5	Modified Radial Distribution Function .....	18
<b>3</b>	<b>Instrumentation.....</b>	<b>23</b>
3.1	UED Instrumental Components .....	24
3.1.1	Vacuum Chambers.....	24
3.1.2	Electron Gun .....	25
3.1.3	Electron Optics.....	26
3.1.4	Detector.....	28
3.1.4.1	Detector Assembly .....	28
3.1.4.2	Phosphor Screen.....	29
3.1.4.3	Image Intensifier .....	31
3.1.4.4	Gradient Filter .....	33
3.1.4.5	CCD Camera .....	34
3.1.4.6	Detector Calibration .....	35
3.1.4.6.1	Single Electron Counts .....	35
3.1.4.6.2	Faraday Cup.....	37
3.1.5	Molecular Sample Delivery .....	38
3.1.5.1	High-Temperature Nozzle for UED3 .....	38
3.1.5.2	IR Laser Desorption .....	41
3.1.5.2.1	Desorption Mechanism.....	41
3.1.5.2.2	UED4 Desorption Source .....	44
3.1.5.2.2.1	Temporal Extent of Molecular Plume.....	46

3.1.5.2.2.2	Spatial Extent of Molecular Plume .....	48
3.1.5.2.2.3	Experimental Considerations for Nanosecond Time-Resolved Laser Desorption–Electron Diffraction .....	50
3.1.5.3	Molecular Beam Nozzle for UED4 .....	51
3.2	Temporal and Spatial Resolution – Ultrashort Electron Pulses for Diffraction, Crystallography and Microscopy: Theoretical and Experimental Resolutions .....	53
3.2.1	Abstract .....	53
3.2.2	Introduction .....	53
3.2.3	Theory .....	56
3.2.3.1	Definition of Width and Length of Electron Packet .....	56
3.2.3.2	Initial Energy Spread .....	58
3.2.3.3	Charge Density Effect .....	59
3.2.3.3.1	Mean Field Theory (MF) .....	59
3.2.3.3.2	Mean Field Theory Including Lens System .....	60
3.2.3.3.3	Monte Carlo Simulation (MC) .....	61
3.2.4	Results and Discussion .....	63
3.2.4.1	Temporal Resolution .....	63
3.2.4.1.1	Initial Energy Spread .....	63
3.2.4.1.2	Space-Charge Effect .....	65
3.2.4.2	Spatial Resolution .....	67
3.2.4.2.1	Coherence .....	67
3.2.4.2.2	Optimal Diffraction Geometry .....	71
3.2.4.2.3	Focusing Behavior .....	72
3.2.4.2.4	Spatial Resolution for Space-Charge Limited Pulses .....	76
3.2.5	Summary and Conclusion .....	80
3.2.6	Appendix .....	84
3.2.6.1	Scattering Signal Intensity .....	84
3.2.6.2	Bunch Dimensions and Standard Deviations .....	85
3.2.6.3	Initial Kinetic Energy .....	86
3.2.6.4	Axial Acceleration in Uniform Disk Charge Distribution .....	88
3.2.6.5	Attenuation of Interference Intensity Due to Incoherence .....	89

3.2.6.6	Suppression of Coulomb Repulsion during Acceleration.....	90
<b>4</b>	<b>Data Processing and Analysis .....</b>	<b>127</b>
4.1	Image Processing.....	128
4.1.1	Frame Averaging .....	128
4.1.2	Ratio Images .....	130
4.1.3	Radial Average.....	133
4.1.4	Temporal Referencing of Time-Dependent Data .....	137
4.2	Mathematics of Structural Fitting ( $\chi^2$ -Fitting).....	139
4.2.1	Linear Parameters .....	141
4.2.2	Nonlinear Parameters.....	143
4.2.3	Estimation of Errors in the Fitted Parameters.....	145
4.2.4	Choice of Structural Coordinates for Fitting .....	146
4.2.4.1	Singular Value Decomposition .....	148
4.3	Defining the Theoretical Model.....	150
4.3.1	Calculating a Starting Molecular Structure.....	151
4.3.2	Calculating the Root-Mean-Squared Amplitudes of Vibration .....	152
4.3.2.1	Empirical Equations .....	152
4.3.2.2	Quantum Chemical Force Constants.....	153
4.4	Fitting Procedure.....	157
4.4.1	Calibration of Instrumental Factors: Camera Length and Point-Spread-Function .....	158
4.4.2	Temperature Fitting of Ground State Molecules .....	158
4.4.3	Determination of Ground State Structure .....	159
4.4.4	Determination of Product Structure(s).....	160
<b>5</b>	<b>Results .....</b>	<b>169</b>
5.1	Structure of Isolated Biomolecules by Electron Diffraction–Laser Desorption: Uracil and Guanine .....	171
5.1.1	Abstract.....	171
5.1.2	Main Text.....	171
5.2	Direct Determination of Structural Conformations of Photoswitchable Molecules by Laser Desorption–Electron Diffraction .....	178
5.2.1	Abstract.....	178

5.2.2	Main Text.....	178
5.2.3	Experimental Section.....	184
5.3	Ultrafast Electron Diffraction: Structural Dynamics of Molecular Rearrangement in the NO Release from Nitrobenzene .....	186
5.3.1	Abstract.....	186
5.3.2	Introduction.....	186
5.3.3	Results.....	188
5.3.4	Discussion.....	191
5.3.4.1	Previous Spectroscopic Studies.....	191
5.3.4.2	Structural Dynamics from UED.....	193
5.3.5	Conclusion .....	196
5.3.6	Experimental Section.....	196
5.4	Ultrafast Electron Diffraction Reveals Dark Structures of the Biological Chromophore Indole.....	198
5.4.1	Abstract.....	198
5.4.2	Main Text.....	198
5.4.3	Experimental Section.....	203
5.5	L-Tryptophan .....	205
5.5.1	Ground State Structure.....	205
5.5.2	Photochemical Reaction Dynamics .....	209
<b>6</b>	<b>Reflections and Future Directions.....</b>	<b>275</b>
6.1	Capabilities of Laser Desorption–Electron Diffraction .....	276
6.2	Inherent Challenges of a Gas-Phase Electron Diffraction Experiment.....	277
6.2.1	Large Distances.....	277
6.2.2	Molecular Ensemble Averaging .....	279
6.3	Possible Improvements of the UED4 Apparatus.....	281
6.4	Future Directions.....	283
6.5	Conclusion.....	284
<b>7</b>	<b>References.....</b>	<b>285</b>

# **Chapter 1.**

## **Introduction**

Time-resolved gas-phase electron diffraction and ultrafast (gas-phase) electron diffraction (UED), as it has been implemented in the Zewail laboratories at Caltech, permits the direct determination of time-dependent structural transitions in isolated molecules. Internuclear distances in a molecular structure can be solved with very high spatial resolution by analyzing the interferences of the scattered electron waves that are recorded on a detector. By interfacing a gas-phase electron diffraction instrument with an ultrafast pulsed laser system for electron pulse generation and sample excitation (pump-probe scheme), current state of the art experiments can achieve picosecond time resolution and a spatial resolution of 0.01 Å, simultaneously.<sup>1,2</sup> Thus, in addition to determining molecular structures in three spatial dimensions, UED is able to follow the structural dynamics at the relevant time scale of the reaction.<sup>3-5</sup> A particular advantage of time-resolved diffraction is its ability to detect, in an unbiased manner, all structures that are formed after photoexcitation. Examples from this laboratory include, for example, photoinduced fragmentations,<sup>6</sup> reaction path bifurcations,<sup>2</sup> and even radiationless processes involving “dark structures”<sup>7</sup> that can be revealed with UED and their time-dependent mole fractions can be determined. The extension of the UED methodology toward the structural investigations of thermally labile compounds, in particular biologically relevant chromophores, is the main focus of this work.

## 1.1 Historical Perspective

For an in-depth discussion of the evolution of conventional gas-phase electron diffraction (GED) into time-resolved electron diffraction and UED, the interested reader is referred to previous theses and reviews from this laboratory.<sup>8-10</sup> The time-resolved

implementation of electron diffraction, achieved through the combination of GED and pump-probe spectroscopy, has been a focus of research in the Zewail labs for two decades. A major development in the field occurred in 1984 with the incorporation of digital detection systems (instead of photographic plates) into electron diffractometers. This method of detection made it possible to collect multiple time-resolved diffraction patterns during the same experiment by adjusting the delay time between an excitation laser pulse (reaction initiation) and an electron probe pulse (probing of resulting structures).<sup>11</sup> The time resolution of the experiment, therefore, became limited only by the duration of the laser and electron pulses that would be used to pump and interrogate the gaseous sample.<sup>12-14</sup>

Using state of the art femtosecond laser systems, the Zewail labs pioneered the use of picosecond electron pulses to achieve ultrafast time-resolved electron diffraction (UED).<sup>1,15-17</sup> Starting from the early 1990s, the UED experiments were continuously improved at Caltech by building subsequent generations of UED instruments (UED1–UED3).<sup>1,9,16,18</sup> These experimental improvements brought the resolution capabilities of the third generation UED apparatus (UED3) to 0.01 Ångstroms and a few picoseconds and the detection limit for structural changes to 1% among all molecules in the gaseous ensemble, which is a record achievement to date still.

Concurrently, analysis of electron diffraction data advanced significantly for the entire field, as high-level quantum chemical calculations became feasible at manageable computational costs.<sup>19-22</sup> Of particular benefit for UED was the possibility to calculate the molecular properties of excited state species and incorporate those results into the diffraction data analysis.<sup>2</sup> These advances permitted (i) accurate high-resolution structure

determination of both reactant and product species, even at significantly elevated temperatures and (ii) quantitative study of the time-dependent population dynamics on complex potential energy surfaces leading to the observed reaction products.<sup>2,18</sup>

The delivery of intact sample molecules into the gas phase as a dense molecular beam remained as a major challenge for UED experiments. Time-resolved structural investigation is particularly valuable for chromophores of biological relevance (e.g., nucleic acid bases or the amino acid tryptophan), because the activity of these species is, in many cases, dependent on their dynamic structural transitions on either the ground- or excited-state potential energy surfaces.<sup>23</sup> However, the conventional approach of thermally heating the sample, until sufficient vapor pressure was achieved for the formation of an effusive molecular beam, is not suitable for thermally labile molecular systems, as, for example, the aforementioned biological chromophores. These samples thermally decompose before the needed experimental condition can be reached, which is reflected in the extreme sparseness of reported structures of biological organic molecules in the entire field of gas-phase electron diffraction. Thus, a new sample delivery method was urgently needed to deliver these molecules into the gas phase without thermal decomposition and in a sufficiently high number density, such that a (time-resolved) electron diffraction signal can be obtained from them.

The construction of the fourth-generation diffraction instrument (UED4) follows the tradition of continued instrument development, described above, and is intended to address the problem of intact gas-phase sample delivery of thermally labile compounds. The unique advance of this instrument is therefore the implementation of a novel sample delivery method based on surface-assisted laserdesorption. This new molecular source

allows for the study of larger and more intricate molecules than encountered previously by this field and pushes the electron diffraction technique to new limits.

## 1.2 This Thesis

The UED4 instrument design and the accompanying advances in diffraction data analysis to handle the increasingly complex diffraction data are the subject of this thesis. The UED4 apparatus and its unique sample delivery method is a particular focus. A thorough account of the theoretical and experimental methodology is given and the application of the UED3 and UED4 instruments to study fundamental photophysical and photochemical processes for several molecular chromophores is presented.

Chapter 2 gives an overview of the physics of gas-phase electron diffraction, which builds the foundation for the understanding of subsequent chapters. Particular emphasis is placed on the assumptions made for the derivation of the analytical scattering equations that are used to model the experimental data. Chapter 3 describes the UED4 experimental apparatus and all of its components in detail. (Some new additions to the UED3 instrument are also included.) This chapter also contains a published theoretical account of the spatial and temporal resolutions achievable in UED experiments.<sup>4</sup> Chapter 4 details the postprocessing steps, by which structural information is extracted from the two-dimensional diffraction intensities, i.e., processing of the diffraction images and subsequent data analysis procedures. The utilized computational algorithms that are implemented for this purpose are described. Chapter 5 summarizes the published and unpublished results that were obtained in the UED lab since 2006. The ground-state and product-state diffraction data for a number of molecules are reported, and the steps taken

---

during structural refinement are outlined. The initial implementation of the laser desorption delivery method for electron diffraction was demonstrated through the study of the intact gas-phase nucleobases, uracil and guanine.<sup>24</sup> Subsequent, time-resolved studies with UED4 include the much larger molecular structure of the photoswitchable spiropyran molecule, 6-nitro-BIPS,<sup>25</sup> and also the amino acid tryptophan. Additionally, during the construction of UED4, the molecular structural dynamics of nitrobenzene<sup>3</sup> and indole<sup>5</sup> were investigated with UED3. Chapter 6 contains the concluding remarks and outlines the future challenges for UED that emerge from the results obtained during this thesis research.

# **Chapter 2.**

## **Electron Diffraction Theory**

This chapter describes the theoretical basis for gas-phase electron diffraction and derives the analytical scattering function (the model function), which is used to analyze the experimental diffraction data and extract structural parameters. The model function will be developed starting from basic principles and additional layers of complexity will be subsequently added. A particular emphasis will be placed on the important assumptions, which are made in the derivations. For a more in-depth treatment, the reader is referred to the treatments of scattering theory given in many quantum mechanics textbooks,<sup>26,27</sup> diffraction textbooks,<sup>28,29</sup> and in a previous thesis from this laboratory.<sup>8</sup>

## 2.1 Atomic Scattering

Electron scattering involves an electron traveling along the  $z$ -axis and encountering an electrostatic potential of an atom located at the origin. Upon interaction with the atomic potential, a portion of the electron wave scatters in all directions, while the remainder continues unaltered. Thus, in the asymptotic limit of distances larger than the range of the potential ( $rV(\mathbf{r}) \rightarrow 0$  as  $\mathbf{r} \rightarrow \infty$ ), the electron wave, after the scattering event, can be expressed as a superposition of the original plane wave and an outgoing spherical wave.<sup>27</sup>

$$\Psi \xrightarrow{r \rightarrow \infty} A \left[ e^{ik_0 z} + f(\mathbf{k}_0, \mathbf{k}) \frac{e^{i\mathbf{k}\cdot\mathbf{r}}}{|\mathbf{r}|} \right] . \quad (2.1)$$

where  $A$  is a normalization factor, and the wavevectors  $\mathbf{k}_0$  and  $\mathbf{k}$  of the plane and the spherical wave, respectively, point in the direction of propagation, as depicted in Figure 2.1. The quantity  $f(\mathbf{k}_0, \mathbf{k})$  is called the scattering amplitude. We speak of elastic

scattering, if, through the scattering process, the momentum of the electron was changed only in its direction and not its magnitude ( $|\mathbf{k}| = |\mathbf{k}_0|$ ), and inelastic scattering otherwise, ( $|\mathbf{k}| \neq |\mathbf{k}_0|$ ).

Because the unscattered wave did not interact with and does not carry any information about the scattering potential, we will not consider it further. Furthermore, the unscattered wave amplitude can be assumed to be zero everywhere except very close to the z-axis,<sup>27</sup> so that the unscattered and scattered amplitudes do not interfere (cross terms are negligible) and we can safely approximate the intensity measured at point  $\mathbf{r} = \mathbf{R}$  as

$$I = |\Psi|^2 \approx \frac{A^2}{R^2} f(\mathbf{k}_0, \mathbf{k})^2 \quad (2.2)$$

Thus,  $f(\mathbf{k}_0, \mathbf{k})$  is the quantity that contains the information about the scattering potential.

To be able to interpret the measured intensity, we are required to define a model, whose functional form and parameters relate to quantities of interest and whose value reproduces the experimental data. To arrive at the model commonly used in the field of electron diffraction, we now have to make two simplifying assumptions. First, we assume the scattering potentials of atoms to have spherical symmetry. We know this assumption to be incorrect, given the shape of atomic p and d orbitals as well as molecular orbitals, but this assumption, nonetheless, holds remarkably well due to the dominant influence of the nuclear point charge on the overall potential at large enough scattering angles (see Section 2.2). For a spherically symmetric potential,  $f(\mathbf{k}_0, \mathbf{k})$  becomes  $f(|\mathbf{k}_0 - \mathbf{k}|)$  and, consequently, the scattering amplitude has no dependence on

the azimuthal angle around the z-axis.<sup>26,27</sup> Second, we assume that the scattering process is elastic, i.e.,  $|\mathbf{k}| = |\mathbf{k}_0|$  (inelastic processes are mentioned later in this chapter). Considering only elastic processes, we can find a geometric relationship between the scattering angle,  $\theta$ , and the magnitude of the momentum transfer vector,  $s$ , as shown in Figure 2.1.

$$s = |\mathbf{s}| \equiv |\mathbf{k}_0 - \mathbf{k}| = 2|\mathbf{k}_0| \sin\left(\frac{\theta}{2}\right) = \frac{4\pi}{\lambda_0} \sin\left(\frac{\theta}{2}\right) \quad (2.3)$$

Given these assumptions, we can write the quantity  $f(\mathbf{k}_0, \mathbf{k})$  either as  $f(\theta)$  or  $f(s)$ , the latter being more common, because  $s$  is generally used as a radial coordinate in the diffraction plane.

The elastic scattering amplitude  $f(s)$  can be calculated either by solving the Schrödinger equation using a Green's function and then making the Born approximation to the desired order or through a partial wave expansion.<sup>26,27</sup> The first-order Born approximation gives only real values for  $f(s)$  and is only valid for weakly scattering atoms of low atomic number. Summation over partial waves using potentials obtained from the relativistic Hartree Fock wavefunctions (which were made centrosymmetric via Poisson's equation) is presently the standard of the discipline and gives scattering amplitudes that include an additional phase shift  $\eta(s)$ ; these scattering amplitudes are available in tabulated form for most elements.<sup>30</sup> Thus, the elastic scattering amplitude  $f(s) = |f(s)|e^{i\eta(s)}$  is a complex quantity and determines the element specific amplitudes and the phase shifts of the spherical wave upon scattering from a given atom.

## 2.2 Electron Scattering from Nuclei and Electrons

To illustrate the contribution of the nuclear potential and the electron density to the atomic scattering amplitudes, the following calculation can provide illuminating insight. Using the first-order Born approximation, the elastic scattering factor is given as the Fourier transform of the three-dimensional scattering potential,

$$f(k, k') = -\frac{m_e}{2\pi\hbar^2} \int d^3x e^{i(\vec{k}-\vec{k}')\cdot\vec{x}} V(\vec{x}) \quad . \quad (2.4)$$

Since the scattering process is mediated through the Coulombic interaction, the scattering potential can be written as

$$V(\vec{x}) = -\frac{Ze^2}{4\pi\epsilon_0|\vec{x}|} + \frac{Z'e^2}{4\pi\epsilon_0} \int d^3\vec{x}' \frac{\rho(\vec{x}')}{|\vec{x}'-\vec{x}|} \quad , \quad (2.5)$$

where the first term represents the attractive potential of a point charge (pc) with atomic number  $Z$ , while the second term represents the repulsive interaction with the extended charge distribution of the  $Z'$  electrons in the atom. Substituting Equation 2.5 into Equation 2.4 and changing the integration variables in the second term  $(\vec{x}, \vec{x}') \rightarrow (y \equiv \vec{x} - \vec{x}', \vec{x}')$ , we obtain

$$\begin{aligned} f(k, k') &= \left[ \frac{m_e}{2\pi\hbar^2} \int d^3x e^{i(\vec{k}-\vec{k}')\cdot\vec{x}} \frac{Ze^2}{4\pi\epsilon_0|\vec{x}|} \right] - \left[ \frac{m_e}{2\pi\hbar^2} \int d^3x e^{i(\vec{k}-\vec{k}')\cdot\vec{x}} \frac{Z'e^2}{4\pi\epsilon_0} \int d^3\vec{x}' \frac{\rho(\vec{x}')}{|\vec{x}'-\vec{x}|} \right] \\ &= \left[ \frac{m_e}{2\pi\hbar^2} \frac{Ze^2}{4\pi\epsilon_0} \int d^3x \frac{e^{i(\vec{k}-\vec{k}')\cdot\vec{x}}}{|\vec{x}|} \right] - \left[ \frac{m_e}{2\pi\hbar^2} \frac{Z'e^2}{4\pi\epsilon_0} \int d^3y \frac{e^{i(\vec{k}-\vec{k}')\cdot y}}{|y|} \times \int d^3\vec{x}' e^{i(\vec{k}-\vec{k}')\cdot\vec{x}'} \rho(\vec{x}') \right] \quad (2.6) \\ &= f_{pc}(k, k') - f'_{pc}(k, k') \times F \quad . \end{aligned}$$

Here, we see that the scattering amplitude due to the extended charge distribution (second term) can be expressed as the scattering amplitude due to a point charge multiplied by a form factor  $F$ .

The scattering potential due to a point charge is spherically symmetric and so the angular integrations can be performed explicitly. We recognize that for a spherical potential (such as Equation 2.5)  $f(k, k')$  is a function of  $|\vec{s}| = |\vec{k} - \vec{k}'| = 2k \sin(\theta/2)$  and Equation 2.4 becomes

$$\begin{aligned}
 f_{\text{spherical}}(s) &= -\frac{m_e}{2\pi\hbar^2} \int d^3x e^{i\vec{s}\cdot\vec{x}} V(r) \\
 &= -\frac{m_e}{2\pi\hbar^2} \int_0^\infty r^2 dr \int_{-1}^1 d(\cos(\theta)) \int_0^{2\pi} d\phi e^{isr \cos(\theta)} V(r) \\
 &= -2\pi \frac{m_e}{2\pi\hbar^2} \int_0^\infty r^2 dr \frac{e^{isr} - e^{-isr}}{isr} V(r) \\
 &= -\frac{2m_e}{\hbar^2} \int_0^\infty dr r \frac{\sin(sr)}{s} V(r) .
 \end{aligned} \tag{2.7}$$

To find an analytical solution for the scattering amplitude due to a point charge, we employ the Yukawa potential,

$$V(\vec{x}) = \frac{V_0 e^{-\mu r}}{\mu r} , \tag{2.8}$$

which, provided that  $\frac{V_0}{\mu} \rightarrow \frac{Ze^2}{4\pi\epsilon_0}$  as  $\mu \rightarrow 0$ , reduces to the coulomb potential of a point charge. With the help of the Yukawa potential, Equation 2.7 can be solved to give

$$f_{\text{Yukawa}}(s) = \frac{2m_e}{\hbar^2} \frac{V_0}{\mu} \frac{1}{s^2 + \mu^2} , \tag{2.9}$$

and

$$f_{\text{Yukawa}}(s) \xrightarrow{\mu \rightarrow 0} f_{\text{pc}}(s) = \frac{2m_e}{\hbar^2} \frac{Ze^2}{4\pi\epsilon_0} \frac{1}{s^2} . \tag{2.10}$$

Here, we see that the scattering amplitude due to a point charge depends linearly on the atomic number  $Z$  and decays as  $\frac{1}{s^2}$ .

It only remains to evaluate the integral for the form factor  $F$ ,

$$F = \int d^3\bar{x}' e^{i(\bar{k}-\bar{k}')\bar{x}} \rho(\bar{x}') \quad . \quad (2.11)$$

Using low-order atomic orbitals, this integral can be evaluated analytically, e.g., for a hydrogen 1s orbital,

$$\Psi_{H,100} = \frac{1}{\sqrt{\pi}} \left( \frac{1}{a_0} \right)^{3/2} e^{-\frac{r}{a_0}} \quad . \quad (2.12)$$

Substituting the absolute square of Equation 2.12 into Equation 2.11 gives

$$\begin{aligned} F_{H,100}(s) &= \int d^3\bar{x}' e^{i(\bar{k}-\bar{k}')\bar{x}} |\Psi_{H,100}|^2 \\ &= \frac{16}{(4 + a_0^2 s^2)^2} \quad . \end{aligned} \quad (2.13)$$

Using these results good agreement with the tabulated amplitudes can be achieved, as shown for the hydrogen atom in Figure 2.2. Also it is evident that the relative contributions of the electron distribution and the nuclear potential vary as a function of the momentum transfer  $s$ .

### 2.3 Molecular Scattering

To set up the discussion for molecular scattering, we need to slightly displace the atomic potential from the origin by the vector  $\mathbf{r}_0$ . The scattered wave at point  $\mathbf{r} = \mathbf{R}$  then becomes<sup>8</sup>

$$\Psi_{scattered}(\mathbf{R}) = \frac{Ae^{i\mathbf{k}\cdot\mathbf{r}}}{|\mathbf{R}|} |f(s)| e^{i\eta(s)} e^{is\cdot\mathbf{r}_0} \quad , \quad (2.14)$$

where we can see that the displacement from the origin merely causes an additional phase shift  $e^{is\cdot\mathbf{r}_0}$  to the scattered spherical wave. Next, we consider a situation, in which we have two or more spherically symmetric scattering potentials, from which the incident electron wave can scatter. The incident electron wave has finite spatial extent, usually termed the coherence length, and all atomic scattering centers within that extent are illuminated coherently and will therefore emit scattered spherical waves with a well-defined phase relationship. (The concept of coherence and how it relates to the spatial resolution attainable in a UED experiment will be treated in detail in Section 3.2) Assuming perfectly coherent illumination, we can write Equation 2.14 to include a sum over all the scattering centers with respective position vectors  $\mathbf{r}_i$

$$\Psi_{scattered}(\mathbf{R}) = \sum_i \frac{Ae^{i\mathbf{k}\cdot\mathbf{r}}}{|\mathbf{R}|} |f_i(s)| e^{i\eta_i(s)} e^{is\cdot\mathbf{r}_i} + O\left(\sum_i \sum_{j \neq i} f_i(s) f_j(s)\right) \quad (2.15)$$

Here, we keep only terms up to first order in the scattering amplitude  $f_i(s)$ , and discard the small higher-order terms. This means that once atom  $i$  has emitted a spherical wave, it is assumed that this spherical wave does not scatter anymore from any additional atom  $j$  in its path, as shown in Figure 2.3. We have thus restricted ourselves to single scattering events only.<sup>31,32</sup> The measured intensity of the scattered electrons then becomes

$$\begin{aligned}
I \approx |\Psi_{scattered}(\mathbf{R})|^2 &= \left( \sum_i \frac{Ae^{i\mathbf{k}\cdot\mathbf{r}}}{|\mathbf{R}|} |f_i(s)| e^{i\eta_i(s)} e^{is\mathbf{r}_i} \right) \cdot \left( \sum_i \frac{Ae^{-i\mathbf{k}\cdot\mathbf{r}}}{|\mathbf{R}|} |f_i(s)| e^{-i\eta_i(s)} e^{-is\mathbf{r}_i} \right) \\
&= \frac{A^2}{\mathbf{R}^2} \sum_i \sum_j \operatorname{Re} \left[ |f_i(s)| |f_j(s)| e^{i(\eta_i(s)-\eta_j(s))} e^{is(\mathbf{r}_i-\mathbf{r}_j)} \right] .
\end{aligned} \tag{2.16}$$

Before we only consider the real part of the quantity in square brackets, we need to carry out the average over the distribution of spatial orientation of the internuclear separation vector,  $\mathbf{r}_i - \mathbf{r}_j$ . It can be shown that the spatial average over an isotropic orientation distribution transforms the exponential term into a sinc function, which is entirely real.<sup>8</sup>

$$\left\langle e^{is(\mathbf{r}_i-\mathbf{r}_j)} \right\rangle_{\text{Spatial Average}} = \frac{\sin(sr_{ij})}{sr_{ij}} , \tag{2.17}$$

where  $r_{ij} = |\mathbf{r}_i - \mathbf{r}_j|$ . Thus, the intensity can now be written as

$$\begin{aligned}
I \approx |\Psi_{scattered}(\mathbf{R})|^2 &= \frac{A^2}{\mathbf{R}^2} \sum_i \sum_j |f_i(s)| |f_j(s)| \cos(\eta_i(s) - \eta_j(s)) \frac{\sin(sr_{ij})}{sr_{ij}} \\
&= \frac{A^2}{\mathbf{R}^2} \sum_i |f_i(s)|^2 + \frac{A^2}{\mathbf{R}^2} \sum_i \sum_{j \neq i} |f_i(s)| |f_j(s)| \cos(\eta_i(s) - \eta_j(s)) \frac{\sin(sr_{ij})}{sr_{ij}} \\
&= I_A(s) + I_M(s) \quad ,
\end{aligned} \tag{2.18}$$

where we have separated the atomic scattering intensity,  $I_A(s)$ , from the molecular intensity,  $I_M(s)$ , which contains the interference terms. It is important to note that the internuclear separation  $r_{ij}$  includes *all* atom pairs in the molecule, whether they are bonded or nonbonded.

In arriving at Equation 2.18, we have made two important assumptions. The first assumption, known as the independent atom model (IAM), states that molecules are made up of spherical atoms, i.e., we neglect the aspherical shape of atomic and molecular orbitals. This assumption can hold, because the electrons are scattered into high angles

dominantly by the nuclear point charges rather than the electron charge density surrounding them (see Section 2.2). The weaker field due to the electron charge density becomes comparable to the nuclear field, only if the electron's impact parameter is large (i.e., the corpuscular high-energy electrons pass far from the nucleus).<sup>8</sup> The consequent momentum transfer is then small, such that the IAM suffers some inadequacy only at small scattering angles ( $s < 5 \text{ \AA}^{-1}$ ), as shown in Figure 2.2.<sup>28,33</sup> The second assumption, made in Equation 2.15, excluded multiple scattering processes and, as such, we obtain only two-atom interferences. If we had included higher-order terms in Equation 2.15, then we would have obtained additional three-atom, and four-atom cross terms in Equation 2.16 and 2.18. The assumption is satisfactory, when using high-energy electrons (30 – 60 keV) in combination with molecules made up of weakly scattering elements ( $Z \leq 14$ ), because under such conditions, the multiple scattering contribution to the molecular intensity,  $I_M(s)$ , is predicted to be less than one percent.<sup>34-36</sup> When using slow electrons (<1-10 keV) and/or strongly scattering elements, multiple scattering effects have to be included.<sup>31,32,37,38</sup> The inclusion of multiple scattering effects greatly increases the complexity of the model with the drawback that the resulting equations have to be solved numerically and the computational efforts increase substantially.

The inelastic scattering processes, which we have ignored thus far, are appended to the atomic scattering intensity in the form of

$$I_A(s) = \frac{A^2}{\mathbf{R}^2} \sum_i \left\{ |f_i(s)|^2 + \frac{4S_i(s)}{a_0^2 s^4} \right\} \quad , \quad (2.19)$$

where  $S_i(s)$  are the tabulated inelastic scattering factors<sup>30</sup> and  $a_0$  is the Bohr radius. By appending inelastic scattering intensity to the atomic scattering intensity we have

assumed that the amplitudes of the inelastically scattered waves are incoherent, do not contribute to any measureable structural information to the diffraction pattern, and can be modeled as a smooth background.<sup>28</sup>

## 2.4 Molecular Vibrations

The internuclear distance,  $r_{ij}$ , which appears as the argument of the sinc function in Equation 2.18, is distributed in space due to vibrational oscillations. As a first approximation, we can assume that the atoms behave like a harmonic oscillator, such that the distance between them is given by the probability distribution

$$P(r, T) = \frac{1}{\sqrt{2\pi l_h(T)^2}} \exp\left(-\frac{(r-r_e)^2}{2l_h(T)^2}\right), \quad (2.20)$$

where  $r_e$  is the equilibrium distance and  $l_h(T)$  is the root-mean-squared (rms) amplitude of vibration at temperature  $T$ . Using this probability function, the molecular ensemble can be averaged over all sampled vibrational geometries to obtain (after dropping higher-order terms of a binomial expansion and simplifying the algebra)<sup>8</sup>

$$\begin{aligned} I_M(s, T) &= \frac{A^2}{\mathbf{R}^2} \sum_i \sum_{j \neq i} |f_i(s)| |f_j(s)| \cos(\eta_i(s) - \eta_j(s)) \int_0^\infty \frac{\sin(sr_{ij})}{sr_{ij}} P_{ij}(r, T) dr \\ &= \frac{A^2}{\mathbf{R}^2} \sum_i \sum_{j \neq i} |f_i(s)| |f_j(s)| \cos(\eta_i(s) - \eta_j(s)) \exp\left(-\frac{1}{2} l_{h,ij}^2 s^2\right) \frac{\sin(sr_{a,ij})}{sr_{e,ij}}, \end{aligned} \quad (2.21)$$

where  $r_{a,ij}$  is the temperature dependent effective internuclear distances between  $i$ th and  $j$ th nuclei given by

$$r_a = r_e - \frac{l_h^2}{r_e}, \quad (2.22)$$

where the temperature dependence of  $I_h$  and  $r_a$  has been suppressed. The exponential damping term attenuates the  $I_M(s, T)$  signal, because the diffraction information is washed out, especially at higher scattering angles, if molecular vibrations are intense. To compare the quantity  $r_a$  (the electron diffraction operational internuclear distance) to reported internuclear distances obtained through other methods, it must first be converted to  $r_e$  using Equation 2.22 (distances reported in subsequent chapters of this thesis are  $r_e$  values).

To highlight the oscillatory diffraction features, the molecular scattering intensity (Equation 2.21) is transformed to the modified molecular scattering function according to

$$sM(s, T)^{Theory} = s \cdot \frac{I_M(s, T)}{f_i(s)f_j(s)} \quad , \quad (2.23)$$

where  $f_i(s)f_j(s)$  are usually chosen to represent the tabulated<sup>30</sup> elastic atomic scattering amplitudes of carbon,  $f_C(s)f_C(s)$ , which is the most abundant element in the sample. The process of defining  $sM(s, T)^{Theory}$  by fitting it to experimental diffraction data using an initial guess molecular structure is described in Section 4.3.

## 2.5 Modified Radial Distribution Function

The modified molecular scattering function, which is given in reciprocal space coordinates  $s$ , can be Fourier transformed into the modified radial distribution function having real space coordinates, according to

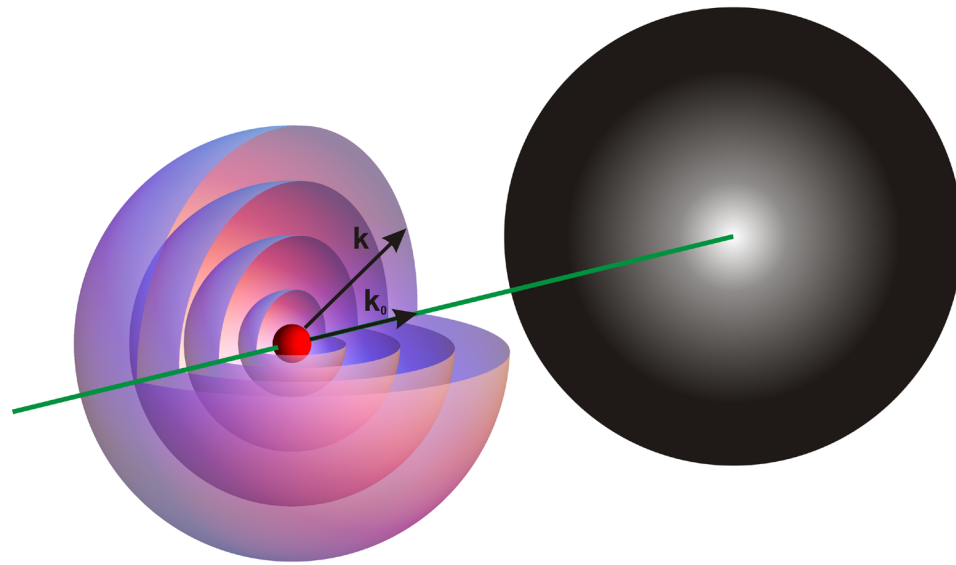
$$f(r, T) = \int_0^{s_{max}} sM(s, T) \sin(sr) \exp(-ks^2) ds \quad , \quad (2.24)$$

where the damping envelope function,  $\exp(-ks^2)$ , has been used to eliminate the spurious ringing that the finite available  $s$ -range of the diffraction data (indicated by the limits of integration) introduces. A value of  $k = 0.02 \text{ \AA}^2$  is typically used for this purpose. If experimental data is to be transformed, a part of  $sM(s,T)^{Theory}$  has to be inserted to cover the  $s$ -range from 0 to  $s_{\min}$ , where experimental data is not available due to the presence of a physical beam block of finite size.

By performing the integration of Equation 2.24 explicitly, it can be shown that<sup>18</sup>

$$f(r,T) \propto \sum_i \sum_{j \neq i} \frac{Z_i Z_j}{r_{e,ij}} \exp \left[ -\frac{(r - r_{a,ij})^2}{2(2k - l_{ij}^2)} \right], \quad (2.25)$$

where we can see that the radial distribution function consists of a series of Gaussian peaks, centered at  $r_{a,ij}$ , that are broadened both by the damping term  $k$  and the mean-squared amplitudes of vibration  $l_{ij}^2$ . For very small molecules and molecules of high symmetry, the modified radial distribution function provides a very intuitive picture of the molecule, because the Gaussian peaks are well separated. For larger, more complex molecules, however, only the peaks for the first- and second-order nearest-neighbor bond distances are usually identifiable, while at larger distances, the peaks are strongly overlapping. Due to the dependence of the radial distribution function on the arbitrarily selected damping parameter  $k$ , fitting of diffraction data is performed exclusively in reciprocal space, in which experimental data was collected in the first place.



$$s = |\mathbf{s}| \equiv |\mathbf{k}_0 - \mathbf{k}| = 2|\mathbf{k}_0| \sin\left(\frac{\theta}{2}\right)$$

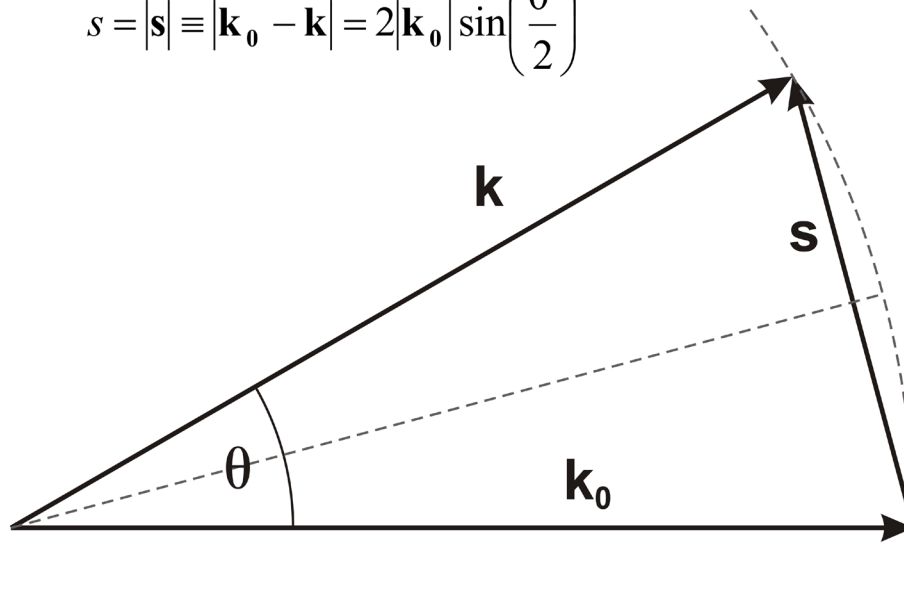


**Figure 2.1.** An atomic scattering center scatters a portion of the incoming electron plane wave with wavevector  $\mathbf{k}_0$  (shown in green) as an outgoing spherical wave with wavevector  $\mathbf{k}$  (concentric spheres). The amplitude of the scattered wave decreases rapidly with increasing scattering angle  $\theta$ , as shown on the schematic intensity distribution recorded on the detector. The difference of the wavevectors defines the scattering vector  $\mathbf{s}$ , which is used as the coordinate to describe the intensity distribution in the diffraction/detection plane.

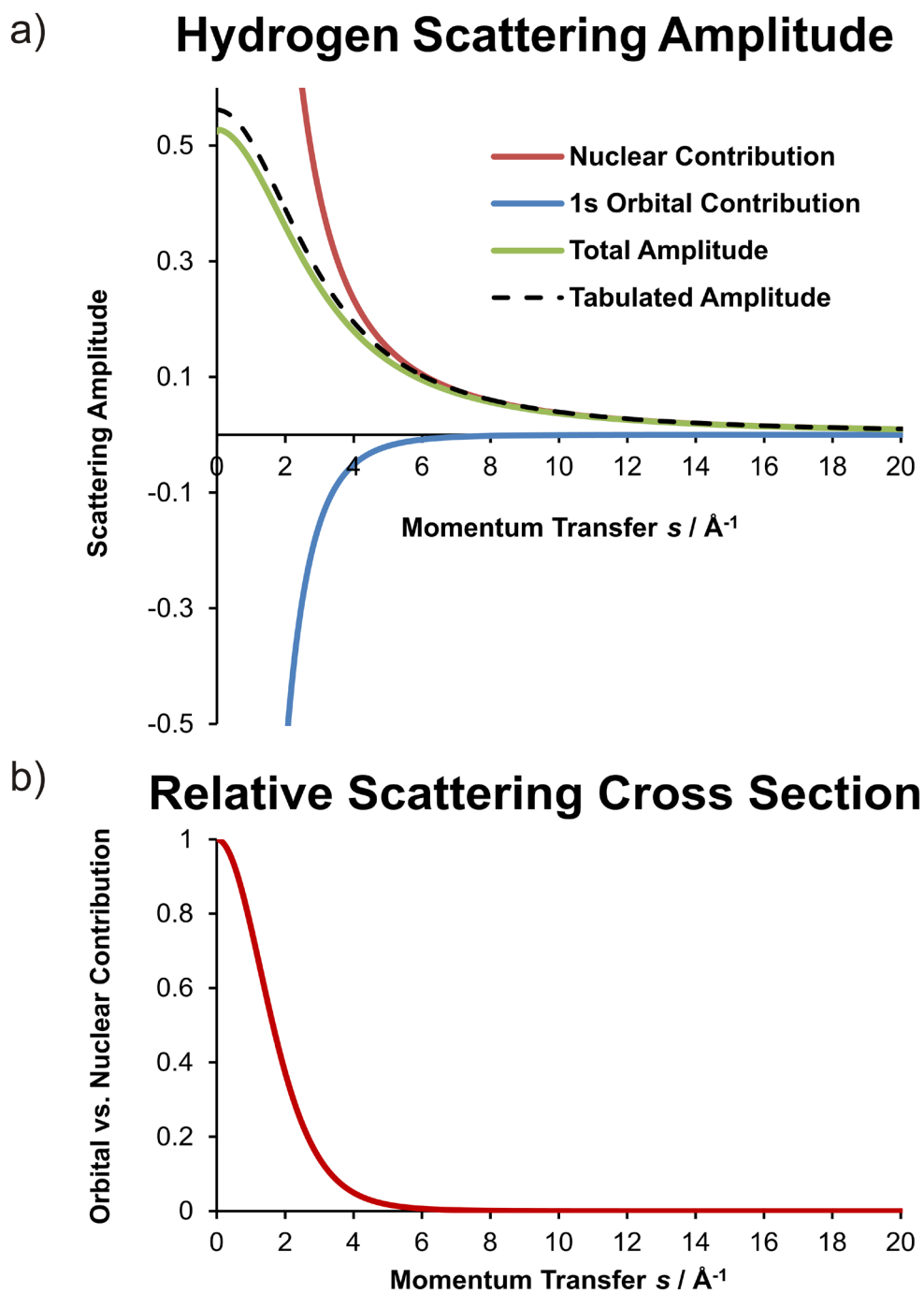


**Figure 2.2.** a) The total scattering amplitude of the hydrogen atom can be expressed as the sum of contributions originating from the nuclear point charge and from the delocalized charge density in the hydrogen 1s orbital. b) The orbital vs. nuclear contribution to the total scattering cross section is equal to square of Equation 2.13 and shows that incoming electrons are dominantly scattered by the nuclear potential at  $s > 5 \text{ Å}^{-1}$ , while at  $s < 5 \text{ Å}^{-1}$  the valence electrons contributions becomes more pronounced until the asymptotic value of one is reached at zero momentum transfer.

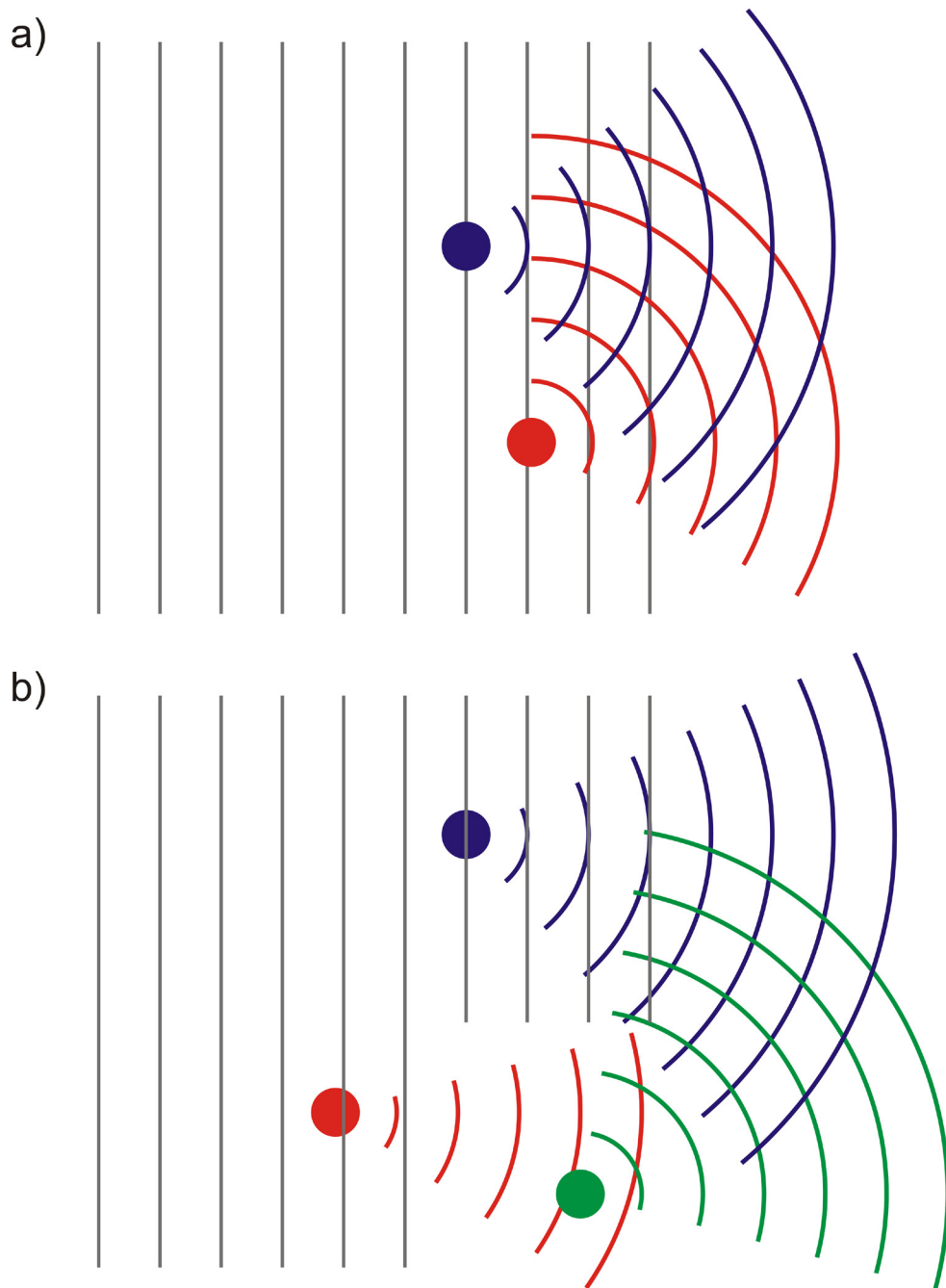


**Figure 2.3.** Interference of scattered wave amplitudes. a) Two atomic scattering centers scatter a portion of the incoming electron plane wave (grey) as outgoing spherical waves (red, blue), which interfere with each other on the detector. Only portions of the wave fronts are shown for clarity. b) In the diffraction theory used in this thesis, the scattered waves (red, blue) are assumed not to scatter again by additional atoms in its path. Thus, the multiple scattering amplitudes (green) are assumed to be zero. The nonzero first-order spherical wave amplitude originating from the green atomic scattering center due to scattering of the incoming plane wave (grey) is omitted for clarity.

# **Chapter 3.**

## **Instrumentation**

This chapter describes the instrumentation used for a gas-phase UED experiment. It will give a detailed description of the entire UED4 apparatus and its individual components, which was built as part of this thesis research and used to obtain the results presented in Chapter 5. Also, the novel additions made to the UED3 apparatus will be covered. For a detailed account of the UED3 apparatus, the reader is referred to previous theses from this lab.<sup>9,18</sup> Section 3.1 will cover the experimental components of UED4 (and some of UED3) and Section 3.2 will address the temporal and spatial resolution of an electron diffraction experiment through an in-depth look at the electron pulse propagation dynamics.<sup>4</sup>

## 3.1 UED Instrumental Components

### 3.1.1 Vacuum Chambers

The UED3 and UED4 diffraction instruments consist of two differentially pumped vacuum chambers, an electron gun chamber and a scattering chamber, as shown in Figure 3.1. The electron gun chamber consists of an upright cylinder with an entrance port on top for the high-voltage feedthrough (60 kV; Ceramaseal), lateral entrance and exit ports for the ultraviolet (UV) laser beams and for the electron pulses, and a port for pumping at the bottom. A vacuum of  $1 \cdot 10^{-8}$  torr is maintained in this chamber by a turbo-molecular pump (BOC Edwards) backed by a mechanical rotary vane pump (BOC Edwards). The electron gun assembly, including the photocathode and the anode (see Section 3.1.2), is mounted on a 8" conflat flange (CF) and fastened onto the chamber from the backside. The scattering chamber, also an upright cylinder, is pumped by a diffusion pump (Varian) to a vacuum of  $1 \cdot 10^{-7}$  torr. As shown in Figure 3.1, the chamber

has a port on top for a desorption laser inlet window and several lateral ports for laser inlet and outlet windows, a viewport, electrical feedthroughs, vacuum gauges, and a port for mounting a UED3-style molecular beam nozzle on a translation stage (see Section 3.1.5.1), as well as a port for a rotational feedthrough (MDC Vacuum Products) that transmits the rotational motion that drives the desorption source (see Section 3.1.5.2). An extension nipple provides the attachment to the mounting flange of the detector assembly (see Section 3.1.4). This nipple also contains an electrical feedthrough port for the Faraday cup (see Section 3.1.4.6.2),

The electron gun chamber and the scattering chamber are connected through several extension nipples that together form the electron optical column. A gate valve makes it possible to seal off the two chambers, such that vacuum can be maintained in one chamber, while the other chamber is vented. The electron optical components (see Section 3.1.3) are mounted onto the optical column to provide the electrical and magnetic fields needed to steer and shape the electron pulses.

### 3.1.2 Electron Gun

The UED4 electron gun differs from the UED3 electron gun in that the photocathode is illuminated from the front rather than from the back. UV laser pulses, either from ns-Nd:YAG laser (A-Optowave, 100  $\mu\text{J}/\text{pulse}$  at 266 nm, 8 ns full width at half maximum (FWHM)) or from a fs-Ti:Sapphire laser (Spectra Physics, Tsunami/Super Spitfire 300  $\mu\text{J}/\text{pulse}$  at 266 nm,  $\sim 130$  fs FWHM),<sup>18</sup> generate free electrons at the photocathode by the photoelectric effect. These free electrons are then accelerated across the potential difference between the cathode and anode and finally extracted through a

small extraction pinhole into the drift region of the electron optical column, as shown in Figure 3.2. The back-illumination design, used for the UED3 electron gun, demands that the cathode material (silver) is deposited onto a sapphire window as a thin film of 20-25 nm thickness. Any dust particles covered by the silver coat will lead to surface irregularities and consequently to electrical arcing across the applied potential difference of 30 kV. The finite lifetime of the UED3 photocathode and its frailty (only about 50% of all newly coated cathodes can hold the 30 kV for the duration of the experiment) often lead to aborted experiments, as well as long start-up times. In contrast, the front-illumination design permits the cathode to be machined out of a solid piece of metal (Ta, Cu, or Mg), which, after polishing can readily hold voltages of 60 kV over a 2-3 mm gap. The robustness of solid metal substrate toward the UV laser beam ensures a lifetime of several years for these cathodes.<sup>14,39</sup>

The UED4 gun can produce  $2.0 \cdot 10^5$  or  $5.0 \cdot 10^7$  electron per pulse, when using UV light pulses of either femtosecond (fs) or nanosecond (ns) duration, respectively. Producing higher electron currents than these by increasing the laser intensity lead to degradation of the beam profile due to space-charge effects among the electrons or destroyed the polished photocathode surface through laser ablation and subsequent electrical arcing. Characterization of the transverse electron beam size is discussed in the following section and the temporal pulse length is treated in Section 3.2.

### 3.1.3 Electron Optics

The electrons emerging from the extraction pinhole in the anode are steered and focused by a variety of electron optical components, as summarized in Figure 3.3.

Alignment of the electron beam involves careful adjustment of each of these components and typically produces an electron probe size of  $\sim 750 \mu\text{m}$  FWHM at the interaction region.

A magnetostatic deflector, consisting of four opposing solenoid coils around an iron core, is located immediately at the exit of the electron gun chamber to steer the electrons through a second pinhole placed further down the optical axis. By adjusting the currents in the coils located opposite of each other, magnetic fields are produced as shown in Figure 3.3a, and the electron beam can be deflected in two orthogonal directions.

A magnetic lens focuses the diverging electron beam, such that its footprint on the detector is smallest. The solenoid holder can be adjusted at six points, as shown in Figure 3.3b, to make the magnetic lens axis coincident with the optic axis in order to achieve optimal focusing behavior. Even though great care was taken to uniformly wind the solenoid coil, the magnetic lens suffers from considerable astigmatism. This astigmatism is corrected by the addition of a magnetic quadrupole field (stigmator), which shapes the electron packet, as shown in Figure 3.3c, into a round footprint at the detector and the interaction region. The coils of the stigmator assembly are freely adjustable on the mounting ring, such that the resulting field can be fine-tuned manually to achieve optimal focusing behavior.

At the entrance of the scattering chamber, the electron beam can be steered toward the interaction region by two mutually perpendicular pairs of electrostatic deflector plates. The aluminum plates are mounted on nonconducting plastic rods inside the vacuum, as shown in Figure 3.3d, and wired to an electrical feedthrough. By

adjusting the independent voltages across the two pairs of deflection plates, two orthogonal electric fields are produced to steer the electrons toward the center of the detection screen.

### **3.1.4 Detector**

#### ***3.1.4.1 Detector Assembly***

Due to the inherently low electron flux of a UED experiment, the detector has to be able to detect every scattered electron to accumulate enough signal intensity in a reasonable amount of time. To maximize the quantum efficiency of electron detection, a scintillator/image intensifier/CCD detection system was chosen, as shown in Figure 3.4, based on the detailed rationale considering the imaging characteristics of all detector components, which were previously evaluated in detail.<sup>8</sup> The principles of the electron detection process employed here are as follows: High-energy electrons (30-60 keV) bombard the phosphor screen and generate photons in the process. These photons are collected by a fiber-optic faceplate (Incom, refractive index = 1.87) and directed onto an image intensifier (Photek), which amplifies the photon signal by several orders of magnitude. The amplified two-dimensional photon signal (image) is then de-magnified by a fiber-optic taper (Incom) and ultimately recorded by a CCD camera (Princeton Instruments). Figure 3.5 shows the detector assembly of UED4, inside its custom built housing. The respective detector components are coupled together using a refractive index matching fluid (Saint Gobain BC-630, refractive index = 1.465) to eliminate reflections at the fiber-optic interfaces, which could result in experimental artifacts, such as Newton fringes, in the acquired images.<sup>40</sup> Stepwise assembly of the detection system

was performed by stacking the fiber-optic components on top of each other, starting with the CCD camera, as shown in Figure 3.6.

#### **3.1.4.2 Phosphor Screen**

The phosphor scintillator screen is manufactured by sedimentation of P47 ( $\text{Y}_2\text{SiO}_5\text{:Ce,Tb}$ ) phosphor grains on a fiber-optic faceplate. After evaporation of the solvent, a powder coating remains on top of the substrate. Grain sizes are typically 1  $\mu\text{m}$  or larger, resulting in a visibly rough, but mechanically very fragile coating. The phosphor layer and the fiber-optic faceplate have limited electrical conductivity, and to avoid charging effects due to electron bombardment during the experiment, an optically transparent, electrically conducting layer of indium tin oxide (ITO) is applied to the fiber-optic prior to depositing the phosphor layer. This ITO layer is then grounded to the metal housing through a chrome ring sputtered on the outer area of the faceplate. In addition, the powder scintillator screen is sealed by sputtering an aluminum overcoat on top of it. The purpose of this aluminum overcoat is twofold: (i) It can increase the scintillator conversion efficiency by reflecting photons, which were isotropically emitted from the phosphor grains, back toward the fiber-optic substrate. (ii) It can block stray light from the scattering chamber and prevent it from triggering the phosphor and/or the photocathode of the image intensifier. Figure 3.7a and Figure 3.7b show the applied layers that make up a phosphor scintillator screen on a glass substrate.

Upon electron impact photons are emitted from phosphor grains in the near vicinity of the impact site. The emission intensity of the phosphor layer decays to 1% within 3  $\mu\text{s}$ , as shown in Figure 3.7c. Thus, there is no detectable afterglow from this

phosphor layer in subsequent images collected at a repetition rate of 1 kHz. Figure 3.7d shows the wavelength dependent emission intensity of the P47 phosphor. This emission spectrum is well matched to the excitation spectrum of the S20 photocathode of the image intensifier, which peaks at  $\sim 440$  nm, resulting in efficient signal transfer. The final conversion efficiency of the phosphor scintillator screen is difficult to estimate, as it depends on the grain size, the phosphor layer thickness, as well as the aluminum overcoat thickness. These parameters are only approximately known and can vary over the area of the detection screen. Conversion efficiency data from Proxitronic for a sample scintillator are shown in Table 3.1 for electron energies up to 15 keV and can serve a rough guideline.

The ability of the aluminum overcoat to block stray light in the scattering chamber is very important to the success of a time-resolved UED4 experiment, in which the presence of a very powerful UV pump laser pulse ( $\lambda = 266$  nm) and an IR desorption pulse ( $\lambda = 1064$  nm) can potentially produce a large and undesired background signal. We found that the light transmission through a commonly utilized 50-80 nm aluminum layer was much too permissive under our experimental conditions, resulting in unacceptably high background levels. To determine the thickness needed, we sputtered aluminum films of various thicknesses on a smooth glass substrate and measured the optical density. The results show that an aluminum film of 700 nm thickness results in an optical density of 15, as shown in Figure 3.7e, should prevent all the photons present in the scattering chamber, from entering the detector. Based on the published<sup>41</sup> electron stopping power of aluminum, a film of such a thickness reduces the kinetic energy of the electrons only minimally ( $<1.5\%$  for 60 keV electrons) as shown in Figure 3.7f.

Unfortunately, due to the aforementioned surface roughness of the powder phosphor layer, the aluminum deposition layer on top of it does not result in a highly reflective, mirror like appearance, but rather it retains a grayish grainy structure. This layer still retains microscopic apertures, through which light can penetrate. As a consequence, it is not possible to easily model the light transmission through this aluminum layer or to extrapolate from the optical densities of mirror like aluminum films.

To make the scintillator layer smoother, we experimented with embedding the phosphor grains in a formvar/nitrocellulose matrix. After sputtering a 1400 nm layer of aluminum on top of the scintillator, we still did not obtain a mirror like finish, but the resulting light transmission under our experimental conditions was reduced to acceptable levels. Given the rough surface, it might be beneficial to coat the aluminum layer from different angles, by mounting the fiber-optic on a swiveling mount during the sputtering process.

#### **3.1.4.3 Image Intensifier**

The gated, single stage, multi-channel-plate (MCP), proximity fused image intensifier with an active area of 75 mm in diameter and spatial resolution of 16 lp/mm (MTF = 5%) was purchased from Photek (Model MCP175). The input and output windows were made of fused fiber-optics (refractive index = 1.9). The unit was purchased with a S20 photocathode having a peak spectral sensitivity at ~440 nm, as shown in Figure 3.8a, which is well matched to the spectral output of the P47 phosphor scintillator, discussed above.

P43 phosphor was chosen as the output scintillator of the image intensifier to achieve optimum spectral overlap with the wavelength dependent detective quantum efficiency of the CCD camera. The drawback of this choice is the relatively long emission lifetime of P43, as was shown in Figure 3.7c. Calibration experiments established that, when scanning a high-intensity electron beam across the detector, a small afterglow is visible at repetition rates higher than 100 Hz. The UED experiment operates at a repetition rate of 1 kHz, such that this afterglow will contaminate each successive image to a small extent. Thus, the experimenter needs to make sure that the experimental conditions do not change during exposure times that involve more than one electron pulse. If the experimental conditions are changed, the image intensifier needs to be gated off for a time period long enough to ensure the luminescence of the P43 phosphor drops to negligible levels.

The image intensifier was delivered with its own power supply and gate module (Photek, PSU/GM10-50 Gate Module). This unit had a 9-pin D-Sub input and a 6-pin output connector; the wiring is shown in Table 3.2. To supply the correct voltage to power supply and to synchronize the gate unit with the master clock of the experiment, an additional control box was assembled as shown in Figure 3.8b. This control box allows the experimenter to adjust the image intensifier gain voltage at any time and combines (logical AND) the TTL gate pulses, supplied at 1 kHz by an external delay pulse generator (Berkeley Nucleonics, Model BNC575), with the electronic gate signal of the CCD camera, as shown in Figure 3.8c. The gate unit turns the image intensifier on and off by switching the photocathode potential between  $-200$  and  $+50$  V relative to the grounded MCP input. The rise and fall times of the gate are estimated to be close to

100 ns due to the large capacitance ( $\sim 400$  pF) of the 75 mm diameter photocathode. The gate delay from the delay generator was set relative to the electron generating laser pulse trigger to ensure that the “opening of the detector window” is always synchronized to the electrons arriving at the detector. The gate width needed to be chosen to be as large as 700 ns to include all scattered background photons of the time-delayed excitation laser, such that the background levels are the same for each time point.

#### 3.1.4.4 Gradient Filter

A radially symmetric neutral density filter (Reynard Corporation) was coated on the fiber-optic faceplate immediately following the image intensifier. As described in Chapter 2, the scattering signal decreases rapidly, but predictably with increasing scattering angle. A radial filter function,  $RFF(r)$ , in units of optical density, was therefore specified as

$$\begin{aligned} RFF(r) &= 2.5 - 0.122r && \text{for } 1.25 < r < 20.48, \\ &= 0 && \text{otherwise,} \end{aligned} \tag{3.1}$$

to increase the dynamic range of the detection system. Figure 3.9 shows the functional form and a schematic of the radially symmetric gradient filter, as well as its ability to reduce the intensity range of the scattering signal from 4 to 2 orders of magnitude. A small hole in the center of the detector was left uncoated to allow the direct beam to pass through unattenuated. The direct beam is used for beam alignment and calibration purposes prior to each experiment and is captured by a physical beam block (Faraday cup) in front of the detector during an experiment to prevent saturation (see Section 3.1.4.6). A fiber-optic taper was then coupled to the faceplate containing the

filter to reduce the size of the image emanating from the 75 mm diameter active area of the image intensifier to the 40 mm active area of the CCD camera.

#### **3.1.4.5 CCD Camera**

The scientific-grade, front-illuminated CCD camera with a 1340×1300 pixel array was purchased from Princeton Instruments (Model PI-SCX:1300W). Each pixel is 20 μm on the side and the array is coupled to the input window (refractive index = 1.9) with a 1:1 fiber-optic taper, giving the camera a resolution of 25 lp/mm. The CCD was cooled by a thermoelectric cooler to -35°C with the aid of a 25°C water circulation system. The quantum efficiency of the CCD chip over visible wavelengths is shown in Figure 3.10a and is well matched to the P43 phosphor emission from the image intensifier (see Figure 3.7d). Additionally the camera is outfitted with a custom designed flange to facilitate high-precision mechanical coupling to the fiber-optic components and to the image intensifier housing, as shown in Figure 3.10b.

The ST-133 camera controller, also provided by Princeton Instruments, contains the power supply, the analog and digital electronics, scan control and exposure timing hardware, and all necessary input and output connectors. Through the software interface the digitization rate of the analog-to-digital conversion can be specified (1 MHz is used for UED4) as well as an analog gain setting for the preamplifier (1x is used for UED4). The ST-133 also features a shutter output that delivers a TTL high signal for the duration of the exposure time and a TTL low signal otherwise. The signal from this shutter output and the 1kHz signal from the delay generator, which controls the gate width and its delay relative to the electron pulse, is combined through an AND gate inside the image

intensifier control box to give the final image intensifier gating signal, as described previously. In addition, the shutter output signal can be used to trigger external mechanical shutters that block the pump and probe laser beams.

### **3.1.4.6 Detector Calibration**

#### **3.1.4.6.1 Single Electron Counts**

As a single electron hits the primary phosphor screen, it generates a signal cascade of photons and electrons that ultimately results in a certain number of analog-to-digital units (ADU) or counts being read out from the CCD array. To calibrate the electron-to-ADU conversion efficiency at different image intensifier gain voltage settings, we performed single-electron count measurements. First, a background image over the entire CCD area was collected with the electron beam blocked to measure the detector dark count distribution, as shown in Figure 3.11a. Then, to measure the signal corresponding to a single electron, the probe laser beam was attenuated to the extent that only a few electrons would hit an unfiltered area of the detector. Usually an  $80 \times 80$  pixel region of interest (ROI) at the center spot was used for this measurement. The electron events need to be well separated spatially on the detector, such that signals corresponding to two or more electrons are not recorded. To achieve a statistically reliable measurement, 3000 individual images were collected with 1 ms exposure times (i.e., single pulses) each, as shown in Figure 3.11b. These images were then analyzed by two separate macros (available in the online supporting material<sup>42</sup>) written for the open source software tool ImageJ.<sup>43</sup> The macro “CustomHistogram.txt” creates an intensity histogram (in ADU) of all the pixels in the background image, as shown in Figure 3.11c.

The macro “IJBatchAnalyzeParticles.txt” analyzes the signal corresponding to every electron detection event in the stack of all signal images. Impact sites are characterized by having signal intensity above the detector background level determined in the previous step. The program identifies these impact sites and reports their area, mean ADU count, the standard deviation of the ADU count, minimum and maximum ADU count, their spatial coordinates in the image, and their total ADU count. After subtracting the background intensity, obtained in the previous step, from the total ADU count, an intensity histogram is generated, as shown in Figure 3.11d.

The probability that a single electron produces an ADU value in the interval  $[a, b]$  is given by the difference of the cumulative distribution function evaluated at the interval limits,  $P(a \leq x \leq b) = F_x(b) - F_x(a)$ . The pulse height distribution for a single-stage MCP system is characterized by an exponential distribution function, which produces the following expression:

$$\begin{aligned}
 P(a \leq x \leq b) &= F_x(b) - F_x(a) \\
 &= (1 - e^{-\lambda b}) - (1 - e^{-\lambda a}) \\
 &= e^{-\lambda a} - e^{-\lambda b} \quad .
 \end{aligned} \tag{3.2}$$

The pulse height distribution histogram, when plotted in a log-linear plot becomes a straight line, which is superposed on top of the (very large) wings of Gaussian background response. Therefore, the result of Equation 3.2 is only fit to the straight section of the experimentally obtained frequency histogram by changing the parameter  $\lambda$  and a global scale factor, as shown in Figure 3.11e and Figure 3.11f. The expectation

value for the electron conversion efficiency at a given image intensifier gain voltage,

$\left\langle \frac{ADU}{electron} \right\rangle_{Gain}$ , for this exponential distribution is then simply equal to  $\frac{1}{\lambda}$ .

#### 3.1.4.6.2 Faraday Cup

A second way to calibrate the detector gain is to record the electron current directly by capturing the electrons pulses in a Faraday cup that is mounted in front of the phosphor screen in the scattering chamber. The resulting voltage spike integrated over time is read out on a digital oscilloscope as  $\frac{Vt}{G}$ , where  $G$  is the gain factor of the current amplifier. The number of electrons can then be computed by

$$N_{electrons/pulse} = \frac{Vt}{GZe} \quad , \quad (3.3)$$

where  $Z$  is the impedance of the oscilloscope and  $e$  is the electron charge. Once the total number of electron per pulse is known, it can be compared to the mean ADU count of the electron pulse signal on the detector at a given image intensifier gain setting and the expectation value for the electron conversion efficiency,  $\left\langle \frac{ADU}{electron} \right\rangle_{Gain}$ , can be determined. In addition to the calibration measurements described here, the Faraday cup is also used to block the direct unscattered beam during an experiment and to monitor the pointing stability of the electron beam and the shot-to-shot stability of the electron count.

### 3.1.5 Molecular Sample Delivery

#### 3.1.5.1 High-Temperature Nozzle for UED3

The previously described gaseous sample delivery system for UED3 consisted of a resistively heated nozzle mounted on the top of the vacuum chamber.<sup>9,18</sup> The needle was assembled using stainless steel tubing culminating in a sharpened tip of chromatography tubing with a 180  $\mu\text{m}$  aperture. Outside the chamber, a cylindrical stainless steel sample reservoir was connected to the nozzle with tubing and fittings. The entire gaseous sample delivery line from the reservoir to the needle tip was electrically heated with thermocouple wire inside the vacuum and with fiberglass heating tape on the outside. The temperature of the line was continuously increased starting from the reservoir and ending at the needle tip to avoid any sample condensation and subsequent clogging of the tip opening. This setup was capable of producing tip temperatures of up to 600 K, which were sufficient to vaporize organic molecules with a low boiling point (e.g., nitrobenzene described in Section 5.3), but higher boiling point compounds were out of reach for UED analysis.

To improve the performance of the sample inlet system, we implemented a nozzle capable of reaching temperatures of up to 850 K, using an air heated jacket, as shown in Figure 3.12. The sample inlet tube is analogous to the old design, but is itself enclosed inside a bigger tube. Hot air from a heat gun is delivered through a third tube ending right above the needle, which ensures a continuous and uniform temperature gradient with the tip being the point of highest temperature. This nonresistive heating technique also eliminates any possible interference between an electric field and the electron beam. The gas line outside the vacuum was left unaltered, since the fiberglass heating tapes

employed there are capable of achieving temperatures that were sufficient for the purpose of current experiments.

The overall length of the sample delivery line is rather long (~40 cm) and, consequently, the chance sample decomposition increases. Given the high temperatures and long data acquisition time of ~7 days, during which the sample has to be continuously boiled, high demands are imposed on the surface properties of the delivery line. To minimize any unwanted sample-surface reactions, the entire inner surfaces of the tubing and the fittings, including the micron-sized needle orifice, were chemically passivated with a general-purpose inert layer (Silcosteel, Restek Performance Coating). This modification made it possible to study indole (see Section 5.4), which, previously, had polymerized in an uncoated sample vessel and clogged the needle tip.

After delivering the high boiling point sample into the gas phase, the vapor needs to be kept from expanding to the walls of the UED3 scattering chamber for several reasons. First, the sample vapor will coat the UV laser inlet window, get burnt on it, and lower the overall transmission of the laser light, which in turn reduces the time-resolved signal intensity. Second, the sample will enter the diffusion pump, which, operating at ~250°C, is not hot enough to vaporize the sample. Consequently the diffusion pump would have to be disassembled and cleaned after every experiment. Third, the phosphor screen of the detector would be damaged by the continued deposition of a chemical that has a very low vapor pressure at room temperature and cannot easily be pumped out of the chamber. To capture the sample, a cryo-trap was designed and mounted inside the vacuum directly below the needle orifice, as shown in Figure 3.13a. The whole cryo-trap assembly is held in place by its own liquid nitrogen delivery lines to ensure that nothing

else inside the chamber is in thermal contact with the cryo-trap. The base unit consists of a ring shaped liquid nitrogen reservoir. The actual trap is a thick-walled aluminum cup that is screwed into the top of the reservoir base unit. Liquid nitrogen is continuously delivered into the reservoir unit to ensure uniform temperatures of  $-196^{\circ}\text{C}$ . This assembly is capable of trapping about 85% of the total sample delivered. The cryo-trap is covered with a cone-shaped wire mesh (not shown) to avoid charging of the accumulating sample on the cup by stray electron bombardment, which, in turn, will alter the trajectory of the electron beam. Because the mesh is not in thermal contact with the cryo-trap, it does not accumulate much sample itself.

An additional aluminum shield was mounted directly onto the stem of the nozzle. This shield consists of a front shield and a bottom shield, as shown in Figure 3.13b, and satisfies several purposes: (i) The bottom shield covers the cryo-trap from the top and prevents stray electrons from charging the sample. Conversely, it also prevents the electric field of the charged sample to influence the electron beam. (ii) The bottom shield helps to reduce the residual gas pressure above the shield, because the sample vapor escapes through a small central hole and is immediately trapped by the cryo-trap. (iii) The front shield has a pinhole for the electron beam only. Therefore, any stray electrons scattered by residual gas before the interaction region are intercepted/filtered by this grounded shield and never reach the detector. We found that the addition of this shield assembly decreased the contribution of background scattering in our data (see Section 4.1.2) from  $\sim 25\%$  to about  $10\%$ .

### 3.1.5.2 IR Laser Desorption

The new sample delivery method implemented in UED4 has many advantages over the effusive molecular beam in UED3, described in the previous section. The process of pulsed laser desorption has proved very useful in the field of mass spectrometry and optical spectroscopy as a means to deliver intact molecules into the gas phase.<sup>44,45</sup> The continuous molecular beam employed in UED3 necessarily consumes a large amount of sample over the duration of the experiment and increases the background pressure in the scattering chamber considerably, which has detrimental effects on the signal quality, as already mentioned above. In UED4, surface-assisted laser desorption is implemented for the first time to deliver molecules into the gas phase in a pulsed molecular plume. This addition of laser desorption to electron diffraction was the major goal behind the construction of UED4 and has opened the door to gas-phase electron diffraction experiments on fragile and large molecules (see Chapter 5).

#### 3.1.5.2.1 Desorption Mechanism

Laser desorption can be accomplished at many different wavelengths from the UV to the infrared and from many different substrates. Consequently, several mechanisms have been proposed in the literature, depending on the specific experimental setup. The sample can be desorbed either directly by resonance excitation of the sample molecules or indirectly by heating the substrate surface. Due to vast variety of wavelength, energy and temporal width of pulsed laser sources, no single microscopic description of the mechanism of desorption has emerged as being consistent with all of the experimental observations.

In IR-laser desorption as employed in UED4, the sample is mostly transparent to the laser light, whereas the substrate material absorbs strongly at the given wavelength. Immediately after the arrival of the laser pulse, only the properties of the substrate are changed, manifested by a fast increase in its local surface temperature. Rapid localized surface heating upon pulsed laser irradiation has been measured to be  $\sim 10^8$ – $10^{13}$  K/s for nanosecond and picosecond pulses, respectively.<sup>46</sup> The very localized thermal energy after laser light absorption can either diffuse into the substrate bulk or be transferred to the sample molecules that are adsorbed to the substrate surface.

Zare and Levine have proposed a “thermal bottleneck” desorption mechanism based on experimental evidence showing that desorption of intact molecules dominates over fragmentation at fast substrate heating rates.<sup>47,48</sup> The energy transfer to the molecules is proposed to occur through surface-adsorbate bonds, which are generally weak van der Waals-type bonds and have a very low frequency of vibration. The frequency of the vibrational modes of these adsorbate bonds is of the same order as the frequency of the substrate surface phonons. In contrast, there exists a substantial frequency mismatch between the adsorbate modes and the high-frequency internal vibrational modes of the sample molecule. Therefore, energy flow between these modes is inefficient and an energy flow bottleneck develops between the adsorbate bond and the bonds inside the molecule. Because a large amount of energy is dumped into the adsorbate mode in a short period of time, the adsorbate bond breaks before significant energy is transferred to the internal modes of the sample, as shown in Figure 3.14. On the other hand, at slow heating rates, only a small amount of energy is supplied to the adsorbate bond and the molecule’s internal modes have enough time to equilibrate with

the surface temperature. At the rapid, but still finite heating rates obtained through laser pulses, Zare and Levine concluded that the molecules desorb internally not completely cold, but rather “lukewarm”. The onset of this bottleneck mechanism has been observed experimentally at heating rates in excess of  $10^{10}$  K/s.<sup>46,49</sup>

Measurements of plume properties, such as translational, vibrational, and rotational energies of desorbed molecules are restricted to several hundreds of micrometers away from the surface and, therefore, are often subject to in-plume processes, such as gas-phase collisions at high number densities. Desorption anywhere from  $<0.5$  to 40 monolayers/pulse have been achieved in various experimental setups,<sup>50-52</sup> but exact amounts of desorbed gaseous material are difficult to measure and have not been reported in the literature. Fortunately, gas dynamic analyses of in-plume processes can give some insight into the density and about the amount of material desorbed. Once the sample molecules are desorbed, gas-phase collisions occur independently of the experimental conditions and the corresponding desorption mechanism. It was shown computationally that the removal of 0.8 monolayers/pulse, on average, led to  $\sim 3$  collisions per desorbed particle.<sup>53</sup>

Gas-phase near-surface collisions enhance the velocity component normal to the substrate surface relative to all other velocity components.<sup>54-56</sup> After several collisions, some molecule’s trajectories will be directed back to the substrate surface and, assuming a high sticking probability, the remaining gas cloud will acquire a center-of-mass velocity, which was found to be comparable to the speed of sound, directed away from the surface.<sup>51</sup> Also, after a collision, the direction of the faster particle was found, on average, to be closer to the direction of the center-of-mass velocity. Therefore, slow

particle are found more likely at larger angles with respect to the surface normal, whereas faster particles are focused toward smaller angles, and the plume shape becomes increasingly forward peaked with higher collision frequencies.<sup>57</sup> Since initially energy is mainly stored into the vibrational and rotational degrees of freedom, there might also be an overall cooling effect, when energy is transferred to translational degrees of freedom through gas-phase collisions.<sup>57</sup>

#### 3.1.5.2.2 UED4 Desorption Source

The desorption source of UED4, shown in Figure 3.15, consists of an intricate assembly of moving and rotating parts that function inside the vacuum of the scattering chamber. These parts function in precise coordination and are synchronized to the master clock of the UED experiment, i.e., the arrival of the electron pulses at the interaction region. For the desorption laser, we use a ns-pulsed Nd:YAG laser (Bright Solutions, Model: Wedge, 1 mJ/pulse at 1064 nm and 1kHz, <2 ns FWHM). The laser pulses are attenuated to 50-200  $\mu\text{J}$ /pulse and cylindrically focused onto the substrate surface, as shown in Figure 5.2, and introduced through a window in the top flange of the scattering chamber.<sup>24</sup>

A rotating substrate wheel design is employed, because the sample yield has to be stable over several hours in order to complete a full time-resolved experiment. The substrate wheel continuously provides a fresh sample-covered surface to the pulsed desorption laser by rotating at 60-120 revolutions per minute (rpm) depending on the desorption laser repetition rate and the size of its footprint on the substrate wheel. Glassy carbon (Tokai Carbon) was chosen as the substrate material due to its optical,

mechanical, electrical, and thermal properties.<sup>58,59</sup> Most importantly, glassy carbon absorbed the laser light very strongly, but was still able to withstand the applied laser fluences without any observable damage due to ablation. (Other tested materials were graphite and crystalline silicon, but these proved inadequate for our purposes.)

Powdered organic sample is continuously applied to the substrate wheel by a felt brush wheel that in turn picks up sample from a scoop reservoir that is loaded prior to each experiment. The motion of the two wheels is coupled through a rubber belt pulley with a gear ratio of 2:3. A slight pressure between the two wheels additionally ensures that a thin and even coat of sample powder is applied on the substrate wheel. To keep the felt brush wheel saturated with sample during the entire UED experiment, the scoop is linearly translated during the course of an experiment through a worm gear assembly powered by an electrical motor that is entirely contained inside the vacuum chamber. Finally, we found that polishing the surface of the substrate wheel to a mirror like finish substantially increases its affinity toward powdered organic samples.

Rotational motion for all the rotational components of the desorption source is provided by an electrical motor located outside the vacuum chamber, as shown in Figure 3.1. Mechanical coupling and full height adjustability of the entire desorption source even during operation is made possible by a gear assembly consisting of three spur gears mounted on swiveling arms and by a home-built elevator unit below the desorption source platform. This elevator is driven by its own electrical motor that is also mounted inside the vacuum chamber.

Surface-assisted laser desorption is able to deliver a large number of molecules into the gas phase in a spatially and temporally well-defined molecular plume, where the

monomeric sample molecules can be easily isolated (see below). A single laser pulse desorbs all sample material within its footprint, as shown in Figure 3.16a, and new sample is efficiently and continuously applied by the felt brush wheel through a single contact.<sup>24</sup> This enables the UED4 desorption source to operate at very stable desorption yields for extended periods of hours and possibly days, as shown in Figure 3.16b. The operation time of the desorption source is limited only by the length of the scoop. The current scattering chamber allows for the full translation of a sample length of 3 inches inside the scoop, which allows for ~60 h of continuous operation. A slightly enlarged scattering chamber could be installed to accommodate a longer scoop, if longer operation times should become necessary (see also Section 6.3).

#### 3.1.5.2.2.1 Temporal Extent of Molecular Plume

Measurement of the desorption yield in UED can be done in two distinct ways in UED4: The electron scattering signal can be integrated over the entire detector or a portion thereof or the diffraction signal can be compared to the expected diffraction pattern corresponding to monomeric molecules of the desorbate. The first way provides information about the total amount of desorbed material, while the second method provides additional information on the chemical identity of the desorbate. By scanning the time delay between the IR desorption laser and the arrival of the electron pulses, the temporal profile of the molecular plume can be mapped out, as shown in Figure 3.17a. The profiles based on integrated electron scattering intensity display a long tail (which lasts longer than 100  $\mu$ s) after the initial signal decay, which indicates that additional material is ejected from the surface for an extended period of time. In contrast, the

profile of the monomeric sample of interest, determined through diffraction pattern similarity, shows a complete decay of the signal within just 15 microseconds. If the velocity of these monomeric molecules in the plume is distributed as

$$P_{Plume}(v_x, v_y, v_z) = \left( \frac{m}{2\pi kT} \right)^{3/2} \exp \left[ -\frac{mv_x^2 + m(v_y - v_0)^2 + mv_z^2}{2kT} \right], \quad (3.4)$$

then their spatial distribution is given by

$$P_{Plume}(x, y, z, t) = \frac{1}{t^3} \left( \frac{m}{2\pi kT} \right)^{3/2} \exp \left[ -\frac{mx^2 + m(y - v_0 t)^2 + mz^2}{2kTt^2} \right], \quad (3.5)$$

where  $m$  is the mass of the desorbed molecules,  $k$  is the Boltzmann constant,  $T$  is the translational temperature,  $v_0$  is the center of mass velocity of the gas cloud, and  $t$  is the flight time. The electron beam that is used to probe this molecular plume has a finite size described by the spatially offset normalized Gaussian distribution,

$$P_{electron}(x, y) = \left( \frac{1}{2\pi\sigma_e^2} \right) \exp \left[ -\frac{x^2 + (y - d)^2}{2\sigma_e^2} \right], \quad (3.6)$$

such that the convoluted plume signal as a function of delay time can be obtained as

$$\begin{aligned} S(t) &= A \iiint_{all\ space} P_{electron}(x, y) P_{Plume}(x, y, z, t) dx dy dz \\ &= A \frac{m}{2\pi(kTt^2 + m\sigma_e^2)} \exp \left[ -\frac{m(d - v_0 t)^2}{2kTt^2 + m\sigma_e^2} \right], \end{aligned} \quad (3.7)$$

where an additional fitting parameters has been introduced to account for the signal amplitude  $A$ . Given the experimentally determined parameters  $d = 850 \mu\text{m}$  and  $\sigma_e = 378 \mu\text{m}$ , Equation 3.7 satisfactorily reproduces the temporal data obtained by

measuring the quality of the diffraction pattern fit (tryptophan in this case), as shown in Figure 3.17b, when using  $T = 1523$  K and  $v_0 = 735$   $\mu\text{m}/\mu\text{s}$ .

The above analysis leads to the conclusion that, during the desorption process, individual molecules as well as larger clusters are desorbed from the substrate. The individual molecules are ejected with higher velocities, such that they are spatially separated from the larger clusters by the time they are probed by the electron pulses at  $d = 850$   $\mu\text{m}$  away from the substrate surface. Thus, by timing the arrival of the electron pulses to the rising edge of the desorption plume ( $t \leq 1$   $\mu\text{s}$ ), it can be ensured that only monomeric species are probed. Indeed analysis of the ground state diffraction pattern of uracil in a separate experiment, where the time delay was set to  $t = 1$   $\mu\text{s}$ , revealed that the plume composition is chemically pure, without detectable background from ions, fragmentation products, or molecular aggregates.<sup>4</sup>

#### 3.1.5.2.2.2 Spatial Extent of Molecular Plume

Measurements of the spatial extent of the molecular plume were performed by transversely scanning the desorption laser through the probing electron pulses, which were fixed in space and set to arrive at a time delay of  $t = 1$   $\mu\text{s}$ , when the scattering signal reaches its maximum. The integrated scattering/diffraction intensity were measured for radii ranging from 150 to 250 pixels at different desorption pulse energies to obtain the signals shown in Figure 3.18a. Because the desorption laser was desorbing molecules from different positions of the wheel, the direction of the surface normal and, thus, the direction of the desorption plume changed during the scan, as shown in Figure 3.18b. The tilt angle  $\alpha$  of the surface normal is obtained by solving

$$\begin{aligned}\tan(\alpha) &= \frac{x}{R_{Wheel}} \cos(\alpha) \\ &\approx \alpha = \frac{x}{R_{Wheel}} \quad ,\end{aligned}\tag{3.8}$$

where  $x \in [-2000, +2000]$   $\mu\text{m}$  is the desorption laser position,  $R_{Wheel} = 31.75$  mm is the radius of the desorption wheel, and the approximation holds for small  $\alpha$ .

The plume intensity is modeled by a cosine distribution raised to a power  $n$ .<sup>51,57</sup> Assuming the velocity distribution of the desorbed molecules to be directed along the surface normal at each point, we obtain

$$P_{Plume}(x, y) = A(y) \cos^n \left[ \arctan\left(\frac{x}{y}\right) - \alpha(x) \right] \quad ,\tag{3.9}$$

where  $A(y)$  is a numerically determined polynomial of second order, used to guarantee the conservation of molecular number density at each distance  $y$ . The plume signal as a function of desorption laser position is obtained by explicitly computing the one-dimensional convolution

$$S(x) = C \int_0^\infty \int_{-\infty}^\infty P_{electron}(x-a, b) P_{Plume}(a, b) da db \quad ,\tag{3.10}$$

where Equation 3.6 and Equation 3.9 have been written using the dummy variables  $a$  and  $b$ , and  $C$  is an arbitrary scale factor. Since the electron beam parameters are all known

( $d = 850$   $\mu\text{m}$  and  $\sigma_e = 200$   $\mu\text{m}$ ), the exponent of the cosine distribution of Equation 3.9 can be used as a variational parameter to fit Equation 3.10 to the measured scattering/diffraction intensity. The fitted result using  $n = 25$  is shown in Figure 3.18c and the corresponding plume profiles are displayed in various forms in Figure 3.18d-f. It

is evident that the plume profile is extremely forward-peaked: a fact that helps to keep the number density high enough for a UED experiment even at considerable distances away from the desorption wheel.

In Figure 3.18c it is evident the measured data shows significant asymmetry resulting in a pronounced tail to the right side. From measurements of the plume temporal profile, it was also found that particulate matter was ejected from the surface even for very long time delays ( $t > 100 \mu\text{s}$ ). Since the wheel is rotating in the negative direction relative to the desorption laser scan direction, x-axis in Figure 3.18b, the persistence of long term desorption from the desorption laser spot gives rise to a residual scattering signal on the positive side of the scan range, whereas on the negative side such a signal is absent.

### 3.1.5.2.2.3 Experimental Considerations for Nanosecond Time-Resolved Laser Desorption–Electron Diffraction

The time resolution,  $\Delta t_{total}$ , of electron diffraction is primarily determined by the excitation laser pulse length, the electron pulse length, and the relative timing jitter between the two pulses.

$$\Delta t_{total} \approx \sqrt{\Delta t_{laser}^2 + \Delta t_{electron}^2 + \Delta t_{jitter}^2} \quad (3.11)$$

For the desorption experiments reported in this thesis, we used a ns-Nd:YAG laser (A-Optowave, 100  $\mu\text{J}/\text{pulse}$  at 266 nm, 8 ns FWHM) to generate the electrons and a fs-Ti:Sapphire laser (Spectra Physics, 300  $\mu\text{J}/\text{pulse}$  at 266 nm,  $\sim 130$  fs FWHM) for sample excitation. The pulse length of the electron packet is expected to be comparable

to the 8 ns FWHM pulse length of the ns-laser due to the absence of significant space-charge effects.<sup>4</sup> The excitation laser pulses are therefore orders of magnitude shorter than the other two contributing factors in Equation 3.11 and they do not affect the total instrumental time resolution. The relative timing jitter has been measured to be 18 ns FWHM, giving a final estimate of  $\Delta t_{total} \approx \sqrt{(130 \text{ fs})^2 + (8 \text{ ns})^2 + (18 \text{ ns})^2} = 20 \text{ ns}$  for the total instrumental time resolution. A delay time should be chosen to eliminate any temporal overlap between the optical pump pulse and the electron probe pulse.

The probed sample molecules traveling at a velocity of 1 mm/ $\mu$ s are not stationary on a nanosecond time scale. Therefore, if a series of time points is to be collected, then the spatial overlap between the laser and electron pulses has to be adjusted to account for this motion. Given the spatial constraints due to the proximity of the desorption wheel, the maximal time delay is practically limited to  $\sim$ 500 ns. If instead the fs-Ti:Sapphire output is split into an excitations beam and an electron-generating probe beam, then the time resolution of the instrument can be brought into the picosecond regime, as previously reported.<sup>2</sup> However, the number of electrons per pulse in such a setup is two orders of magnitude lower and the corresponding reduction in the diffraction signal makes experiments of this kind challenging. However, using an electron optical column with RF compression has the potential to make ultrafast laser desorption–electron diffraction experiments possible in the near future (see Section 6.3).

### **3.1.5.3 Molecular Beam Nozzle for UED4**

The UED4 instrument also requires a gaseous sample inlet nozzle, because reference gas diffraction/scattering data needs to be collected for each experiment to

determine the atomic scattering contribution (see Section 4.1.2) and the camera length.<sup>18</sup>

These reference gases however can be introduced at room temperature and, therefore, the UED4 nozzle does not require any of the heating capabilities described for the UED3 nozzle (see Section 3.1.5.1). As shown in Figure 3.19, this nozzle features a shield with a 1.5 mm pinhole to pass the electron beam and block any stray electrons. The needle tip of this molecular beam nozzle is also used for the mutual spatial alignment of the IR desorption laser beam, the electron beam and the UV pump laser beam.

## 3.2 Temporal and Spatial Resolution – Ultrashort Electron Pulses for Diffraction, Crystallography and Microscopy: Theoretical and Experimental Resolutions\*

### 3.2.1 Abstract

Pulsed electron beams allow for the direct atomic-scale observation of structures with femtosecond to picosecond temporal resolution in a variety of fields ranging from materials science to chemistry and biology, and from the condensed phase to the gas phase. Motivated by recent developments in ultrafast electron diffraction and imaging techniques, we present here a comprehensive account of the fundamental processes involved in electron pulse propagation and make comparisons with experimental results. The electron pulse, as an ensemble of charged particles, travels under the influence of the space-charge effect and the spread of the momenta among its electrons. The shape and size, as well as the trajectories of the individual electrons, may be altered. The resulting implications on the spatiotemporal resolution capabilities are discussed both for the  $N$ -electron pulse and for single-electron coherent packets introduced for microscopy without space-charge.

### 3.2.2 Introduction

In the investigation of complex systems ranging from biology to chemistry to materials science, it is beneficial to obtain structural information as a function of time. To achieve this goal, our laboratory has developed<sup>10</sup> the ultrafast techniques of electron

---

\* Reproduced with permission from Gahlmann, A., Park, S. T. & Zewail, A. H. Ultrashort electron pulses for diffraction, crystallography and microscopy: Theoretical and experimental resolutions. *Phys. Chem. Chem. Phys.* **10**, 2894-2909 (2008). Copyright 2008 Royal Society of Chemistry.

diffraction (UED),<sup>17,60</sup> electron crystallography (UEC),<sup>61,62</sup> and electron microscopy (UEM),<sup>63</sup> for more details of the historical development see Ref. [10](#) and references therein. In striving to identify the relevant degrees of freedom of the structural dynamics, the experimental tools for investigating fundamental physical, chemical, and biological processes need to feature ever improving spatiotemporal resolution. Using electrons as a probe, the resulting high sensitivity allows for the use of ultrashort pulsed beams with unprecedented time resolution, ranging from femtoseconds to picoseconds.

The temporal resolution is mainly determined by the longitudinal extent of the electron pulse, while the spatial resolution limits for both diffraction and imaging are determined by the same requirements that apply to continuous-wave beams. To establish and possibly improve upon the resolution limits of ultrafast electron diffraction and electron imaging instruments, detailed knowledge of the temporal evolution of electron pulses becomes crucial. Here, we present a comprehensive theoretical study of the relevant pulse broadening mechanisms and investigate their effect on the spatiotemporal resolution in electron diffraction, crystallography, and imaging. The geometrical factors caused by the velocity mismatch between the optical and electron pulses in a crossed beam arrangement are treated elsewhere<sup>64,65</sup> and are not considered here.

The electron pulse trajectories are conceptually similar in all of the above-mentioned instruments. The ultrashort electron pulse is formed by illuminating a photocathode material with a pulsed laser beam, thereby generating free electrons by the photoelectric effect. The free electron packet is then accelerated through an electric field and subsequently shaped using an instrument specific combination of pinholes, electrostatic, and magnetostatic lenses, as shown schematically in Figure 3.20. However,

the number of electrons per pulse varies considerably across our instruments: In gas-phase electron diffraction (UED), where the specimen's molecular density is low, the electron pulse contains up to  $10^6$  electrons in order to maximize the signal intensity, while in electron crystallography (UEC),  $\sim 10^3$  electrons per pulse results in sufficient scattering events (see Section 3.2.6.1). Finally, in electron microscopy (UEM), single-electron pulses are employed at an increased repetition rate to build up an image or diffraction pattern in time.

Several factors come into play during the electron pulse trajectory and these factors determine the bunch shape at the specimen in the interaction region. First, the electrons are generated by a laser pulse, which itself has a temporal and spatial extent; the extent defines the initial shape of the electron packet. Second, the electrons are ejected from the photocathode with a range of momenta defined by the distribution in magnitude and direction. Third, at sufficiently high charge densities, pair-wise Coulomb repulsions between electrons become significant and such repulsions may alter the velocities of individual electrons. The latter effect is not operational in the single-electron mode.

Simulating electron packets realistically along the entire path is complicated due to the presence of instrument specific electron optical arrangements. While the electron microscope features a myriad of magnetostatic lenses, electrostatic lenses, deflection coils, stigmator coils and pinholes, the column of our UED or UEC instruments, containing just a single magnetostatic lens, seems fairly simple by comparison. Theoretical studies to date<sup>66-70</sup> have treated electron pulses for diffraction and imaging primarily in the absence of focusing fields, thereby relying on several assumptions to match experimental data, which could be violated in reality.

This section is organized as follows: First, we will consider the propagation of electron pulses in the absence of Coulomb repulsions to determine the magnitude of pulse broadening mechanisms, other than the space-charge effect. Second, the electron pulses in the presence of space-charge will be modeled with typical UED or UEC parameters using two approaches: A mean field model<sup>66,67,69</sup> and an  $N$ -body Monte Carlo simulation.<sup>71,72</sup> The mean field model will be expanded to allow for the incorporation of pulse shaping fields. It is shown that the Monte Carlo simulations give more accurate pulse shapes and, perhaps more importantly, deliver the complete phase space information of the ensemble of electrons. Together these two approaches provide a valuable illustration of the physical processes of electron-electron interactions within the pulse and their subsequent implications for electron-specimen interactions in diffraction and imaging. We will conclude with a discussion about the beam coherence properties and apply these concepts to maximize the spatiotemporal capabilities of our newly developed diffraction instrument, UED4. Comparisons with the experimental resolutions achieved are also made (see Figure 3.21).

### 3.2.3 Theory

#### 3.2.3.1 Definition of Width and Length of Electron Packet

Macroscopically, the electron packet is defined by its longitudinal and lateral spatial profiles and their evolution in time, as it travels from the photocathode to the interaction region and, finally, to the detector. Typically, these distributions can be assumed to be cylindrically uniform, ellipsoidal, Gaussian, or their combinations.<sup>66</sup> When comparing different shapes and distributions of electron packets, a natural measure for

the spatial extent has to be defined. While the “*maximum extent*” would be an obvious choice for a uniform distribution, the full-width-half-maximum (FWHM) is often used for a Gaussian distribution and for experimental measurements; in few cases, the width at 10% height and/or the standard deviation,  $\sigma$ , is also used. For the uniform cylindrical and/or ellipsoidal distribution, the measurement of the diameter often implies a projection of the two-dimensional/three-dimensional density onto the respective axis, resulting usually in a Gaussian-type function. Furthermore, real electron packets do not necessarily maintain their initial shapes, during expansion, with the noted exception of ellipsoidal packets.<sup>73</sup>

For quantitative comparison of the results obtained from the mean field theory, the numerical simulation, and experiment, we choose the standard deviation as the universal metric of size. Two packets are deemed “*equivalent*” when they have the same standard deviations regardless of the shape of the distribution. Only if the actual distribution shape is known or assumed, the standard deviation can be related to more common measures of the spatial extent of the pulse, such as the FWHM (see Section 3.2.6.2). In the mean field theory, for example, in order to simulate a 110 fs FWHM Gaussian pulse ( $\sigma=47$  fs), we would choose a uniform length of 162 fs ( $=\sqrt{12} \times 47$  fs). Alternatively, Miller and co-workers,<sup>70</sup> instead of converting the measure of size, scaled the number of electrons in the packets to match the results of the mean field theory and their *N*-Body simulation, since the FWHM of a Gaussian distribution contains only 76% of the total electrons.

### 3.2.3.2 Initial Energy Spread

In the photoelectric process, free electrons are generated with a distribution of kinetic energies. In order to evaluate the magnitude of the pulse broadening it is instructive to treat the space-charge effect separately from the broadening due to the initial energy spread. To this end, the relativistic equation of motion has been solved for a single electron having an uncertainty in its momentum. Longitudinal broadening,  $\Delta t_{KE}$ , will result from an initial spread in the electron kinetic energy,  $\Delta E_i$ , or the corresponding momentum spread,  $\Delta p_i = \sqrt{\frac{m_0}{2E_i}} \Delta E_i$ , which occurs during the electron photoemission event (see Section 3.2.6.3):

$$\Delta t_{KE} = \left| -\frac{d}{eV} \left( 1 - \frac{v_i}{v_f} \right) - \frac{l}{m_0 \gamma_f^3} \frac{v_i}{v_f^3} \right| \Delta p_i \quad , \quad (3.12)$$

where  $e$  is the electron charge,  $m_0$  is the electron rest mass,  $d$  is the acceleration gap between cathode and anode,  $l$  is the distance of field-free propagation,  $V$  is the acceleration voltage,  $v_i$  and  $v_f$  are the mean initial and final electron velocities,  $\gamma_f$  is the relativistic Lorentz factor (see Section 3.2.6.3) at the velocity  $v_f$ .

The first term represents the broadening of the electron pulse in the acceleration gap, the dominant contribution, while the second term represents broadening in the field-free drift region. We note that the second term corresponds to a packet simply spreading by  $l/(v_f \pm \Delta v_f)$  in the drift region. Since  $v_i \ll v_f$ , the expression can be approximated to yield

$$\Delta t_{KE} \approx \frac{d}{eV} \Delta p_i = \frac{d}{eV} \sqrt{\frac{m_0}{2}} \frac{\Delta E_i}{\sqrt{E_i}} \quad , \quad (3.13)$$

giving a result equivalent to that of Equation 4 in Ref. [74](#). It should be noted that, under this approximation, the temporal spread is solely determined by the energy spread,  $\Delta E_i$ , relative to the square root of the mean energy,  $\sqrt{E_i}$ , and the potential  $V$  across the distance  $d$ .

### 3.2.3.3 Charge Density Effect

#### 3.2.3.3.1 Mean Field Theory (MF)

In the mean field theory, which has been widely used in the literature,<sup>[66-70](#)</sup> the electron pulse is most commonly approximated as a cylindrical slab of radius  $R$  and length  $L$ . Due to the space-charge effect, this slab of continuous charge density extends both in the longitudinal and transverse direction, while always maintaining the shape of a cylinder. The evolution of the spatial pulse length,  $L$ , due to space-charge repulsion is given by (see Section 3.2.6.4 for derivation):

$$\frac{1}{2} \frac{d^2 L}{dt^2} = a_x = \frac{Ne^2}{2m_0 \epsilon_0 \pi R^2} \frac{2}{1 + \left(\frac{L}{R}\right) + \sqrt{1 + \left(\frac{L}{R}\right)^2}} \quad , \quad (3.14)$$

where  $a_x$  is the axial acceleration,  $N$  is the number of electrons in the pulse, and  $\epsilon_0$  is the vacuum permittivity. The time evolution of the radius,  $R$ , of a freely expanding, thin disk ( $R \gg L$ ) is approximated by<sup>[67](#)</sup>

$$\frac{d^2 R}{dt^2} = a_R \approx \frac{Ne^2}{m_0 \epsilon_0 \pi R^2} \quad , \quad (3.15)$$

where  $a_R$  is the radial acceleration. The temporal spread,  $\Delta t_{SC}$ , is then evaluated from the length of packet and its axial velocity,

$$\Delta t_{SC} = \frac{L}{v_f} . \quad (3.16)$$

Here, the capital letters,  $\Delta$  and  $L$ , are used to emphasize that the pulse duration corresponds to the maximum extent of the uniform distribution. The initial condition for  $L$  is chosen to match the excitation laser duration, as previously described.

The one-dimensional mean field model (MF1D) utilizes Equation 3.14 only with a constant radius, while the coupled Equations 3.14 and 3.15 are solved simultaneously to give a two-dimensional result (MF2D). The advantage of the mean field model is that the equations of motion for the pulse can be rapidly integrated for a variety of initial conditions and give a readily estimate of the pulse size as a function of time. To date, the mean field model has been used primarily to model freely drifting electron bunches. While several additions to the theory have been made, e.g., to model the electron bunch inside an electrostatic acceleration field,<sup>68,75</sup> no attempts have been made to model the effect of a magnetic lens on the electron pulse shape. Since these fields are present in all electron diffraction and imaging instruments, this extension to the mean field theory has to be made to validate its predictive power.

### 3.2.3.3.2 Mean Field Theory Including Lens System

To implement the acceleration field inside the electron gun, the mean field theory can be extended by treating the positions at the front and the rear end of electron packet separately and explicitly, as  $F(t)$  and  $B(t)$ .<sup>68,75</sup> The maximum longitudinal extent is

then given by  $L(t) = F(t) - B(t)$ . Approximating the focusing lens as a radial deceleration element, the equation of motion becomes

$$\begin{aligned} \frac{d}{dt} \left( \gamma_F \frac{dF(t)}{dt} \right) &= a_A + a_X \quad (t \geq t_{birth,front}), \\ \frac{d}{dt} \left( \gamma_B \frac{dB(t)}{dt} \right) &= a_A - a_X \quad (t \geq t_{birth,rear}), \\ \frac{d}{dt} \left( \gamma_C \frac{dR(t)}{dt} \right) &= a_R - a_M, \end{aligned} \quad (3.17)$$

where  $\gamma_i$  is the relativistic Lorentz factor for front, rear, and center, respectively,  $a_X$  and  $a_R$  are the axial and the radial accelerations as in Equations 3.14 and 3.15,  $a_A$  is the electrostatic acceleration in the electron source, and  $a_M$  is the deceleration term due to the focusing lens, expressed as a Gaussian function to simulate the finite thickness of a magnetic lens. It should be mentioned that the axial forces are present only after the births of the front and the rear and that the number of electron is now a function of time, which is zero before the birth of the front,  $N$  after the birth of the rear, and linearly increasing in between to mimic the generation of the photoelectrons.

### 3.2.3.3.3 Monte Carlo Simulation (MC)

In contrast to the mean field model, which treats the electron pulse as a continuous charge distribution, a  $N$ -Body Monte Carlo simulation treats the electron pulse as an ensemble of  $N$  randomly generated, discrete particles.<sup>71,72</sup> To this end, we have developed our own electron bunch propagation code, in which each particle in the bunch moves under the influence of three distinct forces: (i) The electrostatic force of acceleration, (ii) the magnetostatic force of the focusing lens, and (iii) the Coulomb force

for each of the  $\frac{1}{2}N(N-1)$  pair-wise interactions within the bunch. The magnetic lens can be simulated by either (i) a sum of current loops, (ii) the finite-sized coil approximation, or (iii) by importing an externally simulated field. Further elements such as the ponderomotive force, gravitation, the earth magnetic field, stigmators coils, and time-dependent streak plates can be straightforwardly implemented, if desired.

Using this physically more realistic model, it is possible to propagate the electron pulse over its entire lifetime, i.e., from the birth of the individual photoelectrons at the photocathode surface to their arrival at the detector. The nascent photoelectrons are randomly generated at the photocathode with a Gaussian temporal and uniform spatial distributions to account for the fact that the extraction pinhole in the anode acts as a spatial filter producing an initially well-defined lateral profile. The direction of the initial electron momentum vectors are given by a  $\cos^2 \theta$  distribution and the initial momentum distribution is chosen to be uniform from zero to a high-energy cutoff corresponding to  $h\nu - W$ , where  $W$  is the effective material-specific work function in the presence of a DC electric field.<sup>76</sup> The treatment of the individual electron trajectories is entirely relativistic and should reproduce the true pulse trajectory, provided that the initial conditions are chosen accurately and the Monte Carlo sampling is fine-grained enough that the results converge. The drawback of this method is its high demand of computational time, which increases in proportion to the number of pair-wise interactions calculated at each time step. To ease computational demand, we treated the pulse as an ensemble of representative particles of appropriately scaled charge and mass in order to model pulses containing more than 1000 electrons in a reasonable amount of time. We found that this level of Monte Carlo sampling was sufficient to achieve convergence to within 10%.

## 3.2.4 Results and Discussion

### 3.2.4.1 Temporal Resolution

#### 3.2.4.1.1 Initial Energy Spread

In order to avoid pulse broadening due to Coulomb repulsion and achieve ultrafast temporal resolution, the ultrafast electron microscope has been designed to operate in the zero-current limit, meaning that the column contains one or a few electrons at a time. For an instrument of this type, the ultimate resolution is mainly determined by the excitation laser pulse length and by the initial kinetic energy spread of the photoelectrons. The pulse broadening in the absence of space-charge is calculated from  $\Delta t = \sqrt{\Delta t_{hv}^2 + \Delta t_{KE}^2}$  with  $\Delta t_{KE}$  given by Equation 3.12 or Equation 3.13. Using instrumental parameters, the results are shown in Figure 3.22 for  $\Delta t_{FWHM}$  vs.  $\Delta E_i$ . We invoke, for simplicity, a uniform photoelectron distribution (see Ref. [77](#)) centered at  $E_i$  and the width increase given by  $\Delta E_i = 2E_i$ . The exact solution (solid lines, Equation 3.12) represents the broadening of the pulses during their flight to the interaction region, while the approximate solution (dashed lines, Equation 3.13) represents the broadening in the acceleration region. Since Equations 3.12 and 3.13 give very similar results, the broadening in the field-free drift region is relatively insignificant.

As evident from Equation 3.13, it would be desirable to produce photoelectrons with a narrow energy distribution, but a large mean kinetic energy to reduce magnitude of the factor  $\Delta E_i / \sqrt{E_i}$ . Experimentally, however, the distribution of photoelectrons always extends to the limit of zero kinetic energy, because electrons below the Fermi level may be photoemitted as well.<sup>[77](#)</sup> To achieve the narrowest possible energy distribution, the

photocathode needs to be operated at a low temperature and the photon energy needs to be matched to the work function of the metal.<sup>78</sup> This approach is taken in our instruments of UED and UEC, resulting in an estimated kinetic energy spread of  $<0.3$  eV; in Ref. [78](#), the experimental  $\Delta E_i$  under similar conditions (for a gold photocathode) was measured to be 0.1 eV.

We consider the electrons pulses produced in UED4 and UEC first. The acceleration gap in these guns is kept as small as possible to maximize the extraction field. Under the influence of a field strength of 20 and 10 MV/m for UED4 and UEC, respectively, the electron pulses are barely elongated by the presence of an initial kinetic energy spread. In contrast, the broadening is more pronounced in UEM1 due to the smaller acceleration field strength of 4.8 MV/m. The UEM1 column, originally designed to operate in continuous-wave mode, features an acceleration gap one order of magnitude larger than the gap found in the home-built guns of UEC and UED. Nonetheless, even at  $\Delta E_i = 0.3$  eV, the pulse length is only 300 fs.

Since UEM operates in the absence of space-charge, the photoelectric energy spread presents the main contribution to the electron pulse broadening. If necessary, the electron pulse duration could be reduced to the excitation laser pulse length by an appropriately designed extraction module. The consequence of the energy distribution,  $\Delta E_i$ , is in another aspect of diffraction and imaging, namely the longitudinal coherence, which will be discussed below.

### 3.2.4.1.2 Space-Charge Effect

Before we evaluate by how much the pulse durations shown in Figure 3.22 will be altered by the space-charge effect, we need to validate the different methods of simulating the electron packet. Figure 3.23 shows the size (standard deviation) evolution of an electron bunch under the exclusive influence of Coulomb repulsions ( $\Delta E_i = 0$ ), calculated using the mean field theory (i) in the longitudinal direction only (MF1D), (ii) in two dimensions with the implementation of a focusing element (MF2D), (iii) in two dimensions with the implementation of a focusing element and the acceleration field (MF2DA), and, ultimately, the Monte Carlo (MC) simulation. We note that  $\sigma_{temporal}$  in millimeter (mm) is the longitudinal extent of the space-charge limited electron packet and, knowing the speed (post acceleration), can be expressed in the time domain using Equation 3.16. The initial conditions were chosen as follows: 10,000 electrons per pulse, 30 kV acceleration voltage, Gaussian FWHM (110 fs) or the equivalent uniform profiles in time, uniform profile in the lateral direction ( $r = 100 \mu\text{m}$ ). In each case, the current of the magnetic lens was optimized, such that the electron beam would have the smallest beam waist as it hits the detector.

Not surprisingly, the MF1D approximation with a fixed radius clearly overestimates the longitudinal spreading of the pulse, while the other methods give a good agreement. The radial acceleration used in the mean field models (Equation 3.15) is only valid for infinitely thin disks and, therefore, overestimates the spreading in the lateral direction as the pulse elongates, such that even after optimizing the magnetic lens, the radius remains too large. In spite of this large error, the longitudinal spread is only affected slightly, at least at this particular charge density. We can conclude that the mean

field model may give a reasonable estimate of the pulse duration for a space-charge limited beam for a choice of arbitrary initial conditions. However, the radial expansion is not accurately reproduced by the current model and would require modification of Equation 3.15.

The extent of the space-charge induced broadening is mainly determined by the magnitude of the Coulomb repulsions as well as the time scale of this interaction. By employing higher acceleration voltages, the effective propagation time of the electron pulse can be reduced, since the electrons arrive at the interaction region in a shorter time and the space-charge induced broadening has less time to act. We used the mean field model to estimate the pulse length in our instruments as a function of propagation distance. The extraction voltages are 30, 60, and 120 kV for UEC, UED4, and UEM1, respectively. The effect of the acceleration voltage on the temporal duration (Gaussian FWHM) of the pulses as a function of the propagation distance is shown in Figure 3.24. It is clear that UEM1 in single-electron pulsed mode is not limited by the space-charge effect, while the pulses in UED4 and UEC are broadened to several picoseconds once they arrive at the interaction region. Alternatively, the time of the space-charge induced broadening could also be reduced by placing the interaction region very close to the electron source.<sup>79</sup>

To isolate the role of the initial charge density, we calculated the temporal extent of the electron pulses under identical acceleration conditions. The initial conditions were kept identical to the conditions used for the comparisons of the models in Figure 3.23, while the number of electrons was increased by an order of magnitude at a time. Figure 3.25 shows the theoretical (MF2DA and MC) pulse duration after 2 ns of

propagations time together with the experimental measurement for validation.<sup>1</sup> Both models reproduce the pulse broadening reasonably well in the region where experimental data is available. Using the MC simulation, two curves were calculated for different initial kinetic energy spreads corresponding to 0.1 and 0.3 eV. There is a slight difference between these two calculations in the low electron density regime, where the space-charge effect does not play a dominant role. However, the curves quickly begin to overlap each other as the electron density grows and for a pulse containing as few as 1000 electrons, the space-charge induced broadening already masks any contribution of the initial kinetic energy spread after 2 ns of propagation. The mean field model can reproduce the results from the MC simulation quite accurately, but a more pronounced deviation occurs at higher charge densities, since the error in Equation 3.15 is exacerbated in this regime. Again, the temporal resolution capability of the pulsed electron probe can be successfully estimated with the mean field model; however, the spatial resolution capability remains uncertain.

### **3.2.4.2 Spatial Resolution**

#### **3.2.4.2.1 Coherence**

The evaluation of the spatial resolution of the pulsed electron probe requires a detailed discussion of the coherence of the electron packet. Coherence is the degree of a phase relationship, which can give rise to interferences. In light optics, an aperture is often employed to generate a pseudo point source. For a single illuminated object, the analogue of the double-slit experiment, the coherence length is defined as the maximum length, beyond which the interference fringe is attenuated. Below, we will consider the

effect of many, spatially separated objects (interaction region). If the aperture is small and the distance to the object is far, then the coherence length is defined as  $r_c = \lambda/(2\pi\alpha)$ , where  $\alpha$  is the half-angle subtended by the aperture. In such a case, the object is illuminated by spherical waves emanating from every point of the aperture. It should be mentioned that the criterion  $r_c = \lambda/(2\pi\alpha)$  corresponds to only a 12% reduction of the perfectly coherent visibility.<sup>80</sup> This definition holds true, only as long as  $\alpha$  is smaller than the photon's intrinsic divergence,  $\delta\alpha$ , which can be estimated using the uncertainty principle:

$$\delta\alpha \approx \frac{\Delta p_r}{p_z} \geq \frac{\hbar}{2\Delta x} \frac{\lambda}{\hbar} = \frac{\lambda}{4\pi\Delta x} \quad , \quad (3.18)$$

where  $p_r$  and  $p_z$  are the photon momenta in the radial and longitudinal direction, respectively, and  $\Delta x$  is the aperture dimension. However, when  $\alpha$  is bigger than  $\delta\alpha$ , then the object is illuminated only by an area within the angle  $\delta\alpha$  and the contribution from the rest of the source can be neglected. In such a case, the coherence length should be defined as  $r_c = \lambda/(2\pi\delta\alpha)$ .

In contrast to photons, free electrons are generated with an initial momentum spread, which determines the intrinsic divergence  $\delta\alpha$  for each electron, since the contribution originating from the uncertainty principle term is negligible due to the small de Broglie wavelength. Using an acceleration voltage of 60 kV and assuming  $\Delta E_i \approx 2E_i \approx 0.3eV$ , the value of

$$\delta\alpha = \frac{\Delta p_r}{p_f} \leq \frac{\Delta p_i}{p_f} \approx \sqrt{\frac{\frac{m_0}{2E_i} (\Delta E_i)^2}{2m_0 E_f}} = \sqrt{\frac{(\Delta E_i)^2}{4E_i E_f}} \quad (3.19)$$

becomes 1.6 mrad, which is an upper limit value. (The presence of a  $\delta\alpha$  ultimately gives rise to a nonzero transverse beam emittance.<sup>81</sup>)

The coherence length defined above only applies for a single scattering object. Blurring of the interference fringes needs to be taken into account in the case of scattering from objects with spatial extent as in molecules or in the condensed phase. In this context, it is more appropriate to derive the coherence length in terms of interference fringe blurring. During the elastic scattering process, the magnitude of the momentum transfer is given by

$$s = |\vec{k} - \vec{k}_0| = \frac{4\pi}{\lambda} \sin\left(\frac{\theta}{2}\right), \quad (3.20)$$

where  $\vec{k}_0$  and  $\vec{k}$  are incident and scattered wave vectors of the electron,  $\lambda$  is the electron's de Broglie wavelength, and  $\theta$  is the scattering angle. When the ensemble of electrons and the interaction volume have a finite size, each electron has an uncertainty in its position, when it scatters. The error in the observable momentum transfer at a given radial position  $s$  on the observation plane can be evaluated by

$$\delta s = \sqrt{\left(\frac{\partial s}{\partial \theta}\right)^2 \delta \theta^2 + \left(\frac{\partial s}{\partial \lambda}\right)^2 \delta \lambda^2 + \left(\frac{\partial s}{\partial x}\right)^2 \delta x^2 + \left(\frac{\partial s}{\partial y}\right)^2 \delta y^2 + \left(\frac{\partial s}{\partial z}\right)^2 \delta z^2 + \left(\frac{\partial s}{\partial b}\right)^2 \delta b^2}. \quad (3.21)$$

The  $\delta\theta$  term represents the uncertainty in the scattering angle, originating from the incident angular spread at each position in the interaction volume (lateral coherence length), the  $\delta\lambda$  term represents the longitudinal energy spread (longitudinal coherence length) and the  $\delta x$ ,  $\delta y$  and  $\delta z$  terms are reflective of the three-dimensional size of the interaction region and the electron bunch. The  $\delta b$  term is an uncertainty in measuring the momentum transfer due to the electron detection process, e.g., through blurring and

binning the image (signal converter, amplifier, and digitizer). In case of gas-phase electron diffraction, each distinct internuclear distance produces sinusoidal interference fringes,<sup>2</sup> while in crystallography, repeated long-range order of scattering centers produces a series of Bragg spots with a corresponding frequency in spacing.<sup>82</sup> The uncertainty in  $s$  will reduce the visibility of the interference fringes or the Bragg spots, such that they become unobservable and indistinguishable (see Section 3.2.6.5). The instrumental coherence length can then be defined as

$$R_c = \frac{1}{\delta s} \equiv \frac{1}{2\sigma_s} . \quad (3.22)$$

We note that this definition reduces to  $r_c = \lambda/(2\pi\delta\alpha)$ , the lateral coherence length, only in the single scattering center limit and assuming the detection process is perfect and  $\delta\lambda$  is negligible. Additionally, from discrete Fourier transformation theory, it is known that the maximum resolvable distance after collecting discrete data in the frequency domain, is given by

$$r_{\max} = \frac{1}{\Delta s} = \frac{1}{s_{i+1} - s_i} . \quad (3.23)$$

Therefore, these values give an estimate of the maximum distance that can be decisively resolved in an electron diffraction experiment.

In the high-resolution imaging mode of the transmission electron microscope, the coherence of the electron ensemble is exploited to form contrast in the image. Conceptually, the same limitations as stated above apply for the instrument's spatial resolution. Since each electron interferes only with itself, the image is composed of the

independent superposition of single electron interferences and image blurring occurs in the presence of an uncertainty in the electrons' trajectory and their wavelength.

However, in the more complicated microscope column additional resolution limiting factors have to be considered. In the wave-optical theory of imaging,<sup>83</sup> contrast in the image is formed as dictated by the phase contrast transfer function (CTF), which is a function not only of the properties of the electron beam (incidence angle spread and wavelength spread) but also of instrumental parameters such as the spherical and chromatic lens aberrations, as well as aperture sizes and the particular defocus setting. Most commonly used is the Scherzer defocus, which, in combination with an appropriate aperture size, maximizes the contrast and allows for easily interpretable images. The Scherzer resolution can be improved upon by exit wave reconstruction techniques using images collected at different defocus settings, but the ultimate information limit of the instrument remains limited by the beam properties and the quality of the electron optics. Since UEM in single-electron mode operates outside of the space-charge limit, the spatial resolution achievable is the same as is obtained in continuous-wave mode and we will not comment on it further.

#### 3.2.4.2.2 Optimal Diffraction Geometry

In conventional diffraction physics,<sup>28,29</sup> it has been established that  $\delta$  is minimized, when, for each electron, the incident wave vector,  $\vec{k}_0$ , is coincident with a line from the electron's position in interaction volume to the center of detector. As is shown schematically in Figure 3.26, the most extensive blurring occurs, if the beam arrives at the interaction region on a diverging trajectory, i.e., the particles' radial

divergence angle,  $\kappa = \tan^{-1}(p_r/p_z) > 0$ . On the other hand, if the electrons are perfectly collimated ( $\kappa = 0$ ), then the blurring on the detector is identical to the size of the electron beam waist. The optimal resolution is achieved, if the electrons are focused to a point on the center of the detector and impinge on the interaction region on an ideally focused converging ( $\kappa < 0$ ) trajectory. It follows that for a given camera length, the ideal radial convergence angle,  $\kappa$ , in the interaction region is given by an approximately linear function of the off-axis distance. Using an interaction volume with dimensions  $\delta x = \delta y = \delta z = 300 \mu\text{m}$ , an intrinsic electron divergence  $\delta\theta = 0.5 \text{ mrad}$ , a wavelength spread  $\delta\lambda$  corresponding to a kinetic energy spread of 0.3 eV, and a detector blurring  $\delta b = 100 \mu\text{m}$ , a coherence length of  $\sim 12 \text{ \AA}$  is achieved in the converging beam configuration, while the collimated beam and the diverging beam only give  $\sim 4$  and  $\sim 3 \text{ \AA}$ , respectively. The  $\delta\lambda$  term in Equation 3.21 is much smaller compared to the remaining terms, such that the blurring of the interference fringes is not affected by longitudinal coherence.

#### 3.2.4.2.3 Focusing Behavior

In the absence of Coulomb repulsion,  $\delta\theta$ , which originated from the intrinsic divergence,  $\delta\alpha$ , will lead to a finite spot size on the detector. Therefore, the ability to focus the beam to a small point on the detector can be a direct measure of the instrumental coherence length, because  $\delta s$  is dominated by  $\delta\theta$  after all other terms have been minimized.

For high-energy electrons, the de Broglie wavelength is much smaller than the source dimension and we can rather treat each electron in the bunch as a classical particle

and its trajectory as a ray, which is influenced by external forces, if any. However, due to the presence of  $\delta\alpha$ , the focusing behavior of the electron beam becomes less than ideal, as shown schematically in Figure 3.27. Assuming that the electrons are generated in a source of radius  $R_0$ , having an overall beam divergence  $\Omega_0$ , if any, and further assuming that each emitting point in the source inherently diverges with an angle  $\delta\alpha$  after acceleration, then these two components are focused at different positions. The focal distances,  $B$  and  $b$ , produced a lens of a focal length,  $f$ , for the  $\Omega_0$  and  $\delta\alpha$  components, respectively, are given by the lens equation:

$$\begin{aligned}\frac{1}{f} &= \frac{1}{A} + \frac{1}{B} \quad \text{for } \Omega_0, \\ \frac{1}{f} &= \frac{1}{a} + \frac{1}{b} \quad \text{for } \delta\alpha.\end{aligned}\tag{3.24}$$

The  $\delta\alpha$  components are perfectly focused at the imaging plane  $b$ , where a magnified image of the source can be formed, while the smallest overall beam waist is obtained near the focal plane  $B$ . If the radius due to each component ( $\delta\alpha$  and  $\Omega_0$ ) can be determined independently from the two different focal distances, then the resulting beam size along the beam path may be computed by convoluting the radii of these two components, i.e.,

$$R(x) = \sqrt{R_{\Omega_0}(x)^2 + r_{\delta\alpha}(x)^2},\tag{3.25}$$

where

$$R_{\Omega_0}(x) = \left| R_0 \frac{A}{A-a} \frac{B-x}{B} \right| = \left| R_0 \frac{A}{A-a} \left( 1 + \frac{x}{A} - \frac{x}{f} \right) \right|,\tag{3.26}$$

and

$$r_{\delta\alpha}(x) = \left| a \tan\left(\frac{\delta\alpha}{2}\right) \frac{b-x}{b} \right| = \left| a \tan\left(\frac{\delta\alpha}{2}\right) \left(1 + \frac{x}{a} - \frac{x}{f}\right) \right|, \quad (3.27)$$

and

$$A = a + R_0 \cot\left(\frac{\Omega_0}{2}\right). \quad (3.28)$$

The optimal focal length of the lens can then be determined by minimizing  $R$  with respect to  $f$ . Figure 3.28a shows a result of Equations 3.25, 3.26, and 3.27 using typical UED parameters. It can be readily seen that, even though the  $\Omega_0$  component is focused, the minimized spot size is finite and effectively determined by the diverging  $\delta\alpha$  component. Sufficiently small radii can be obtained either by (i) making  $R_0$  very small (point source), or (ii) by making  $\Omega_0$  large. Both approaches essentially bring the virtual source position,  $A$ , closer to the actual source plane,  $a$ . Figure 3.28b shows how the final focus size depends on the initial source dimension. Additionally, a smaller focal size can be obtained by reducing the intrinsic divergence  $\delta\alpha$  by using higher acceleration potentials. In conventional electron beam sources, a small probe size can be readily obtained by using a nanometer scale field emission tip in combination with high acceleration voltages.<sup>83,84</sup> In the high-current limit of pulsed electron guns, however, where bunches contain thousands or possibly millions of electrons, a finite-sized source becomes a necessity due to extraction quantum efficiency of the cathode material. Therefore, the electron beam has to be given a macroscopic divergence,  $\Omega_0$ , if a small focus size is desired. Experimentally, this can be accomplished by utilizing the negative lensing effect of Coulomb repulsions (which depends on the initial charge density) and/or

by inserting a diffusive lens immediately after the source to controllably induce this divergence.

For pulsed electron guns in the space-charge limit, any effort to minimize the photoelectric momentum spread is inconsequential, since generation of a sufficiently cold beam does not totally eliminate the  $\delta\alpha$  component. The random and discrete nature of the electron's position within the pulse and the corresponding irregular Coulomb repulsions can also produce an intrinsic divergence for each electron. An estimation of its magnitude can be made as follows: When the probability of electron to be at position  $\vec{r}$  is given by  $P(\vec{r})$ , the mean Coulomb potential energy becomes

$$V(\vec{r}_i) = \int \frac{1}{4\pi\epsilon_0} \frac{e_2}{|\vec{r} - \vec{r}_i|} NP(\vec{r})d\vec{r} \quad , \quad (3.29)$$

and its deviation is given by

$$\delta V(\vec{r}_i) = \int \frac{1}{4\pi\epsilon_0} \frac{e_2}{|\vec{r} - \vec{r}_i|} \delta(NP(\vec{r}))d\vec{r} \quad , \quad (3.30)$$

which can be approximated to give

$$\begin{aligned} \delta V(\vec{r}_i) &\approx \int \frac{1}{4\pi\epsilon_0} \frac{e_2}{|\vec{r} - \vec{r}_i|} N\delta P(\vec{r})d\vec{r} \\ &\approx \sqrt{\left(\frac{1}{4\pi\epsilon_0} \frac{Ne_2}{\langle|\vec{r}\rangle + \delta\vec{r} - \vec{r}_i}\right)^2 - \left(\frac{1}{4\pi\epsilon} \frac{Ne_2}{\langle|\vec{r}\rangle - \vec{r}_i}\right)^2} \\ &\approx \frac{1}{4\pi\epsilon_0} \frac{Ne_2}{r_i^2} \delta r \quad . \end{aligned} \quad (3.31)$$

Thus,  $\delta V(\vec{r}_i)$  becomes  $\sim 0.7$  eV for  $r = 1$  mm and  $N = 10^6$ . MC simulations confirm that, when  $10^6$  electrons are generated within a sphere of 1 mm radius, an angular deviation of

$\delta\alpha = 0.5$  mrad develops after a few nanoseconds, which is equivalent to an initial photoelectric kinetic energy spread of  $\sim 0.2$  eV.

#### 3.2.4.2.4 Spatial Resolution for Space-Charge Limited Pulses

Unlike in continuous beam diffraction, a well-focused converging beam of small size is hard to achieve when using space-charge limited electron pulses as a probe. In the high charge density regime, the smallest probe size achievable is limited by the magnitude of the Coulomb repulsion among electrons. Consequently, it becomes impossible to focus the beam to a small point on the detector. However, the actual spot size of the unscattered beam is not important, as long as the Coulomb repulsions do not alter the converging electron trajectories *before* the pulse has passed the interaction region. Once the pulse has passed the interaction region, the scattered electrons separate from the main beam and carry the information about the specimen (encoded in the scattering angle) to the detector. Coulomb repulsions do not affect these trajectories, since the fraction of scattered electrons is small and the scattering angles are large compared to the divergence angle of the unscattered beam. This is in contrast to the imaging mode in the electron microscope, where the signal carrying electrons are focused again after the specimen. At the high peak currents in single-pulse operation, these focusing processes can lead to trajectory displacements through random scattering of the imaging electrons and, subsequently, to a stochastic reduction of the image resolution. [85,86](#)

To investigate a pulsed beam's spatial resolution capability, it is necessary to obtain more detailed insights into the electron bunch properties than can be obtained from the mean field model. The  $N$ -body Monte Carlo simulation delivers the three-dimensional

position and the three-dimensional momentum vectors for each of the particles in the bunch and is an ideal tool to study the coherence of the pulsed electron probe. We simulated electron pulses containing  $10^6$  electrons using an arbitrary gun design for a typical UED experiment. Figure 3.29a and Figure 3.29b show the evolution of the pulse radius and duration, respectively, with four different initial conditions, which determine the extent of the initial electron packet. It is evident that a spatially and temporally confined pulse goes through an initial Coulomb explosion and expands vigorously in both the lateral and the longitudinal direction.

The lateral expansion can be compensated for by the magnetic lens, but the longitudinal expansion is unaffected by the focusing field resulting in a larger temporal extent of the pulse at later times. After the initial Coulomb explosion, the pulse expansion is approximately linear, indicating that the space-charge effect has ceased to alter the pulse expansion in the drift region. The same cannot be said for the other pulses, where the stress of high initial potential energy had been alleviated by initially stretching or expanding the excitation laser pulse in either the lateral or the longitudinal direction or both. For these pulses, the evolution of the radius and the length remains upward curved (with the exception of the lateral expansion in the region of magnetic lens focusing) for the entire drift region. All but one of the electron pulses collide with the sample as a diverging bunch, which, as was shown above, is detrimental to the spatial resolution attainable in the instrument.

Figure 3.30 shows the lateral phase space projection of the four pulses at longitudinal positions of a)  $z = 100$  mm, b)  $z = 300$  mm, c)  $z = 500$  mm, and d)  $z = 645$  mm (interaction region): the particles' radial divergence angle,

$\kappa = \tan^{-1}(p_r/p_z)$ , defined as the angle directing the electron toward ( $\kappa < 0$ ) or away from ( $\kappa > 0$ ) the optical axis as a function of its radial distance from the optical axis. The initially positive, i.e., radially diverging chirp is reversed in direction by the magnetic lens. After passing the magnetic lens, the electrons once again come in close proximity further downstream in the region of the smallest beam waist. In this region of high charge density, Coulomb repulsions gradually reverse the sign of the linear correlation between radial positions and the convergence angles, until a new diverging chirp has developed. The ideal convergence angle, shown as the black line in Figure 3.30d, is only reproduced by the initially well confined pulse, since this pulse was able to expand initially and escape the sphere of influence of detrimental space-charge effects. For this pulse,  $\delta\theta = 1$  mrad and the resulting coherence length is  $7 \text{ \AA}$ , using the previously stated uncertainties for the other terms in Equation 3.21 and Equation 3.22. This particular pulse, although capable of producing high-resolution information, will result in a reduced signal (for gas-phase scattering), since the probability of the scattering events is directly proportional to the integrated areal density of the scattering centers, as well as the number of electrons passing through the interaction region. The signal intensity is increased, if the cross-sectional area of both the electron beam and the interaction region is reduced in size (assuming the sample delivery rate is constant).

The results in Figure 3.29 and Figure 3.30 suggest that in order to obtain a small probe size and the corresponding convergence angles at the interaction region, the electron pulse has to avoid excessive Coulomb repulsion until the electrons have scattered from the specimen in the interaction region. Consequently, for a beam of free electrons, the high charge density has to be relieved by stretching the pulse in the

longitudinal direction, such that the trajectories of the electrons are not altered by Coulomb repulsion before the interaction region and the pulse remains ideally focused. In other words, if the molecular density is low (e.g., in gas-phase diffraction) or the signal averaging time is limited such that the diffraction image has to be acquired in a single shot, then good spatial resolution and good signal intensity can only come at the expense of temporal resolution. On the other hand, if the experiment can afford an intermediate number of electrons ( $10^3$ – $10^5$ ), then the trade-off between temporal and spatial resolution becomes less demanding.

To quantify these statements, we optimized instrumental parameters to obtain a smaller beam waist at the interaction region. To produce the required convergence angle, the electron beam must have expanded laterally by the time it is being focused by the magnetic lens. If, however, the pulse is initially stretched in time to say  $\sim 100$  ps, then, for this prolate pulse, the intrinsic rate of the lateral expansion is too small to produce a beam wide enough. Experimentally, a larger beam size at the magnetic lens position can be realized in three ways: (i) by using a diverging lens in the source region, (ii) by increasing the acceleration gap, or (iii) by placing the magnetic lens farther away from the photocathode. In the last two instances, which depend on the initial charge density, the pulse is given more time to expand before it is being focused toward the interaction region, i.e., the space-charge effect is used as a diverging lens. Interestingly, a longer acceleration region must not necessarily have a detrimental effect on the temporal expansion of the electron pulse, as was previously postulated.<sup>87</sup> Since the early events in the lifetime of the electron pulse determine its future behavior, this measure can, under

certain conditions, bring about a reduction in the longitudinal momentum spread (see Section 3.2.6.6).

Using the second approach to expand the beam, a pulse containing  $10^6$  electrons giving improved spatial resolution compared to the previous pulses is shown in Figure 3.31. The experimental conditions in this case are the following: A uniform lateral profile with a small initial radius ( $r=100\ \mu\text{m}$ ), a broad Gaussian profile in time ( $\Delta t=100\ \text{ps}$ ), a large acceleration gap ( $d=25\ \text{mm}$ ), a magnetic lens located at  $z=180\ \text{mm}$ , and a shorter drift space to the interaction region at  $z=300\ \text{mm}$ . For this pulse,  $\delta\theta=0.5\ \text{mrad}$  and the resulting coherence length is  $12\ \text{\AA}$ , using the previously stated uncertainties for the other terms in Equation 3.21 and Equation 3.22. Alternatively, a small probe size could also be realized, if the pulse started out with a big initial diameter. However, we found that due to spherical aberration of the magnetic lens, this approach was less successful. It should be noted that the optimized pulse shown in Figure 3.31, although being better than the pulse under the original design, might not be the best pulse given the multitude of experimental parameters. The search for the optimal configuration would involve minimizing the pulse waist and the convergence angles to acceptable values by simultaneously changing several experimental parameters, including the electron pulses initial length and width, the length of the acceleration gap, the position of the magnetic lens, and the drift length to the interaction region.

### 3.2.5 Summary and Conclusion

The electron propagation dynamics determine the spatiotemporal resolution of diffraction of imaging. In this section, we addressed the fundamental issues involved in

capturing ultrafast dynamics on the atomic scale using pulsed electrons in diffraction and microscopy. The approach involves analytical expressions and MC simulations, together with comparisons with the experimental results.

The key findings of the present study are the following. First, as the number of electrons is increased within a pulse, the space-charge effect overpowers the contribution of the initial kinetic energy distribution. The dependence on electron density, acceleration voltage, lens geometry, dispersion in electron momentum, and the propagation time, are factors that were considered here. In the absence of space-charge, the temporal extent can be obtained from Equation 3.12 or Equation 3.13, while in the presence of space-charge, Equation 3.14 must be invoked with appropriate initial conditions. Both the MC simulations and the mean field theory give similar results only for longitudinal extent of pulses, as shown in Figure 3.23 and Figure 3.25.

Second, for space-charge limited electron bunches, the mean field theory gives a good estimation of the longitudinal spreading of the pulses, but the evolution of the pulse radius is not well predicted using this approach. The mean field theory, therefore, can give an estimate of the temporal resolution (as determined by the longitudinal extent). However, for a converging geometry (see Figure 3.20 and Figure 3.26), the observed at-the-detector coherence length, which is given by  $1/\delta s$  of Equation 3.21, is very large when considering the mean field theory, since it relies on the assumption that  $\delta\theta = 0$  (i.e., all electrons fall perfectly on the black line in the electron phase space diagrams of Figure 3.30d and Figure 3.31), and coherence is only limited by the smaller terms of Equation 3.21. In reality, coherence is mainly limited by the distribution of scattering angles resulting from the individual electron trajectories and its value is clear from the

results of our MC simulations in Figure 3.31. If the beam geometry is not converging ideally, the lateral size of the interaction region needs to be considered in Equation 3.21. Thus, the use of  $r_c = \lambda/2\pi\delta\alpha$  by many as a measure of coherence is incomplete. We also note that, because the fraction of scattered electrons is very small, the space-charge effect can be considered absent after the interaction region.

Finally, for an electron (imaging) microscope operating in the single-electron pulsed mode or continuous-wave mode, the spatial resolution limits are the same, i.e., mainly determined by the electron source brightness and the quality of lenses. The temporal resolution is determined by the spread in the initial kinetic energy of the photoelectrons and the strength of the acceleration field. If such instruments are operated at high charge densities (single-shot mode), the evaluation of the spatial and temporal resolution has to account for the space-charge effect each time the electrons come in close proximity to each other both prior and after scattering by the specimen.<sup>85,86</sup>

From these studies, we now address the experimental regimes of this laboratory. For single-electron UEM, it is clear that two effects have been suppressed by this development, namely the severe influence of space-charge not only on the temporal (longitudinal) broadening, but also on the spatial (lateral) dispersion, which introduces divergence and, hence, a loss in image resolution. The kinetic energy distribution, when using a cold photocathode, is limited by the excess photon energy available above the work function, which can be tuned to be less than 0.1 eV,<sup>78</sup> resulting in a femtosecond pulse duration. The spatial resolution achieved in single-electron pulsed mode has reached the atomic scale in UEM2 with features resolved below 3 Å,<sup>88</sup> which is comparable to the resolution capabilities of conventional electron microscopes.

In the high charge density regime, the situation is very different. In UED4, the pulse length ranges from 1 to 30 ps (when using 120 fs laser excitation) depending on the number of electrons in the pulse ( $10^4$ - $10^6$ ). Using a convergent beam geometry, it is possible to determine internuclear distances up to 12 Å (possibly more) with a resolution of 0.01 Å in diffraction. In UEC, the temporal resolution can be increased to the femtosecond regime, when using a very low electron density per pulse and a newly implemented tilted wave-front excitation scheme.<sup>89,90</sup>

All of the above treatments are for acceleration voltages of  $\leq 200$  kV. At higher kinetic energies, where the electrons approach the speed of light, the space-charge effect becomes less of an issue due to relativistic effects (the effective force is attenuated by a factor of  $\gamma^{-3}$ ). Recent results suggest that single-shot electron diffraction patterns can be obtained using pulses containing  $10^7$  electrons, which were accelerated to 5.4 MeV.<sup>91</sup> It was suggested that this technique could reach sub-picosecond time resolution by utilizing the longitudinal pulse compression induced through time-dependent rf-acceleration.<sup>92</sup> Theoretically, longitudinal focusing at lower kinetic energies ( $\leq 200$  kV) can also be realized, either by acceleration through a static voltage gradient<sup>90</sup> or by rf-acceleration.<sup>93,94</sup> However, care should be taken in evaluating the spatial resolution capabilities of such self-compressing electron pulses, since the space-charge effect will, at high enough charge densities, adversely affect the electron trajectories in the interaction region, thereby possibly obscuring any spatial information about the specimen.

### 3.2.6 Appendix

#### 3.2.6.1 Scattering Signal Intensity

The probability that an incident electron is scattered by an atom is given by that atom's scattering cross section  $\sigma_e$ . The scattered signal is proportional to the overlap of the electron beam with the scattering centers. Considering a pulse containing  $N_e$  electrons within an area  $A_e$  (perpendicular to the propagation direction) incident on  $N_a$  scattering centers in a volume  $V_a$ , the scattering signal intensity is given by

$$I = \sigma \int \frac{N_e}{A_e} \frac{N_a}{V_a} dV = \sigma N_e N_a \int \rho_e(x, y) \rho_a(x, y, z) dV \quad , \quad (3.32)$$

where  $\rho_e$  and  $\rho_a$  are the spatial distributions of the electrons and the scattering centers, respectively. The value of  $N_e$  is assumed to remain constant throughout the interaction volume, because only a small fraction of electrons are scattered without depletion of the original density. If the distributions are assumed to be uniform, then the expression further simplifies to

$$I = \sigma \frac{N_e}{A_e} \frac{N_a}{V_a} \int dV = \sigma \frac{N_e}{A_e} \frac{N_a}{V_a} A_e l = N_e \rho_a \sigma_e l \quad , \quad (3.33)$$

where  $\rho_a$  is now the volume density of scattering centers.

The electron scattering cross section for carbon is  $\sigma_{carbon,60keV} = 1.21 \cdot 10^{-18} \text{ cm}^2$ ,<sup>95</sup> which results in a total scattering probability per electron of  $\sim 10^{-3}$  for a gas density  $\rho = 3 \times 10^{16} \text{ cm}^{-3}$  (=1 torr) and  $l = 300 \mu\text{m}$ . (For comparison, the scattering cross section of X-rays,  $\sigma_{carbon,8keV} = 9.17 \cdot 10^{-23} \text{ cm}^2$  and  $\sigma_{carbon,60keV} = 3.19 \cdot 10^{-24} \text{ cm}^2$ .<sup>96</sup>) For a diffraction pattern using pulses of  $10^4$  electrons, ten electrons are scattered per pulse and,

with a repetition rate of 1 kHz,  $10^4$  electrons are collected in one second and acquisition times of 240 seconds are common in UED3. In UEC, the density of the specimen is much higher, such that almost all the electrons are scattered, which allows for 1-5 second exposures to collect  $10^6$  electrons using  $10^3$  electrons per pulse at 1 kHz. Furthermore, Bragg spots are much more localized in  $s$ -space, which results in an improved signal quality. In single-electron UEM, an image can be obtained, when the electron pulse train contains a total of  $\sim 10^7$  electrons, i.e., the image is formed in  $\sim 1$  second, when using a repetition rate of 80 MHz.

### 3.2.6.2 Bunch Dimensions and Standard Deviations

For a Gaussian distribution, the full-width-half-maximum (FWHM) is given as  $\sqrt{8 \ln 2} \sigma$  by solving

$$\frac{1}{\sqrt{2\pi}\sigma} \exp\left[-\frac{x^2}{2\sigma^2}\right] = \frac{1}{2} \frac{1}{\sqrt{2\pi}\sigma} \quad \text{for } 2x = FWHM \quad . \quad (3.34)$$

For a one-dimensional uniform distribution, the standard deviation is given as

$$\sigma^2 = \int_{-L/2}^{+L/2} (x-0)^2 \frac{1}{L} dx = \frac{L^2}{12} \quad . \quad (3.35)$$

For a two-dimensional radial uniform distribution, the standard deviation is given as

$$\sigma^2 = \int_{-R}^{+R} (x-0)^2 \frac{2\sqrt{R^2-x^2}}{\pi R^2} dx = \frac{R^2}{4} \quad . \quad (3.36)$$

The conversion relations for the length and radius of cylindrical, ellipsoidal and Gaussian pulse shapes are given in Table 3.3.

### 3.2.6.3 Initial Kinetic Energy

The temporal length of the laser pulse and its photon energy directly affect the temporal length of the electron packet. A free electron is generated with an initial momentum of magnitude  $p_i$  at  $t = 0$  and then accelerated between the cathode and the anode, which are separated by a distance  $d$  and held at a potential difference  $V$ . The electron gains momentum under the influence of the constant electric field:

$$p(t) = p_i + \frac{qV}{d}t \quad . \quad (3.37)$$

The time the electron spends in the acceleration region is thus  $t_a = \frac{d}{qV}(p_f - p_i)$ , where  $p_f$  is the electron momentum after exiting the acceleration gap. In the field-free region, the electron travels at a constant velocity  $v_f$  for a drift time  $t_d = l/v_f$ . The total flight time is then simply  $t = t_a + t_d$ .

The time spread of an ensemble of electrons with an initial momentum spread  $\Delta p_i$  will be

$$\Delta t^2 = \left( \frac{\partial t}{\partial p_i} \right)^2 \Delta p_i^2 \quad . \quad (3.38)$$

To evaluate the coefficient  $\partial t / \partial p_i = \partial t_a / \partial p_i + \partial t_d / \partial p_i$  relating the momentum spread to time spread, we need equations for the relativistic kinetic energy,  $E$ , and the relativistic momentum,  $p$ :

$$E = \sqrt{p^2 c^2 + m_0^2 c^4} - m_0 c^2 \quad , \quad (3.39)$$

$$p = \frac{m_0 v}{\sqrt{1 - \left(\frac{v}{c}\right)^2}} = \gamma m_0 v \quad , \quad (3.40)$$

and their derivatives

$$\frac{\partial E}{\partial p} = \frac{pc^2}{\sqrt{p^2 c^2 + m_0^2 c^4}} = \frac{p}{m_0} \frac{1}{\sqrt{\left(\frac{p}{m_0 c}\right)^2 + 1}} = \frac{p}{m_0} \frac{1}{\gamma} = v \quad , \quad (3.41)$$

$$\frac{\partial p}{\partial v} = \frac{m_0}{\left[1 - \left(\frac{v}{c}\right)^2\right]^{3/2}} = \gamma^3 m_0 \quad . \quad (3.42)$$

Such that

$$\begin{aligned} \frac{\partial t_a}{\partial p_i} &= \left(\frac{d}{qV}\right) \left(\frac{\partial p_f}{\partial p_i} - 1\right) \\ &= \left(\frac{d}{qV}\right) \left(\frac{\partial p_f}{\partial E_f} \frac{\partial E_f}{\partial E_i} \frac{\partial E_i}{\partial p_i} - 1\right) \\ &= \left(\frac{d}{qV}\right) \left(\frac{v_i}{v_f} - 1\right) \quad , \end{aligned} \quad (3.43)$$

upon using Equation 3.41 and  $\partial E_f / \partial E_i = 1$ . Also

$$\begin{aligned} \frac{\partial t_d}{\partial p_i} &= \frac{\partial t_d}{\partial v_f} \frac{\partial v_f}{\partial p_f} \frac{\partial p_f}{\partial p_i} \\ &= -\frac{1}{v_f^2} \frac{1}{\gamma_f^3 m_0} \frac{v_i}{v_f} \quad . \end{aligned} \quad (3.44)$$

Substituting the combined Equation 3.43 and Equation 3.44 into Equation 3.38 and taking the square root leads to

$$\delta t = \left| -\frac{d}{eV} \left( 1 - \frac{v_i}{v_f} \right) - \frac{l}{m_0 \gamma_f^3} \frac{v_i}{v_f} \right| \delta p_i \quad . \quad (3.45)$$

### 3.2.6.4 Axial Acceleration in Uniform Disk Charge Distribution

For thin disk of uniform charge distribution, the Coulomb force at an axial position,  $z$ , can be evaluated as

$$\begin{aligned} F_x(z) &= \frac{e}{4\pi\epsilon_0} \int dV \rho \frac{\vec{r}}{r^3} \\ &= \frac{e}{4\pi\epsilon_0} \rho \int_0^R R' dR' \int_0^{2\pi} d\Theta' \int_{-L/2}^{L/2} dZ' \frac{z + Z'}{\left( \sqrt{R'^2 + (z + Z')^2} \right)^3} , \end{aligned} \quad (3.46)$$

where  $R$  is the radius,  $L$  is the thickness of disk, and  $\rho = Ne/\pi R^2 L$  is the uniform charge density. The integration yields

$$F_x(z) = \frac{e}{4\pi\epsilon_0} \rho \pi \left( \frac{\sqrt{(L+2z)^2} - \sqrt{(L-2z)^2} + \sqrt{4R^2 + (L-2z)^2} - \sqrt{4R^2 + (L+2z)^2}}{2} \right) . \quad (3.47)$$

The force at the axial position  $z = L/2$  becomes

$$\begin{aligned} F_x\left(\frac{L}{2}\right) &= \frac{e}{4\pi\epsilon_0} \rho 2\pi \left( R + L - \sqrt{R^2 + L^2} \right) \\ &= \frac{e}{4\pi\epsilon_0} \left( \frac{Ne}{\pi R^2 L} \right) 2\pi \frac{2RL}{R + L + \sqrt{R^2 + L^2}} \\ &= \frac{e}{2\pi\epsilon_0} \frac{Ne}{R^2} \frac{2}{1 + \frac{L}{R} + \sqrt{1 + \left(\frac{L}{R}\right)^2}} . \end{aligned} \quad (3.48)$$

And the axial acceleration becomes

$$\frac{1}{2} \frac{d^2 L}{dt^2} = \frac{d^2 z}{dt^2} = a_x = \frac{F_x(z = L/2)}{m_e} , \quad (3.49)$$

which is Equation 3.14. The result is in agreement with that of Ref. [69](#), in which the authors integrate Poisson's equation for a charge distribution to get the axial potential. Differentiation of the potential with respect to the longitudinal coordinate gives the electric field and ultimately the acceleration in that direction.

### 3.2.6.5 Attenuation of Interference Intensity Due to Incoherence

In UED, the sinusoidal intensity is attenuated by blurring through a normally distributed  $s$  as

$$\begin{aligned}
 I(s) &\propto \int \sin(xr) \frac{1}{\sqrt{2\pi}\sigma_s} \exp\left[-\frac{(x-s)^2}{2\sigma_s^2}\right] dx = \sin(sr) \exp\left[-\frac{r^2\sigma_s^2}{2}\right] \quad , \\
 \exp\left[-\frac{r^2\sigma_s^2}{2}\right] &= \frac{1}{\sqrt{e}} \approx 0.88 \quad \text{at} \quad r = \frac{1}{2\sigma_s} \quad , \\
 \exp\left[-\frac{r^2\sigma_s^2}{2}\right] &= \frac{1}{e} \approx 0.61 \quad \text{at} \quad r = \frac{1}{\sigma_s} \quad , \\
 \exp\left[-\frac{r^2\sigma_s^2}{2}\right] &= \frac{1}{e} \approx 0.37 \quad \text{at} \quad r = \frac{\sqrt{2}}{\sigma_s} \quad , \\
 \exp\left[-\frac{r^2\sigma_s^2}{2}\right] &= \frac{1}{e^2} \approx 0.14 \quad \text{at} \quad r = \frac{2}{\sigma_s} \quad .
 \end{aligned}
 \tag{3.50}$$

The conventional definition of coherence length corresponds to where the intensity is attenuated down to 88%.

In UEC, the Bragg spot is blurred and the signal contrast is attenuated as

$$\begin{aligned}
I(s) &\propto \sum_i \int \frac{1}{\sqrt{2\pi}\sigma_i} \exp\left[-\frac{(x-s_i)^2}{2\sigma_i^2}\right] \frac{1}{\sqrt{2\pi}\sigma_s} \exp\left[-\frac{(x-s)^2}{2\sigma_s^2}\right] dx \\
&= \sum_i \frac{1}{\sqrt{2\pi(\sigma_s^2 + \sigma_i^2)}} \exp\left[-\frac{(s-s_i)^2}{2(\sigma_s^2 + \sigma_i^2)}\right] \quad \text{where } s_i = \frac{2\pi i}{r} \quad . \\
\text{Contrast} &= \frac{I(s_i) - I(s_i + \frac{\pi}{r})}{I(s_i)} = 1 - \frac{\sum_{i=1}^m 2 \exp\left[-\frac{(\frac{2\pi(i-1/2)}{r})^2}{2(\sigma_s^2 + \sigma_i^2)}\right]}{1 + \sum_{i=1}^m 2 \exp\left[-\frac{(\frac{2\pi i}{r})^2}{2(\sigma_s^2 + \sigma_i^2)}\right]} \\
&\approx 1 - 2 \exp\left[-\frac{(\frac{\pi}{r})^2}{2\sigma_s^2}\right] \quad . \\
\text{Contrast} &= 0.99 \quad \text{at} \quad r = \frac{1}{\sigma_s} \quad . \\
\text{Contrast} &= 0.83 \quad \text{at} \quad r = \frac{\sqrt{2}}{\sigma_s} \quad . \\
\text{Contrast} &= 0.43 \quad \text{at} \quad r = \frac{2}{\sigma_s} \quad . \\
\text{Contrast} &= 0.00 \quad \text{at} \quad r = \frac{4}{\sigma_s} \quad .
\end{aligned} \tag{3.51}$$

### 3.2.6.6 Suppression of Coulomb Repulsion during Acceleration

Commonly efforts have been made to shorten the acceleration gap in order to accelerate the electron packet as quickly as possible to shorten their propagation time and, thereby, minimize the effects of the initial Coulomb explosion. This school of thought was mostly based on the concern that at the moment of generation of the photoelectrons, the charge density is unfavorably high. From Equation 3.12 and Equation 3.13 it is evident that the temporal spread due to initial kinetic energy spread is directly proportional to the acceleration gap, though this contribution is in the femtosecond regime. Interestingly, from Equation 3.14 it can be deduced that in the case of a very thin disk, the initial thickness does not alter the magnitude of Coulomb

repulsion, since the aspect ratio,  $L/R$ , is vanishingly small and remains small for early times. Therefore, the Coulomb repulsion can be treated as an approximately constant acceleration in the beginning. It can be shown using the mean field theory that the space-charge induced momentum spreads of both freely drifting electrons and accelerating electrons are the same after traveling the same distance. To illustrate this point, we separately consider the mechanical work done on the front and the rear end of the pulse, by the acceleration field and Coulomb repulsion. In the thin-disk limit we have

$$\begin{aligned} W_F &= m(a_A + a_X)d \quad , \\ W_B &= m(a_A - a_X)d \quad . \end{aligned} \quad (3.52)$$

This work results in changes of the kinetic energies according to

$$\begin{aligned} W_F &= E_{f,F} - E_{i,F} \quad , \\ W_B &= E_{f,B} - E_{i,B} \quad . \end{aligned} \quad (3.53)$$

For acceleration,  $E_i = 0$  and  $ma_A d = qV$ , while for a free drifting,  $E_i = qV$  and  $a_A = 0$ .

Either way, the final kinetic energies are

$$\begin{aligned} E_{f,F} &= qV + ma_X d \quad , \\ E_{f,B} &= qV - ma_X d \quad . \end{aligned} \quad (3.54)$$

Therefore, they both result in an energy spread of  $2ma_X d$ , or a momentum spread

$$\Delta p = \frac{m}{p} \Delta E = \frac{m}{\sqrt{2mE}} \Delta E = \sqrt{\frac{m}{2E}} \Delta E = \sqrt{\frac{m}{2qV}} 2ma_X d = \sqrt{\frac{2m^3}{qV}} a_X d \quad . \quad (3.55)$$

We note that it takes accelerating electrons twice as long to travel the same distance. Also it can be shown that the spatial expansion of the accelerating electrons is four times larger than of free flying electrons after traveling the same distance, resulting in a four times larger increase in the temporal spread.

$$\begin{aligned}
 L_{\text{accelerating}}(x=d) &= L_i + 2a_x \left( \frac{2d}{v_i + v_f} \right)^2 \approx 8a_x \left( \frac{d}{v_f} \right)^2, \\
 L_{\text{drifting}}(x=d) &= L_i + 2a_x \left( \frac{d}{v_f} \right)^2 \approx 2a_x \left( \frac{d}{v_f} \right)^2,
 \end{aligned}
 \tag{3.56}$$

$$\begin{aligned}
 R_{\text{accelerating}}(x=d) &= R_i + a_R \left( \frac{2d}{v_i + v_f} \right)^2 \approx R_i, \\
 R_{\text{drifting}}(x=d) &= R_i + a_R \left( \frac{d}{v_f} \right)^2 \approx R_i.
 \end{aligned}
 \tag{3.57}$$

However, in reality, the expanding diameter will reduce the Coulomb repulsions and therefore the momentum spread can be smaller, at the cost of a larger beam size.

**Table 3.1.** Electron to photon conversion efficiency of a phosphor screen (thickness ca. 4-5  $\mu\text{m}$ , grain size ca. 1  $\mu\text{m}$ , aluminium reflection layer)

Phosphor Type	Efficiency (photons per electron at given electron kinetic energy)			
	6 keV	10 keV	12 keV	15 keV
P 43	185	330	420	550
P 46	90	160	200	265
P 47	212	380	480	630
P 20	240	430	115	715
P 11	200	360	455	600

**Table 3.2.** Image intensifier power supply wiring diagram

Pin	Input Type <sup>[a]</sup>	Input Wire Color	Output Type	Output Wire Color
1	Not connected	-	Cathode (+50 - -200V)	Blue
2	Gate Trigger (TTL)	White	MCP in (0V)	Green & Red
3	Gain (0-1000V)	Orange	MCP out (600-900V)	Black
4	WAPSU (+5V)	Red	Not connected	-
5	GM10-50 (+5V)		Screen (6.1-6.4kV)	Yellow
6	Not connected	-	Not connected	-
7	Trigger (0V)	Black	N/A	N/A
8	WAPSU (0V)		N/A	N/A
9	GM10-50 (0V)		N/A	N/A

<sup>[a]</sup> Input voltages are supplied by the home built power supply control box, shown in Figure 3.8b

**Table 3.3.** Relations between standard deviation ( $\sigma$ ) and other measured widths

	maximum-extent		full-width-half-maximum	
	length	diameter	longitudinal	lateral
cylindrical	$\sigma\sqrt{12}$	$4\sigma$		$\sigma\sqrt{12}$
ellipsoidal	$\sigma\sqrt{20}$	$\sigma\sqrt{20}$	$\sigma\sqrt{10}$	$\sigma\sqrt{10}$
Gaussian			$\sigma\sqrt{8\ln 2}$	$\sigma\sqrt{8\ln 2}$

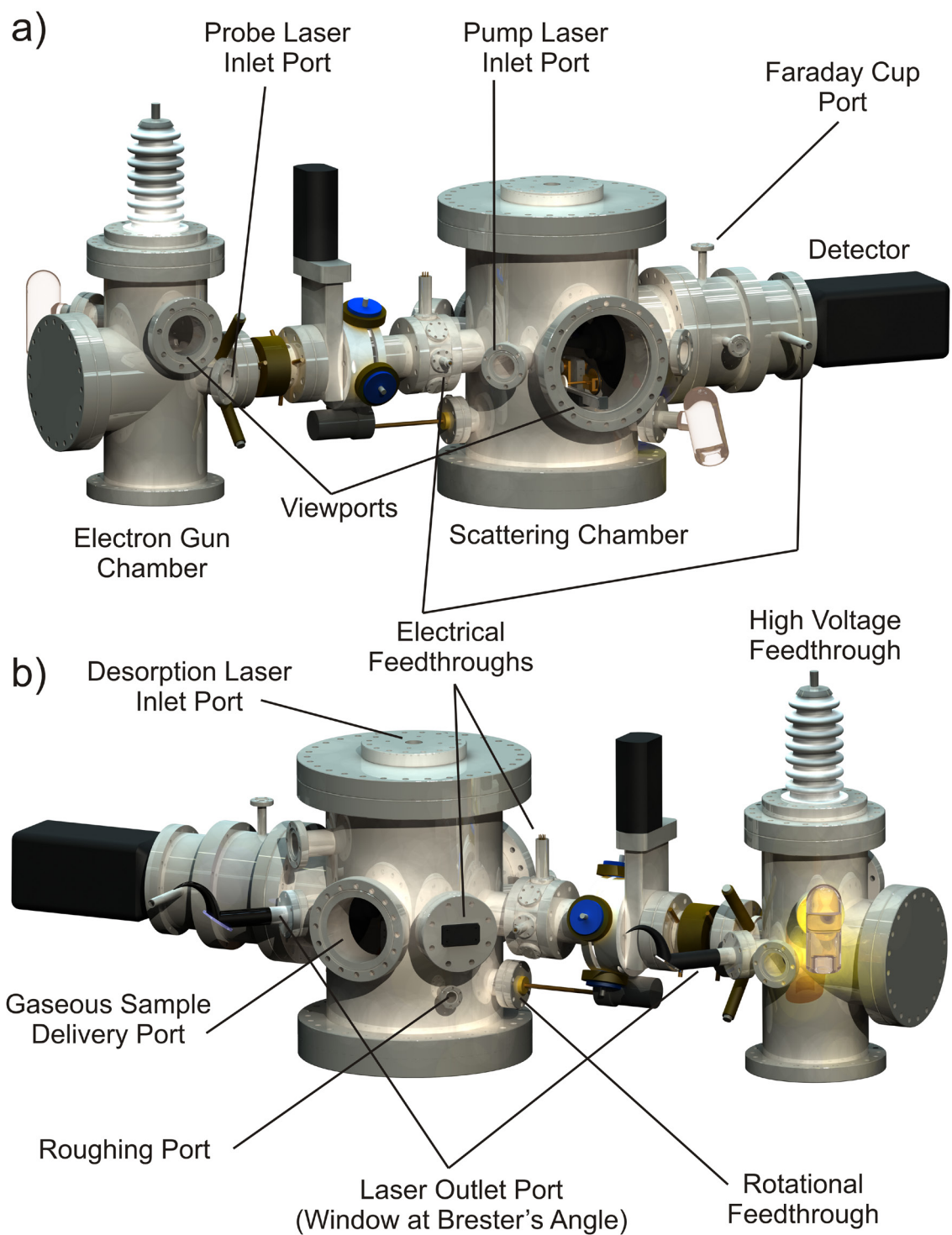


**Figure 3.1.** The a) front and b) back of the UED apparatus with the relevant ports indicated. A high vacuum is maintained in both chambers by pumping through the ports at the bottom.

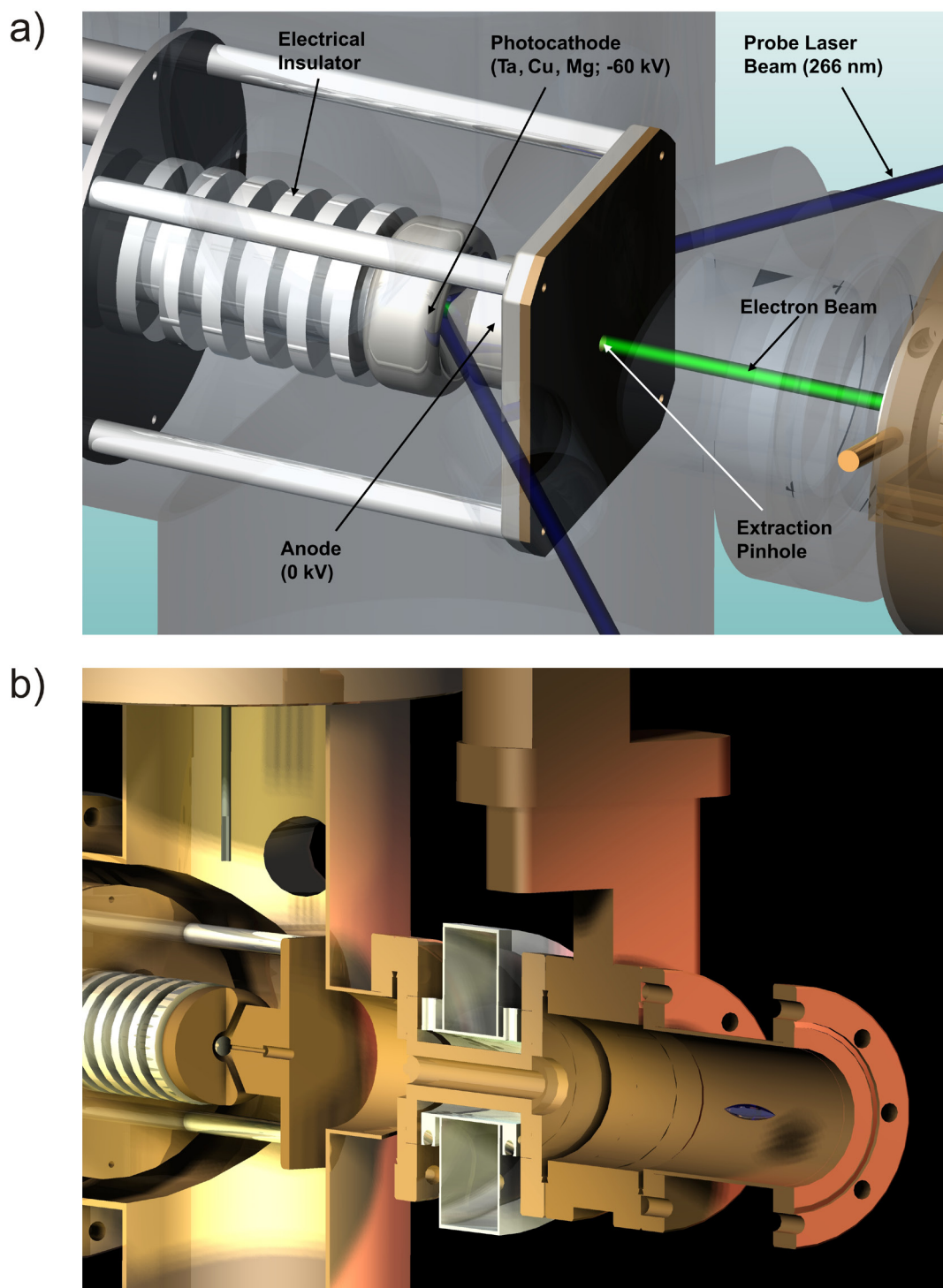


**Figure 3.2.** The UED4 electron gun. a) Free electrons, generated by front illumination of a solid metal photocathode with a femtosecond or nanosecond laser pulse, are accelerated through a potential difference of 60 kV. b) Cutaway view of the electron gun showing the internal geometry of the extraction pinhole and an electron pulse in the drift region of the electron optical column.

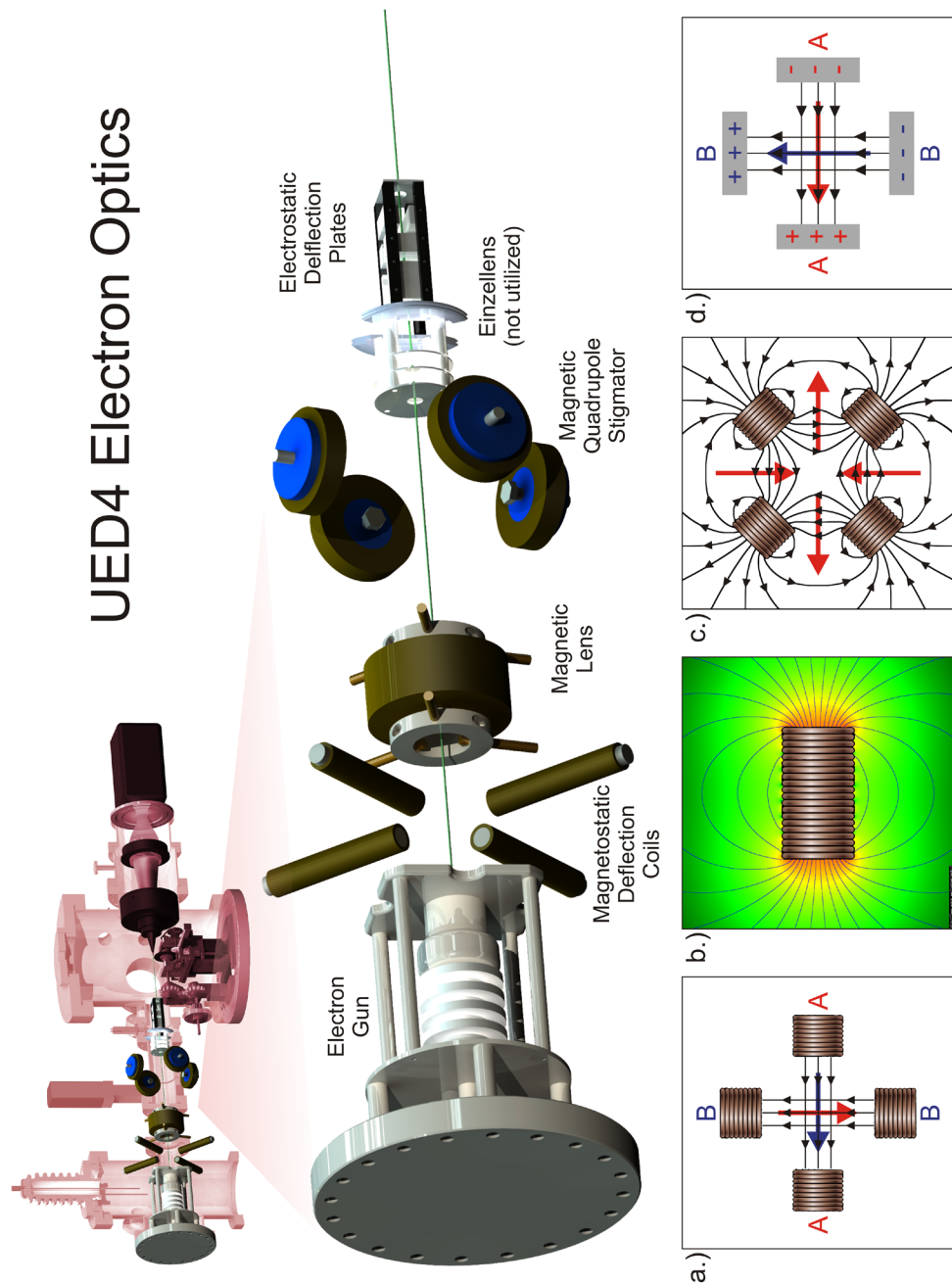


**Figure 3.3.** a) The electron bunches emerging from the pinhole in the anode are steered and shaped by a variety of electron optical components, as indicated by the red arrows in the panels. a) By adjusting the separate currents through two pairs of coils (A and B) two orthogonal magnetic fields are produced to steer the electrons in the x- and y-direction. b) A magnetic lens (solenoid) focuses the electron onto the detector. c) A magnetic quadrupole field corrects the astigmatism of the magnetic lens by exerting differential radial forces on the electrons. d) By adjusting the separate voltages across two pairs of deflection plates (A and B) two orthogonal electric fields are produced to steer the electrons in the x- and y-direction.

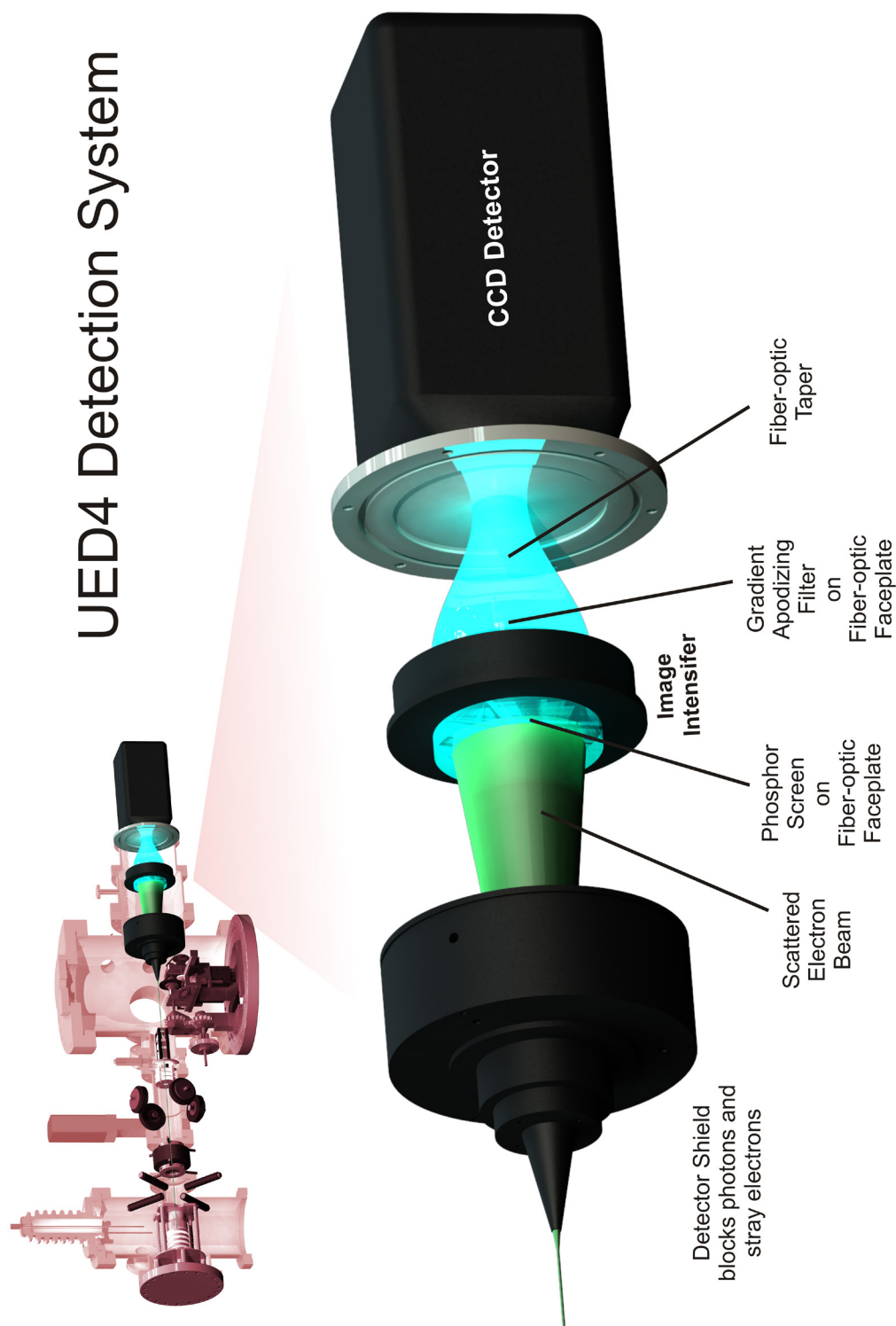


**Figure 3.4.** UED4 detection system. The 60 keV electrons generate a photon signal after hitting the phosphor scintillator screen. The photon signal is subsequently amplified using a multi-channel-plate (MCP) image intensifier, attenuated by a gradient apodizing filter, demagnified through a fiber-optic taper, and finally recorded on a CCD chip.

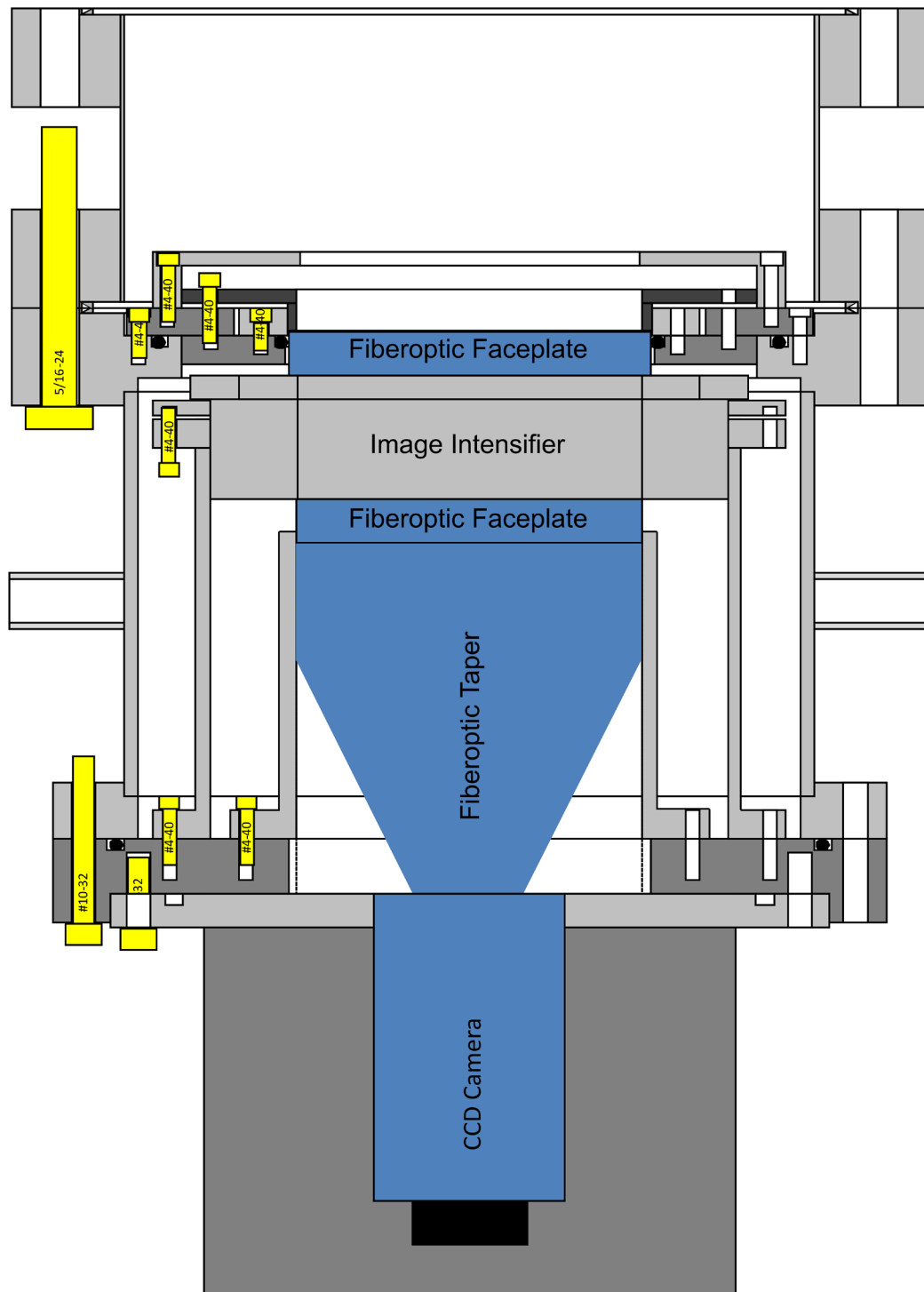


**Figure 3.5.** The detector assembly of UED4 inside its custom-built housing. Several cylindrical housing parts hold the coupled fiber-optic components in place and ensure the correct spacing and parallelism between them. A vacuum seal is accomplished through a series of o-rings (black circles).

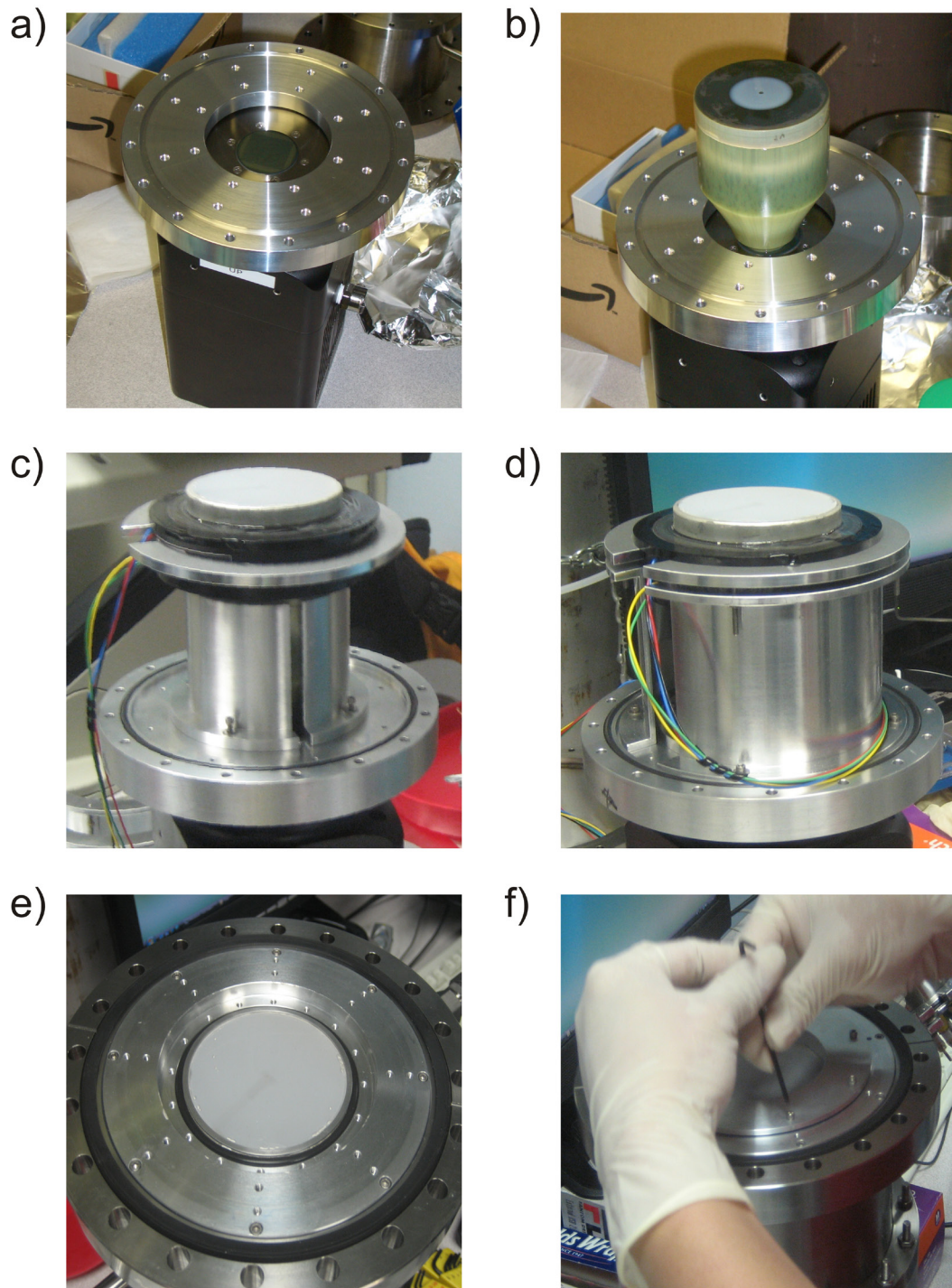


**Figure 3.6.** Assembly of the detection system. a) The fiber-optic input window to the CCD chip. b) The fiber-optic taper and faceplate showing the aluminum gradient apodizing filter. c) The image intensifier tube and the fiber-optic faceplate with the applied phosphor screen. d) A two-part aluminum sleeve holds the image intensifier tube in place. e) The aluminum ring holds the phosphor screen in place. f) The final aluminum cap applies slight pressure to the entire stack of fiber-optic components.

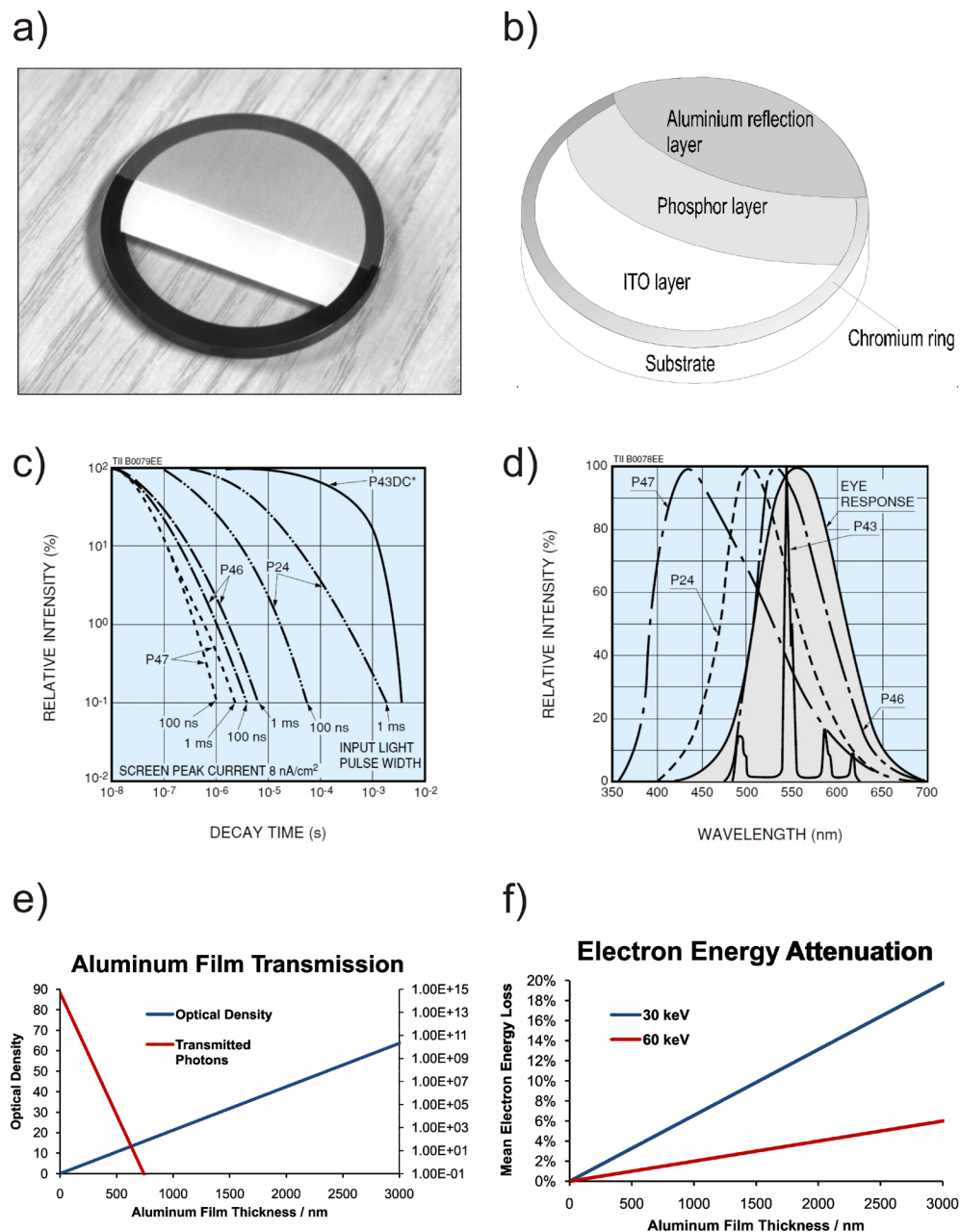
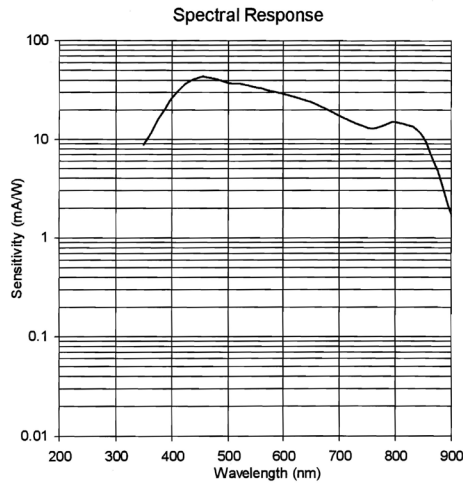
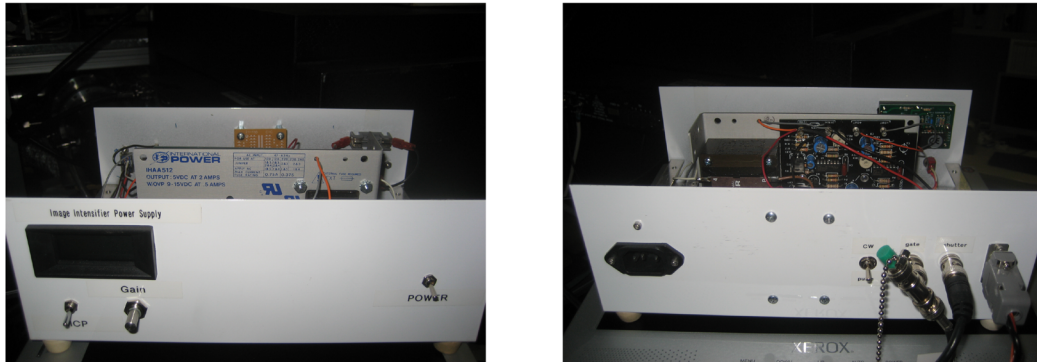


**Figure 3.7.** Phosphor scintillator screen. a) and b) Applied layers that make up the phosphor scintillator screen on a glass substrate (taken from Proxitronic manufacturing brochure). c) and d) The emission characteristics of different phosphor materials (according to Hamamatsu manufacturing brochure). P47 is used for the UED4 detector. e) Transmission measurements show that an aluminum film of 700 nm thickness results in an optical density of 15, which should prevent all the photons possibly present in the scattering chamber from entering the detector. f) Given the published<sup>41</sup> electron stopping power of aluminum, a film of 700 nm thickness should reduce the kinetic energy of the electrons only minimally (<1.5% for 60 keV electrons).

a)



b)



c)

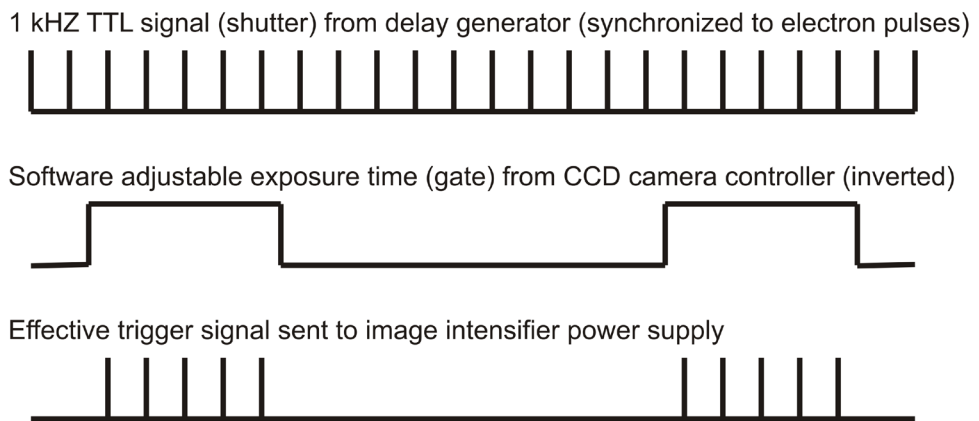


**Figure 3.8.** a) Image intensifier spectral response (from the provided test report). b) and c) Image intensifier control box, which combines (logical AND) the trigger signal from the experiment master clock and the CCD exposure time setting to supply the effective trigger signal to the image intensifier.

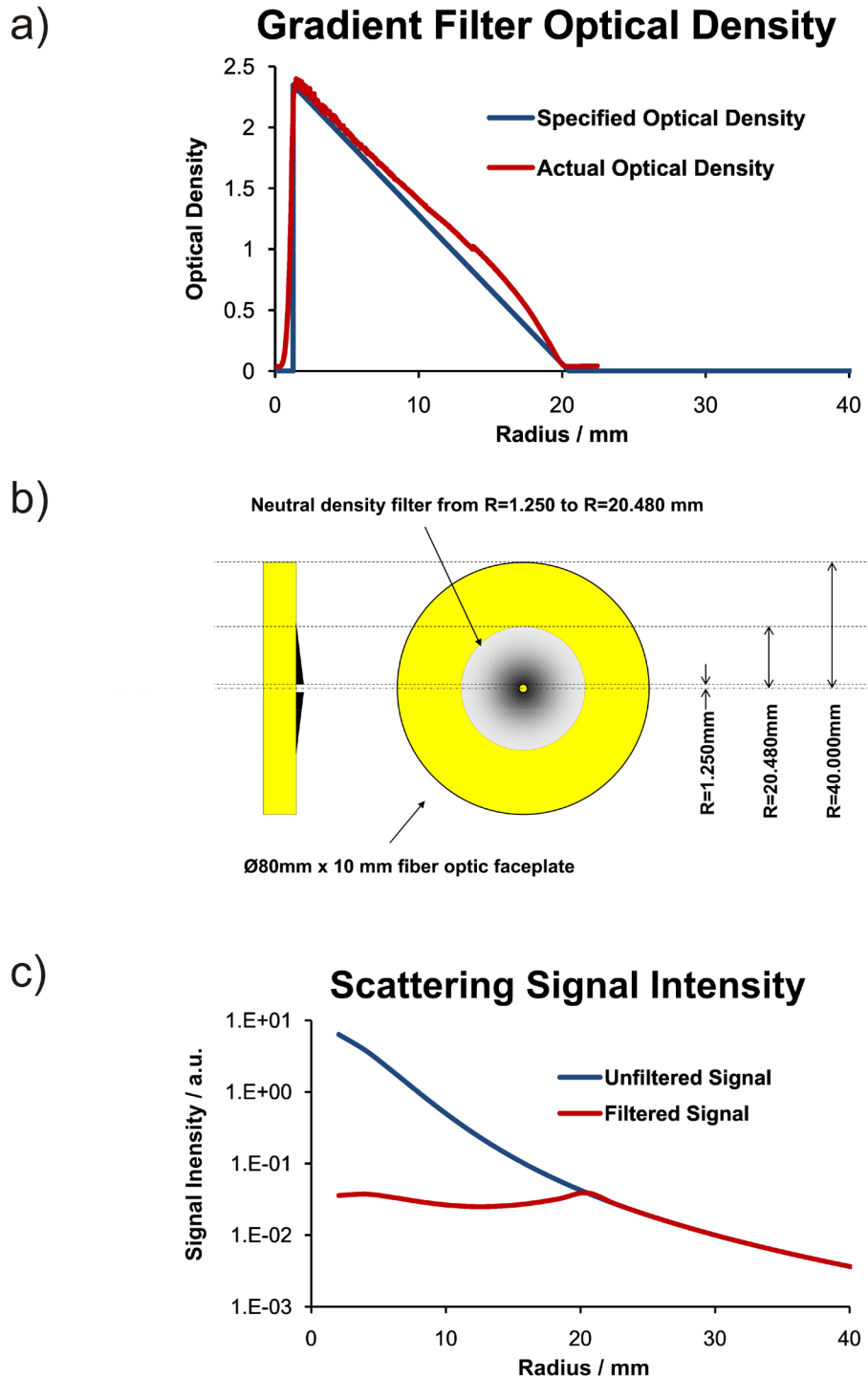


**Figure 3.9.** Gradient apodizing filter. a) A plot of the specified and measure optical density according to Equation 3.1. b) Schematic showing the dimensions of the aluminum coat on the fiber-optic faceplate. c) The dynamic range of the detector for scattered electrons is improved by roughly two orders of magnitude by the addition of the filter.

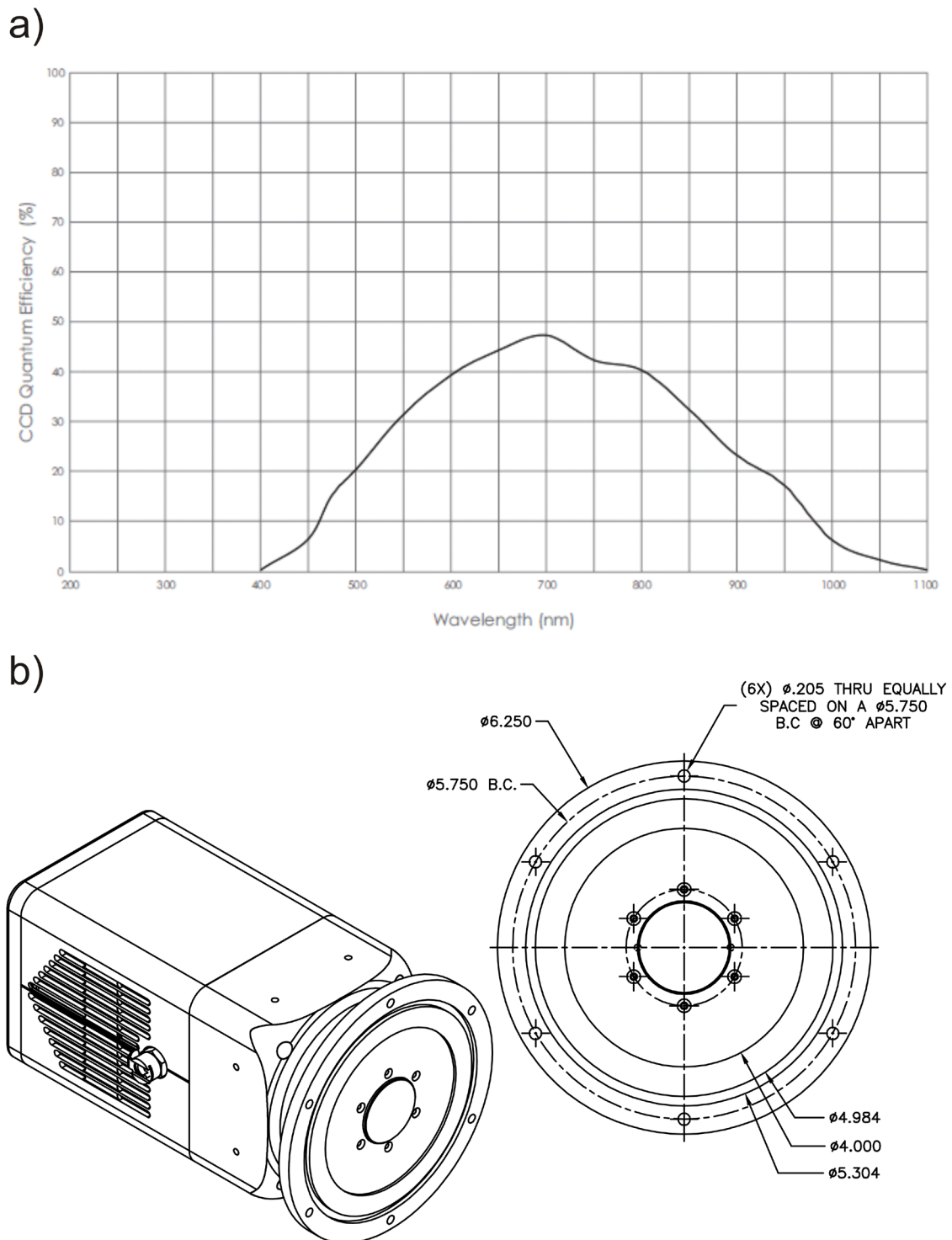


**Figure 3.10.** a) The quantum efficiency of the CCD chip over visible wavelengths (taken from Princeton Instruments manufacturing brochure). b) The CCD camera is outfitted with a custom-designed flange to facilitate high-precision mechanical coupling to the image intensifier housing.

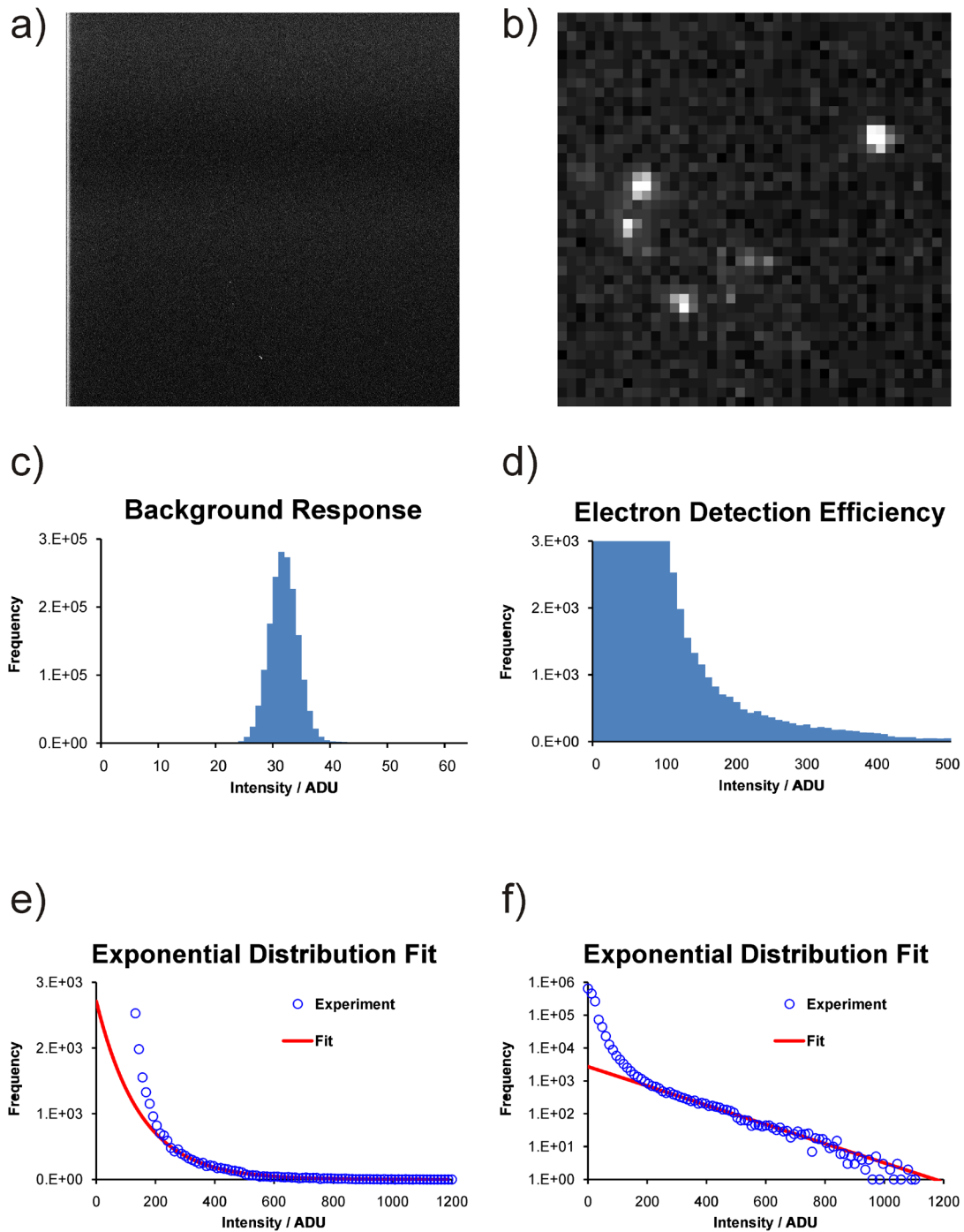


**Figure 3.11.** Single electron detection calibrations. a) Background response over the entire detection screen. b) Single electron detection events in an unfiltered ROI. c) Intensity histogram of the image shown in a). d) Intensity histogram of single electron detection events. e) and f) Equation 3.2 is fit to the recorded intensity distribution to extract the expectation value for the detective quantum efficiency.

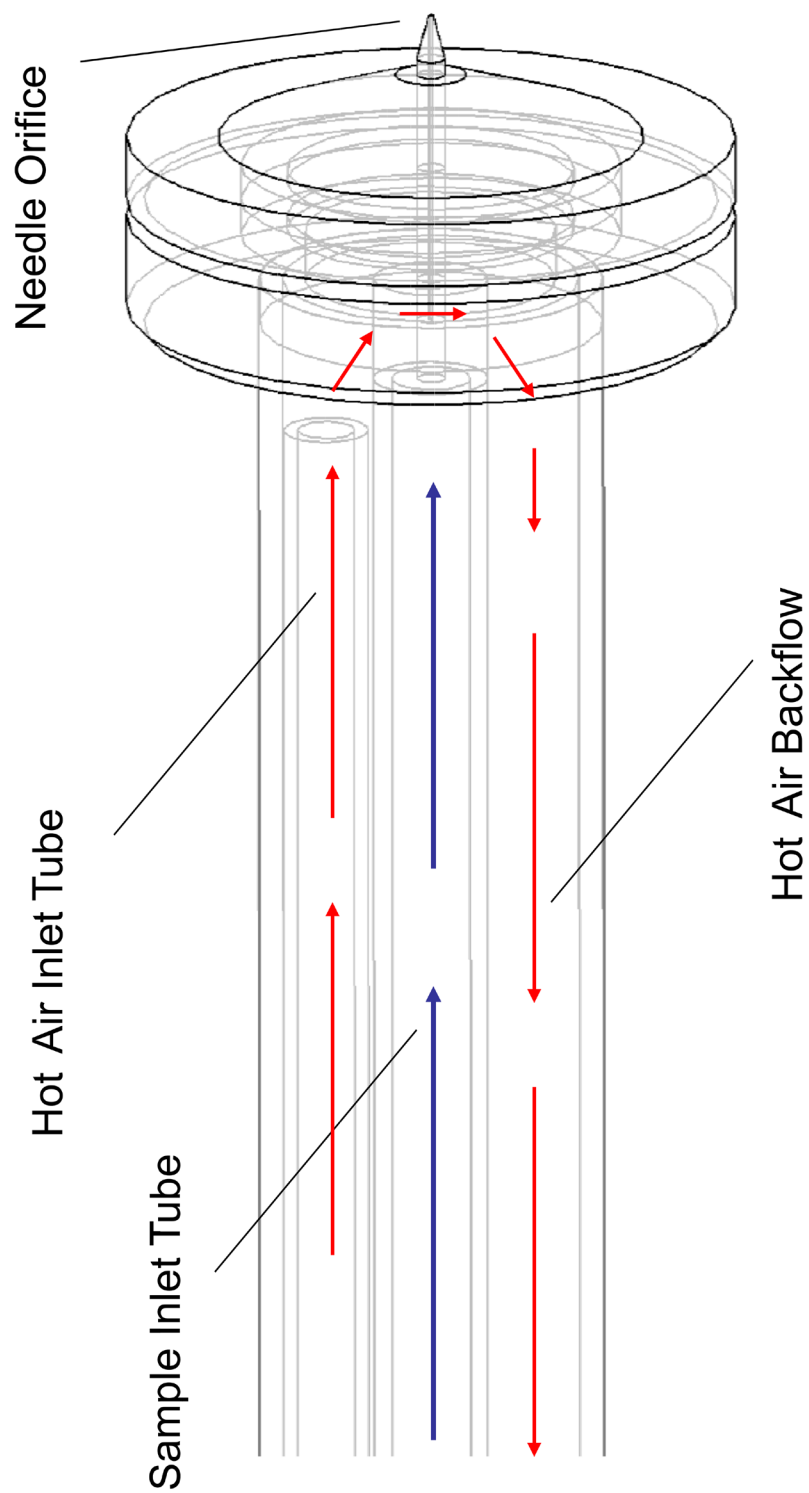


**Figure 3.12.** a) Design of the air-heated sample delivery system for UED3. Hot air flow is indicated with red arrows and sample vapor flow in blue arrows.

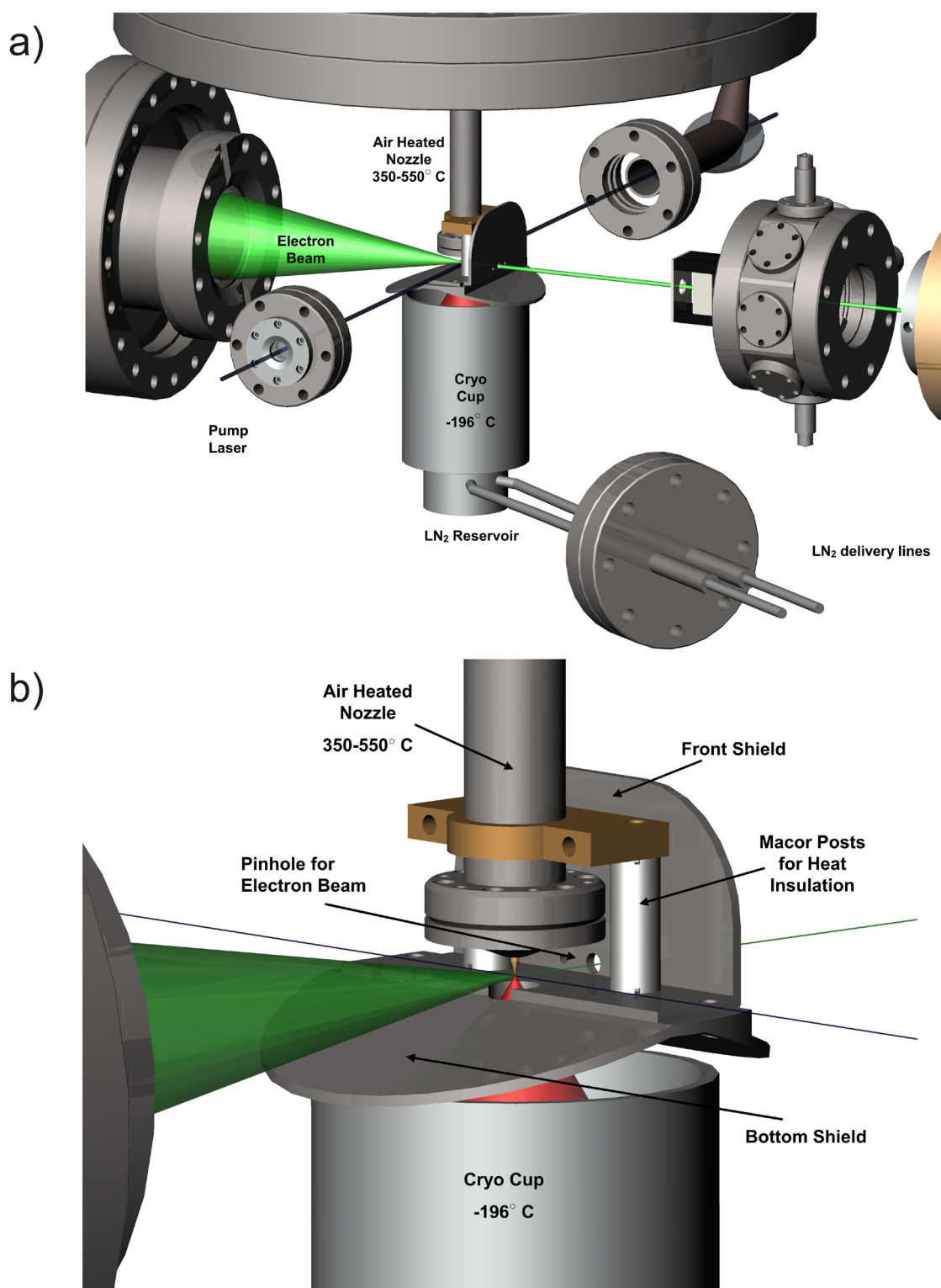


**Figure 3.13.** a) Sample trapping inside the UED3 scattering chamber. The sample vapor (red) is trapped immediately after the interaction region by liquid nitrogen cooled cryo-trap. b) Close-up view of the interaction region in UED3

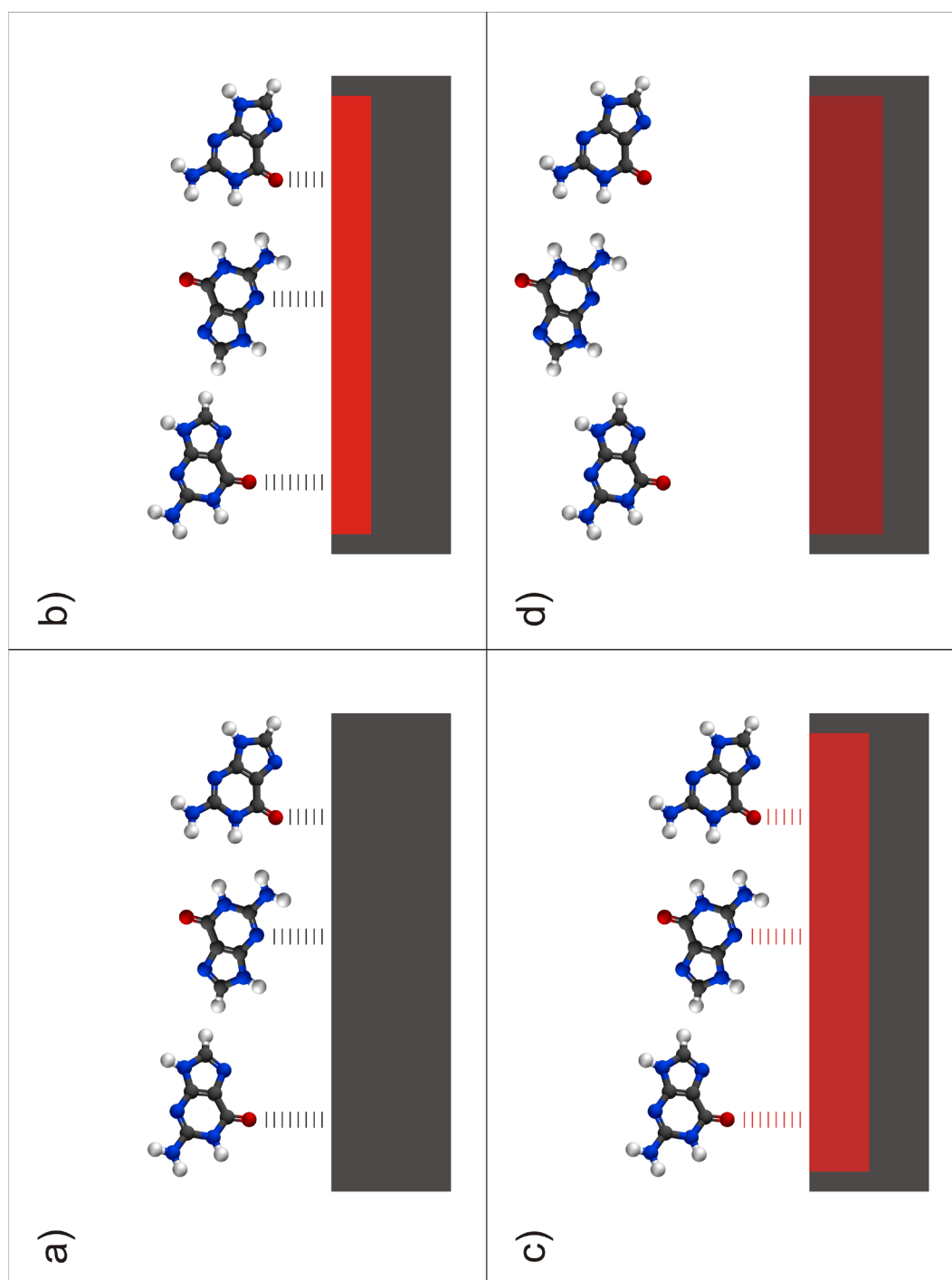


**Figure 3.14.** Proposed mechanism for surface-assisted IR laser desorption. a) Sample molecules interact with the substrate surface through weak adsorbate bonds. b) After absorption of a nanosecond IR laser pulse, the substrate surface is heated up locally on the nanosecond time scale. c) Thermal energy is efficiently transferred to the adsorbate bonds. d) The adsorbate bonds break and the molecules desorb, before a significant amount of energy is transferred to their internal vibrational modes.

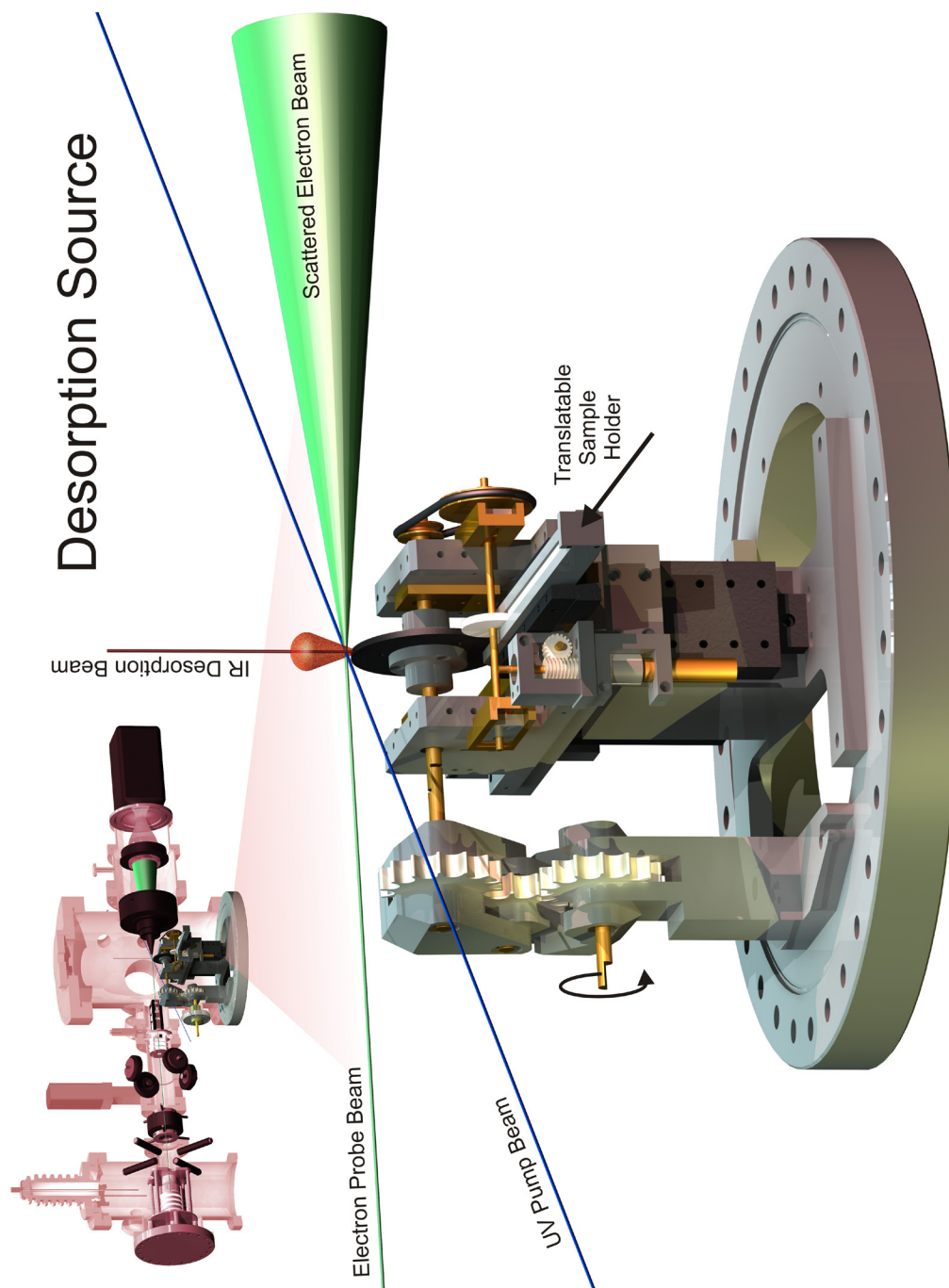
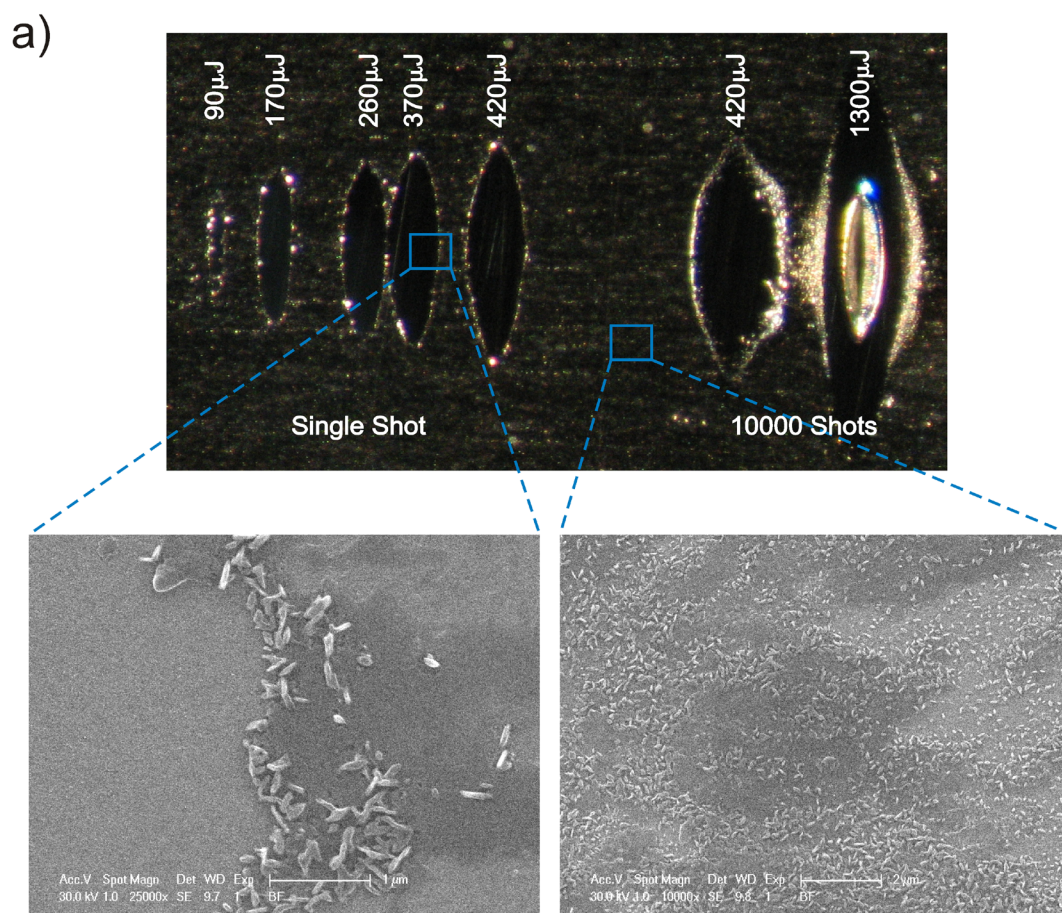


**Figure 3.15.** UED4 laser desorption source. A ns-pulsed IR laser desorbs molecules from a glassy carbon substrate wheel. The gaseous molecules are then excited (pumped) and probed by a fs-pulsed UV laser beam and a ns-pulsed electron beam, respectively. Rotational motion for wheel rotation is transferred from outside the vacuum through a series of spur gears and pulleys. A translatable sample holder, driven by the worm gear assembly, continually delivers sample to the felt brush wheel, which delivers the sample to the substrate wheel. The entire assembly is height adjustable through a home-built elevator unit.



b) **Desorption Signal Stability**

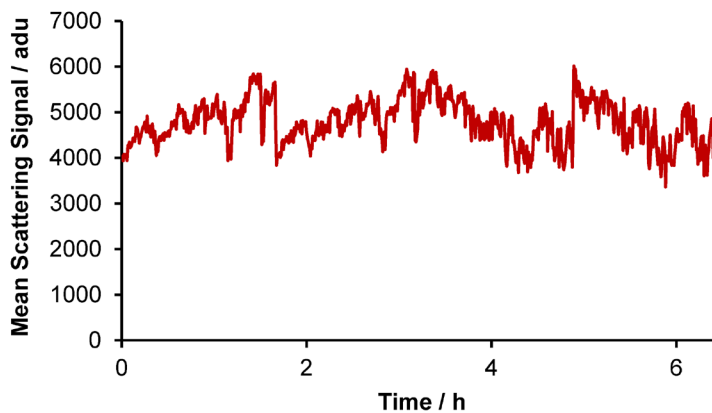


**Figure 3.16.** Surface-assisted laser desorption a) Light microscopy and scanning electron microscopy images of the desorption laser footprint show that the nanocrystalline sample is desorbed from the undamaged glassy carbon substrate in a single shot at low pulse energies. At pulse higher energies, the substrate can be ablated. b) The yield of gas-phase molecules obtained by laser desorption is stable over the extended period of many hours.

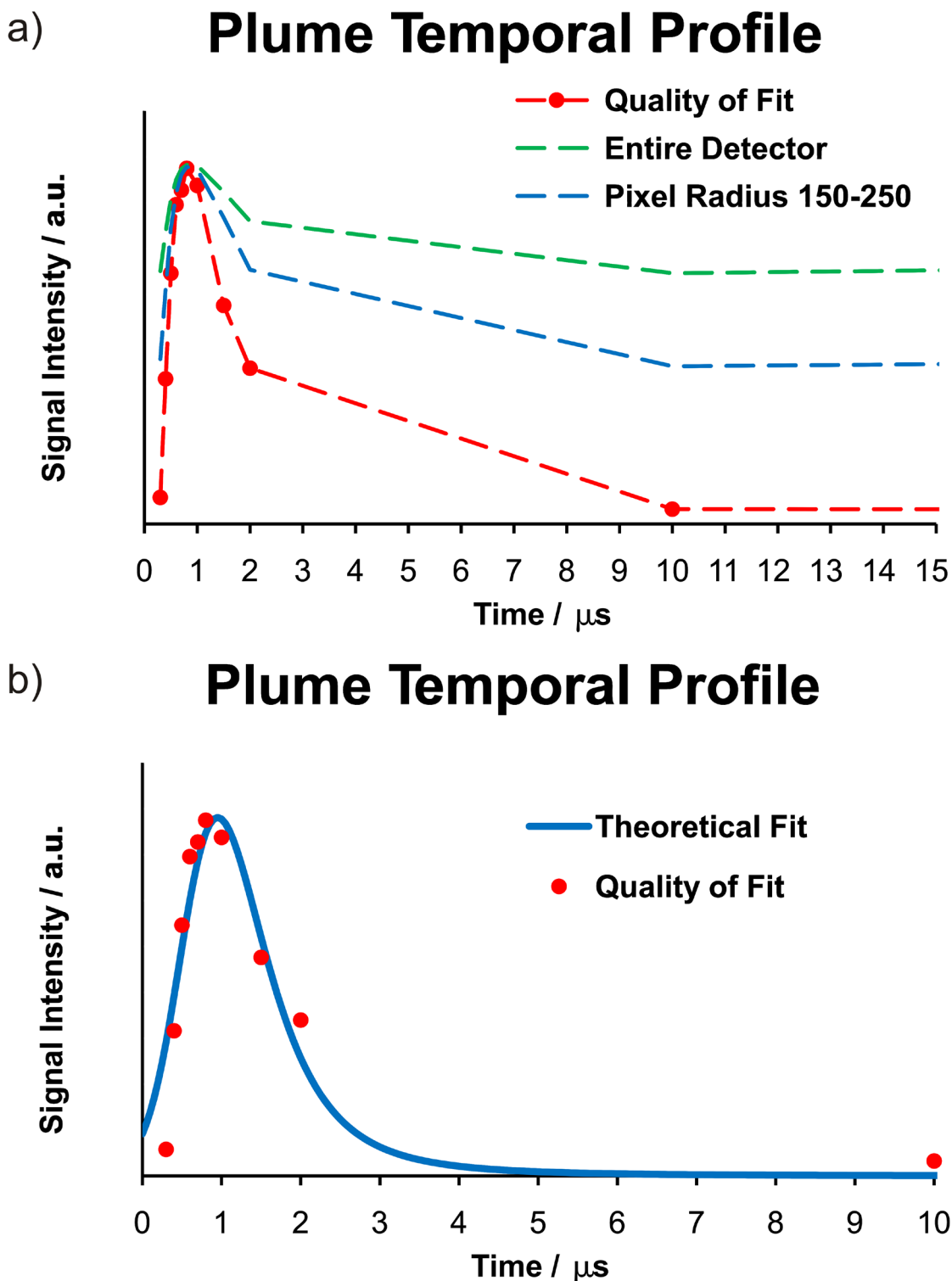


**Figure 3.17.** a) The desorption plume's temporal profile is mapped out by scanning the time delay between the IR desorption laser and the arrival of the electron pulses. The delay time dependence of three different quantities is shown (see text for details). b) Equation 3.7 is fit to the temporal profile of monomeric tryptophan.

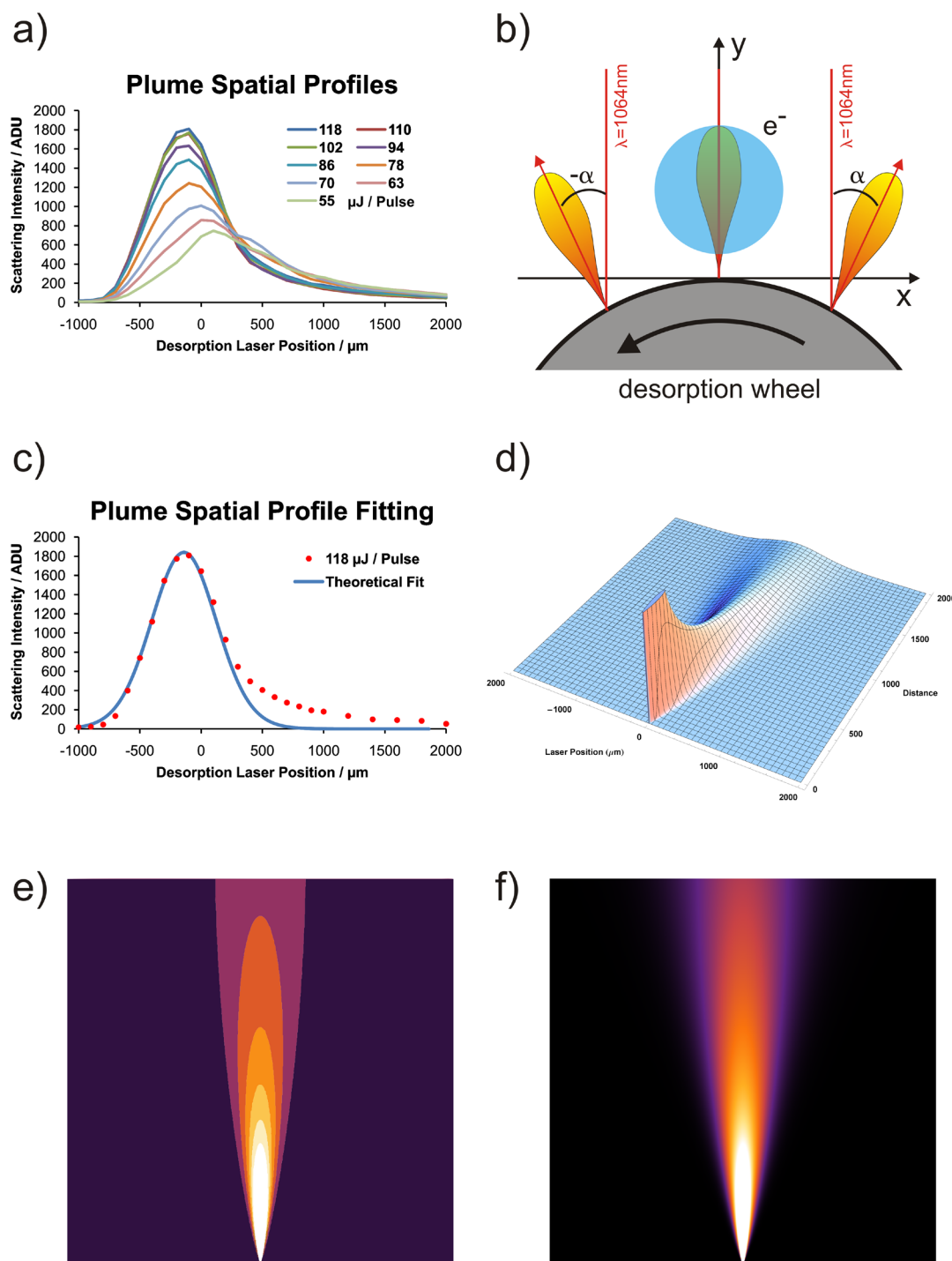


**Figure 3.18.** a) and b) The plume spatial profile is determined by scanning the IR laser beam transversely (x-direction) through the electron beam and recording the scattered intensity. Depending on the laser position, the direction of the surface normal is inclined by an angle  $\alpha$ . c) Fit of Equation 3.10 to the measured scattering intensity using  $n = 25$ . d)-f) Corresponding representations of the real space plume profiles according to Equation 3.9.

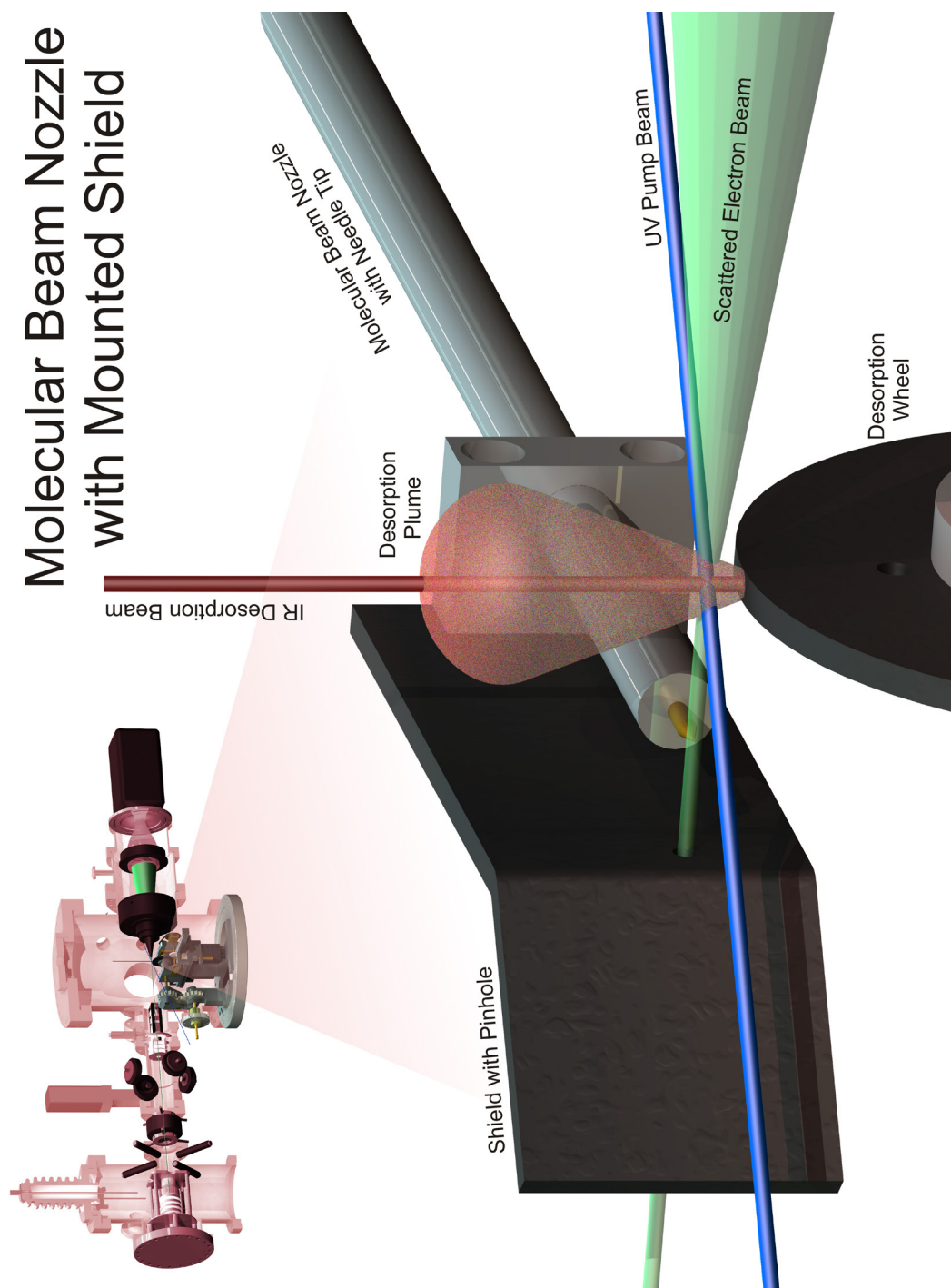


**Figure 3.19.** UED4 molecular beam nozzle and shield. Reference gases can be introduced at room temperature through a small orifice at the tip of the nozzle. The mounted shield blocks any stray electrons, but passes the electron beam through a 1.5 mm pinhole. The needle tip of the molecular beam nozzle is also used for the mutual spatial alignment of the IR desorption laser beam, the electron beam and the UV pump laser beam prior to each experiment.

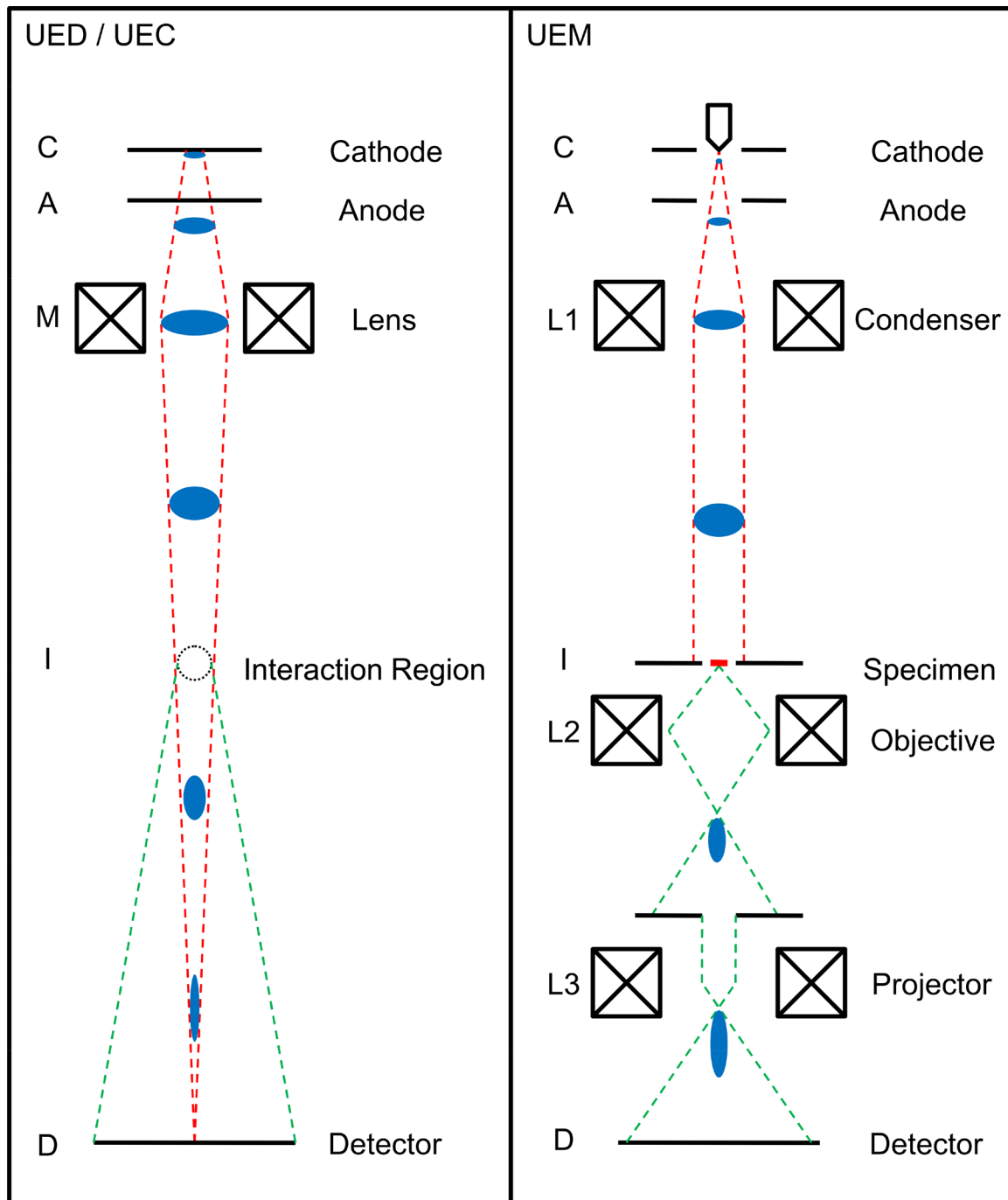


**Figure 3.20.** Schematic of the optical column in UED / UEC and UEM. Electrons are generated by the photoelectric effect at the cathode (C) with the given profile, accelerated between a single electrode pair, radially focused by a solenoid coil (M). The electron pulse evolution is monitored, from the source until they reach the detector (D). In UEM, the pulses are shaped using lens systems (L1, L2, and L3), rather than simple solenoid coils.

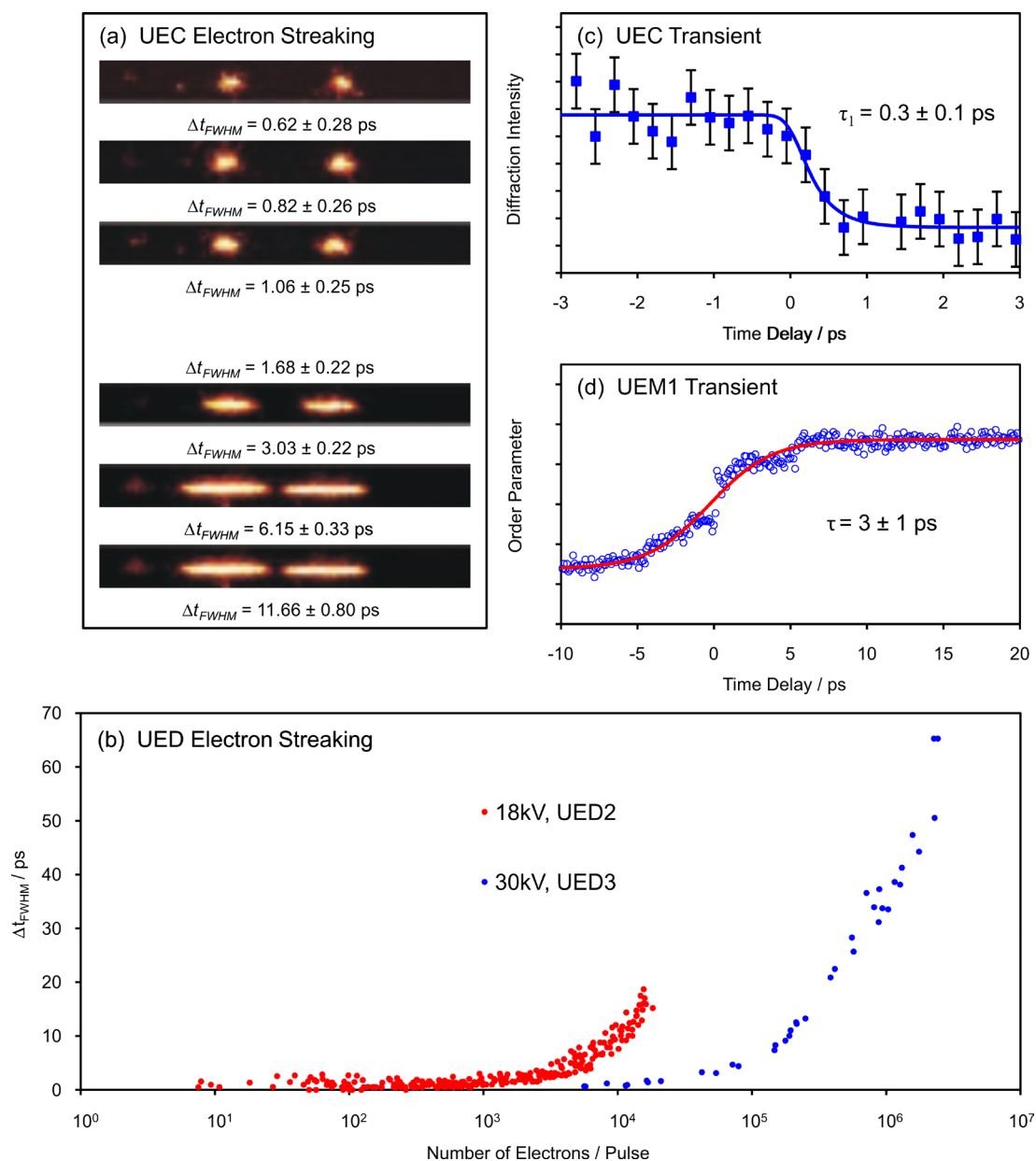


**Figure 3.21.** Measured resolutions for UEC and UED and experimental transients obtained by UEC and UEM1. (a) Streaked electron pulses on the CCD (charge-coupled device) detector together with the calculated pulse lengths. (b) Measured electron pulse widths as a function of the number of electrons. The blue curve (UED3) shows more than an order-of-magnitude improvement in the electron gun performance in comparison to the red curve (UED2). (c) Ultrafast dynamics of structural phase transition in vanadium dioxide. Intensity change of the (606) Bragg spot with time. A decay with a time constant  $\tau_1$  of 307 fs was reported in Ref. [89](#). Here the data was deconvoluted (electron pulse width of 344 fs) and we obtained  $\tau_1 = 0.3 \pm 0.1$  ps. (d) Temporal evolution of the structural order parameter. The order parameter is defined as the integrated intensity of the diffraction peak for different temporal frames. Adopted from Refs. [61](#), [1](#), [89](#), and [97](#).

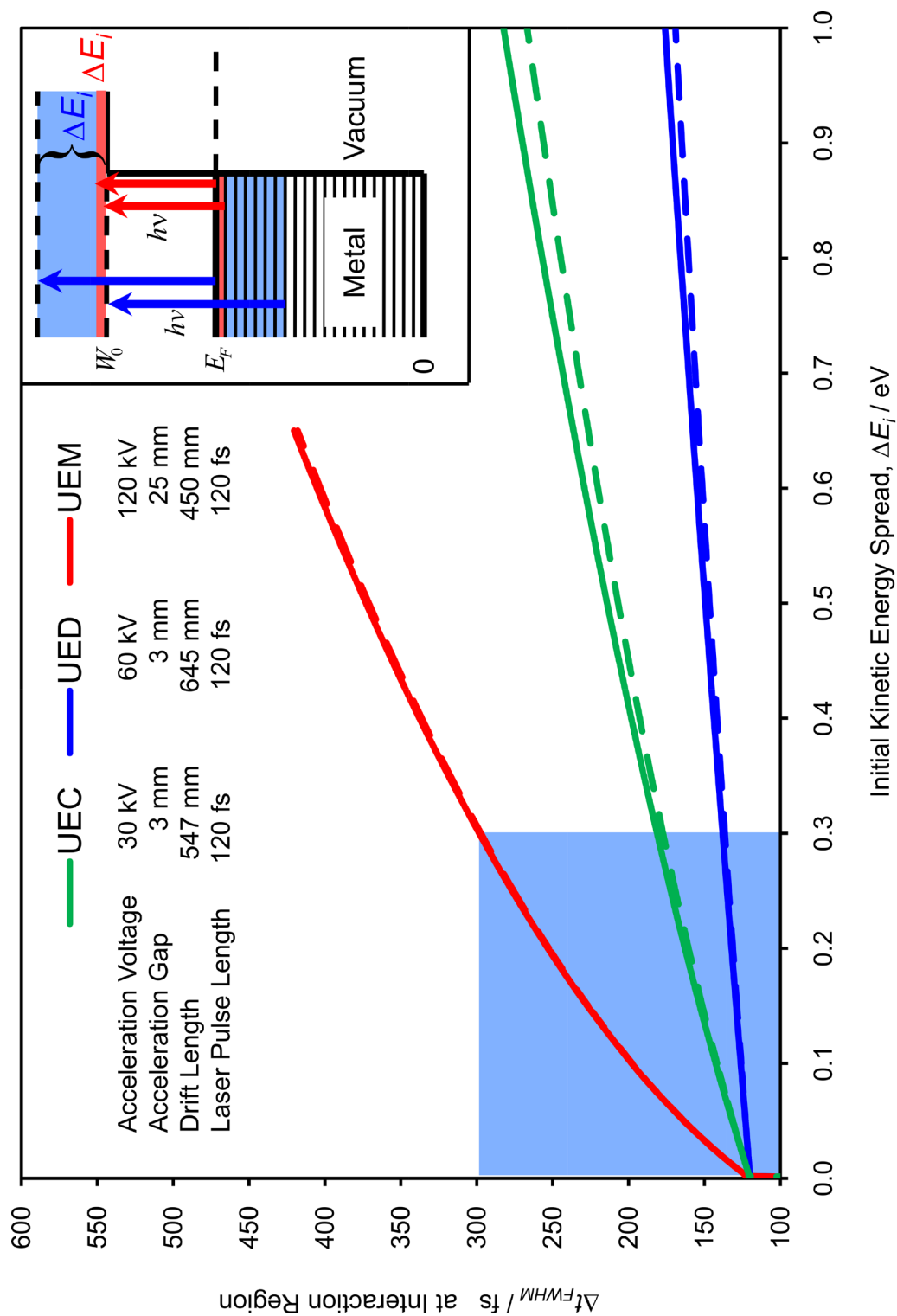


**Figure 3.22.** Temporal broadening of the electron pulse due excess energy of the electrons above the photocathode work function for the UED4 (blue), UEC (green) and UEM1 (red) instruments. The pulse length at the specimen interaction region is computed in the absence of space-charge using the instruments specific parameters.

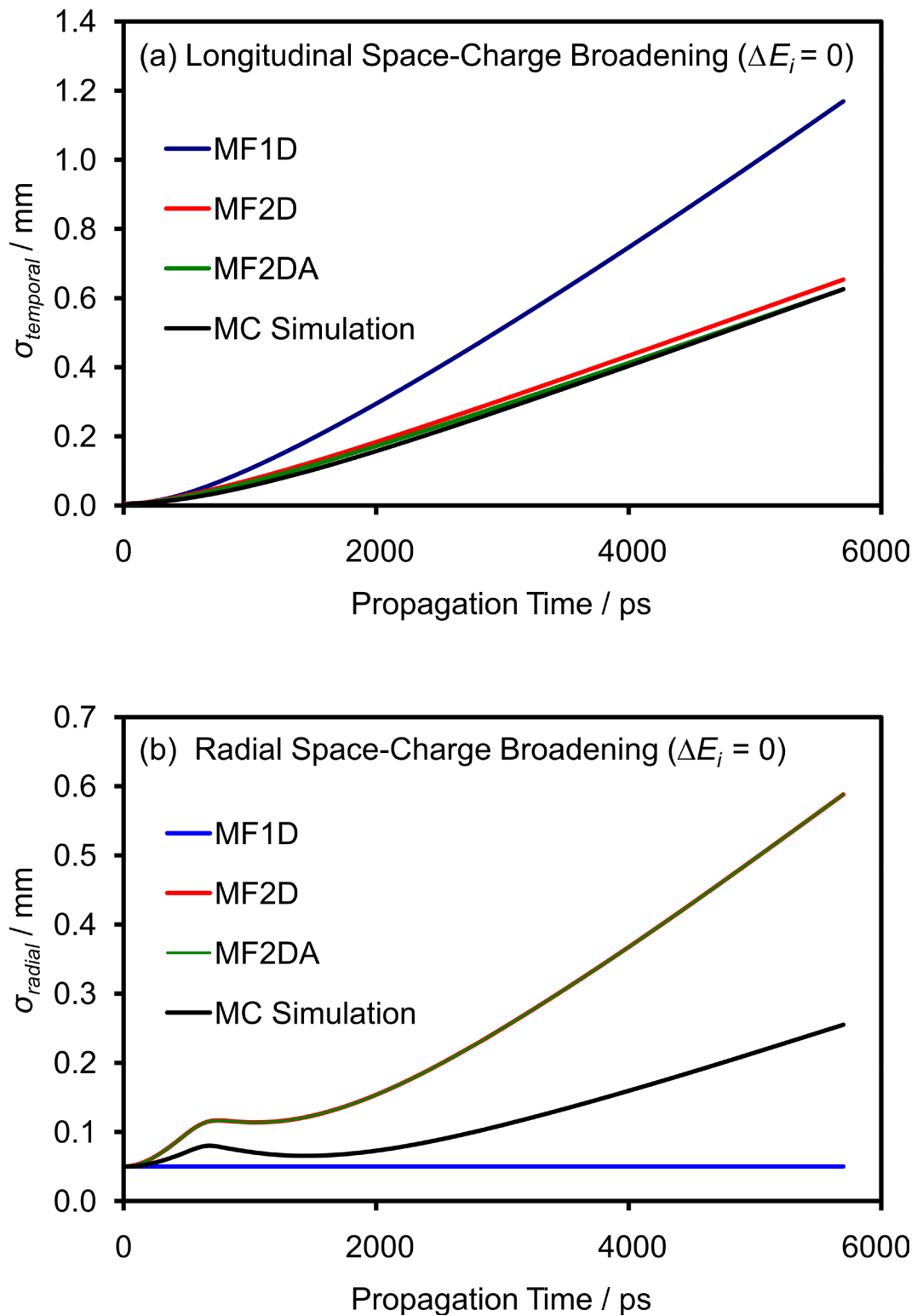


**Figure 3.23.** Comparison of the length (a) and the radius (b) of the electron pulse predicted by the mean field theories and the  $N$ -Body Monte Carlo simulation in the absence of an initial kinetic energy spread.

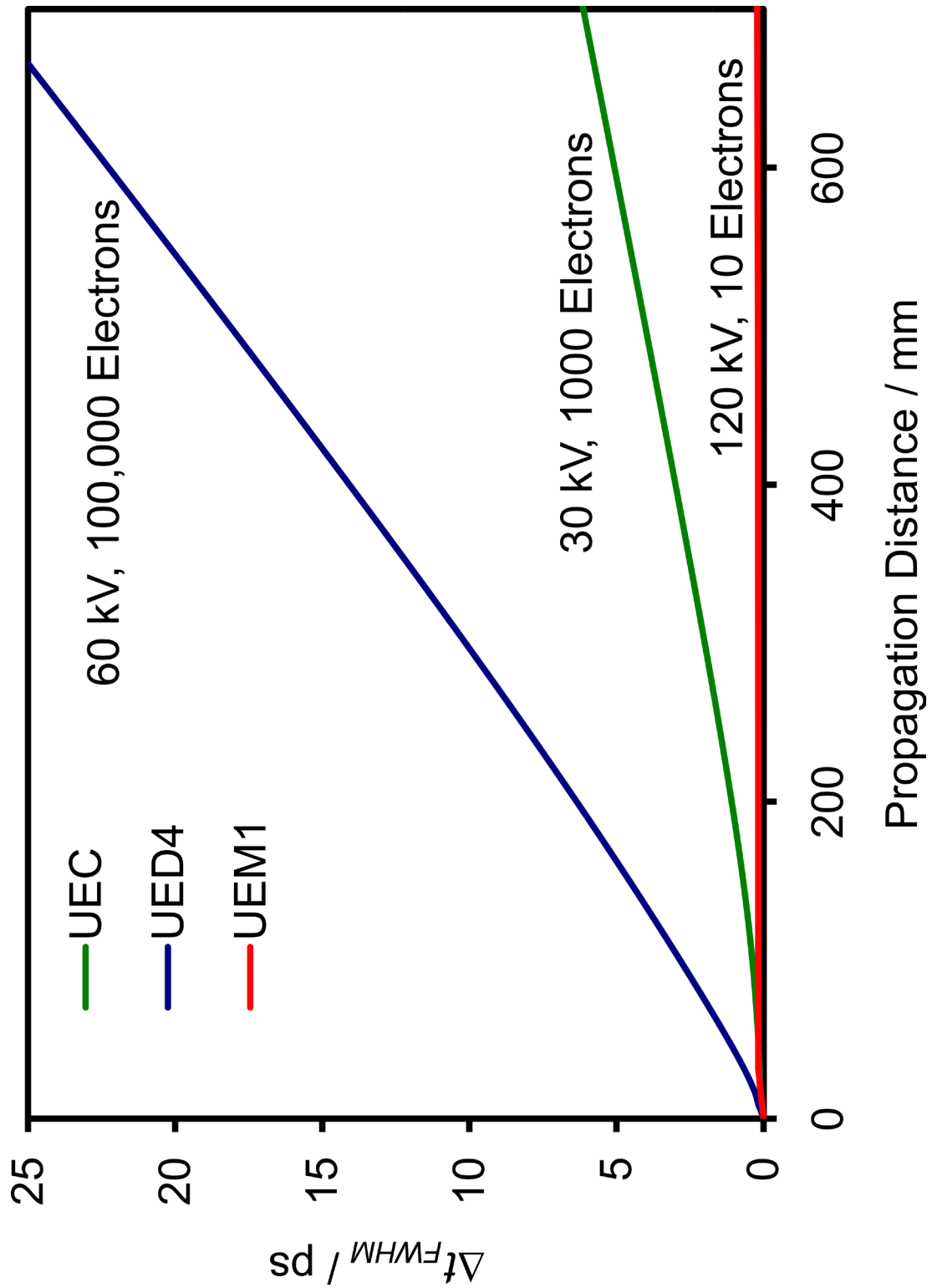


**Figure 3.24.** Comparison of temporal broadening due to the space-charge effect ( $\Delta E_i = 0$ ) as a function of the propagation distance in UEC (green line), UED4 (blue line), and UEM1 (red line) using MF2DA.

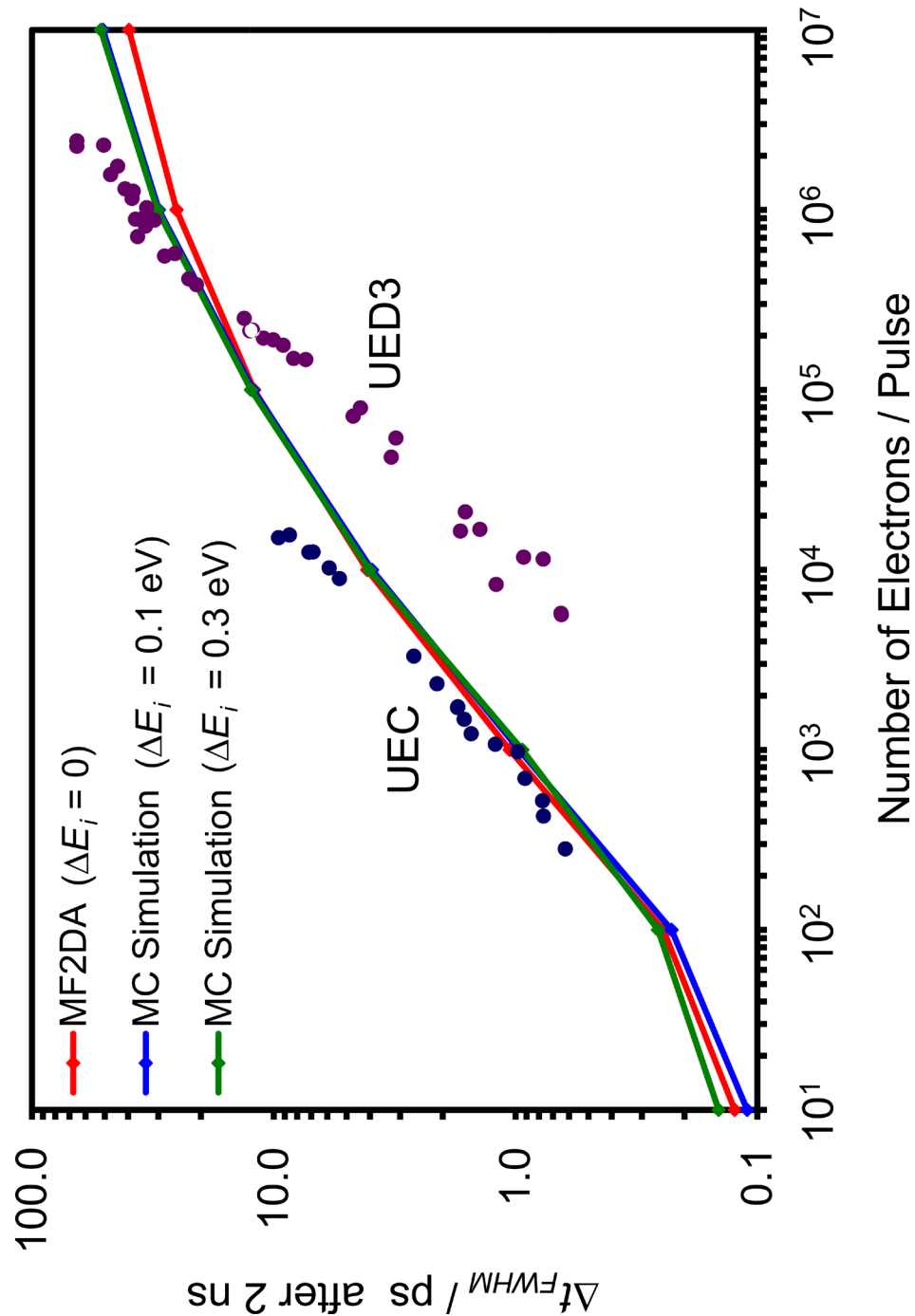


**Figure 3.25.** Comparison of total temporal broadening due to the space-charge effect after 2 ns of propagation using MF2DA (blue line), MC 0.1eV (red line), and MC 0.3eV (green line). Available experimental data are given for UEC (blue dots), and UED3 (red dots); see Figure 3.21 (UEC and UED3, 30kV). Given that the theory, both MC and mean field, agrees with the UEC streaking data, it may be that the number of electrons was overestimated in UED.

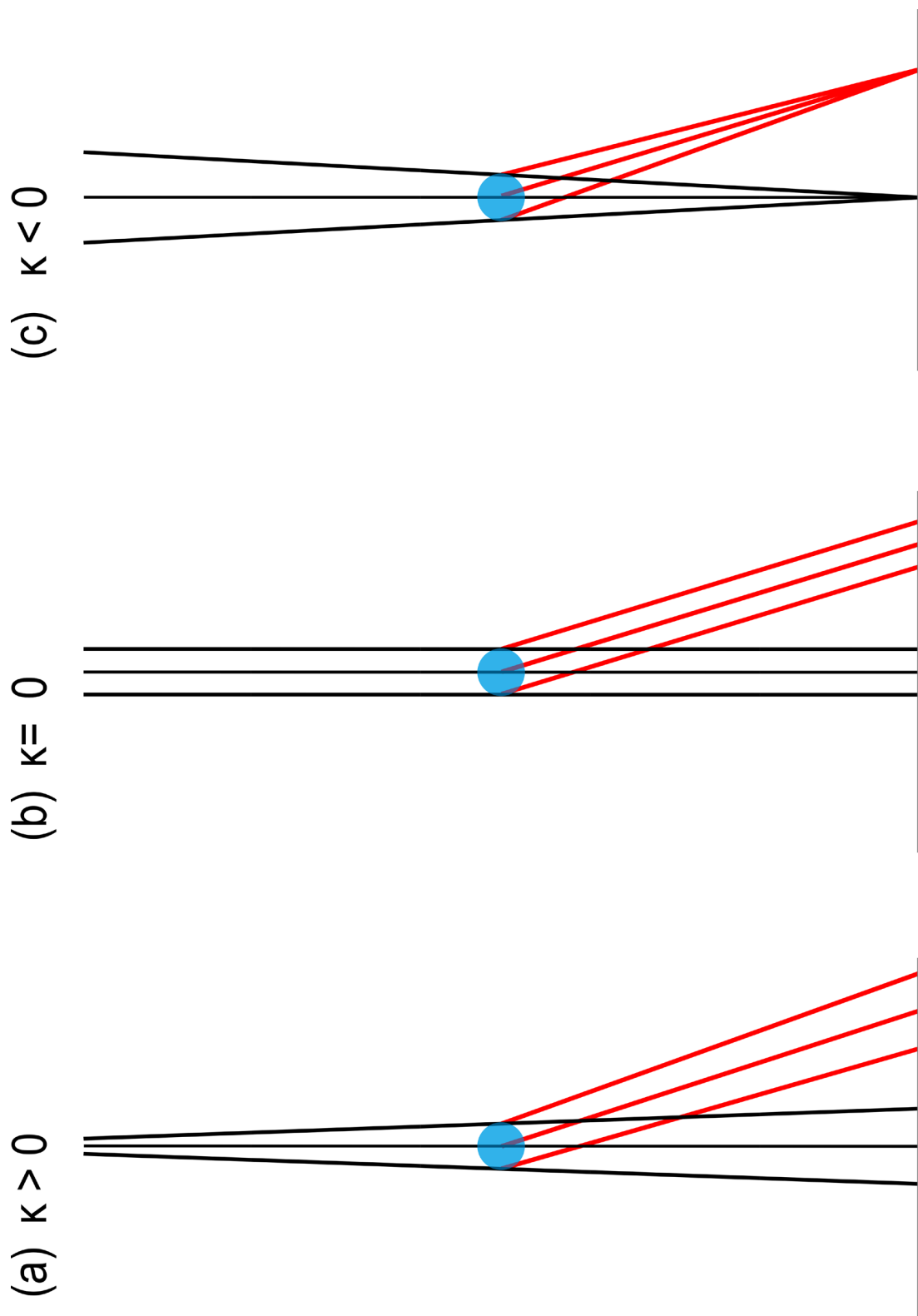


**Figure 3.26.** Effect of the beam geometry on interference blurring for a finite-sized beam using diverging (a), collimated (b), or converging (c) electron trajectories.

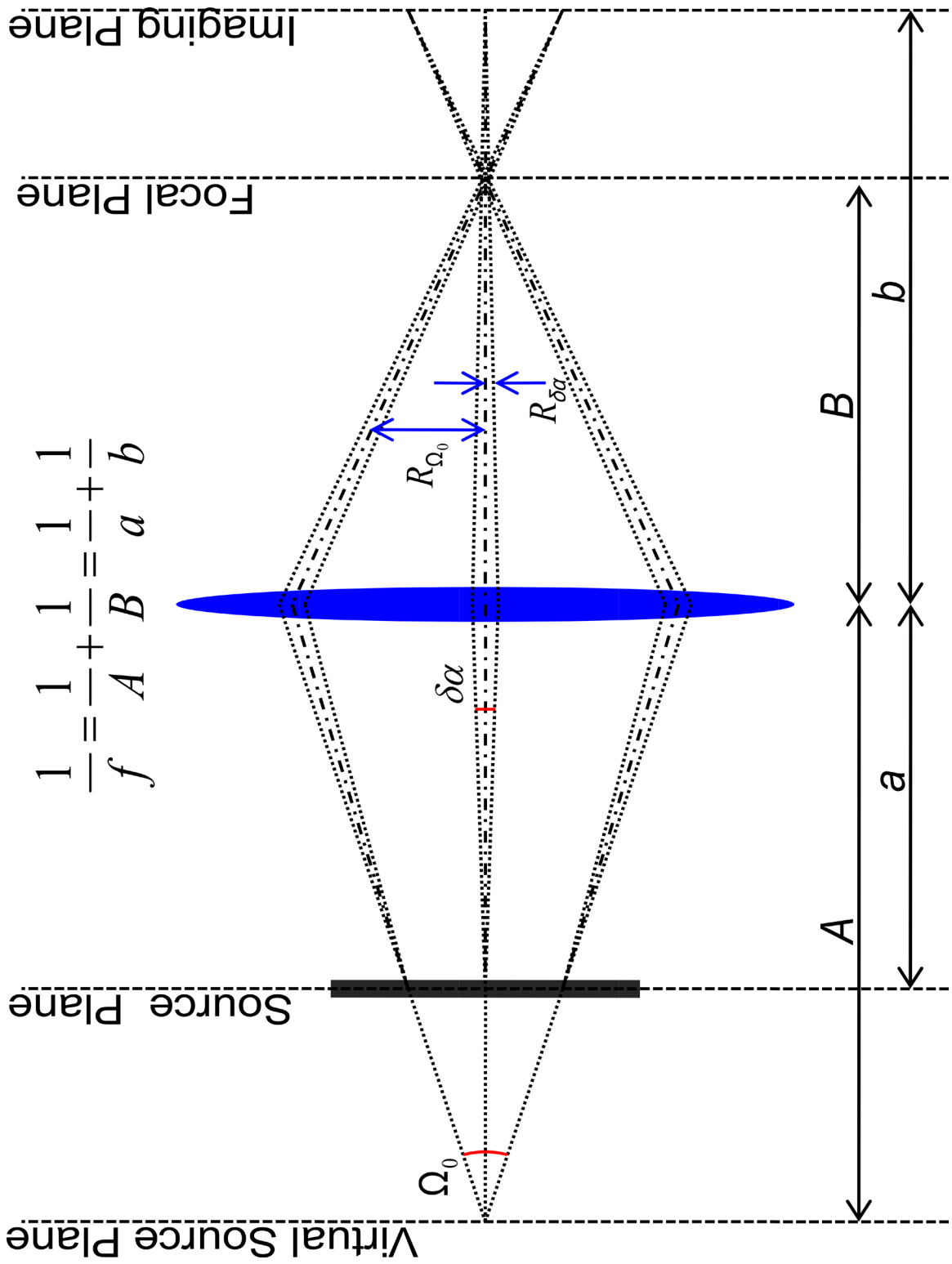


**Figure 3.27.** Radial focusing behavior of a finite-sized beam in the absence of space-charge.

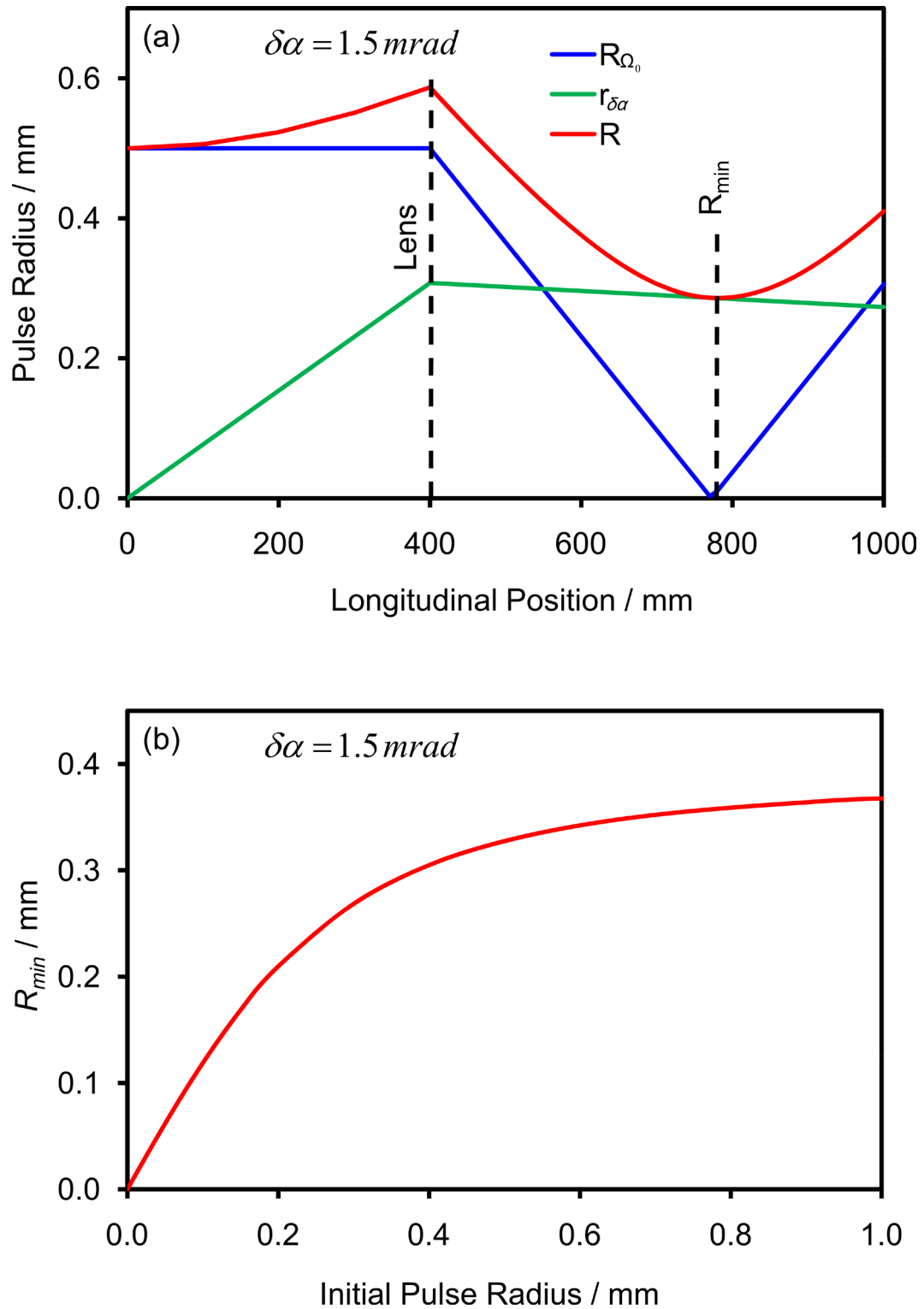


**Figure 3.28.** Evolution of the beam waist calculated using the two-component convolution model of Equation 3.25 (a), and dependence of the focal spot size on the initial source dimensions (b).

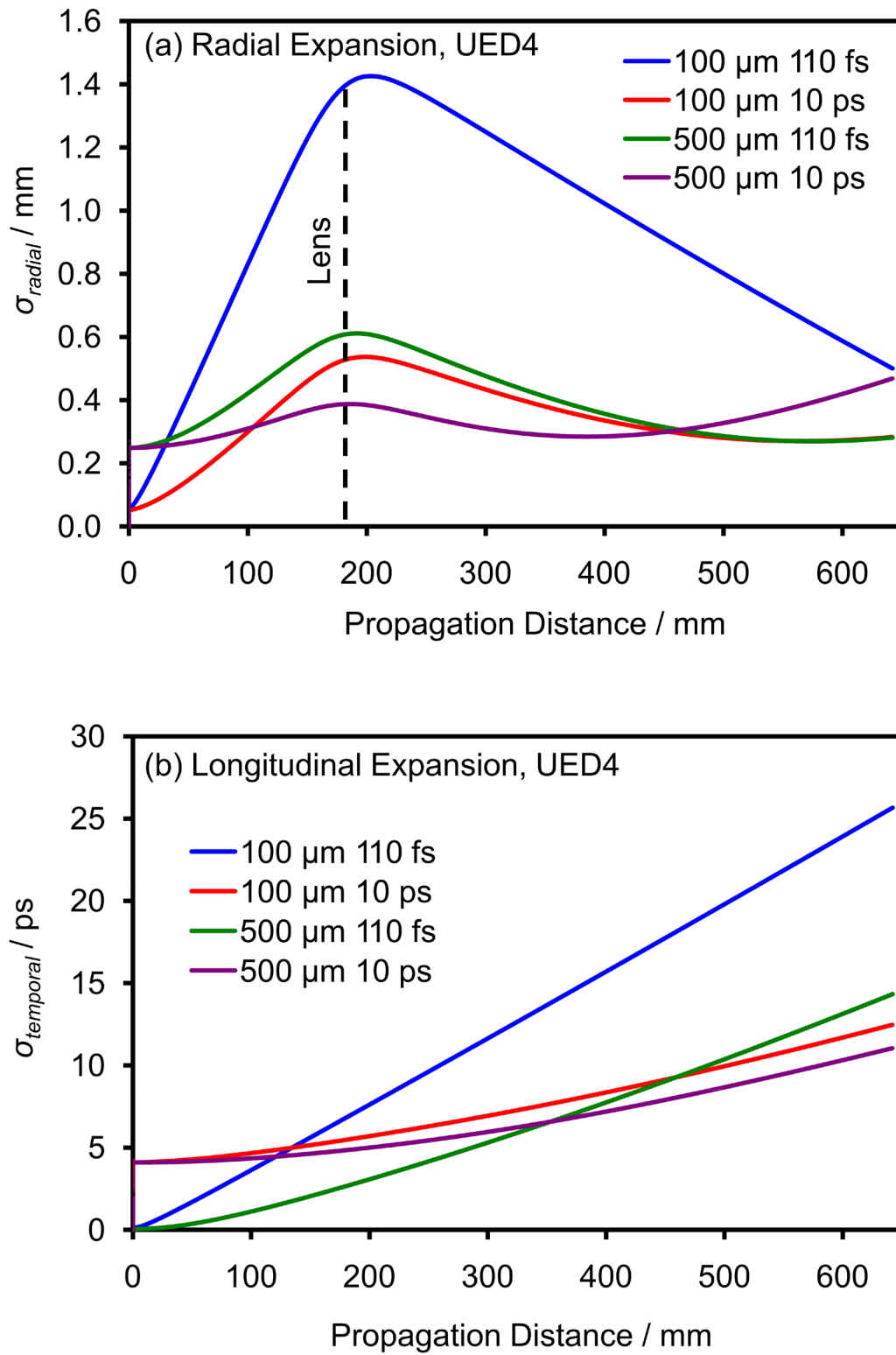


**Figure 3.29.** Monte Carlo simulations of the radius (a) and the pulse length (b) of a bunch containing  $10^6$  electrons using UED4 instrumental parameters.

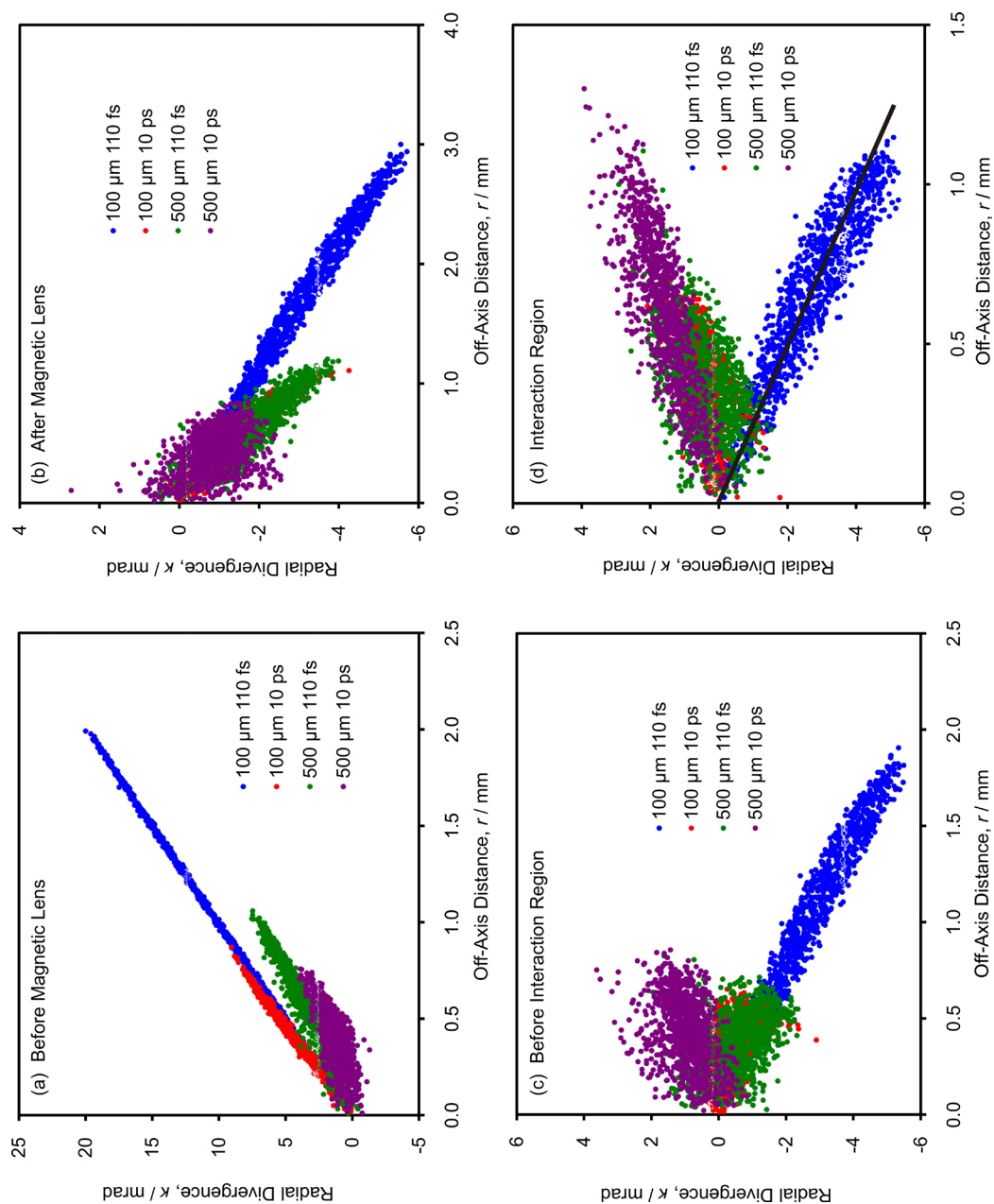


**Figure 3.30.** Radial divergence angles of individual electrons. The results are for the pulses shown in Figure 3.29 at axial distances of  $z = 100$  mm (a),  $z = 300$  mm (b),  $z = 500$  mm (c), and  $z = 645$  mm (d). All pulses develop a diverging chirp ( $\kappa = \tan^{-1}(p_r/p_z) > 0$ ) due to space-charge. This linear correlation is reversed in sign ( $\kappa < 0$ ) by the magnetic lens, a condition necessary for converging beam diffraction. However, the space-charge effect alters the converging electron trajectories for three of the four pulses in the figure by the time they arrive at the interaction region. Only the initially confined pulse (shown in blue), which undergoes a Coulomb explosion at early times, is able to escape the sphere of influence of the space-charge effect and reproduce the ideal convergence angle (black line) in the interaction region.

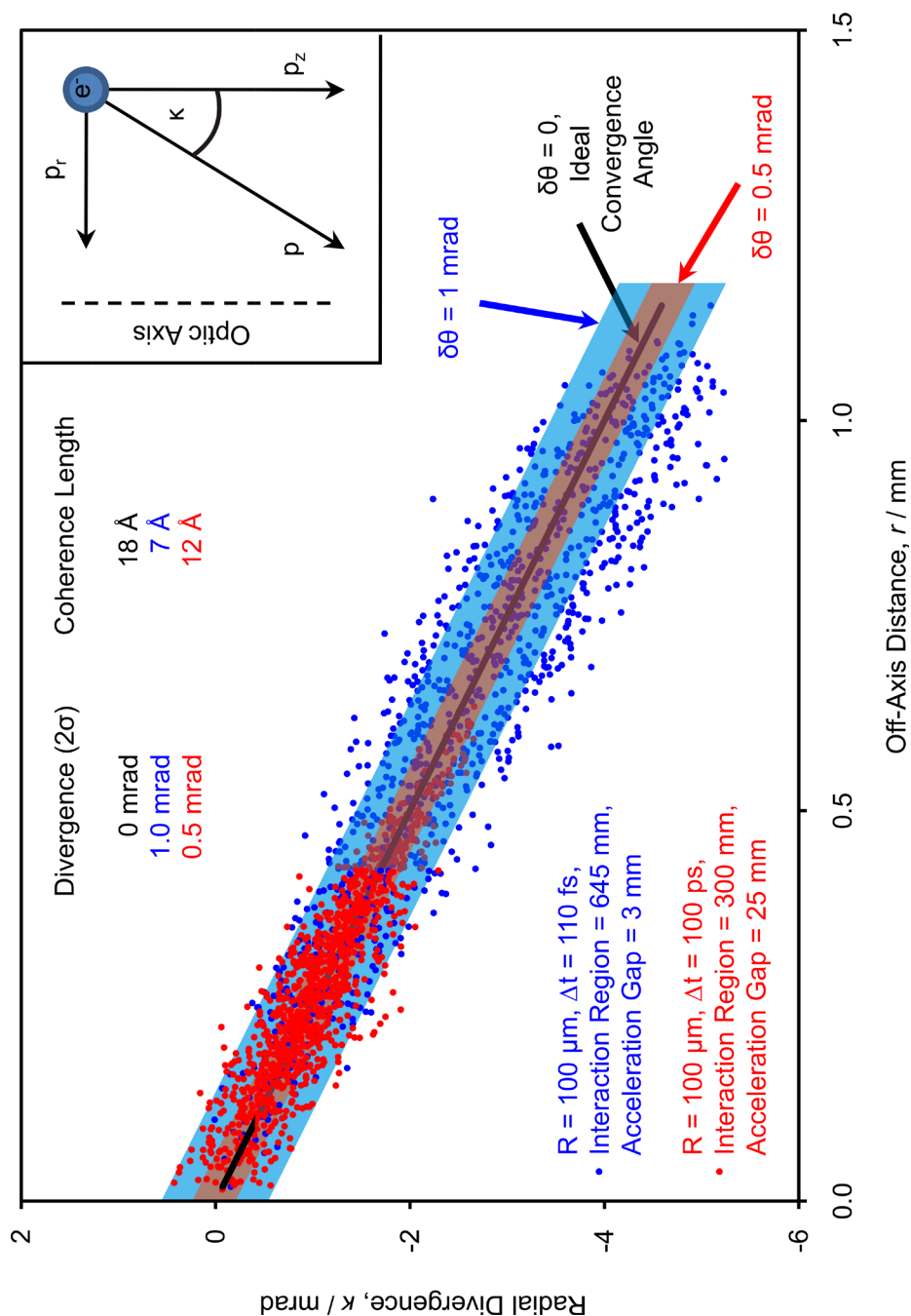


**Figure 3.31.** Radial divergence angles of individual electrons using original (blue colors) and optimized (red colors) geometries. The uncertainty in scattering angle directly results from the deviation of incident angle from the ideal convergence angle. The red and blue shaded areas cover particles falling within an angular spread of  $\pm\sigma$ . The mean field theory assumes a perfect correlation between electron momenta and position, such that  $\delta\theta = 0$ . It is evident that, in reality, electron trajectories are not perfectly correlated ( $\delta\theta > 0$ ). The optimized instrumental geometry improves the coherence of the beam by reducing  $\delta\theta$  and, additionally, gives a smaller probe size (see text).

# **Chapter 4.**

## **Data Processing and Analysis**

The time-resolved electron diffraction patterns, as they are recorded on the detector, contain contributions from several instrumental factors in addition to the interference signal, which provides the structural information. To isolate this interference signal, it is necessary to collect additional images to quantify and subsequently remove contributions arising from sources other than diffractive scattering. The removal of these instrumental factors by image processing routines will be addressed in Section 4.1. The resulting one-dimensional diffraction signal is then fitted by the theoretical model, which was developed in Chapter 2. The nonlinear least-squares fitting routine, which is used to optimize this fit, is the subject of Section 4.2. Software modules for these computations were developed in-house and are available in the online supporting material.<sup>42</sup> In Section 4.3, the quantum chemical calculations and the methods to estimate the initial parameter values that are used to define the theoretical model are described. In Section 4.4, a general step-by-step fitting procedure is described that leads to the determined structures for reactant and time-dependent product species.

## **4.1 Image Processing**

### **4.1.1 Frame Averaging**

Due to the signal conversion process in the CCD detector, namely the accumulation of stored charges, there is a maximum amount of signal that can be accumulated in a given pixel, before the pixel saturates and charges start to overflow into the neighboring pixels. Therefore, the exposure time for a frame has to be limited to 4 min (UED3)<sup>18</sup> and to 20-60 sec (UED4), which results in noisy individual diffraction images, especially at high scattering angles where the electron flux is very low. The

digital nature of image acquisition allows for computational frame averaging multiple diffraction images, which improves the signal-to-noise ratio (SNR) at each pixel and smoothes the average image across the entire detection screen, as shown in Figure 4.1.

Frame averaging is accomplished by treating each pixel, designated by the coordinate pair  $(x, y)$ , as a separate and independent experimental observable. The average image is then obtained according to the following formula:

$$F(x, y) = \frac{\sum_{i=1}^N F_i(x, y) \cdot M_i(x, y)}{\sum_{i=1}^N M_i(x, y)}, \quad (4.1)$$

where the index  $i$  numbers the  $N$  individually collected frames,  $F_i$ , and  $M_i$  designates the corresponding binary mask image with all pixels set to 1 in the beginning. Similarly, the standard deviation image and the standard error image are obtained according to

$$Stddev(x, y) = \sqrt{\frac{\sum_{i=1}^N \{F(x, y) - F_i(x, y)\}^2}{\sum_{i=1}^N M_i(x, y)}}, \quad (4.2)$$

and

$$Stderr(x, y) = \frac{Stddev(x, y)}{\sqrt{\sum_{i=1}^N M_i(x, y)}}. \quad (4.3)$$

The averaging procedure additionally provides a method to remove pixels from individual frames, whose values are statistically outside an acceptable range. If any pixel in any frame  $F_i$  has a value outside the range given by  $F(x, y) \pm \mu \cdot Stddev(x, y)$ , its value is rejected, i.e., that pixel value is set to zero in both  $F_i$  and  $M_i$ . The parameter  $\mu$

is chosen to satisfy Chauvenet's condition<sup>98,99</sup> and a value of 3.5 is typically used. After the outlier pixels have been removed from the stack of images, the average, standard deviation and standard error images are recalculated with the updated mask images and a second round of pixel rejection is performed. The resulting diffraction image and the corresponding standard error image after two rounds of pixel rejections serve as the input data for the next step.

#### 4.1.2 Ratio Images

The averaged intensity,  $F(x, y)$ , contains the effect of the aluminum gradient filter that is built into the detector assembly, as well as any imperfections in the detector's components (such as heterogeneities in the phosphor screen thickness, etc.), which together modulate the overall detective quantum efficiency over the entire active area (see Chapter 3). We can therefore express the recorded intensity in the average frame as the true intensity,  $I(x, y)$ , multiplied by the unknown quantum efficiency,  $\phi(x, y)$ :

$$F(x, y) = I(x, y) \cdot \phi(x, y) \quad . \quad (4.4)$$

Although great efforts have been taken during the assembly of the detector components to make the detector assembly sensitive to electrons only, there is always undesired background intensity,  $I_B$ , which in turn can be decomposed into its contributing terms (the pixel coordinates have been omitted for clarity):

$$I(x, y) = I^{Diffraction} + I^B = I^{Diffraction} + I^a + I^l + I^d \quad . \quad (4.5)$$

Here  $I^a$  is the electron scattering contribution from ambient gas in the scattering chamber,  $I^l$  is the contribution of scattered light from either the UV pump laser or the IR

desorption laser or both, and  $I^d$  is the detector's dark response. If the scattering signal is collected by utilizing a continuous molecular source (as in UED3), the  $I^a$  term is relatively large (typically  $\sim \frac{1}{3}I$ , depending on the pumping speed of the vacuum system). The desorption source of UED4, in contrast, is pulsed and uses nonvolatile samples, such that the  $I^a$  term becomes negligibly small. Similarly, when not using a pump laser or a desorption laser, the respective terms become zero. The detector background is always present in every frame, but it may not be linearly dependent on the exposure time. Thus, it is good practice to collect all frames using the same exposure time.

To eliminate the detector quantum efficiency modulation and the background contributions, we define the following ratio images, using xenon as a reference gas to quantify the atomic scattering background,<sup>18</sup> for effusive beam/diffraction (EB) and desorption/diffraction (DD), respectively. In the following formulae, the superscripts list the type of contribution and the subscripts indicate the source of these contributions.

$$\begin{aligned}
 R_{Sample}^{EB}(x, y) &= \frac{F_{Sample}^{EB} - F_{UV}^{l,d}}{F_{Xe}^{EB} - F^d} \\
 &= \frac{\left( I_{Sample}^{Diffraction} + I_{Sample}^a + I_{UV}^l + I^d \right) - \left( I_{UV}^l + I^d \right)}{\left( I_{Xe}^{Diffraction} + I_{Xe}^a + I^d \right) - I^d} \\
 &= \frac{I_{Sample}^{Diffraction} + I_{Sample}^a}{I_{Xe}^{Diffraction} + I_{Xe}^a} \\
 &= \left( \frac{I_{Sample}^{Diffraction}}{I_{Xe}^{Diffraction}} \right) + \left( \frac{I_{Xe}^{Diffraction} \cdot I_{Sample}^a - I_{Sample}^{Diffraction} \cdot I_{Xe}^a}{\left( I_{Xe}^{Diffraction} \right)^2 + I_{Xe}^{Diffraction} \cdot I_{Xe}^a} \right),
 \end{aligned} \tag{4.6a}$$

and

$$\begin{aligned}
R_{Sample}^{DD}(x, y) &= \frac{F_{Sample}^{DD} - F_{UV}^{l,d} - F_{IR}^{l,d} + F^d}{F_{Xe}^{MB} - F^d} \\
&= \frac{(I_{Sample}^{Diffraction} + I_{UV}^l + I_{IR}^l + I^d) - (I_{UV}^l + I^d) - (I_{IR}^l + I^d) + I^d}{(I_{Xe}^{Diffraction} + I_{Xe}^a + I^d) - I^d} \\
&= \frac{I_{Sample}^{Diffraction}}{I_{Xe}^{Diffraction} + I_{Xe}^a} \\
&= \left( \frac{I_{Sample}^{Diffraction}}{I_{Xe}^{Diffraction}} \right) + \left( \frac{-I_{Sample}^{Diffraction} \cdot I_{Xe}^a}{(I_{Xe}^{Diffraction})^2 + I_{Xe}^{Diffraction} \cdot I_{Xe}^a} \right).
\end{aligned} \tag{4.6b}$$

The intensity in the resulting ratio images have been decomposed into two terms in the final forms of Equations 4.6: The first and dominant term is the background-free diffraction signal of interest containing the structural information, while the second term is a background contribution originating from nonzero ambient gas scattering from either a sample or a reference gas (xenon), which cannot be eliminated or subtracted using the current experimental methodology. This background could potentially be reduced by some extent through the use of a pulsed nozzle instead of the effusive molecular beam that is currently employed. However, since the isolation of the purified diffraction signal is never 100% perfect and completely background-free ratio images are therefore unattainable in practice, the ambient gas background contribution is left in the ratio images and taken into account later as a polynomial background in the  $\chi^2$ -fitting routine (see Section 4.2).

In theory, the ratio image will show a diffraction ring pattern with smoothly varying contrast. In reality, however, instrumental artifacts, which results in abrupt contrast variations, are often present. These variations are easily distinguishable at this stage of image processing as they include, e.g., the shadow of the Faraday cup or the beam block, but they may also manifest themselves as bubbles that might have formed in

the optical coupling fluid, which was used to fuse together the fiber-optic components of the detector assembly. Since the sources of these artifacts are known and individual pixels are treated independent of each other, it is justifiable to manually remove these erroneous pixels. Binary mask images are again used to filter out these incorrect pixels from the ratio images, as is illustrated in Figure 4.2.

Once the ratio image has been reduced to its viable data only, it is normalized to the number of active pixels according to

$$\hat{R}(x, y) = R(x, y) \frac{\sum_{pixel} M(x, y)}{\sum_{pixel} R(x, y)} . \quad (4.7)$$

This normalization, empirical in nature, is used to ensure that the temporally referenced (i.e., time-resolved) signal is free from systematic variations as a function of temporal delay.<sup>9</sup>

In addition, the standard error associated with each pixel in the ratio image is calculated by propagating the standard errors of the input images to obtain a corresponding standard error ratio image,  $\hat{R}_{StdErr}(x, y)$ .

### 4.1.3 Radial Average

The model derived in Chapter 2 describes a scattering process that produces a diffraction pattern with no dependence on the azimuthal angle. Thus, the diffraction pattern should be radially symmetric about the diffraction pattern center and a radial average can be employed to reduce the two-dimensional image to a one-dimensional diffraction intensity curve, which only depends on the radial distance,  $s$ . The model, of

course, does not take into account instrumental considerations, such as the distortion of the ring pattern that occurs, if the optical axis and the detection plane normal originating from the detector center are not parallel. A situation like this can arise due to the curved flight path of the electrons from the gun to the detector. The Lorentz force originating from the Earth's magnetic field  $\vec{B}$  acts on the electrons traveling at velocity  $\vec{v}$  according to  $\vec{F} = e(\vec{v} \times \vec{B})$ , such that the beam has to be steered/corrected by the electron optics. As a result, the interaction region may *not* lie on the geometrical axis of the instrument (straight line from photocathode to detector center), but may be offset from it. This misalignment results in the detection plane intersecting the scattering cone at a tilt angle,  $\alpha$ . Figure 4.3a shows that such a detection geometry yields an elliptically distorted scattering pattern, as opposed to perfect circles. In addition, the center of the indicated ellipse does not coincide with the axis of the scattering cone. In fact, the center shift becomes a function of the electron scattering angle  $\theta$  and the camera distance  $L$  given by

$$\text{Center Shift} = \frac{L}{2} \left( \frac{\sin(\theta)}{\cos(\alpha + \theta)} - \frac{\sin(\theta)}{\cos(\alpha - \theta)} \right), \quad (4.8)$$

and we can define the ellipticity  $\varepsilon$  in terms of the major and minor semi-axis  $a$  and  $b$  of the ellipse as

$$\begin{aligned} a &= \frac{1}{2} L \sin(\theta) \left( \frac{1}{\cos(\alpha + \theta)} + \frac{1}{\cos(\alpha - \theta)} \right), \\ b &= L \tan(\theta), \\ \varepsilon &\equiv \frac{a}{b} = \frac{1}{2} \cos(\theta) \left( \frac{1}{\cos(\alpha + \theta)} + \frac{1}{\cos(\alpha - \theta)} \right). \end{aligned} \quad (4.9)$$

It should be noted here that the minor semi-axis  $b$  does not change with the tilt angle and is in fact equal to the radius of the circle that would have been obtained in the ideal scattering geometry. The major semi-axis  $a$  in contrast, grows as a function of the scattering angle, resulting in larger and larger elliptical distortions of the outer diffraction rings.

To determine the orientation angle  $\beta$  of the elliptical distortion, the center position of each diffraction ring, indexed in Figure 4.3b, is found separately. Center determination is accomplished by comparing the circularly averaged, one-dimensional data from the left and right sides or the top and bottom halves of the detector and eliminating any oscillatory feature in the difference intensity for the given diffraction ring. This method has been employed and described previously and can reveal the ring centers to an accuracy of 0.2 pixels.<sup>18</sup> Figure 4.3c plots the coordinates of the center positions, which all fall on a straight line. Because the images are treated as  $N \times N$  matrices (positive y-axis points downward), the orientation angle  $\beta$  is given by

$$\beta = -\arctan\left(\frac{\Delta y}{\Delta x}\right), \quad (4.10)$$

such that  $\beta$  represents the angle of the major semi-axis of the ellipse with the positive x-axis of the image. Figure 4.3d shows the agreement between the experimental center shift, obtained by evaluating the linear distance between the center positions, and the calculated results based on the tilted detector model. Figure 4.3e highlights the skewed results that are obtained, when using a plain circular average with a single center position: The intensities measured in two separate halves (top vs. bottom, left vs. right) of the detector are shifted relative to each other, especially at high scattering angles. In

contrast, the elliptical average in Figure 4.3f eliminates these discrepancies, as evidenced by the flat difference intensities. A radial average of a pattern using an incorrect center or ignoring elliptical distortions is known to produce data that may, upon analysis, lead to the wrong conclusions.<sup>100</sup> This is particularly important for time-resolved data, which is richer in oscillatory features, but much lower in intensity due to the subtraction by temporal frame referencing (see Section 4.1.4).

Once the center coordinates, the ellipticity, and the ellipse orientation angle is known, elliptical mask images can be formed by parameterizing the ellipses as

$$\begin{aligned} x(t) &= x_c + a \cos(t) \cos(\beta) - b \sin(t) \sin(\beta) \quad , \\ y(t) &= y_c + a \cos(t) \sin(\beta) + b \sin(t) \cos(\beta) \quad , \end{aligned} \quad (4.11)$$

where  $a$  and  $b$  are expressed in units of pixel,  $b$  is an integer in the interval  $[0,600]$ , and the results obtained for  $x(t)$  and  $y(t)$  are rounded to next nearest integer. A weighted average using the standard errors at each pixel is then performed using the individual mask images for each  $b$  according to

$$R_{Mean}(b) = \frac{\sum_{pixel} \frac{\hat{R}(x, y) \cdot M_b(x, y)}{(\hat{R}_{StdErr}(x, y))^2}}{\sum_{pixel} \frac{1}{(\hat{R}_{StdErr}(x, y))^2}} \quad , \quad (4.12)$$

where the sum is over all nonzero pixels in the resulting images. Since  $b$  is equivalent (up to a conversion factor) to the momentum transfer  $s$ , we have thus obtained the distortion-free one-dimensional diffraction intensity.

The corresponding weighted standard deviation is calculated using

$$R_{StdDev}(b) = \sqrt{\frac{\sum_{pixel} \frac{1}{(\hat{R}_{StdErr}(x,y))^2}}{\left(\sum_{pixel} \frac{1}{(\hat{R}_{StdErr}(x,y))^2}\right)^2 - \sum_{pixel} \left(\frac{1}{(\hat{R}_{StdErr}(x,y))^2}\right)^2}} \times \sum_{pixel} \frac{(\hat{R}(x,y) - R_{Mean}(b))^2 \cdot M_b(x,y)}{(\hat{R}_{StdErr}(x,y))^2}. \quad (4.13)$$

As before, the calculation of  $R_{Mean}(b)$  and  $R_{StdDev}(b)$  are repeated three times to filter out statistically rejectable data points, which fall outside the interval  $R_{Mean}(b) \pm \mu \cdot R_{StdDev}(b)$ .

To satisfy Chauvenet's condition,<sup>98,99</sup> the parameter  $\mu$  is here set to a value of 4, because there are about 500 – 3000 nonzero pixels in a given mask image,  $M_b(x,y)$ .

After all outlier pixels have been rejected, the final standard error in the determination of the weighed mean is obtained by

$$R_{StdErr}(b) = \frac{R_{StdDev}(b)}{\sqrt{\sum_{pixel} M_b(x,y)}}. \quad (4.14)$$

The processed data in its final form,  $R_{Mean}(b)$ , and the corresponding error estimation,  $R_{StdErr}(b)$ , shown in Figure 4.4b, are used as input for the data analysis procedures described in Section 4.2.

#### 4.1.4 Temporal Referencing of Time-Dependent Data

For time-dependent diffraction patterns, the above procedures are applied to all images acquired at different pump-probe delays. The resulting ratio intensities  $R_{Mean}(b;t)$  are then temporally referenced by subtracting the data collected before time zero (reference data) from the data collected at each time point after time zero. Using a temporal reference highlights the changes in the diffraction pattern with time. Relative to the total intensity, these temporal changes are small; typically on the order of a few

percent, due to the large fraction (~90%) of unreacted molecules being probed alongside the product structures. Thus, by subtracting data containing a 100% contribution of unreacted molecules, we obtain an equal (but opposite) contribution of reacted species and unreacted molecules in the temporal difference data:

$$\begin{aligned} \Delta R_{Mean}(b; t, t_{ref}) &= R_{Mean}(b; t) - R_{Mean}(b; t_{ref}) \\ &= \left\{ g_{ref}(t)R_{ref}(b) + \sum_{\alpha \neq ref} \{g_{\alpha}(t)R_{\alpha}(b)\} \right\} - 1 \times R_{ref}(b) \\ &= \sum_{\alpha \neq ref} g_{\alpha}(t) \{R_{\alpha}(b) - R_{ref}(b)\} \end{aligned} \quad (4.15)$$

where the time dependence has been shifted to the fractional population coefficients  $g_{\alpha}$  and  $R_{ref}(b)$  and  $R_{\alpha}(b)$  represent the *static* ratio intensities, which would obtain for the reference structure *ref* and any possible product structures  $\alpha$ . The standard errors  $R_{StdErr}(b; t)$  and  $R_{StdErr}(b; t_{ref})$  are propagated accordingly to obtain the standard error for the difference data  $\Delta R_{StdErr}(b; t, t_{ref})$ , shown in Figure 4.4d.

Thus, if the  $R_{ref}(b)$  and  $R_{\alpha}(b)$  are known, measurement of  $\Delta R_{Mean}(b; t, t_{ref})$  makes it possible to follow the population dynamics of nascent species during the course of the reaction. The challenge is to determine the reference (ground state) structures and any possible production structures, which emerge upon photoexcitation. It should be noted that the absolute error bar for fitted fractions is ~0.1.<sup>25</sup> Thus, fractions less than 0.1 are below the detection limit of UED4, which places a limit on how many different product species can be observed at once.

## 4.2 Mathematics of Structural Fitting ( $\chi^2$ -Fitting)

The following discussion outlines the mathematical procedures that are used to analyze electron diffraction data. The algorithms used to solve the stated equations are discussed in detail in Ref. [101](#) and implemented in the program ueda.x (initially written by Dr. Sang Tae Park here at Caltech),<sup>[102](#)</sup> which is available in its most up-to-date version in the online supporting material.<sup>[42](#)</sup>

To enable comparison of the experimentally measured diffraction intensity data to the theoretical model, it is necessary to transform the experimental ratio intensity data accordingly (cf. Equation 2.23)

$$sM(s)^{Experiment} = C \cdot s \cdot \frac{R_{Mean}(s) \cdot I_{Xe}^{Theory}(s)}{f_i(s)f_j(s)} \cong C \cdot s \cdot \frac{I^{Diffraction}(s) + I^B(s)}{f_i(s)f_j(s)}, \quad (4.16)$$

where  $C$  is an arbitrary scale factor and we have written everything in terms of the momentum transfer vector,  $s = \frac{4\pi}{\lambda_0} \sin\left(\frac{\theta}{2}\right)$ .  $I_{Xe}^{Theory}(s)$  is the simulated (according to Equation 2.19) atomic scattering of xenon (without any background) and  $f_i(s)f_j(s)$  are usually chosen to represent the tabulated<sup>[30](#)</sup> elastic atomic scattering amplitudes of carbon,  $f_c(s)f_c(s)$ , which is the most abundant element in the sample. The unknown background contribution, which was left in  $R_{Mean}(s)$  (Equation 4.6) is still present in the transformed data as the unknown background intensity,  $I^B(s)$ . Using Equations 2.19, 2.21, and 2.23, we can write the atomic scattering and the molecular scattering (interference terms) separately as  $A_\alpha(s)$  and  $M_\alpha(s)$  and write our theoretical scattering model in the following way.

$$sM(s)^{Theory} = \sum_{\alpha} g_{\alpha} \{A_{\alpha}(s) + M_{\alpha}(s)\} + \sum_n b_n P^n(s) \quad , \quad (4.17)$$

where the  $g_{\alpha}$  are the fractional population coefficients corresponding to product species  $\alpha$  formed during the reaction and the second term is a polynomial function to approximate the unknown background in Equation 4.16. It should be noted that the function  $sM(s)^{Theory}$  is only defined, if structural coordinates corresponding to the species  $\alpha$  are specified as input parameters (see Section 4.3).

We assume that our experimental data can be satisfactorily modeled by Equation 4.17, which depends on adjustable parameters that directly relate to quantities of experimental interest, such as the molecular structure and the fractional coefficients of produced species. To determine these quantities from the experimental data, we define the weighted difference function, which we wish to minimize.

$$\chi^2 = \sum_s \frac{\{sM(s)^{Theory} - sM(s)^{Experiment}\}^2}{\left\{ \frac{s \cdot 3 \cdot R_{StdErr}(s)}{f_i(s)f_j(s)} \right\}^2} = \sum_s \{sM(s)^{Theory} - sM(s)^{Experiment}\}^2 \cdot w(s) \quad (4.18)$$

To find the best-fit parameters that optimally and globally reproduce the experimental data, the sum of squares in Equation 4.18 must be minimized (method of least-squares). Solving for the linear and the nonlinear parameters that relate to experimental quantities of interest is discussed in the following sections.

### 4.2.1 Linear Parameters

Substituting Equation 4.16 and 4.17 into Equation 4.18 we obtain the explicit difference function.

$$\chi^2 = \sum_s \left\{ \sum_{\alpha} g_{\alpha} \{A_{\alpha}(s) + M_{\alpha}(s)\} + \sum_n b_n P^n(s) - C \cdot s \cdot \frac{R_{Mean}(s) \cdot I_{Xe}^{Theory}(s)}{f_i(s) f_j(s)} \right\}^2 \cdot w(s) \quad (4.19)$$

For ground state (static) diffraction data, the sum of fractions is one,  $\sum_{\alpha} g_{\alpha} = 1$ , while for time resolved data, the sum of fractions is constrained at zero,  $\sum_{\alpha} g_{\alpha} = 0$ , because every product molecule formed must have originated from a reactant molecule (cf. Equation 4.15). However, we cannot fit the arbitrary scale factor,  $C$ , if the sum of fraction is zero. Given this constraint and adding another constraint,  $g_a = g_b$ , we employ two Lagrangian multipliers to define the Lagrange function

$$\chi'^2 = \sum_s \left\{ \sum_{\alpha} g_{\alpha} \{A_{\alpha}(s) + M_{\alpha}(s)\} + \sum_n b_n P^n(s) - C \cdot s \cdot \frac{R_{Mean}(s) \cdot I_{Xe}^{Theory}(s)}{f_i(s) f_j(s)} \right\}^2 \cdot w(s) - 2\lambda_1 \sum_{\alpha} g_{\alpha} - 2\lambda_2 (g_a - g_b) \quad (4.20)$$

In this equation,  $g_{\alpha}$ ,  $b_n$ , and  $C$  are linear parameters that can be analytically determined<sup>101</sup> (or, alternatively, be held fixed at initial values), while  $\{A_{\alpha}(s) + M_{\alpha}(s)\}$ ,  $P^n(s)$ , and  $s \cdot \frac{R_{Mean}(s) \cdot I_{Xe}^{Theory}(s)}{f_i(s) f_j(s)}$  are the basis functions. We can rewrite Equation 4.20

more concisely as

$$\chi'^2 = \sum_s \left\{ \sum_j a_j x_j(s) + \sum_k y_k(s) \right\}^2 \cdot w(s) - 2\lambda_1 \sum_j a_j \delta_j - 2\lambda_2 (g_a - g_b) \quad (4.21)$$

where we have grouped together all the linear parameters,  $a_j$ , and their corresponding basis functions,  $x_j$ . The parameters that are held at fixed values are incorporated into the constants,  $y_k$ , and the flag parameter,  $\delta_j$ , is equal to one for population fraction parameters and equal to zero otherwise.

To find a stationary point of  $\chi^2$ , we use  $\sum_k y_k(s) = y(s)$  and set its derivative equal to zero:

$$0 = \frac{1}{2} \frac{\partial \chi^2}{\partial a_k} = \sum_s \left\{ \sum_j a_j x_j(s) + y(s) \right\} \cdot x_k(s) \cdot w(s) - \lambda_1 \delta_k - \lambda_2 (\delta_{ka} - \delta_{kb}) \quad , \quad (4.22)$$

where  $\delta_{ka}$ ,  $\delta_{kb}$  are Kronecker deltas. Rearranging terms we obtain

$$\sum_j a_j \left\{ \sum_s x_j(s) x_k(s) w(s) \right\} = \sum_s y(s) x_k(s) w(s) + \lambda_1 \delta_k + \lambda_2 (\delta_{ka} - \delta_{kb}) \quad , \quad (4.23)$$

which we can rewrite in matrix form

$$\mathbf{a} \cdot \mathbf{a} = \mathbf{\beta} + \lambda_1 + \lambda_2 \quad . \quad (4.24)$$

Finally, the linear parameters of interest,  $a_j$ , and the Lagrangian multipliers,  $\lambda_1$  and  $\lambda_2$ , can be analytically found by solving the coupled system of equations consisting of  $k = j$  linear equations combined with the two equations for the initial constraints:

$$a_j = \sum_k \alpha_{jk}^{-1} \beta_k + \sum_k \alpha_{jk}^{-1} \lambda_{1,k} + \sum_k \alpha_{jk}^{-1} \lambda_{2,k} \quad , \quad (4.25)$$

$$\sum_j a_j \delta_j = 0 \quad , \quad (4.26)$$

$$g_a - g_b = a_a - a_b = 0 \quad . \quad (4.27)$$

### 4.2.2 Nonlinear Parameters

The model defined by Equation 4.18 and Equation 2.21 depends nonlinearly on the structural coordinates and internuclear root-mean-squared (rms) vibrational amplitudes of the incorporated molecular species. To determine these parameters from the experimental data, we proceed the same way as described for the linear parameters, with the exception that minimization of  $\chi^2$  has to proceed iteratively. We start from an initial set of trial values for the nonlinear parameters  $\{a_i\}$  and employ a procedure to find a new set, which stepwise minimizes  $\chi^2$  and improves our fit to the data, until we have found the global minimum on the multi-dimensional  $\chi^2$ -surface. (For a discussion of the Levenberg–Marquardt algorithm, which is employed here, as well as other algorithms that are used to locate the minimum on the  $\chi^2$ -surface, the reader is referred to Refs. [101](#) and [18](#))

Given the nonlinear parameters,  $a_i$ , the  $\chi^2$ -function can be approximated in the vicinity of its minimum by the quadratic expression

$$\chi^2 \approx \chi_0^2 + \mathbf{d} \cdot \mathbf{a} + \frac{1}{2} \mathbf{a} \cdot \mathbf{D} \cdot \mathbf{a} \quad , \quad (4.28)$$

where  $\mathbf{a}$  is a vector with the nonlinear parameters,  $a_i$  as components,  $\mathbf{d}$  is the first derivative vector (gradient), and  $\mathbf{D}$  is the matrix of second derivatives (Hessian matrix). This approximation assumes that the  $\chi^2$ -function is well approximated by a set of parabolas and, if the approximation is a good one, we can calculate the parameter change needed to reach the minimum in a single step: By setting the derivative of Equation 4.28 to zero, it can be shown that the minimum is located at

$$\mathbf{a}_{\min} = \mathbf{a}_{\text{current}} + \mathbf{D}^{-1} \cdot [-\mathbf{d}] \quad . \quad (4.29)$$

If, however, the approximation is poor, then the best thing to do is take a step in the direction of the gradient (method of steepest descent).

$$\mathbf{a}_{\text{new}} = \mathbf{a}_{\text{current}} - \text{constant} \cdot \mathbf{d} \quad (4.30)$$

Because we know the explicit form of the  $\chi^2$ -function, we can evaluate the gradient vector and the Hessian matrix for any given parameters values:

$$\beta_i \equiv -\frac{1}{2} \mathbf{d} = -\frac{1}{2} \frac{\partial \chi^2}{\partial a_i} = -w(s) \sum_s \left\{ sM(s|\mathbf{a})^T - sM(s)^E \right\} \frac{\partial sM(s|\mathbf{a})^T}{\partial a_i}, \quad (4.31)$$

and

$$\begin{aligned} \alpha_{ij} &\equiv \frac{1}{2} \mathbf{D} = \frac{1}{2} \frac{\partial^2 \chi^2}{\partial a_i \partial a_j} \\ &= w(s) \sum_s \left[ \frac{\partial sM(s|\mathbf{a})^T}{\partial a_i} \frac{\partial sM(s|\mathbf{a})^T}{\partial a_j} - \left\{ sM(s|\mathbf{a})^T - sM(s)^E \right\} \frac{\partial^2 sM(s|\mathbf{a})^T}{\partial a_i \partial a_j} \right] \\ &\approx w(s) \sum_s \left[ \frac{\partial sM(s|\mathbf{a})^T}{\partial a_i} \frac{\partial sM(s|\mathbf{a})^T}{\partial a_j} \right], \end{aligned} \quad (4.32)$$

where the superscripts designate the theoretical (T) and experimental (E) modified molecular scattering functions and the dependence of  $sM(s|\mathbf{a})^T$  on the structural coordinates and the rms vibrational amplitudes of the molecules is written explicitly. The second term in Equation 4.32 is generally small and can be dropped.<sup>101</sup>

To find the minimizing change in parameters,  $\Delta \mathbf{a} = \mathbf{a}_{\min} - \mathbf{a}_{\text{current}}$ , Equation 4.29 can be rewritten using Equation 4.31 and 4.32 as

$$\boldsymbol{\alpha} \cdot \Delta \mathbf{a} = \boldsymbol{\beta} \quad , \quad (4.33)$$

or explicitly as a set of linear equations

$$\sum_j \alpha_{ij} \Delta a_j = \beta_i \quad . \quad (4.34)$$

Equation 4.30 can be similarly rewritten as

$$\Delta a_j = \text{constant} \cdot \beta_j \quad . \quad (4.35)$$

### 4.2.3 Estimation of Errors in the Fitted Parameters

For the estimation of both the linear and the nonlinear parameters, we ultimately had to solve a set of linear equations, as can be seen by comparing Equation 4.24 and Equation 4.33. Therefore, the method of propagating the uncertainties of the diffraction data, obtained in Equation 4.14, into the error in the fitted parameters is the same in both cases. For all UED studies contained in this thesis, the uncertainties are propagated as  $3 \cdot R_{StdErr}(s)$  ( $3\sigma$ ) into the  $\chi^2$ -function (cf. Equation 4.18). As such, the published error bars for any fitted parameters also represent the standard error multiplied by a factor of three.

After the values of all fitted parameters have been obtained, the variances (squared uncertainties) of the estimated parameters  $a_j$  can be read off the diagonal elements of the covariance matrix  $\mathbf{C} \equiv \mathbf{\alpha}^{-1}$ , where  $\mathbf{\alpha}$  is defined as described in the previous two sections.<sup>101</sup>

$$\sigma^2(a_j) = C_{jj} \quad (4.36)$$

The error ( $3\sigma$  in this case) associated with the estimated parameter is then given by

$$\delta a_j = \sqrt{\Delta \chi_{v,p}^2} \sqrt{\sigma^2(a_j)} \quad , \quad (4.37)$$

where the coefficient  $\Delta \chi_{v,p}^2$  can be calculated for a given confidence level,  $p$ , and for the

number of simultaneously fitted parameters,  $\nu$ , by solving

$$\Gamma\left(\frac{\nu}{2}, \frac{\Delta\chi_{\nu,p}^2}{2}\right) = 1 - p \quad , \quad (4.38)$$

where  $\Gamma(s, x) = \int_x^\infty t^{s-1} e^{-t} dt$  is the upper incomplete gamma function.<sup>101</sup>

#### 4.2.4 Choice of Structural Coordinates for Fitting

So far, we have not specified a coordinate basis, in which the molecular structure is defined. An intuitive way to define a molecular structure is to specify the  $3N$  Cartesian coordinates of the individual positions of all  $N$  atoms atom in the molecule. However, internal coordinates are a better choice for the fitting parameters, because it eliminates 3 translational and 3 rotational degrees of freedom from the problem. The choice of which internal coordinates to use is, however, not unique. Previously, structural refinement in the UED lab at Caltech was conducted using a minimal set of  $3N - 6$  internal coordinates defined through a z-matrix formalism, using  $N - 1$  bond lengths,  $N - 2$  bond angles and  $N - 3$  dihedral angles.<sup>9,18</sup> A drawback of using such a minimal set of internal coordinates is that they are often strongly coupled, that is a change in one coordinate produces a change in another coordinate, e.g., changing a bond angle in a ring structure necessarily changes other bond lengths as well. Mathematically, coupling between structural coordinates manifest itself as large off-diagonal elements in the Hessian matrix  $\mathbf{\alpha}$  defined in Equation 4.32. Furthermore, the simultaneous fitting of two correlated coordinates could lead to a large change in both coordinates, but the cumulative effect results only in a negligible reduction in the

$\chi^2$ -value, such that the values of the two coordinates cannot be determined reliably based on the diffraction data. The use of  $3N - 6$  z-matrix coordinates was sufficient for studies on very small molecules and molecules of high internal symmetry, where correlations between fitting parameters could be easily identified by manually fitting each coordinate separately. For larger molecules, however, and for molecules of low symmetry, which are reported in this thesis (see Chapter 5), this was no longer possible, such that an automated fitting procedure had to be developed.

Redundant internal coordinates, which use more than  $3N - 6$  coordinates, are advantageous, because they allow for a more complete and physically reasonable description of the molecular structure, especially ring structures.<sup>103</sup> Additionally, they provide significant improvements in efficiency, when used in optimization/minimization problems, compared to nonredundant internal coordinates (e.g., z-matrix coordinates) or Cartesian coordinates.<sup>104</sup> To avoid the problem of coupling between coordinates, we have implemented a fitting routine based in singular value decomposition (SVD) in *ueda.x* (see below) that identifies, from an initial set of redundant internal coordinates, a new set of fitting coordinates, in the direction of which the  $\chi^2$ -surface curvature is most pronounced.

The redundant internal coordinate system  $\mathbf{s}$  is related to the Cartesian coordinate system through

$$\mathbf{s} = \mathbf{B}\mathbf{x} \quad , \quad (4.39)$$

where the transformation matrix  $\mathbf{B}$  is evaluated at the equilibrium geometry  $\mathbf{x}_e$  and the equality is only valid for infinitesimal Cartesian displacements. Since  $\mathbf{x}$  is a  $3N$ -vector

and  $\mathbf{s}$  is an  $M$ -vector ( $M > 3N$ ), the dimension of  $\mathbf{B}$  is  $M \times 3N$ , i.e.,  $\mathbf{B}$  is not a square matrix and cannot be readily inverted. A recipe for calculating the matrix  $\mathbf{B}$  is given in many textbooks.<sup>105,106</sup>

#### 4.2.4.1 Singular Value Decomposition

For automated analysis of electron diffraction data, the fitting algorithm has to have two important capabilities. First, the coordinate, which reduces the  $\chi^2$ -value to the largest extent, has to be identified among all specified coordinates. Second, all the other coordinates need to be identified, which have changed simultaneously with the chosen coordinate. By employing new coordinates, which consist of an appropriate linear combination of the initially specified internal coordinates, this can be accomplished. In fact, the second issue can be avoided altogether, if the new internal coordinates can be defined to be orthogonal to each other. According to the spectral theorem,<sup>107</sup> for any real and symmetric matrix (such as  $\mathbf{a}$ ), there exists a real orthogonal matrix  $\mathbf{Q}$ , such that

$$\mathbf{a} = \mathbf{Q}\mathbf{\Lambda}\mathbf{Q}^T = \mathbf{Q}\mathbf{\Lambda}\mathbf{Q}^{-1} \quad , \quad (4.40)$$

where  $\mathbf{\Lambda}$  is a diagonal matrix containing the eigenvalues (or in this context the singular values) of  $\mathbf{a}$  in ascending order and we have used the property  $\mathbf{Q}^T = \mathbf{Q}^{-1}$  for orthogonal matrices. The columns of the matrix  $\mathbf{Q}$  consist of the eigenvectors of  $\mathbf{a}$  and these eigenvectors together form an orthonormal basis, in which this problem can be solved.

We can see this by substituting Equation 4.40 into Equation 4.33 to obtain

$$\mathbf{\Lambda}\mathbf{Q}^T\Delta\mathbf{a} = \mathbf{Q}^T\boldsymbol{\beta} \quad . \quad (4.41)$$

Since the same linear transformation,  $\mathbf{Q}^T$ , is being applied to both  $\Delta\mathbf{a}$  and  $\boldsymbol{\beta}$ , we can rewrite this equation as

$$\mathbf{\Lambda}\Delta\mathbf{a}' = \boldsymbol{\beta}' \quad . \quad (4.42)$$

Thus, the new fitting parameters,  $\Delta a_j'$ , are composed of a linear combination of the originally defined structural coordinates with coefficients given by the columns of  $\mathbf{Q}$  (or the rows of  $\mathbf{Q}^T$ ).

$$\Delta a_j' = \sum_i Q_{ji} \Delta a_j \quad (4.43)$$

Since this new basis is orthogonal, the coupling between individual fitting parameters has been eliminated.

The parameters with the lowest associated fitting error (the directions of highest  $\chi^2$ -curvature and therefore highest confidence) are automatically identified through SVD. It was already pointed out that the variances of the estimated fitting parameters can be read off the covariance matrix  $\mathbf{C} \equiv \boldsymbol{\alpha}^{-1}$ , which in this new basis can be evaluated trivially as the diagonal matrix  $\mathbf{C}' \equiv \mathbf{\Lambda}^{-1}$ . Thus, when fitting in the direction of parameter

$\Delta a_j'$ , a large eigenvalue  $\lambda_j$  corresponds to a small variance  $\frac{1}{\lambda_j}$  and a small eigenvalue

$\lambda_j$  corresponds to a large variance  $\frac{1}{\lambda_j}$ . In other words, the  $\chi^2$ -surface is very shallow

along the coordinates corresponding to small eigenvalues. The minimum position obtained along these directions is likely to be affected by noise in the experimental data.

For this reason, it would be prudent not to try to fit these parameters, but rather freeze

them at their initial value. This can be accomplished by setting to zero all values  $\frac{1}{\lambda_j}$ , where  $\lambda_j$  falls below a certain threshold value. As a consequence, Equation 4.42 is solved using the pseudo-inverse of  $\Lambda$ , namely  $\Lambda_{Thresh}^{-1}$ , with the result that fitting occurs only in the (orthogonal) directions, in which the curvature of the  $\chi^2$ -surface is most pronounced, and to which the experimental data is most sensitive.

$$\Delta \mathbf{a}' = \Lambda_{Thresh}^{-1} \boldsymbol{\beta}' \quad (4.44)$$

In practice, fitting of the diffraction data is best accomplished by the stepwise unfreezing of fixed parameters, while monitoring the molecular structure at each point. Thus, after finding the  $\chi^2$ -minimum in the first direction, the  $\chi^2$ -minima in the second, third, ... orthogonal direction are found. If the quadratic approximation to the  $\chi^2$ -surface is poor, then the method of steepest descent can be employed, as before, in this structural parameter basis by transforming Equation 4.35,

$$\Delta \mathbf{a}' = \text{constant} \cdot \boldsymbol{\beta}' \quad (4.45)$$

The values determined for the fitted parameters and their associated covariance matrix can then be projected back onto the initially defined structural coordinates basis using  $\Delta \mathbf{a} = \mathbf{Q} \Delta \mathbf{a}'$  and  $\mathbf{C} = \mathbf{Q} \Lambda_{Thresh}^{-1} \mathbf{Q}^{-1}$ , respectively.

### 4.3 Defining the Theoretical Model

As shown in Chapter 2, the construction of a physically meaningful molecular scattering model (Equation 2.21) requires a priori knowledge of the molecular structure and the rms amplitudes of vibration at the experimental temperature. For the molecular

systems studied in this thesis, these initial parameters are obtained through quantum chemical calculations.

### 4.3.1 Calculating a Starting Molecular Structure

UED data analysis is performed by comparing a simulated one-dimensional diffraction pattern of a theoretical initial-guess structure to the actual experimental data. Since the  $\chi^2$ -surface may be fairly shallow and might have many local minima, it is very important that the initial guess geometry corresponds to a structure that is already close to the “true” structure, i.e., is already located inside the funnel containing the global minimum. Gas-phase electron diffraction groups and the UED lab in particular, routinely rely on high-level quantum chemical calculations to provide the starting points, i.e., physically reasonable initial guess parameter, from which the molecular structure can be determined.

Density functional theory (DFT) at the B3LYP level with the 6-311G(d,p) basis set has been found to produce very accurate molecular structures, energies, and vibrational frequencies for singlet ( $S_0$ ) or triplet ( $T_1$ ) ground state properties.<sup>108-110</sup> Several methods are available to calculate the properties of excited states, which were described in detail in a previous thesis from this lab.<sup>18</sup> For all the studies contained in this thesis, the molecular properties were calculated using either Gaussian98<sup>111</sup> or GAMESS<sup>112</sup> quantum chemical software packages.

### 4.3.2 Calculating the Root-Mean-Squared Amplitudes of Vibration

There exist several methods to calculate the rms amplitudes of vibration, either based on experimental spectroscopic data,<sup>113</sup> empirical equations,<sup>114,115</sup> or quantum chemical force constants.<sup>19,22,116,117</sup> The last two methods have been used for the studies contained in this thesis and their use will be described in detail here.

#### 4.3.2.1 Empirical Equations

For UED3 studies, the calculation of the rms amplitudes of vibration has traditionally been carried out by using the following empirically determined formulae for C–C distances in the range of  $1.217 \text{ \AA} \leq r_e \leq 5.618 \text{ \AA}$ ,<sup>114</sup>

$$l_h = 0.013837 + 0.023398r_e - 0.000147r_e^2 \quad , \quad (4.46)$$

and for C–H distances in the range of  $1.080 \text{ \AA} \leq r_e \leq 4.677 \text{ \AA}$ ,<sup>115</sup>

$$l_h = 0.050134 + 0.027368r_e - 0.001805r_e^2 \quad . \quad (4.47)$$

These values, which were experimentally determined for molecules at 298 K, are then scaled to any arbitrary temperature  $T$  using the relation for normal mode vibrations based on a harmonic model.<sup>28,106</sup>

$$l_h^2 = \frac{h}{8\pi^2\mu\nu} \coth\left(\frac{h\nu}{2kT}\right) \quad , \quad (4.48)$$

where  $h$  is Planck's constant,  $k$  is the Boltzmann constant,  $\mu$  is the reduced mass of the internuclear pair,  $\nu$  is the harmonic vibrational frequency. Equation 4.48 is used to solve for  $\nu$  at 298 K and then the rms vibrational amplitudes  $l_h$  at the desired  $T$  can be obtained by assuming that  $\nu$  is independent of temperature. These empirically determined rms

amplitudes can be used for small molecules, whose size falls within in the ranges stated above, e.g., nitrobenzene, described in Section 5.3. However, it is difficult to justify the physical basis of extrapolating these empirical results for the calculation of the rms amplitudes of vibration to larger nonbonded internuclear distances of large molecules. Therefore, a new method was implemented using the calculation output from the quantum chemical software packages mentioned above.

#### 4.3.2.2 *Quantum Chemical Force Constants*

Quantum chemical calculations also allow for the calculation of vibrational frequencies of a molecular structure and the associated harmonic force constants, which in turn can be used to evaluate the harmonic rms amplitudes of vibration. In the following, the steps to obtain these parameters from the calculation output will be described. The described routines have been implemented in the program *amplitude.x* (initially written by Dr. Sang Tae Park here at Caltech), which is available in the online supporting material.<sup>42</sup>

After running a quantum chemical geometry optimization and frequency calculation, the following output is obtained: The equilibrium geometry in Cartesian coordinates, represented by the  $3N$ -vector  $\mathbf{x}$  and the  $3N \times 3N$  matrix of second derivatives of the potential energy  $\mathbf{H}_{\mathbf{x}} = \frac{d^2V}{d\mathbf{x}^2}$  (Cartesian Hessian matrix or force constant matrix). (The Cartesian gradient is equal to zero at the equilibrium geometry, which is located at the potential energy minimum.)

To describe the distortion of the molecular frame due to molecular vibrations, the Cartesian force constants are projected onto the redundant internal coordinate basis described in Section 4.2.4. Using Equation 4.39, the Cartesian Hessian matrix can be transformed into the redundant internal coordinate basis by

$$\mathbf{H}_s = (\mathbf{B}^{-1})^T \mathbf{H}_x \mathbf{B}^{-1} \quad , \quad (4.49)$$

where  $\mathbf{B}^{-1}$  is the generalized inverse of the matrix  $\mathbf{B}$ , defined as<sup>106</sup>

$$\mathbf{B}^{-1} = \mathbf{M}^{-1} \mathbf{B}^T (\mathbf{B} \mathbf{M}^{-1} \mathbf{B}^T)^{-1} = \mathbf{M}^{-1} \mathbf{B}^T \mathbf{G}^{-1} \quad . \quad (4.50)$$

The Hessian matrix in redundant internal coordinates is then further transformed into mass-weighted redundant internal coordinates according to

$$\mathbf{m}\mathbf{s} = \mathbf{G}^{-1/2} \mathbf{s} \quad , \quad (4.51)$$

and

$$\mathbf{H}_{ms} = \mathbf{G}^{1/2} \mathbf{H}_s \mathbf{G}^{1/2} \quad . \quad (4.52)$$

Since the Hessian matrix  $\mathbf{H}_{ms}$  is real and symmetric it can be diagonalized by a real orthogonal matrix  $\mathbf{L}_{ms}$  according to (cf. Equation 4.40)

$$\mathbf{L}_{ms}^T \mathbf{H}_{ms} \mathbf{L}_{ms} = \mathbf{F} \quad , \quad (4.53)$$

where  $\mathbf{F}$  is a diagonal matrix containing the eigenvalues of  $\mathbf{H}_{ms}$  in ascending order and the columns of the matrix  $\mathbf{L}_{ms}$  are the corresponding eigenvectors of  $\mathbf{H}_{ms}$ . Because we are using mass-weighted coordinates, the eigenvalue matrix  $\mathbf{F}$  contains the mass-weighted force constants of the normal modes of vibration, such that the frequency of the  $k$ th normal mode is obtained through

$$v_k = \frac{1}{2\pi} \sqrt{F_{kk}} \quad . \quad (4.54)$$

Since  $\mathbf{F}$  is a matrix of dimension  $M \times M$ , the first  $M - (3N - 6)$  eigenvalues will be (numerically) zero. It follows from the above discussion that the eigenvector matrix  $\mathbf{L}_{ms}$  can be expressed in redundant internal coordinates as

$$\mathbf{L}_s = \mathbf{G}^{1/2} \mathbf{L}_{ms} \quad , \quad (4.55)$$

or Cartesian coordinates as

$$\mathbf{L}_x = \mathbf{B}^{-1} \mathbf{L}_s = \mathbf{B}^{-1} \mathbf{G}^{1/2} \mathbf{L}_{ms} \quad . \quad (4.56)$$

The eigenvectors of the  $\mathbf{L}$  matrices allow us to determine the distortion to the molecular frame in  $3N - 6$  orthogonal directions, which are the normal coordinates  $\mathbf{Q}$ , defined as

$$\mathbf{Q}_x = \mathbf{L}_x^T \mathbf{x} \quad , \quad (4.57)$$

$$\mathbf{Q}_s = \mathbf{L}_s^T \mathbf{s} \quad , \quad (4.58)$$

$$\mathbf{Q}_{ms} = \mathbf{L}_{ms}^T \mathbf{ms} \quad , \quad (4.59)$$

and we see that the columns of  $\mathbf{L}$  (or the rows of  $\mathbf{L}^T$ ) contain the coefficients of the linear combinations of respective coordinates that make up the normal coordinates.

Under the harmonic approximation, the mean-squared amplitude of vibration along the  $k$ th normal mode can then be obtained using the equivalent of Equation 4.48

$$l_{h,k}^2 = \frac{h}{8\pi^2 \mu v_k} \coth\left(\frac{h v_k}{2kT}\right) \quad , \quad (4.60)$$

where the equilibrated internal temperature of the molecule under the experimental conditions is used. Another consequence of the harmonic approximation is that the probability density of internuclear distance is given as (cf. Equation 2.20)

$$P(\Delta) = \frac{1}{\sqrt{2\pi l_h^2}} \exp\left(-\frac{\Delta^2}{2l_h^2}\right) . \quad (4.61)$$

To determine the molecular structure due vibrational distortion along the normal coordinates  $\mathbf{Q}_s$ , the molecular frame is iteratively displaced by an amount  $\Delta \in [-4l_{h,k}, 4l_{h,k}]$  along each direction  $k$ . The corresponding changes in the values of the individual redundant internal coordinates are then calculated as

$$s_{i,k}(\Delta) = s_{i,e} + \Delta \cdot L_{s,ik} , \quad (4.62)$$

where  $L_{s,ik}$  are the coefficients in the matrix  $\mathbf{L}_s$  that corresponds to the  $i$ th redundant internal coordinate and the  $k$ th normal mode.

As stated earlier, the transformation matrix  $\mathbf{B}$  is only defined in an infinitesimal region around the equilibrium geometry, such that the relation between the correspondingly displaced Cartesian coordinates  $\mathbf{x}_k(\Delta)$  and the displaced redundant internal coordinates  $\mathbf{s}_k(\Delta)$  is linear only at  $\Delta = 0$  (equilibrium geometry).<sup>19</sup> However, because the displacement  $\Delta$  can take on finite values, the coordinates  $\mathbf{x}_k(\Delta)$  have to be found iteratively in a series of  $n$  Cartesian displacement steps and through the recalculation of an instantaneous matrix  $\mathbf{B}_n$  obtained from the resulting molecular geometry after each step. Once the Cartesian coordinates  $\mathbf{x}_k(\Delta)$  corresponding to  $\mathbf{s}_k(\Delta)$  are determined, the Cartesian distances between internuclear pairs,  $r_{ij,k}(\Delta)$ , are readily found.

The distortion of an internuclear distance between atom  $i$  and atom  $j$  from the equilibrium value,  $r_{ij,e}$ , due to overall vibrational motion is obtained by

$$\begin{aligned} \partial r_{ij} &= \langle r_{ij} \rangle - r_{ij,e} \\ &= \sum_k \int_{4l_{h,k}}^{4l_{h,k}} r_{ij,k}(\Delta) P(\Delta) d\Delta - r_{ij,e} \end{aligned} \quad (4.63)$$

where the brackets denote average quantities. Finally, the overall mean-squared amplitude of vibration between atom  $i$  and atom  $j$  is obtained by<sup>8</sup>

$$\begin{aligned} l_{h,ij}^2 &= \langle r_{ij}^2 \rangle - \langle r_{ij} \rangle^2 \\ &= \sum_k \left[ \int_{4l_{h,k}}^{4l_{h,k}} (r_{ij,k}(\Delta))^2 P(\Delta) d\Delta - \left( \int_{4l_{h,k}}^{4l_{h,k}} r_{ij,k}(\Delta) P(\Delta) d\Delta \right)^2 \right] \end{aligned} \quad (4.64)$$

#### 4.4 Fitting Procedure

The succession of steps that are needed to arrive at the final structures differ slightly between molecules, because each molecule poses its own challenges, especially for structural fitting. Even though specific cases will be described in Chapter 5, a general “road map” can be laid out that is commonly followed.

In an initial step the camera distance and the instrumental point-spread-function need to be calibrated. In the steps that follow, the ground state temperature and structure is determined. Once this structure is known, the product structure(s) involved in the reaction is (are) determined and then refined using temporal frame-referenced diffraction data.

#### 4.4.1 Calibration of Instrumental Factors: Camera Length and Point-Spread-Function

A diffraction pattern of CO<sub>2</sub> reference gas, is collected in each experiment and the resulting experimental  $sM(s)^{CO_2}$  is fit by its theoretical counterpart using its known structural parameters of CO<sub>2</sub>.<sup>118</sup> Because CO<sub>2</sub> contains only two distinct bond lengths,  $sM(s)^{CO_2}$  is defined by a superposition of only two sine waves, as shown in Figure 4.5a. The only parameters that are varied during the fitting procedure are the instrumental camera length and point-spread-function, defined in Section 3.2.<sup>4</sup> Figure 4.5b shows the minimum that is obtained for the point-spread-function and the corresponding camera length.

#### 4.4.2 Temperature Fitting of Ground State Molecules

For electron diffraction experiments on UED3, the temperature of the ground state molecules is well-defined, because the molecules are in thermal equilibrium with the gas inlet system by the time they enter into the vacuum chamber. In contrast, for electron diffraction experiments using the laser desorption source in UED4, the internal temperature of the desorbed molecules has to be estimated from the diffraction data, because of the unknown thermal energy transfer during the desorption process (see Section 3.1.5.2).

The temperature is estimated by explicitly calculating the rms amplitudes of vibration  $l_{ij}$  at different temperatures using *amplitude.x* (see Section 4.3.2.2). Then, by loading the calculated DFT-structure and the rms amplitudes of vibration at different

temperatures  $T$ , the best fit is determined by only fitting the linear parameters. Figure 4.6 shows the behavior of  $\chi^2(T)$  obtained for the ground state of 6-nitro-BIPS. A clear minimum is found at  $T = 510$  K.

### 4.4.3 Determination of Ground State Structure

Once the temperature and the linear parameters (see Section 4.2.1) have been determined, the molecular structure is refined. Structural refinement is conducted using the method of SVD and by stepwise unfreezing of the most relevant structural parameters (see Section 4.2.4.1). After fitting each parameter, which locates a  $\chi^2$ -minimum in the corresponding direction, the entire molecular structure at that stationary point is assessed together with the resulting improvement in the  $\chi^2$ -value. If the  $\chi^2$ -value was reduced considerably, but the structure was only changed slightly, then the  $\chi^2$ -surface in that direction had a deep minimum and the value of the structural parameter could be determined with high confidence. In contrast, if the molecular structure had to be changed considerably (often to something that is not physically reasonable, e.g., an excessively large change in bond lengths of 0.05 Å or more compared to the DFT-structure), then the validity of the determined value has to be examined and, if needed, the user has to reject the value based on chemical intuition. It should be noted that, when fitting subsequent structural parameters, the previous structural parameters are always fit simultaneously. Therefore, it is possible that fitting structural parameter 3, for example, results in a unphysical structure, but subsequent fitting structural parameter 4 (along with structural parameter 1, 2, and 3) corrects the molecular structure back to

physically reasonable values. This is possible because the structural parameters are themselves made up of (overlapping) linear combinations of structural coordinates. If, however, the molecular structure continues to structurally diverge, fitting is stopped and the last physical structure is then designated the experimentally determined structure. Depending on the quality of the diffraction data and the sensitivity of diffraction to changes in molecular structure, up to seven structural parameters can be fit simultaneously for ground state diffraction patterns.

#### 4.4.4 Determination of Product Structure(s)

The internal temperatures of the product species is determined based on conservation of energy. The vibrational energy of a molecular system is given by the vibrational partition function,

$$E_{\text{Vibrational}} = \sum_{i=1}^{3N-6} h\nu_i \frac{\exp\left[-\frac{h\nu_i}{kT}\right]}{\left(1 - \exp\left[-\frac{h\nu_i}{kT}\right]\right)}, \quad (4.65)$$

where  $h$  is Planck's constant,  $k$  is the Boltzmann constant,  $\nu_i$  is vibrational frequency of the  $i$ th normal mode. The vibrational energy of a product species after the absorption of a photon of the pump laser is then given by (neglecting translational and rotational energies)

$$E_{\text{Vibrational}}^{\text{Product}} = \left( E_{\text{Electronic}}^{\text{Reactant}} + E_{\text{ZeroPointEnergy}}^{\text{Reactant}} + E_{\text{Vibrational}}^{\text{Reactant}} + E_{\text{h}\nu}^{\text{Photon}} \right) - \left( E_{\text{Electronic}}^{\text{Product}} + E_{\text{ZeroPointEnergy}}^{\text{Product}} \right), \quad (4.66)$$

and the corresponding internal temperature can then be obtained through substitution of Equation 4.65.

To identify the structures present and their abundance, the experimental frame-referenced  $\Delta sM(s)$  curve (see Section 4.1.4), is fit with a linear combination of theoretically calculated  $sM(s)$  curves (Equations 2.23 and 4.17). The coefficients of this linear combination report directly on the fractional abundance of a given species. While the identity of the parent structure is always known, the identity of the structures formed is often undetermined. Relying on previously reported reaction products and the available energies, it is often the case that multiple structures can theoretically be formed in the gas phase. Because UED is sensitive to all structures present, even those that are spectroscopically undetectable (dark structures),<sup>7</sup> all possible reaction channels have to be screened. Screening is performed (using the DFT-determined product structures) by including the possible species in their single, double, and triple combinations in Equation 4.17. The most likely reaction channels are then ranked by the quality of the fit, which is assessed visually and quantitatively through the  $\chi^2$ -value. For the reaction channels with the best rank, structural fitting is then performed, as described in the previous section, and through the resulting drop in the  $\chi^2$ -value, the structures are reshuffled. The experimentally determined product structures and their fractional abundance is then determined from the best fit resulting from the most reasonable structure.

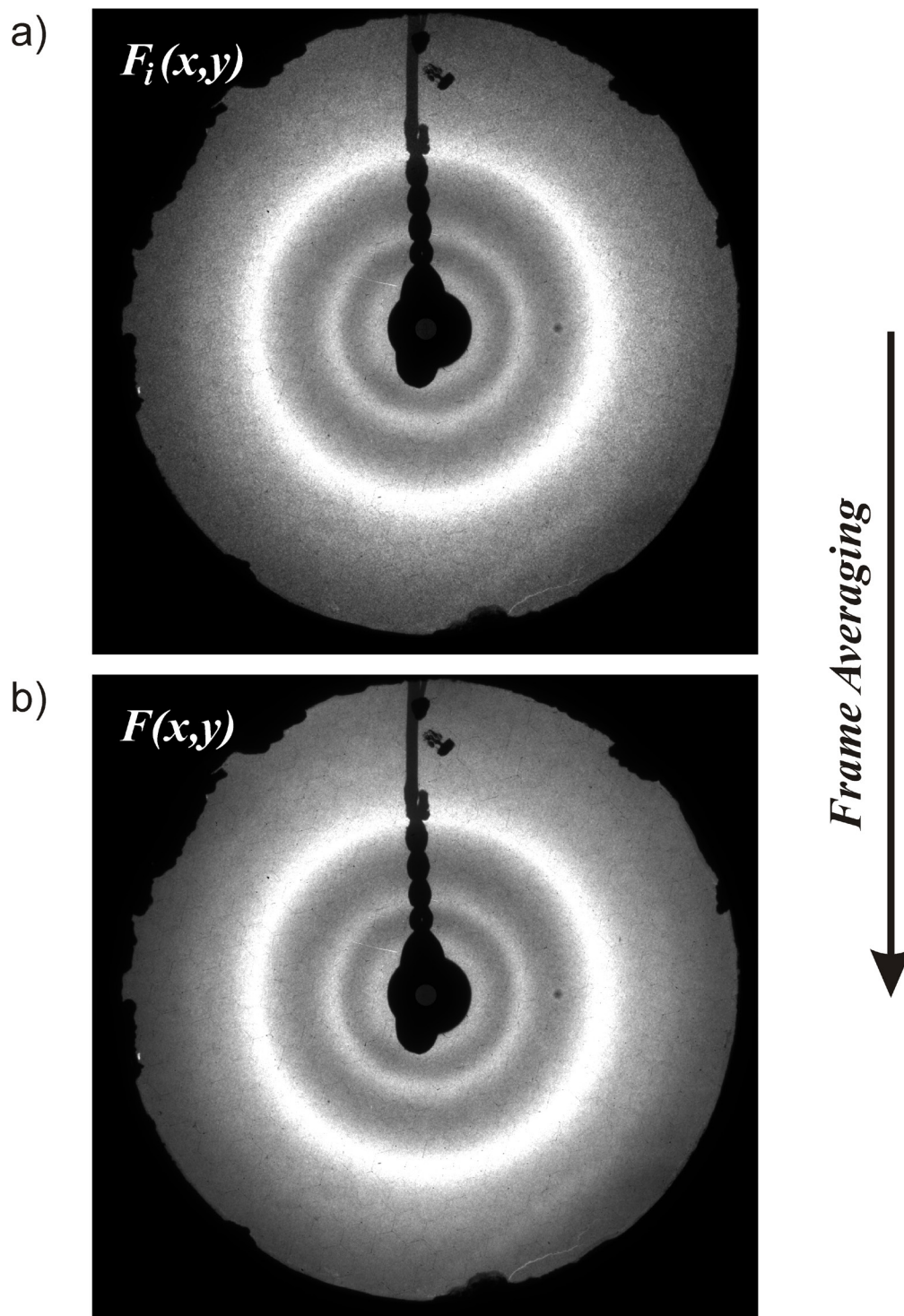


**Figure 4.1.** The frame averaging procedure. a) Individual diffraction images, obtained in a limited exposure time, are noisy due to the limited number of electron counts that can be recorded, before the detector saturates. b) Through a pixel-by-pixel average a smooth diffraction pattern is obtained.

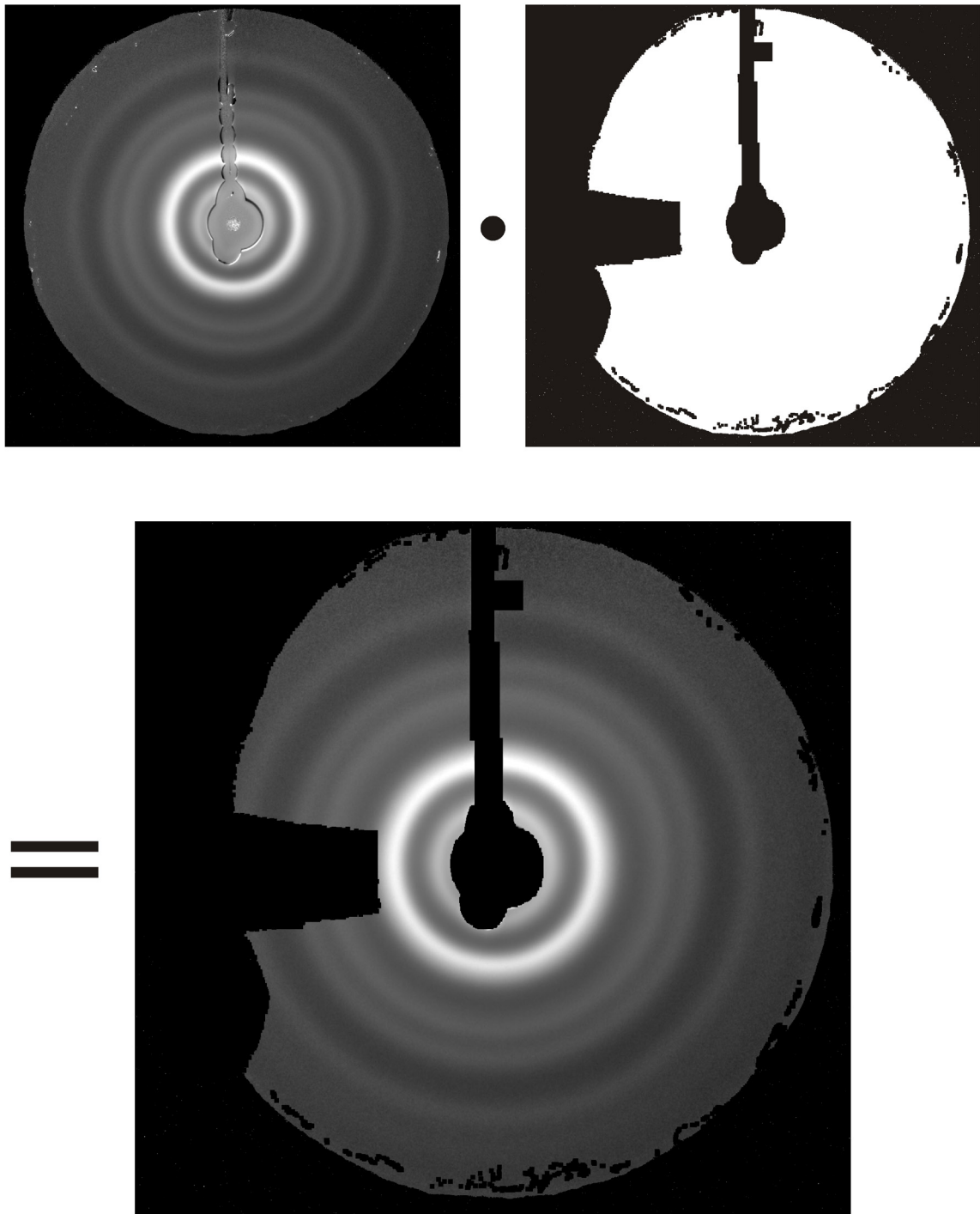


**Figure 4.2.** A ratio image is masked to remove artificially high- or low-intensity pixels.

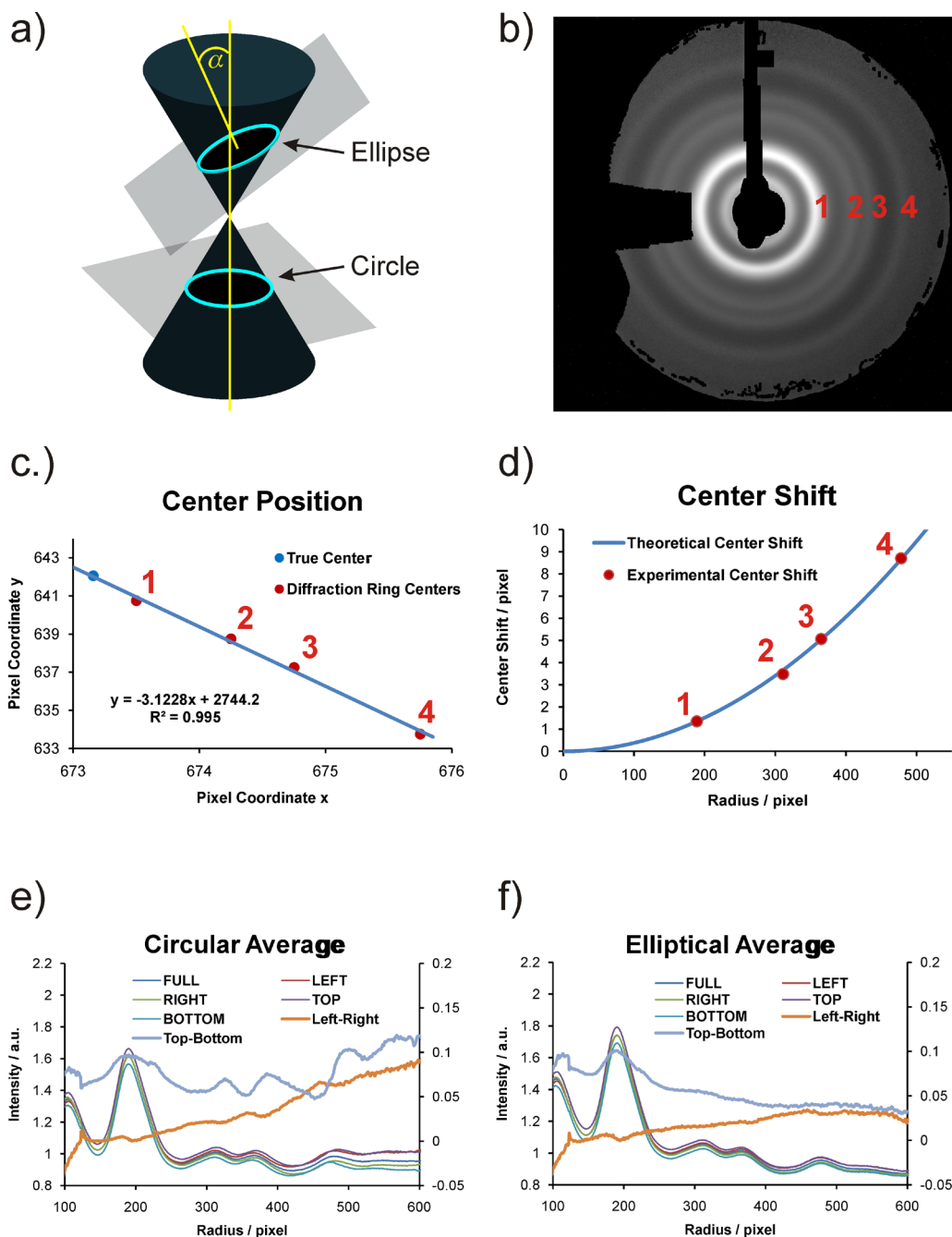


**Figure 4.3.** a) The detection plane intersects the scattering cone at a tilt angle,  $\alpha$ , which results in b) an elliptically distorted diffraction pattern. According to geometrical considerations, c) the center coordinates of the indicated diffraction rings form a straight line on the detector and d) the distance between the center coordinates is given by Equation 4.8. As indicated by the diffraction intensities of parts of the detector and their differences, e) the circular average results in artificially broadened diffraction peaks, while f) the elliptically corrected average reproduces the correct diffraction signal.

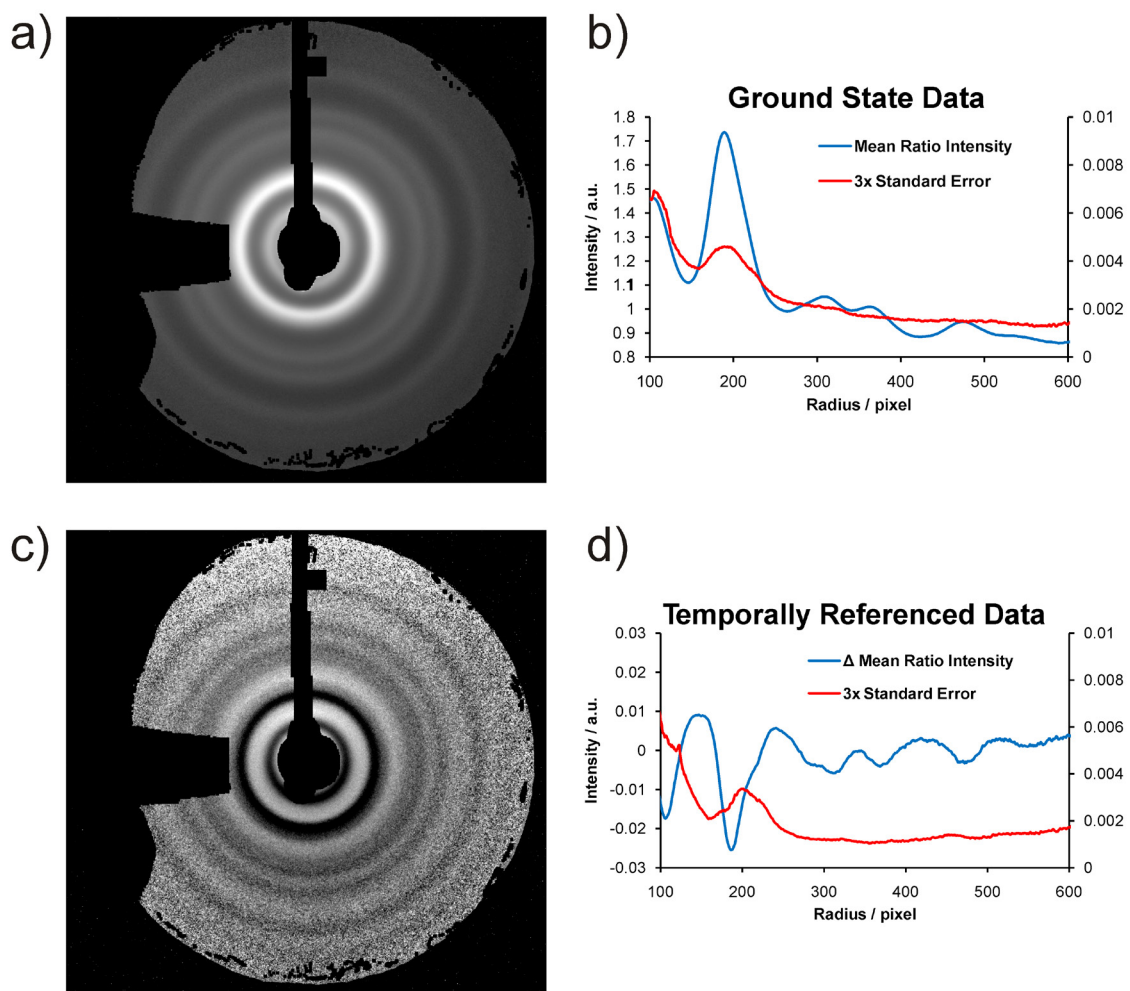


**Figure 4.4.** a) A ground state diffraction pattern (ratio image) and b) its corresponding one-dimensional mean intensity distribution with the associated errors at each pixel. c) A frame-referenced diffraction pattern and d) its corresponding one-dimensional mean intensity distribution with the associated errors at each pixel.

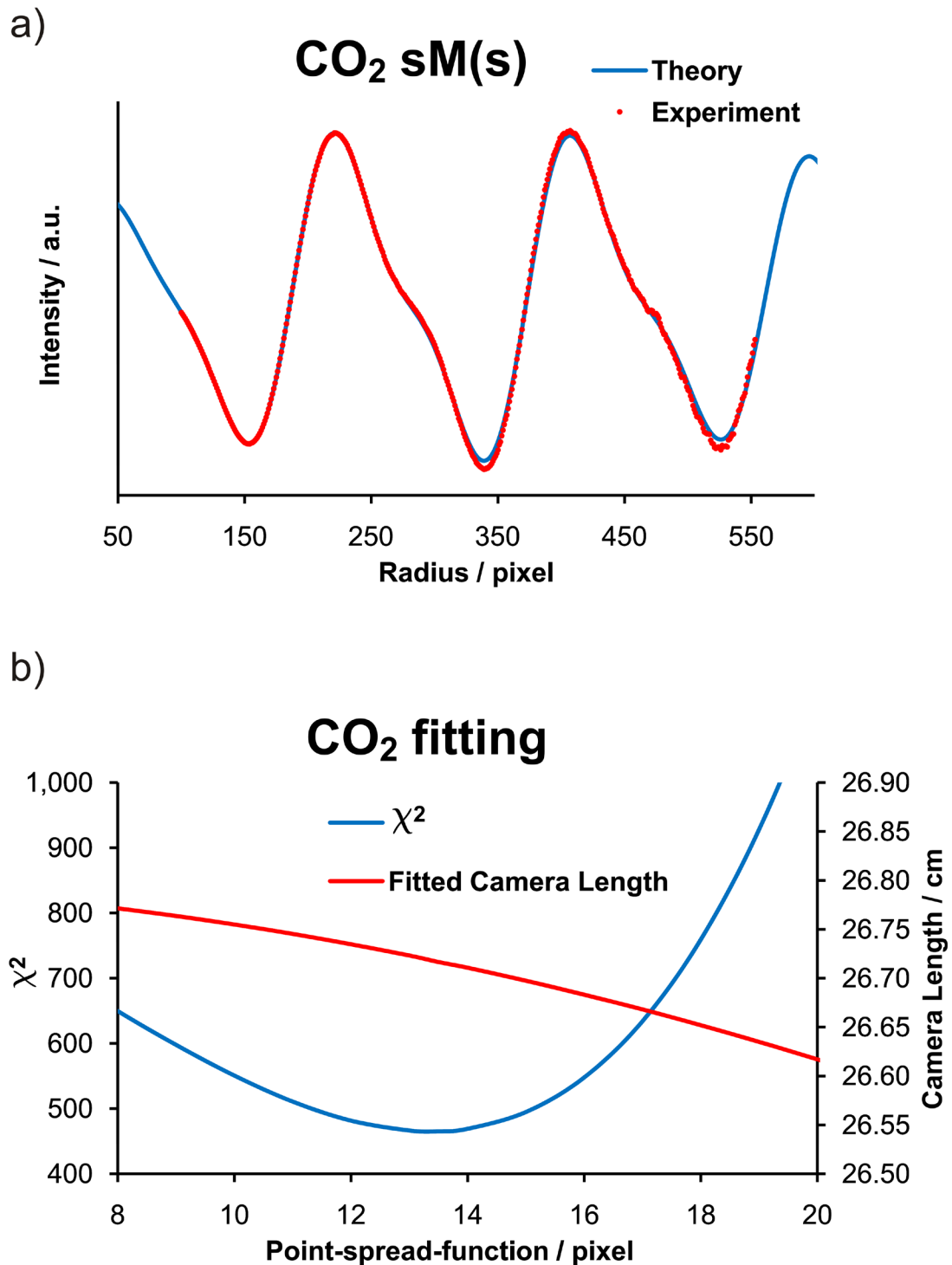


**Figure 4.5.** a) The molecular scattering function of CO<sub>2</sub> is the superposition of two sine waves. b) Because the structural parameters of CO<sub>2</sub> are known, it can be used as a reference gas to calibrate the camera length and the point-spread-function of the instrument.

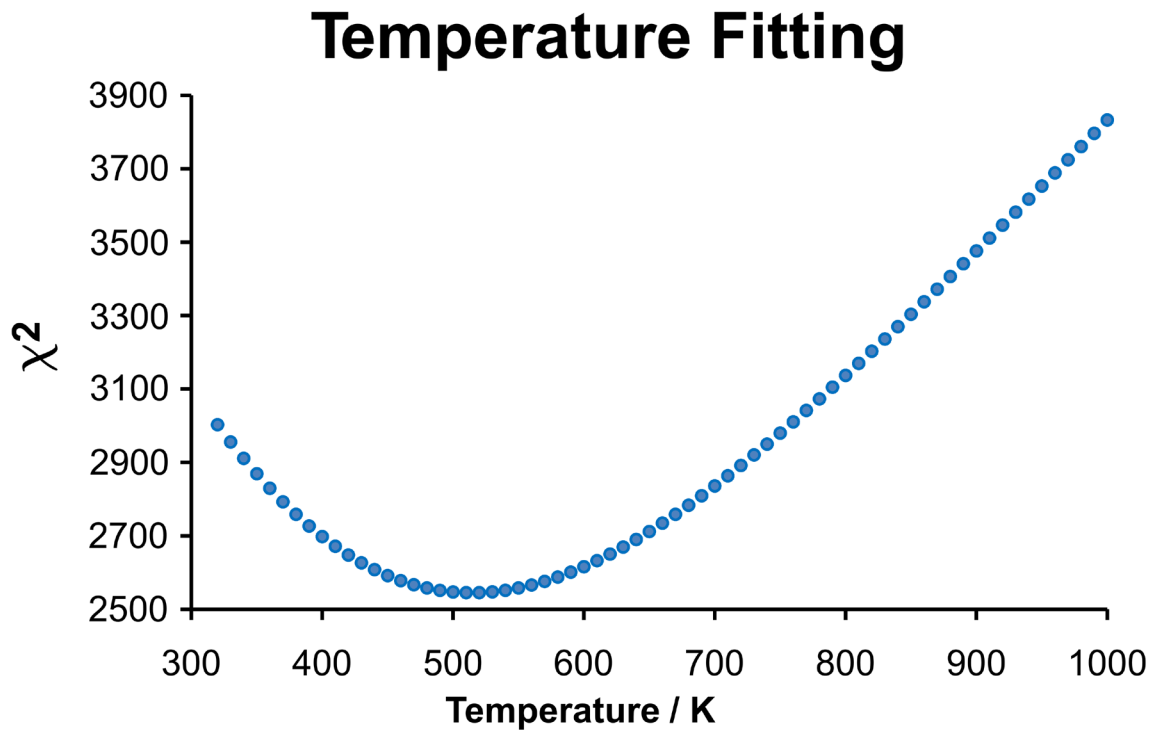


**Figure 4.6.** The temperature of the ground state molecules after laser desorption is obtained from the diffraction data. Here,  $\chi^2(T)$  obtained for the ground state of 6-nitro-BIPS shows a clear minimum at  $T = 510$  K.



# Chapter 5.

## Results

The results that were obtained in the UED lab at Caltech since 2005 are compiled in this chapter. The papers are ordered according to their content, rather than in chronological order. In Section 5.1 the first use of surface-assisted laser desorption in a pulsed electron diffraction experiment is reported.<sup>24</sup> The ground state structure of the thermally labile nucleobases uracil and guanine are determined using the newly developed UED4 apparatus. In Section 5.2, the use of laser desorption in a pump-probe electron diffraction experiment on the photochromic molecule 6-nitro-BIPS is described.<sup>25</sup> The structures of the photochemically generated species are solved using UED4. Section 5.3 contains a UED3 study on the organic molecule nitrobenzene.<sup>3</sup> The structural dynamics of molecular rearrangement leading to the observed NO release are discussed. Section 5.4 contains a UED3 study on indole, the chromophore of the amino acid tryptophan.<sup>5</sup> The involvement of a dark structure, formed on the picosecond time scale, is revealed in the nonradiative decay pathway of the initially excited state. In Section 5.5, the amino acid tryptophan itself was studied with UED4 in a pump-probe experiment. The rigid structural coordinates were determined for the intact ground state molecule, while the overall conformation of the amino acid moiety is too extensive to be resolved. Nonetheless, the sensitivity to structural change remains, as evident from the time-resolved diffraction data.

## 5.1 Structure of Isolated Biomolecules by Electron Diffraction-Laser Desorption: Uracil and Guanine<sup>†</sup>

### 5.1.1 Abstract

We report the structure of isolated biomolecules, uracil and guanine, demonstrating the capability of a newly developed electron diffraction apparatus augmented with surface-assisted IR laser desorption. This UED4 apparatus provides a pulsed, dense molecular beam, which is stable for many hours and possibly days. From the diffraction patterns, it is evident that the plume composition is chemically pure without detectable background from ions, fragmentation products, or molecular aggregates. The vibrational temperature deduced is indeed lower than the translational temperature of the plume indicating incomplete energy transfer on the time scale of desorption. The structures of uracil and guanine were refined at the deduced internal temperatures, and we compare the results with those predicted by density functional theory. Such experimental capability opens the door for many other studies of structure (and dynamics) of biomolecules.

### 5.1.2 Main Text

Ultrafast electron diffraction (UED) has been developed to study structural dynamics in isolated molecules in the gas phase with combined spatial and temporal resolutions.<sup>1,2,5</sup> The power of diffraction is in the ability of determining structures, and, when time-resolved, providing those of excited states and dark structures.<sup>7</sup> However, all

---

<sup>†</sup> Reproduced in part with permission from Gahlmann, A., Park, S. T. & Zewail, A. H. Structure of isolated biomolecules by electron diffraction-laser desorption: Uracil and guanine. *J. Amer. Chem. Soc.* **131**, 2806-2808 (2009). Copyright 2009 American Chemical Society.

forms of gas-phase electron diffraction (GED)<sup>28</sup> have been limited to molecular specimen, which develop an appreciable vapor pressure upon thermal heating. With conventional heating, GED studies of uracil<sup>119</sup>, cytosine,<sup>120</sup> and thymine<sup>121</sup> have been reported and, for all, transitional heating (below the decomposition threshold) had to be controlled. In general, large molecules, and in particular those of biological importance, tend to undergo thermal reactions and degradation, making them out of reach for structural and dynamic studies.

Given this limitation with respect to large biomolecules, it is of great value to develop an alternate methodology to deliver these systems into the gas phase in sufficient density, such that their structure as well as their intrinsic structural dynamics can be investigated with UED in the absence of a perturbing solvent. However, it is essential to achieve high density and sensitivity. In GED experiments, the typical average current is microampere ( $6 \times 10^{12}$  e/s), orders of magnitude larger than the current generated in UED3, picoampere ( $2 \times 10^7$  e/s). Thus to perform any successful UED experiment, given the difference in electron count, the molecular density has to be significantly higher, by at least four orders of magnitude, in the interaction region. With heating, such a density of molecules will not be reached without decomposition.

In this contribution, we report the first successful electron diffraction of biomolecules achieved with surface-assisted infrared laser desorption. The capability of this method in the newly constructed fourth-generation electron diffraction apparatus (UED4) is demonstrated by determining the structures of the RNA nucleobase, uracil, and the DNA nucleobase, guanine. The density is estimated to be higher than needed,

reaching  $\sim 10^{15}$  molecules/cm<sup>3</sup>, and the sensitivity is sufficient to determine the structures. The refined structures are compared to those obtained using density functional theory.

When interfacing the UED apparatus with a laser desorption system, it is critical that the vapor plume contains only the species of interest in its monomeric form, because the probing electron pulse does not discriminate between the different chemical species it interacts with. Any significant fragmentation or cluster formation of the sample would make the analysis of the resulting diffraction pattern complex. Surface-assisted laser desorption in the absence of matrix molecules or particles, but utilizing a strongly absorbing immobilized substrate,<sup>58</sup> avoids the presence of a chemical background in the vapor plume. Furthermore, because the molecular sample is largely transparent to the infrared (IR) light, the energy deposited into the internal degrees of freedom of the molecule is limited by the extent of energy transfer between the sample and the surface.<sup>46,49</sup> In fact, in mass spectrometry, with relatively low molecular densities ( $\sim 10^6$  molecules/shot),<sup>44</sup> far below what is needed here, surface-assisted laser desorption has been employed to vaporize polypeptides containing as many as 10 amino acids without significant degradation,<sup>122</sup> but most desorption studies have been made using matrices to deliver massive biomolecules into the gas phase in low density.<sup>44,45</sup>

The experimental setup of the UED4 apparatus is shown in a schematic representation in Figure 5.1, which highlights the newly designed sample-delivery assembly and the electron-pulse generation source. Briefly, two wheels in contact with each other, a felt brush wheel and a glassy carbon substrate wheel, were positioned inside a “scoop” with the brush wheel adjacent to the sample. Fine powder of uracil or guanine (Aldrich) was filled into this rectangular scoop and mounted inside the scattering

chamber. During the experiment, the scoop and the sample within were slowly translated, by a precision mechanical stage, toward the brush wheel, which then transferred small amounts of the powder onto the surface of the substrate wheel. The two wheels were rotated in the same direction to ensure that, through friction, a thin and uniform film of sample was continuously applied onto the substrate surface. A cylindrically focused IR laser (1064 nm, <2 ns pulse width, <200 mJ/cm<sup>2</sup>) was used to desorb the sample from the substrate. Because a single pulse of the desorption laser vaporized all the sample within its footprint (see Figure 5.2a), the substrate wheel was rotated at 80 rpm to ensure that a freshly covered surface was exposed to every laser pulse at a repetition rate of 1 kHz.

The gas plume was intersected by a pulsed electron beam (700 μm full width at half maximum, 200,000 electrons/pulse) at a distance of 750 μm from the substrate surface. The electron pulses were generated by front illumination of a magnesium target using an attenuated femtosecond ultraviolet (UV) laser (267 nm, 120 fs pulse width), accelerated to 60 keV, focused by a magnetic lens, and steered by electrostatic deflection. Temporal synchronization between the desorption IR laser pulses and the electron generating UV laser pulses was achieved using a digital delay generator. Diffraction patterns were recorded on an intensified CCD camera, and analyzed using home-built software. The stability of the plume is evident in the current ability to record diffraction for 13 hours. However, the machine is designed to operate continuously for several days, if needed. For structural refinement, starting geometries and vibrational force constants were obtained at the B3LYP/6-311G(d,p) level of theory using the Gaussian 98 software package.<sup>111</sup>

From the temporal and the spatial alignment between surface-desorbed molecules and the electron pulse, we can obtain the translational profile of the plume. Figure 5.2b gives the recorded scattering as a function of the delay time between the electron and the IR pulses. The scattering signal is maximum at a delay time of 0.6  $\mu\text{s}$  and when the electron pulse probes the plume 750  $\mu\text{m}$  above the surface. Using a simple model with a shifted Gaussian distribution of initial velocity, we obtained a translational temperature of  $\sim 4900$  K and a mean velocity of  $\sim 0.54$  mm/ $\mu\text{s}$ .<sup>‡</sup> The mean velocity value is larger than the speed of sound, being in the supersonic regime of plume expansion.<sup>51</sup>

In Figure 5.3, we depict the electron diffraction obtained for uracil using the surface-desorption method. Shown are the molecular scattering function,  $sM(s)$ , and the radial distribution,  $f(r)$ . From them, we determined the molecular structure; the methodology is described elsewhere.<sup>2</sup> Uracil, one of RNA bases, can exist in four different tautomers. Quantum chemical calculations predict that the diketo form is more stable than enol forms by at least 10 kcal/mol.<sup>123</sup> The calculations were substantiated by spectroscopic studies that only detected the diketo form.<sup>123,124</sup> Dimers and clusters can also form,<sup>125</sup> but they are less favorable at high-temperature and low-pressure conditions. Here, we considered both the lowest- and higher-energy tautomers for the recorded diffraction, using DFT calculations of the structures.

The experimental and theoretical (modified) molecular scattering functions in Figure 5.3a show a good agreement, with the quality of fit,  $R$ , of 0.0476, which is near

---

<sup>‡</sup> From the known fluences and heat capacities, the estimated temperature is found to be in the range calculated by thermodynamic consideration. After laser absorption, the temperature of the substrate is estimated to be  $\sim 6000$  K and for solid uracil (different heat capacity and mass) an upper value of  $\sim 5800$  K will be reached, if all energy is exchanged. We note that the melting temperature of uracil is 608 K, but the system, on such short time scales, transfers into the gas phase at the low pressure of the chamber ( $10^{-6}$  torr).

the optimum value of  $R = 0$ . The observed  $sM(s)$  and  $f(r)$  were analyzed and refined for the most stable diketo tautomer. A vibrational temperature of 1400 K was deduced from the best fit to the experimental diffraction pattern, which is less than the measured translational temperature (an incomplete energy exchange), explaining the abundance of intact molecular species on the microsecond time scale. It is to be noted that uracil is planar, even though it is not aromatic; conjugation of the C=O and C=C double bonds is reflected in the change of bond lengths shown in Figure 5.3.

Guanine, which is a base for both RNA and DNA, was the second molecular structure we studied. Many isomers can exist due to tautomerism as well as possible hydrogen presence on nitrogen atoms.<sup>126</sup> However, the keto forms are lowest in energy,<sup>127</sup> and the four most stable isomers were identified in a helium nanodroplet study.<sup>128</sup> Figure 5.4 depicts the diffraction data of guanine, which were analyzed for the G7K isomer, one of the stable keto forms. The electron diffraction patterns of the G9K form, which only differs by the hydrogen position, is very similar to the assumed G7K isomer and almost indistinguishable within our current sensitivity (see Figure 5.4b inset); thus, their relative fractions cannot be determined reliably at this stage. Experimental and theoretical modified molecular scattering functions in Figure 5.4a show a satisfactory agreement, with the quality of fit,  $R$ , of 0.0597, despite the one-tautomer assumption made. A vibrational temperature of 1600 K was deduced, again, based on the best fit of the diffraction pattern. Guanine is also a conjugated system; the single bonds are shorter than typical single-bond lengths, indicating that aromaticity is not totally lost.

Given the success of the electron diffraction-laser desorption studies reported here, UED4 is now poised to explore the dynamics of isolated biomolecules. As with

---

other UED studies, introducing an initial (clocking) pulse, as shown in Figure 5.1, will enable the study of structural dynamics to follow the molecular rearrangements in real time, from the picosecond to the microsecond regime.

## 5.2 Direct Determination of Structural Conformations of Photoswitchable Molecules by Laser Desorption–Electron Diffraction<sup>§</sup>

### 5.2.1 Abstract

Electron diffraction reveals the involvement of multiple structures in the complex photochemistry of the photoswitchable molecule, nitro-substituted 1,3,3-trimethylindolinobenzospiropyran. The spiropyran-to-merocyanine isomerization due to ring opening produces primarily the *cis-trans-cis* structure, while competing nonradiative pathways lead to other structures, the closed forms in their triplet and singlet ground states. After nanoseconds of reaction initiation, we determine the structures and the product yields of all present species to elucidate the intrinsic photochemistry of the isolated molecule itself. Because of its very low vapor pressure, the technique of electron diffraction by laser desorption was essential for obtaining the diffraction patterns of intact molecules, which would otherwise decompose at high temperatures.

### 5.2.2 Main Text

The reversible isomerization between the closed spiropyran (SP) and the open merocyanine (MC) forms of photoswitchable molecules, such as derivatives of 1,3,3-trimethylindolinobenzospiropyran (BIPS), have attracted considerable experimental and theoretical interest over the last decades. Because light of different wavelength can initiate both the forward and the reverse reaction in some BIPS derivatives, the

---

<sup>§</sup> Reproduced with permission from Gahlmann, A., Lee, I. R. & Zewail, A. H. Direct structural determination of conformations of photoswitchable molecules by laser desorption-electron diffraction. *Angew. Chem. Int. Ed.* **49**, 6524-6527 (2010). Copyright 2010 Wiley-VCH.

photochromic pair of isomers presents interesting opportunities in holographic data storage<sup>129</sup> and as molecular switches to control material properties and biological function.<sup>130</sup>

The closed form consists of an indoline and a chromene subunit joined together at the central spiro-carbon, with the two fused ring systems forming two perpendicular planes. Absorption of a UV photon leads to cleavage of the spiro-carbon–oxygen bond and to subsequent rearrangement of the two subunits to form the extended open form(s) connected by a central bridge segment consisting of three bonds, labeled  $\alpha\beta\gamma$ , as shown in Figure 5.5 and Figure 5.6. Due to the larger conjugated  $\pi$ -electron system, the open forms have a strong  $S_0 \rightarrow S_1$  absorption maximum that is red-shifted relative to the absorption of the closed form.

A large range of isomers is possible for the open forms, because each of the three ethylenic bonds can exhibit either the *cis* or the *trans* conformation. In addition, the involvement of a triplet state mechanism has been discussed extensively for nitro-substituted BIPS derivatives.<sup>131-137</sup> Thus, a priori,  $2 \cdot 2^3 = 16$  possible structures can exist for the open product(s). Quantum chemical calculations have shown that the isomers having the central bond in the *trans* configuration (designated TTT, CTT, TTC, CTC) are very similar in energy and are more stable than the *cis* isomers.<sup>138-140</sup>

In solution, time-resolved spectroscopic studies have concluded that the open photoproduct is formed on the picosecond time scale.<sup>141-146</sup> Even though a distribution to different isomers has been proposed,<sup>141,142,147,148</sup> the number and identity of species formed are still subject of discussion.<sup>135,144</sup> Because the time scales of product formation are heavily dependent on the nature of the solvent,<sup>134,144,146</sup> it is difficult to deduce the

molecular basis of the mechanism.<sup>132-136,142,149</sup> Using NMR, the TTC isomer, in rapid equilibrium with the TTT isomer, was identified as the thermally populated species of 6,8-dinitro-BIPS, which exists in its more stable open forms at room temperature;<sup>150</sup> similarly, the TTC and CTC isomers have been detected in the related compound spironaphthoxazine.<sup>151</sup> The TTT isomer of 6,8-dinitro-BIPS<sup>150</sup> and the TTC isomer of 6-nitro-8-bromo-BIPS<sup>152</sup> could be crystallized from acetone and water solutions, respectively, and identified using X-ray crystallography.

Here, we report our study of the molecule 6-nitro-BIPS using laser desorption–electron diffraction in order to determine the nascent product structures upon photoexcitation.<sup>24</sup> In this study, the diffraction is from isolated molecules made into a plume with no perturbations from a solvent. While ambiguities continue to exist regarding the competition among reaction pathways, the various product yields, and the transient structures involved in solution, complete structural determination of all species involved in the absence of a perturbing solvent sheds light on the intrinsic chemistry of the molecule itself.

With electron diffraction we are able to determine both ground state and product structures for excitation of 6-nitro-BIPS at 266 nm. For the ground state structure, the experimental and the theoretical molecular scattering function,  $sM(s)$ , together with the radial distribution,  $f(r)$ , are shown in Figure 5.7. Starting with a calculated structure of the ground state, we refined seven orthogonal structural parameters, as well as the internal temperature of the molecule (fitted value: 510 K), to achieve satisfactory agreement between the experimental data and the theoretical model.<sup>24</sup> The refined structural parameters are listed in Table 5.1 together with values obtained from density

functional theory (DFT) calculations; they have discrepancies of less than 0.056 Å and 0.33° for bond lengths and angles, respectively.

For studies of structural dynamics following UV excitation, we recorded time-resolved diffraction patterns at -100 and +100 ns. To identify the structures present and their abundance, the experimental frame-referenced  $\Delta sM(s)$  curve,<sup>2</sup> obtained by subtracting the reference diffraction pattern recorded at -100 ns from the diffraction pattern recorded at +100 ns, is fit with a linear combination of theoretically calculated  $sM(s)$  curves (see Experimental Section 5.2.3 for structure and temperature calculations). The coefficients of this linear combination report directly on the fractional abundance of a given species.

In the initial screening for product structures, we considered all possible open isomers (except the TCC structure, for which no stationary point could be located)<sup>139</sup> as well as the closed forms in their lowest singlet and triplet electronic states (see Table 5.2 and Table 5.3 for calculated structure parameters and frequencies, respectively). The quality of the fit is quantified in the  $\chi^2$ -value and the linear combinations are ranked in order of their ability to reproduce the experimental data. We found that fitting the data with less than two products is insufficient to produce a good fit. If three or more products are included, then ~70% of the product species tend to be in a closed form while ~30% are in an open form. Additionally, the linear combinations, which assign about equal abundance to the vibrationally hot ground state and to the closed form in its lowest triplet state, produce the best fits. Finally, the open structures, for which the central bridge segment is in the CTC or CTT conformation, are highly favored.

With the most plausible reaction products identified, we attempted to refine the product structures (with their temperatures constrained at calculated values) in each linear combination separately to further improve the quality of the fit. Table 5.4 shows the resulting ranking of linear combinations after the attempt at structural refinement in each case. Only three of the combinations allowed for the fitting of four and five orthogonal parameters in each structure, while the rest produced unphysical geometries after only fitting one or two orthogonal parameters. The three combinations differ only in the identity of the open form, while the fractions remain similar. The  $\chi^2$ -value of the combination including the CTC structure represents the global minimum (best fit) on the  $\chi^2$ -hypersurface for the indicated number of orthogonal parameters. We thus conclude that, based on the quality of the fits, the following species are produced in the gas phase: SP(S<sub>0</sub>) at 1164 K, SP(T<sub>1</sub>) at 843 K, and MC CTC(S<sub>0</sub>) at 1132 K.

Using these product species, Figure 5.8 displays the fitted  $\Delta sM(s)$  curve with the experimental data at the +100 ns time delay and the corresponding  $\Delta f(r)$  curve; also shown are the theoretical curves, where the temperatures of all species are held at the initial temperature of 510 K, thus isolating the difference signal due to structural rearrangement only. However, because electron diffraction is recording vibrationally-averaged structures and is therefore sensitive to temperature, it is necessary to constrain the temperature of the product species to calculated values, accounting for photon absorption, when refining structural parameters (see Experimental Section 5.2.3).

Regardless, the depletion of the first-, second-, and higher-order interatomic distances due to the ring opening and bond twisting manifest itself in the more prominent negative peaks in the  $\Delta f(r)$  curve. The refined structural parameters are listed in Table 5.5

and Table 5.6 together with values obtained from DFT calculations. The successful identification of the product structure among the many candidates demonstrates the ability of electron diffraction to solve a complex (nanometer-scale) molecular structure of low symmetry, even though the largest internuclear distances are beyond the present instrumental coherence length, which we estimate, given the different parameters involved in these experiments, to be  $\sim 6\text{-}7$  Å (88% visibility).<sup>4</sup>

The structural dynamics reported here support the involvement of a triplet state mechanism in the overall photochemistry of 6-nitro-BIPS, because we detect a closed form in the  $T_1$  state. However, the open CTC structure is detected in its electronic ground state and it is uncertain whether this product was formed through that triplet-state pathway or through a separate singlet-state pathway. Through theoretical means, the CTC structure has been found to be the first *trans* structure formed from the *cis* intermediate structure (CCC) after ring opening, due to the steric hindrance between the two methyl groups on the tetrahedral indoline carbon and the oxygen atom.<sup>139,140</sup> The quantum yield (30%) of the internally hot ground state determined here is comparable to the quantum yield (34%) found spectroscopically in trichloroethylene solution.<sup>149</sup> However, in our case, this species could have been formed either through internal conversion from the initially excited state, or through the thermal reverse reaction of ring-closing.

In a recent gas-phase study, 6-nitro-BIPS was also excited at 266 nm ( $S_0 \rightarrow S_3$ ) and the results of the picosecond kinetics were accounted for using a sequential mechanism involving four distinguishable species. The authors detected a long-lived ( $>500$  ps) photoproduct emerging with a formation time of 12 ps, which they argued to

represent an open form.<sup>153</sup> However, as shown in this section, three long-lived product structures in different states at 100 ns have been identified. Efforts to determine whether these species are already present on the picosecond time scale will be the subject of a future contribution using ultrafast electron diffraction.<sup>2</sup>

In summary, we have determined the isolated-molecule structure of photochromic 6-nitro-BIPS, as well as its major photoproducts after excitation at 266 nm. We were able to identify three different nascent species and their abundances: The closed form in the ground state (30%) and the lowest triplet state (39%) and the open form in the CTC conformation (31%) in the ground state. This study from electron diffraction combined with laser desorption elucidates the importance of identifying and following all major product structures, if the mechanism of this complex reaction in its entirety is to be established.

### 5.2.3 Experimental Section

Electron diffraction experiments were performed in our newly constructed UED4 apparatus.<sup>24</sup> Briefly, electron pulses ( $5 \cdot 10^7$  electrons/pulse, 60 keV, 1 kHz) were generated using the 266 nm output from a ns-Nd:YAG laser. The camera distance (26.716 cm) and the instrumental point spread function<sup>4</sup> (13.5 pixel FWHM) were calibrated by fitting the measured diffraction data of CO<sub>2</sub> gas to its known structural parameters.<sup>118</sup>

The 6-nitro-BIPS sample powder (Sigma Aldrich, CAS#: 1498-88-0) was ground with a mortar and pestle to reduce the particle size and loaded into our desorption source. During the course of the experiment, the fine powder was continuously transferred onto

the glassy carbon substrate by circular mechanical motion and subsequently desorbed into the gas phase by a second ns-Nd:YAG laser. Once vaporized, the sample was photoexcited at 266 nm using the frequency-tripled output from a Ti:Sapphire femtosecond laser system and subsequently interrogated by the electron pulses.

Structural analysis was conducted using home-built software, as described previously.<sup>2,5</sup> Theoretically calculated curves were obtained using the starting geometries and vibrational frequencies from density functional theory calculations at the B3LYP/6-311G(d,p) level using the Gaussian 98 suite,<sup>111</sup> and we calculated the internal temperature of the product species by considering the absorbed photon energy, the vibrational frequencies, and the difference in electronic energy relative to the ground state species. Refinement of the (nonlinear) structural parameters was conducted using the method of singular value decomposition.<sup>101</sup> Thus, the orthogonal structural parameters that are fitted during refinement are composed of linear combinations of the redundant internal coordinates that are used to initially define the geometry of the molecules.

## 5.3 Ultrafast Electron Diffraction: Structural Dynamics of Molecular Rearrangement in the NO Release from Nitrobenzene\*\*

### 5.3.1 Abstract

Nitro compounds release NO, NO<sub>2</sub>, and other species, but neither the structures during the reactions nor the time scales are known. Here, using ultrafast electron diffraction (UED), we provide our first study of the NO release from nitrobenzene. We determine the molecular pathways and the structures of transient species therein. It is observed, contrary to previous inferences, that nitric oxide and phenoxy radicals are formed dominantly and that the time scale of formation is  $8.8 \pm 2.2$  ps. The structure of the phenoxy radical is determined for the first time, and found to be quinoid-like. The mechanism proposed here involves a repulsive triplet state, following intramolecular rearrangement. This efficient generation of NO may have important implications for the control of by-products in drug delivery and other applications.

### 5.3.2 Introduction

Nitrobenzene, the prototypical member of a family of nitro compounds, is a common environmental pollutant<sup>154-157</sup> and a frequent ingredient in energetic explosives.<sup>158</sup> Elimination reaction pathways from nitrobenzene are those known to produce NO<sub>2</sub>, NO, and O radicals. The fragment nitric oxide (NO) is unique in that its mechanism of release may be relevant to the development of nitroaromatic NO donor drugs<sup>159,160</sup> important in the regulation and maintenance of physiologically vital

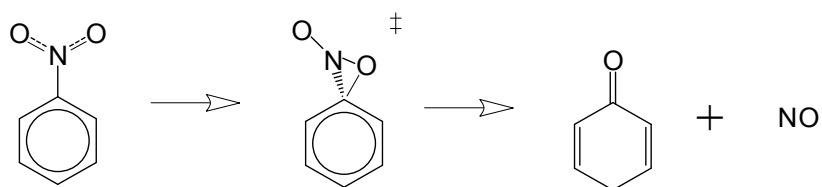
---

\*\* Reproduced in part with permission from He, Y. G., Gahlmann, A., Feenstra, J. S., Park, S. T. & Zewail, A. H. Ultrafast electron diffraction: Structural dynamics of molecular rearrangement in the NO release from nitrobenzene. *Chem. Asian J.* **1**, 56-63 (2006). Copyright 2006 Wiley-VCH.

functions.<sup>161-164</sup> Even in the apparently simple reaction of NO loss from nitrobenzene, ambiguities continue to exist regarding the competition among reaction pathways, the various product yields, and the transient structures involved. Furthermore, an intramolecular rearrangement may occur in the release of NO and only with complete structural determination can we directly establish the pathways involved.

The phenoxy radical, a resulting fragment of NO elimination from nitrobenzene, has been recognized as important in biological processes and combustion chemistry (see Refs. [165](#) and [166](#) and references therein) but its structure has not been determined. It has been the subject of both experimental and theoretical investigations, since it was observed as a reaction product in the vapor phase,<sup>167</sup> in solution,<sup>168</sup> and in a matrix.<sup>169</sup> The experimental information on phenoxy has been provided by resonance Raman,<sup>170-172</sup> IR spectroscopy,<sup>173,174</sup> and ESR hyperfine couplings,<sup>175-177</sup> which have elucidated that C–O has double bond character. Combined with the finding of a radical electron in the  $\pi$  ring system,<sup>176</sup> and the known chemical reactivity of the phenoxy radical, it was suggested that the ring of the phenoxy radical is quinoid-like. Theoretical studies largely agree; for reviews, see Refs. [178](#) and [179](#).

In this section, we report our first study of structural dynamics of the elimination reaction of nitrobenzene using ultrafast electron diffraction (UED) to directly determine transient structures. It is shown that the dominant pathway upon excitation is not that involving a single-bond rupture to produce NO<sub>2</sub> and phenyl radical, but instead is a pathway of intramolecular rearrangement involving bond breaking and bond making to yield NO and the phenoxy radical:



This UED study sheds new light on the significant and long-debated problem regarding the reactions of nitroaromatic compounds by providing evidence of a dominant pathway, contrary to spectroscopic observations.

### 5.3.3 Results

The diffraction pattern of nitrobenzene in the ground state was directly recorded in two dimensions. This pattern was radially averaged to give the one-dimensional molecular scattering function,  $sM(s)$ , of which the sinusoidal oscillations contain all contributions from each internuclear distance. Refined structures were obtained following the methodology we outlined in Refs. [1](#) and [2](#). The experimental and the refined theoretical modified radial distribution,  $f(r)$ , and the molecular scattering function,  $sM(s)$ , are shown in Figure 5.9. The refined structural parameters, including the rotational barrier height, are compared to those from previous experiments, as well as density functional theory (DFT) values, and listed in Table 5.7. They are in satisfactory agreement, with discrepancies within 0.02 Å and 1.5° for distances and angles, respectively. The exception is with the nitro torsional angle values ( $\phi$ ) reported by Domenicano et al.[180](#) and by Shishkov et al.[181](#) These are  $13.3 \pm 1.4^\circ$  and  $22.7^\circ$ , respectively, and are strongly dependent on temperature. In these studies only a single torsional angle was employed for the nitro group internal rotation. Using this approach,

our data gives a value of  $19.4^\circ$ . This value represents  $\langle|\phi|\rangle$  since, due to the symmetry of the molecule, positive and negative torsional angles are equivalent. Based on this mean deviation, and the potential function  $V_2 = RT/\pi\langle\phi\rangle^2$ , Domenicano et al. estimated the rotational barrier to be around  $4 \pm 1 \text{ kcal mol}^{-1}$ .<sup>180</sup>

Due to the low rotational barrier, the torsion of the nitro group was treated with explicit consideration of the large amplitude motion.<sup>182</sup> Thermal populations of internal rotational modes (with an angle binning of  $2.5^\circ$ ) were evaluated using the potential function,  $V = \frac{1}{2}V_0[1 - \cos(2\phi)]$ , with the contribution of each angle being population-averaged. The shrinkage effect and stretching anharmonicity were also incorporated.<sup>19</sup> This dynamic model fixes the torsional angle at  $0^\circ$  with the standard deviation of the distribution ( $\sigma$ ) defining the range of angles. From our data we obtain  $\sigma = 28.7^\circ$ . Our structural refinement based on the dynamic model puts the rotational barrier at  $3.1 \pm 0.4 \text{ kcal mol}^{-1}$ , in agreement with the values of  $2.9 \pm 0.2 \text{ kcal mol}^{-1}$  and  $3.3 \text{ kcal mol}^{-1}$  obtained from microwave<sup>183</sup> and Raman<sup>184</sup> studies, respectively.

For studies of structural dynamics during the course of the reaction, we recorded time-resolved diffraction patterns at different times, from  $-100$  to  $+100$  ps in one set of experiments, and from  $-100$  ps to  $+1$  ns in other sets of experiments. To identify the reaction channel(s) upon  $266.7 \text{ nm}$  excitation, the experimental and theoretical  $\Delta sM(s)$  and  $\Delta f(r)$  curves for energetically allowed channels (Figure 5.10), as well as their multiple combinations, were compared. Vibrational temperatures of each of the products were estimated using calculated vibrational frequencies and available energies. Mean

translational energy release and rotational energy partitioning were also taken into account.<sup>185</sup>

Figure 5.11 displays the comparison of the experimental  $\Delta f(r)$  curves with theory at the +1 ns time delay (reference at -100 ps). Theoretical structures that poorly matched the data were excluded. The experimental  $\Delta sM(s)$  and  $\Delta f(r)$  curves for NO<sub>2</sub> eliminations (with the ground and the excited states of the NO<sub>2</sub> fragment), and NO elimination are highlighted in Figure 5.12. Structural refinement attempted for these NO<sub>2</sub> channels resulted in unphysical structures. The best fit was obtained using  $\text{C}_6\text{H}_5\text{NO}_2 \rightarrow \text{C}_6\text{H}_5\text{O} + \text{NO}$  as the dominant reaction. Multicomponent fits (not shown) performed by floating the fraction of several channels also favored an exclusive NO elimination reaction. Similar results were also found at both +50 and +100 ps time delays. These results establish that the dominant reaction channel of nitrobenzene upon 266.7 nm excitation is NO elimination. With the reaction channel identified, the structure of its corresponding product, the phenoxyl radical, was then refined. Figure 5.13 shows the experimental and the refined theoretical molecular scattering and radial distribution curves for the NO elimination reaction channel. The refined structural parameters are listed in Table 5.8 together with DFT values. The C–O bond length was found to be 1.232 Å. Aryl C–C bonds are 1.465, 1.382, and 1.420 Å at their primary, secondary, and tertiary positions (with respect to the O atom), giving the average value of 1.423 Å.

From the temporal frame-referenced diffraction data, the population of the product structures as a function of time was determined. Figure 5.14 displays the one-dimensional difference radial distribution curves from -100 to +100 ps. The curves clearly map out the reaction showing both negative peaks (blue regions), which

correspond to the loss of *old internuclear distances*, and positive peaks (red regions) corresponding to the formation of *new internuclear distances*. The curves retain the same features over time but simply increase in amplitude, indicating the growth in population of a common product structure. Figure 5.15 shows the growth of the product fraction with time. Nonlinear fitting, for a single step reaction, gives a rise time of  $8.8 \pm 2.2$  ps.

### 5.3.4 Discussion

#### 5.3.4.1 Previous Spectroscopic Studies

Spectroscopic characterization of nitrobenzene has been the subject of study for decades. The gas-phase UV absorption spectrum of nitrobenzene consists of three broad and structureless bands, centered at 280, 240, and 195 nm.<sup>186-189</sup> A much weaker absorption band at  $\sim 350$  nm was also observed.<sup>190</sup> Excitation to these states results in no observable fluorescence or phosphorescence. An early gas-phase study assigned the 240 nm band to be a charge transfer state from the phenyl ring to the -NO<sub>2</sub> moiety.<sup>186</sup> Similar conclusion has also been made by other experimental and theoretical investigations.<sup>191,192</sup> However, polarization spectroscopy indicates that the 240 nm band possesses a transition dipole moment that is mostly perpendicular to the molecular figure axis, while that of the 280 nm band was inferred to be parallel, providing contrary evidence to some previous spectroscopic and theoretical assignments.<sup>188,189</sup> The energy of the lowest triplet state in solution was deduced to be  $58 \text{ kcal mol}^{-1}$ .<sup>193</sup> The photophysical dynamics of nitrobenzene is fairly limited. The lifetime of the triplet upon  $\sim 366$  nm excitation in liquids was deduced to be  $\sim 1$  ns from measurement of ISC yield using photosensitization.<sup>194</sup> The lifetime of the lowest excited singlet state (S<sub>1</sub>) has been

measured to be 6 ps and that of presumably the lowest triplet state ( $T_1$ ) to be 400–900 ps depending on the solvent, with ISC yield of 0.8.<sup>195-197</sup>

Rich photochemistry of nitrobenzene has been reported in the vapor,<sup>187,198-206</sup> in solutions,<sup>207</sup> and in matrices.<sup>166,173,174</sup> Early discharge lamp studies detected  $\text{NO}_2$  and  $\text{C}_6\text{H}_5\text{NO}$  as photodissociation products,<sup>198,199</sup> suggesting two reaction processes:  $\text{C}_6\text{H}_5\text{NO}_2 \rightarrow \text{C}_6\text{H}_5 + \text{NO}_2$  and  $\text{C}_6\text{H}_5\text{NO}_2 \rightarrow \text{C}_6\text{H}_5\text{NO} + \text{O}$ . Flash photolysis has also led to  $\text{C}_5\text{H}_5$  as a product.<sup>200</sup> A number of mass spectrometry studies on the photodissociation of nitrobenzene using nanosecond laser pulses at various wavelengths have reported the co-existence of multiple dissociation channels, including those yielding  $\text{NO}_2$ , O, and NO.<sup>187,202,204-206</sup> Pyrolysis by pulsed IR laser heating found  $\text{C}_6\text{H}_5\text{--NO}_2$  bond-breaking as the primary reaction channel.<sup>201</sup> Another pyrolysis study using a single-pulse shock tube method identified the formation of phenoxy radical as a minor channel.<sup>203</sup>

In spite of these extensive photodissociation studies, the lack of ionization cross-section data has hindered the quantitative analysis of the branching ratio among the reaction channels. Based on ion signal intensity data, NO elimination had been considered a relatively minor reaction.<sup>187,204,205</sup> Assuming both  $\text{NO}_2$  and NO are produced in the ground state, Galloway et al. estimated the branching ratio between  $\text{NO}_2$  and NO elimination to range from 1.3 to 5.9 for excitation wavelengths between 280 and 222 nm, using ion signal intensities detected and the single photon ionization cross sections from ground states.<sup>187</sup> Because  $\text{NO}_2$  may form in the excited state,<sup>187,198</sup> the authors<sup>187</sup> noted that the branching ratio should be viewed as an upper limit; excited  $\text{NO}_2$  supposedly has a higher ionization efficiency.

### 5.3.4.2 Structural Dynamics from UED

The structural dynamics reported here using UED indicate the dominance at 266.7 nm of the NO elimination channel. Our result would be consistent with the spectroscopic analysis, only if NO<sub>2</sub> is generated in the excited state. However, its yield relative to NO must be very small; the apparent enhanced detection is due to the presumed higher cross section for ionization from excited NO<sub>2</sub> and the ratio of yield to NO becomes less than one. Also consistent with our findings are the results of infrared studies of photoexcited nitrobenzene in an Ar matrix,<sup>174</sup> which report the exclusive observation of a weakly bound C<sub>6</sub>H<sub>5</sub>O···NO complex, while those corresponding to O and NO<sub>2</sub> eliminations were not found. The refined structure of the phenoxyl radical with strong C–O double bond character (1.232 ± 0.064 Å) is in agreement with the value obtained from DFT (1.253 – 1.270 Å),<sup>179,208-210</sup> as well as CASSCF/6–311G(2*d,p*) (1.228 Å) calculations.<sup>178,179</sup> The refined C–C distances of the phenyl ring, in general, agree with previous high-level calculations: the C1–C2 (1.465 Å) and C2–C3 (1.382 Å) bond distances are close in value to typical C–C single and double bonds, respectively, while the C3–C4 bond distance (1.420 Å) shows partial double bond character, quinoid-like, resulting from the conjugation effect of the radical center.

The rise time for the formation of the phenoxyl and NO radicals from UED is 8.8 ps. At our wavelength, the molecule is excited to a high-energy state (see previous subsection), which, known from photophysical studies, does not fluoresce. Relative yields and product energy partitioning, measured between 320 and 240 nm, show no abrupt change over the range,<sup>185,187</sup> and, therefore, it is reasonable to deduce that excitation to states higher than S<sub>1</sub> results in an efficient internal conversion (IC), as we

reported elsewhere for related systems.<sup>2,211</sup> Moreover, vapor phase nitroaromatics in  $S_1$  ( $> 300$  nm) undergo highly efficient intersystem crossing (ISC).<sup>212</sup> In the liquid phase, the ISC yield of nitrobenzene has been determined to be greater than 0.80 and the lifetime of the  $S_1$  state to be 6 ps at 320 nm.<sup>195,213</sup> This ultrafast ISC can be rationalized by the proximity effect<sup>214</sup> and efficient one-center overlap between  $S_1$  ( $n\pi^*$ ) and  $T_1$  ( $\pi\pi^*$ ).<sup>215</sup> Accordingly, the rise time of 8.8 ps covers both the rates of ISC and the triplet state reaction yielding NO and phenoxy radicals (see Figure 5.16). Using the calculation of the barrier (see below) to release NO from  $T_1$ , the statistical time constant for the formation of products is  $\sim 1$  ns. However, considering a directed motion involving only “local” modes the reaction time becomes  $\sim 1$  ps.

In order to examine the nature of potential surfaces and the reaction rates, we performed DFT calculations of the likely nuclear motions for the rearrangement-elimination process on both  $T_1$  and  $S_0$  (Figure 5.17);<sup>††</sup> The  $S_0$  surface has been invoked to describe pyrolysis reactions,<sup>201,203,216-218</sup> but the results do not agree with the photochemical behavior of nitrobenzene.<sup>185,216</sup> For comparison, the  $C_6H_5 + NO_2$  pathway is also presented in Figure 5.17. The  $T_1$  state is mainly of  $^3\pi\pi^*$  character localized on the nitro group. Thus, direct C–N bond scission adiabatically correlates with excited  $NO_2$  ( $1^2B_2$ ) and ground state phenyl radical. This is affirmed by our calculation, which predicts that no direct pathway leading to phenyl radical +  $NO_2$  ( $1^2A_1$ ) exists on the  $T_1$  surface.

---

<sup>††</sup> The zero-point energy is not incorporated in the calculation of potential energy curves along the intrinsic reaction coordinate. For open shell DFT calculations the errors may result in this case in underestimation of some product energies by  $\sim 10$  kcal mol<sup>-1</sup> or less. The energy of  $T_1$  in THF is 58 kcal mol<sup>-1</sup> from Ref. 193. The experimental changes of enthalpy at 0 K are  $21 \pm 1$ ,  $76 \pm 2$ , and  $103 \pm 2$  kcal mol<sup>-1</sup> for NO,  $NO_2$  ( $1^2A_1$ ), and  $NO_2$  ( $1^2B_2$ ) channels, respectively, which are evaluated from NIST heat of formation at 298 K and corrected to 0 K values using DFT frequencies. The obtained DFT values are 55, 15, 66, and 93 kcal mol<sup>-1</sup>, respectively.  $T_1$  values are 57 and 66 kcal mol<sup>-1</sup> from CASSCF and MCQDPT, respectively, and 55, 52, and 58 kcal mol<sup>-1</sup> from Refs. 192 and 196, respectively.

Furthermore, NO<sub>2</sub> ( $1^2B_2$ ) elimination involves the surmounting of a high barrier (~45 kcal/mol). These findings are consistent with the negligible contribution of the NO<sub>2</sub> elimination channel in our data, and also with the high yield of NO<sub>2</sub> ion signal reported previously by Galloway et al.<sup>187,198</sup> The loose character of the C–N cleavage transition state explains the small relative translation energy partitioning into the fragments and the yield increase with photon energy.<sup>187</sup> The production of excited NO<sub>2</sub> has been seen in the photodissociation of nitromethane at 193 nm.<sup>219,220</sup>

In contrast to the dissociation producing NO<sub>2</sub> ( $1^2B_2$ ), NO elimination on T<sub>1</sub> involves a lower energy barrier (~25 kcal/mol) and a large exothermic energy change due to the stability of the phenoxy radical. This relatively low barrier explains its dominance over the other channels. Since phenyl nitrite, the NO elimination intermediate structure on S<sub>0</sub>, is not stable on the T<sub>1</sub> surface, the exit channel from the TS is direct and efficiently results in phenoxy and NO radicals. The exit channel barrier is rather high (2.64 eV), consistent with the product energy partitioning reported from multiphoton ionization (MPI) and laser induced fluorescence (LIF) studies<sup>185,217,221</sup> of the NO product (*translational energy* = 1.1, 0.86, and 0.56 eV at 226, 240, and 280 nm excitation, respectively, and *rotational energy* = 0.32 and 0.20 eV at 226 and 280 nm excitation, respectively).<sup>185</sup> In an orbital valence bond description, the  $^3\pi\pi^*$  excitation generates an unpaired electron on each oxygen atom. Rotation of the nitro moiety then results in favorable overlap of the nonbonding orbital of the O atom (in the plane of NO<sub>2</sub>) with the adjacent  $\pi$  orbital of the aromatic ring, and forms the pseudo-three-membered ring. The R–N–O bonds with weakened  $\pi$  bonding ( $^3\pi\pi^*$ ) are severed as the new C–O bond is formed.

### 5.3.5 Conclusion

Structural dynamics obtained directly with UED reveal that NO release in 8.8 ps involves intramolecular rearrangement and is the dominant elimination reaction pathway. The structure of transient phenoxy radical was determined, and, with the aid of theory, the reaction pathway is suggested to involve the lowest triplet potential energy surface. A quantitative determination of the time-dependent populations of individual product species was obtained by resolving their transient structures. This advantage, absent in previous spectroscopic studies, dispels the uncertainty regarding the reaction mechanism. Compared to pyrolysis on the ground state, which leads to various byproducts, the dominance of NO release on the triplet surface may be utilized in designing an effective NO delivering drugs with minimized side reactions (NO<sub>2</sub> release, for example). It may also assist in studies of atmospheric nitro-aromatics.<sup>221</sup>

### 5.3.6 Experimental Section

A detailed description of the UED3 apparatus and data analysis has been given in previous publications.<sup>1,2</sup> Briefly, ultrashort laser pulses of 120 fs at 800 nm were frequency-tripled. The resulting UV light (450 μJ/pulse) was split into two beam paths. The pump beam (~93% of the total energy, time delayed using a translation stage) was focused to a size of ~400 μm in diameter and directed into the scattering chamber to initiate the reaction. The weaker beam (~7% of the total energy) was attenuated, focused and directed onto a back-illuminated silver-coated cathode to yield ultrashort electron pulses via the photoelectric effect. The electron pulses were accelerated at 30 keV ( $\lambda_{\text{de Broglie}} = 0.067 \text{ \AA}$ ), to form a beam with a size of ~370 μm FWHM and were then

directed through the molecular beam. Zero-of-time was established via maximizing the lensing effect,<sup>16,65</sup> using 1,3-butadiene.

For the present study, two separate experiments were performed: A full series of time-resolved diffraction patterns was obtained to determine the reaction dynamics ( $3.1 \times 10^4$  electrons/pulse, 5 ps pulse width). Another series of patterns was also taken using more electrons per pulse and fewer time points (data collected at four time points) to determine the structure of the transient species ( $8.8 \times 10^4$  electrons/pulse, 11 ps pulse width). The temperature was increased progressively from the sample reservoir through the manifold to the needle tip, from 433 to 493 K, in order to avoid condensation. The sample vapor enters the chamber through a 180  $\mu\text{m}$  aperture via effusive expansion to form a molecular beam with an estimated FWHM of  $\sim 325$   $\mu\text{m}$  at the interaction region. Nitrobenzene (>99%) was purchased from Aldrich and used without further purification.

For the study of transient structures, diffraction patterns were recorded at different time delays between initiating laser pulse and electron pulse. Temporal frame-referenced data were then generated by subtracting the reference diffraction pattern recorded before time-zero ( $t_{ref} = -100$  ps) from patterns obtained at all other time delays.

The starting geometries for structural analysis were obtained by quantum chemical calculations using DFT at the B3LYP/6-311G(d,p) level (Gaussian 98 suite).<sup>111</sup> Structural analysis was conducted on home-built software using the methodology previously described.<sup>2</sup>

## 5.4 Ultrafast Electron Diffraction Reveals Dark Structures of the Biological Chromophore Indole<sup>‡‡</sup>

### 5.4.1 Abstract

Ultrafast electron diffraction of the tryptophan chromophore (indole) reveals the involvement of dark structures in the nonradiative pathways of the isolated molecule. Such dark structures have to be part of the understanding of biological chromophore stability.

### 5.4.2 Main Text

Ultraviolet (UV) photodamage of biological chromophores, such as nucleic acid bases and amino acids, is critically controlled by the relaxation pathways following the initial excitation.<sup>222-233</sup> Photostability as a concept involves “dark structures”,<sup>7</sup> which undergo photophysical and/or photochemical pathways.<sup>234</sup> Of major relevance is the time scale of structural change, since long-lived species would not be desirable for the photostability. Hence, it is important to identify the photophysical (intersystem crossing (ISC) and internal conversion (IC)) and photochemical (e.g., Hydrogen (H) atom abstraction) processes involved, and the associated structural transformations. These structures are not amenable to detection by conventional optical probing methods. Here, we report our first Ultrafast Electron Diffraction (UED) study of the structural dynamics of indole, the UV chromophore of the amino acid tryptophan.

---

<sup>‡‡</sup> Reproduced in part with permission from Park, S. T., Gahlmann, A., He, Y., Feenstra, J. S. & Zewail, A. H. Ultrafast electron diffraction reveals dark structures of the biological chromophore indole. *Angew. Chem. Int. Ed.* **47**, 9496-9499 (2008). Copyright 2008 Wiley-VCH.

Being an important fluorescence probe in protein studies,<sup>235</sup> tryptophan has been the subject of many spectroscopic investigations. The chromophore indole has complicated excited-state interactions, and the photophysics and photochemistry vary depending on the excess energy. In the isolated molecule, the fluorescence quantum yield and lifetime on the nanosecond time scale were studied, when the molecule was excited around the origin of the first excited state (283.78 nm).<sup>236</sup> When excited at shorter wavelengths (below 271 nm), broad and structureless features in the electronic spectrum suggest the onset of an ultrafast nonradiative process of unknown nature.<sup>237-242</sup> Using time-resolved photoelectron spectroscopy, this ultrafast process was not observed, possibly due to cross-section consideration.<sup>243</sup> However, at higher energies the H-atom loss channel was observed at 193/248 nm<sup>244</sup> and below 260 nm.<sup>245</sup> The theoretical calculations of conical intersections between the singlet excited states and the  $^1\pi\sigma^*$  repulsive state<sup>246-248</sup> have in fact predicted such behavior.

With UED, as detailed in the experimental section, we are able to determine both ground- and excited-state structures and obtain the temporal behavior for excitation of indole at 267 nm. For the ground-state structure (see Figure 5.18 for atomic numbering), the experimental and the theoretical molecular scattering function,  $sM(s)$ , together with the radial distributions,  $f(r)$ , are shown in Figure 5.19. The refined structural parameters are listed in Table 5.9, together with values obtained from density functional theory (DFT) calculations. The satisfactory agreement between experiment and theory gives the refined structural parameters, which were found to have discrepancies at most within 0.007 Å and 0.1° for bond lengths and angles, respectively.

The ground-state of indole clearly exhibits some aromatic character in both the six- and five-membered rings. The C-C and the C-N bond lengths were determined with the values given in Figure 5.19; they all are in the range of 1.376 to 1.438 Å. However, the six-membered ring shows a slight “quinoid” character with elongated bond lengths of C3-C4 and C6-C1. The structure of the five-membered ring is very similar to that of pyrrole, except for the shared bond C6-C1, which is somewhat stretched. The aromaticity in the five-membered ring is maintained via conjugated  $\pi$  orbitals with the six-membered ring. This delocalization of  $\pi$  electrons results in the slight quinoid character of the six-membered ring.

For studies of structural dynamics following UV excitation, we recorded time-resolved diffraction patterns at different times, from  $-100$  ps to  $+1$  ns. The experimental frame-referenced  $\Delta sM(s)$  curves are compared to the theoretical ones for the possible structures involved (see Figure 5.20 and Figure 5.21). Theoretical structures of the  $L_b$ ,  $L_a$ ,  $T_2$ , *hot*  $S_0$  state and photoproducts (H-atom loss) are excluded on our time scale, because of the relatively poorer fits. The best fit was obtained using the structure of the  $T_1$  state as the product (Figure 5.20d). We also performed multicomponent fits by floating the fraction of several channels at once. In this way, the  $T_1$  structure was exclusively favored at all time points.

With the major reaction channel identified, the structure was then refined (listed in Table 5.10 and shown in Figure 5.22). Figure 3.2a displays the experimental product-only  $f(r)$  curve with the theory at the  $+100$  ps time delay (frame referenced at  $-100$  ps). The  $\pi\pi^*$  character of the  $T_1$  state is readily seen from the broken aromaticity, which results in distinctly alternating single and double bonds. From the temporal frame-

referenced diffraction data, the population of this product structure as a function of time was determined, and the result for the temporal change of the fraction is shown in Figure 3.2b. A nonlinear fit to an exponential function, for a single-step process, gives a rise time of  $6.3 \pm 1.1$  ps.

The structural dynamics following 267 nm excitation thus indicate that the triplet-state channel is significant in the depopulation of the initial structure. The previous spectroscopic studies on indole and substituted indoles, which reported a complete loss of vibronic structure above the  $S_1$  origin,<sup>237-242</sup> a feature reflective of a short-lived species at this energy,<sup>240,249</sup> can now be understood in relation to our findings. Of particular interest to the present study are the reported drop-off of the fluorescence yield at  $\sim 900$   $\text{cm}^{-1}$  above the origin of 3-methylindole, which has been attributed to an accelerated rate of ISC,<sup>238</sup> and the broad band of the NH stretching mode in the  $S_1$  state,<sup>249</sup> which suggests a longer than 3 ps lifetime at an excess energy ( $3478$   $\text{cm}^{-1}$  above  $S_1$ ) comparable to ours ( $\sim 5000$   $\text{cm}^{-1}$  including thermal energy; energy redistribution lowers this value for the coordinate of interest).

The rise time of 6.3 ps for the triplet state, determined by UED, may appear rather short given the fact that ISC, in this case of 267 nm excitation, is between  $\pi\pi^*$  singlet and triplet states. However, this symmetry rule<sup>215</sup> is normally applicable for a planar geometry and, when nonplanar distortions are involved, vibronic couplings must be included.<sup>250</sup> It has been shown in the case of cytosine that significant spin-orbit coupling, and consequently efficient ISC, can occur provided the  $^1\pi\pi^*$  and  $^3\pi\pi^*$  states cross at a nonplanar geometry.<sup>251</sup>

In order to test such a conjecture for indole, we carried out calculations at the CASSCF(12,11)/6-311G(d,p) level and found that the  $T_2$  ( $^3\pi\pi^*$ ) state of indole possesses a nonplanar equilibrium geometry. Furthermore,  $T_2$  ( $^3\pi\pi^*$ ) crosses  $S_1$  at  $\sim 828$   $\text{cm}^{-1}$  above the  $S_1$  origin with a quasi-nonplanar geometry at the point of crossing. The proximity of the crossing point to the  $S_1$  energy minimum enhances the Franck-Condon overlap,<sup>252,253</sup> resulting in ultrafast ISC. It should be noted that the  $L_a$  and  $L_b$  states are heavily mixed, but at our wavelength the contribution of the  $L_a$  ( $S_2$ ) state seems to be larger than that of  $L_b$  ( $S_1$ ).<sup>254</sup> We observe the final structure in the  $T_1$  state in 6.3 ps, which suggests that  $T_2$  and  $T_1$  mixing/conversion is very efficient. Future experiments with polarized photoselection<sup>255</sup> would address such a state mixing effect on UED.<sup>256,257</sup>

In Figure 5.24, we summarize the experimental and theoretical findings on the indicated potential energy curves for indole. In this picture, the  $S_1$  and  $T_2$  states cross right above the  $S_1$  origin, whereas singlet and triplet  $\pi\pi^*$  states cross with the  $\pi\sigma^*$ ,<sup>246-248</sup> which leads to H-atom loss at higher energies. On our time scale, for the 267 nm excitation, it can thus be concluded that the involvement of the repulsive  $^1\pi\sigma^*$  state is minor. Above the  $S_1/{}^1\pi\sigma^*$  crossing, which has been observed to be at  $\sim 260$  nm,<sup>245</sup> a competition between ISC to the triplet manifold and IC to the  $^1\pi\sigma^*$  state would take place, perhaps with the latter dominating at high energies. The long-lived  $T_1$  state can also lose an H-atom over a shallow reaction barrier but on a longer time scale. The slow component of H-atom loss, observed at 248 nm in the mass spectrometry study,<sup>244</sup> may accordingly originate from the  $T_1$  state, because the ground-state reaction would be too slow to be observed.

In conclusion, the structural dynamics reported here for the tryptophan chromophore (indole) using ultrafast electron diffraction reveals the involvement of triplet state(s) in the nonradiative pathway of excited states. The product, excited triplet, has a broken aromatic structure, whereas the ground-state structure was determined to have aromaticity both for the six- and five-membered rings, with a slight “quinoid” character; the C-C and the C-N bond distances were thus determined and they are in the range from 1.376 to 1.438 Å. The rate of product formation is  $1.6 \times 10^{11} \text{ s}^{-1}$ , which accounts for the broad spectra observed in the excited state. This perspective from the UED study on the photophysics and photochemistry of indole emphasizes the direct role of intermediate dark structures in the overall relaxation pathways. Partial population of these states has to be taken very seriously in addressing photostability of biological chromophores. Moreover, given the involvement of reactive triplets, the solvent effect, especially water, will have to be integrated into any picture of the dynamics and stability.

### 5.4.3 Experimental Section

A detailed description of the UED3 apparatus and data analysis has been given in previous publications.<sup>2</sup> Briefly, ultrashort laser pulses (120 fs) at 800 nm were frequency tripled to generate the UV light (450 μJ/pulse), which was then split into two beam paths. The pump beam (~93 % of the total energy) was time delayed using a translation stage, and was directed into the scattering chamber to initiate the reaction. The weaker beam (~7% of the total energy) was attenuated, focused and directed onto a back-illuminated silver-coated cathode to generate the ultrashort electron pulses ( $2.5 \times 10^4$  electrons/pulse at 30 keV) via the photoelectric effect. An effusive beam of indole was introduced into the

chamber via our newly implemented, air-heated inlet system at 543 K. Indole (>99%) was purchased from Aldrich and used without further purification.

The starting geometries for structural analysis were obtained from quantum chemical calculations using approximated singles and doubles coupled-cluster (CC2) method with the aug-cc-pVTZ basis set, and density functional theory calculations at the B3LYP/6-311G(d,p) level using Gaussian 98 suite.<sup>111</sup> Structural analysis was conducted using home-built software, following the methodology described previously.<sup>2</sup> We have also implemented the redundant-internal-coordinate<sup>105,106</sup> system and the correlation-elimination method<sup>101</sup> by near-singularity removal in our UED analysis.

## 5.5 L-Tryptophan

The UED4 studies on the photochemical reaction of isolated tryptophan have not been published at the time of this writing. Therefore, only a brief description of the first results is given here. A full account of this work will be the subject of a forthcoming publication.

### 5.5.1 Ground State Structure

Tryptophan is an essential amino acid having the indole chromophore as its side chain. Structurally, this molecule can be separated into a rigid portion, the indole moiety, and a floppy portion, the amino acid moiety, which contains three dihedral angles as shown in Figure 5.25a. Tryptophan is therefore an excellent case example to assess the capabilities of time-resolved electron diffraction in the presence of considerable conformational heterogeneity across the gas-phase molecular ensemble.

As was shown in the case of nitrobenzene (see Section 5.3), large amplitude torsional motion about a dihedral angle with a low rotational barrier can be treated explicitly.<sup>182</sup> Because the potential function for the torsional mode of the symmetric nitrobenzene molecule could be reasonably approximated as  $V = \frac{1}{2}V_0[1 - \cos(2\phi)]$ , the thermal populations of internal rotational modes could be evaluated straightforwardly and the contribution of each angle could be population-averaged over the entire gas-phase ensemble. This procedure, which is often referred to as the dynamic model,<sup>120,182,258,259</sup> allowed for the refinement of the parameter  $V_0$ , to obtain an energetic barrier height of  $3.1 \pm 0.4 \text{ kcal mol}^{-1}$ , in good agreement with values obtained spectroscopically.<sup>183,184</sup>

In the case of tryptophan, the application of the dynamic model is more complex, because the torsional motions about the three dihedral angles cannot be decoupled from each other, and because the resulting three-dimensional potential energy (PE) hypersurface can no longer be approximated by a simple analytical function. Furthermore, quantum chemical calculations revealed that the (upper bound) barriers to internal rotations between the numerous PE minima are  $\sim 4.5 - 10 \text{ kcal mol}^{-1}$ , as shown in Figure 5.25b,c. At the high internal temperature of 1000 K, the amino acid moiety can therefore readily sample a large region of the conformational space, as shown in the Boltzmann-weighted thermal population contours in Figure 5.25d,e.

Conventionally, the UED methodology (as see Section 4.3) always begins with the calculation of the minimum energy conformation of the molecular structure. Once this structure has been found, the curvature of the PE surface is calculated in the immediate vicinity of the PE minimum to obtain the Cartesian force field (Hessian calculation). Diagonalizing the Hessian matrix yields the  $3N - 6$  normal modes of vibration, which are then projected onto a user-defined redundant internal coordinate basis and the rms amplitudes of vibration are calculated between each internuclear pair, assuming each normal mode is a harmonic oscillator.

From the quantum chemical calculation results presented in Figure 5.25, it is obvious that the harmonic approximation fails for the large amplitude torsional degrees of freedom in tryptophan, because of the presence of multiple and easily accessible PE wells. To construct an improved model of the conformational ensemble a multi-conformer model was tested.<sup>259</sup> For this purpose, the eleven putative PE wells were verified by full geometry optimization and frequency calculations at the

B3LYP/6-311G(*d, p*) level of theory, as shown in Figure 5.26. However, modeling the diffraction data with a Boltzmann-weighted linear combination (multi-conformer model) of the eleven minimum energy conformations did not result in an improved fit.

The large conformational heterogeneity due to torsional motion produces a significant distribution of certain affected internuclear distances, as shown in Figure 5.27. The resulting effect for electron diffraction is that the electron interferences originating from the affected internuclear pairs are washed out in the ensemble-averaged diffraction pattern, i.e., sine waves of different frequencies (different  $r_{ij}$ ) are incoherently added in the detection plane and the visibility of the otherwise sharp interference fringes becomes a contribution to the monotonous background intensity, especially at higher scattering angles. To quantify this effect, we decomposed the theoretical model function (cf. Equations 2.21 and 2.23),

$$sM(s)^{Theory} \propto \sum_i \sum_{j \neq i} \exp\left(-\frac{1}{2} l_{ij}^2 s^2\right) \frac{\sin(sr_{ij})}{r_{ij}}, \quad (5.1)$$

and only included terms in the distance range  $r_{ij} \in (0, r_{\max})$  and the amplitude range  $l_{ij} \in (0, l_{\max})$  and neglected terms outside these intervals. By scanning the two threshold terms,  $r_{\max}$  and  $l_{\max}$ , we quantified the earliest point, at which the quality of the fit by the partial model function,  $sM(s)_{Partial}^{Theory}(r_{\max}, l_{\max})$ , reaches the quality of the fit of the full model function,  $sM(s)_{Full}^{Theory}$ , i.e., when the quantity  $\chi_{Full}^2 / \chi_{Partial}^2(r_{\max}, l_{\max})$  reaches its asymptotic value of unity. As shown in Figure 5.28a, that point is clearly identified by  $r_{\max} = 4.8 \text{ \AA}$  and  $l_{\max} = 0.2 \text{ \AA}$ . Detailed inspection of the included terms in this range revealed that all internuclear distances within the indole moiety are included, but within

the amino acid moiety only the first- and second-order bond distances were present. The excluded terms therefore contained the information on the dihedral conformations of the amino acid moiety. Plotting  $sM(s)_{Full}^{Theory}$  and the included and excluded terms of  $sM(s)_{Partial}^{Theory}(r_{max} = 4.8\text{\AA}, l_{max} 0.2\text{\AA})$  together with the experimental data, as shown in Figure 5.28b, illustrates that the electron diffraction data at  $s > 6 \text{\AA}^{-1}$  carries no information about the conformation of the amino acid moiety. In addition, the fact the our quality of fit was unaffected by the inclusion of 11 conformers in our model, instead of only one conformer, demonstrates that the electron diffraction data has limited sensitivity to conformations even in the low  $s$  region, where the majority of the signal is still dominated by interference terms corresponding to first- and second-order bond distances and distances corresponding to rigid portions of the molecule. We can therefore conclude that the shallowness to the PE surface with respect to the three torsional degrees of freedom in the amino acid moiety of tryptophan precludes electron diffraction, with its current signal-to-noise levels, to solve the complete structure of tryptophan at 1000 K due to significant conformation heterogeneity across the molecular ensemble.

Due to the shallowness of the PE minima, those internuclear distances that do not contribute significantly to the diffraction signal can be readily identified by quantum chemical calculations and a reduced internal coordinate set can be used to fit the more rigid part of the molecular structure. However, because experimental data cannot be decomposed into its component terms, any structural refinement henceforth must include all terms in the theoretical model function, i.e.,  $sM(s)_{Full}^{Theory}$ , and must be carried out under the assumption that the refinement of “rigid” internal coordinates is unaffected by the

small scattering contributions of “floppy” parts of the molecule at low  $s$ . In the case of tryptophan, our quantum chemical calculations indeed showed that, for all eleven identified conformers, the rigid parts within the indole moiety are identical to within 0.0025 Å for direct bond lengths, 0.55° for bond angles, and 0.65° for dihedral angles, providing further support for the validity of this assumption.

The experimental partial ground state structure of the tryptophan molecule was determined using the minimum energy structure and the harmonic rms amplitudes of the individual conformers. In all cases, the already excellent fit, produced by the DFT structures, could be improved slightly by fitting three orthogonal structural parameters. Subsequent refinement steps did not result in further improvements in the quality of the fit and refinement was therefore halted after three parameters were fitted. Notably, the singular value decomposition (SVD) routine chose predominantly linear combinations of bond lengths to be fitted, while bond angles and dihedral angles remained unaltered, i.e., the initial and fitted values of the angular degrees of freedom are the same within error bars. The refined structural coordinates for the  $(\Phi_1, \Phi_2, \Phi_3) = (80^\circ, 58^\circ, 229^\circ)$  conformer, which gave the overall best fit, are listed in Table 5.11 together with single conformer and conformer-averaged values obtained from DFT calculations (see also Figure 5.29). The corresponding fit of the experimental molecular scattering function,  $sM(s)$ , together with the radial distribution,  $f(r)$ , are shown in Figure 5.30.

### 5.5.2 Photochemical Reaction Dynamics

To identify the structural dynamics following UV excitation, we recorded time-resolved diffraction patterns at -100 and +100 ns. The experimental frame-referenced

$\Delta sM(s)$  curves were compared to the theoretical ones for a number of possible structures or linear combinations thereof. The coefficients of this linear combinations report directly on the fractional abundance of a given species. Even though the final results of the structural refinement and the determined mole fractions of the product species have not been fully obtained at the time of this writing, the diffraction data is able to clearly discriminate between fragmentation products, as shown in Figure 5.31. Thus, in spite of the only partially determined ground state structure of tryptophan, time-resolved electron diffraction remains sensitive to the breaking of chemical bonds and the subsequent loss of internuclear distances and is still able to investigate the structural dynamics of tryptophan after photoexcitation.

**Table 5.1.** Refined closed structure of ground-state 6-nitro-BIPS at 510 K

Bond Lengths	Refined Value		DFT	Bond Angles	Refined Value		DFT
	[a]	[b]	[c]		[a]	[b]	
C1-C2	1.512	± 0.003	1.520	C9-C1-C2	100.6	± 0.9	100.427
C2-C3	1.409	± 0.003	1.383	C1-C2-C7	109.1	± 0.4	108.801
C3-C4	1.427	± 0.003	1.402	C2-C7-N8	109.9	± 0.8	110.186
C4-C5	1.413	± 0.002	1.391	C7-N8-C9	108.5	± 0.5	108.736
C5-C6	1.418	± 0.003	1.400	N8-C9-C1	103.2	± 0.4	103.201
C6-C7	1.433	± 0.003	1.391	C3-C2-C7-C1	-10.5	± 0.2	-10.583
C7-N8	1.424	± 0.005	1.403	C6-C7-C2-N8	-7.5	± 0.5	-7.356
N8-C9	1.448	± 0.005	1.446	C4-C3-C2	119.4	± 0.2	119.245
C9-C10	1.503	± 0.002	1.500	C5-C4-C3	120.1	± 0.5	120.040
C10-C11	1.375	± 0.003	1.337	C6-C5-C4	121.2	± 0.4	121.223
C11-C12	1.471	± 0.003	1.452	C7-C6-C5	117.8	± 0.2	117.987
C12-C13	1.407	± 0.004	1.393	C1-C9-C10	115.8	± 0.2	115.738
C13-C14	1.405	± 0.003	1.389	N8-C9-O18	107.5	± 0.3	107.448
C14-C15	1.409	± 0.003	1.396	C10-C9-O18	111.2	± 0.3	111.275
C15-C16	1.396	± 0.003	1.385	C1-C9-O18	106.1	± 0.1	106.059
C16-C17	1.423	± 0.001	1.400	N8-C9-C10	112.4	± 0.3	112.442
C17-O18	1.380	± 0.004	1.344	C9-C10-C11	123.9	± 0.3	123.650
O18-C9	1.527	± 0.003	1.487	C10-C11-C12	121.6	± 0.4	121.411
C9-C1	1.604	± 0.004	1.586	C11-C12-C17	117.3	± 0.3	117.379
C2-C7	1.414	± 0.003	1.400	C12-C17-O18	121.8	± 0.3	122.055
C12-C17	1.426	± 0.003	1.410	C17-O18-C9	123.9	± 0.5	123.909
C1-C1a	1.540	± 0.005	1.546	C13-C12-C17-C11	-4.7	± 0.3	-4.498
C1-C1b	1.494	± 0.004	1.532	C16-C17-C12-O18	3.2	± 0.4	3.183
N8-C8a	1.472	± 0.005	1.453	C12-C13-C14	119.5	± 0.3	119.669
C14-N14a	1.412	± 0.007	1.468	C13-C14-C15	121.8	± 0.8	121.504
N14a-O14a1	1.255	± 0.008	1.226	C14-C15-C16	119.3	± 0.3	119.284
N14a-O14a2	1.254	± 0.008	1.226	C15-C16-C17	119.8	± 0.3	119.920
				C1a-C1-C2	108.6	± 0.3	108.599
				C1a-C1-C1b	109.5	± 0.2	109.535
				C1b-C1-C9	112.5	± 0.6	112.548
				C1a-C1-C9	110.9	± 0.3	110.765
				C1b-C1-C2	114.5	± 0.2	114.647
				C8a-N8-C7-C9	0.6	± 0.1	0.539
				N14a-C14-C13-C15	-0.17	± 0.04	-0.170
				O14a1-N14a-C14	117.8	± 0.4	117.750
				O14a2-N14a-C14-O14a1	-6.7	± 0.3	-6.766

*continued on next page*

<sup>[a]</sup> The error bars reported here are  $3\sigma$ .

<sup>[b]</sup> Theoretical structures were obtained using DFT at B3LYP/6-311G(*d, p*).

<sup>[c]</sup> If four atoms are listed, A1-A2-A3-A4, the angle is defined as

$$(A1-A2-A3)-(A1-A2-A4)$$

**Table 5.1.** Refined closed structure of ground-state 6-nitro-BIPS at 510 K (continued)

Dihedral Angles	Refined Value [a]	DFT [b]
C3-C4-C5-C6	-0.24 ± 0.02	-0.249
C4-C5-C6-C7	0.377 ± 0.002	0.379
C2-C3-C4-C5	0.11 ± 0.01	0.107
C5-C6-C7-C2	-0.39 ± 0.03	-0.378
C7-C2-C3-C4	-0.12 ± 0.03	-0.106
C6-C7-C2-C3	0.3 ± 0.1	0.249
C1-C2-C7-N8	-1.9 ± 0.2	-1.857
C3-C2-C7-N8	-179.3 ± 0.2	-179.252
C6-C7-C2-C1	177.6 ± 0.1	177.644
C2-C7-N8-C9	-17.7 ± 0.4	-17.701
C7-C2-C1-C9	18.2 ± 0.3	18.217
C2-C1-C9-N8	-27.6 ± 0.1	-27.479
C7-N8-C9-C1	28.3 ± 0.3	28.416
C1a-C1-C9-N8	87.1 ± 0.3	87.141
C1a-C1-C2-C7	-98.2 ± 0.4	-98.032
C1b-C1-C9-N8	-149.9 ± 0.3	-149.859
C1b-C1-C2-C7	139.0 ± 0.2	139.108
C8a-N8-C7-C2	-163.3 ± 0.3	-163.154
C8a-N8-C9-C1	174.1 ± 0.2	174.088
C10-C9-C1-C2	-150.8 ± 0.2	-150.735
C10-C9-N8-C7	153.7 ± 0.2	153.830
O18-C9-C1-C2	85.3 ± 0.4	85.351
O18-C9-N8-C7	-83.6 ± 0.2	-83.396
C11-C10-C9-C1	-124.3 ± 0.2	-124.337
C11-C10-C9-N8	117.4 ± 0.2	117.407
C17-O18-C9-C1	133.3 ± 0.2	133.271
C17-O18-C9-N8	-116.8 ± 0.2	-116.877
C9-O18-C17-C12	-6.31 ± 0.04	-6.334
C9-C10-C11-C12	-0.5 ± 0.1	-0.475
C10-C9-O18-C17	6.6 ± 0.1	6.614
C10-C11-C12-C17	1.4 ± 0.1	1.385
O18-C9-C10-C11	-3.2 ± 0.2	-3.187
O18-C17-C12-C11	1.97 ± 0.03	1.976
O18-C17-C12-C13	-178.82 ± 0.01	-178.817
C11-C12-C17-C16	-178.74 ± 0.02	-178.743
C13-C12-C17-C16	0.46 ± 0.01	0.464
C13-C14-C15-C16	0.080 ± 0.002	0.080
C14-C15-C16-C17	0.268 ± 0.002	0.268
C14-C13-C12-C17	-0.116 ± 0.004	-0.116
C15-C16-C17-C12	-0.543 ± 0.004	-0.543
C15-C14-C13-C12	-0.156 ± 0.002	-0.156
N14a-C14-C15-C16	179.988 ± 0.002	179.988
N14a-C14-C13-C12	179.936 ± 0.002	179.936
O14a1-N14a-C14-C15	-179.867 ± 0.002	-179.866
O14a1-N14a-C14-C13	0.044 ± 0.002	0.044
O14a2-N14a-C14-C15	0.123 ± 0.002	0.123
O14a2-N14a-C14-C13	-179.967 ± 0.002	-179.967

**Table 5.2.** Cartesian coordinates (in Å) of 6-nitro-BIPS isomers calculated at B3LYP/6-311G(*d, p*)

	SP S <sub>0</sub>			SP T <sub>1</sub>		
	x	y	z	x	y	z
C1	-2.063234	1.165916	-0.729070	-2.091323	1.189844	-0.702233
C2	-3.120870	0.086844	-0.560450	-3.138280	0.097996	-0.549910
C3	-4.177290	-0.279465	-1.374130	-4.204027	-0.252159	-1.358486
C4	-5.056650	-1.283234	-0.944550	-5.069518	-1.275380	-0.946816
C5	-4.863299	-1.897603	0.288790	-4.852939	-1.925150	0.264328
C6	-3.796065	-1.537223	1.119490	-3.776074	-1.581455	1.089570
C7	-2.934900	-0.537651	0.679200	-2.928897	-0.561803	0.667730
N8	-1.817881	0.004997	1.331910	-1.807066	-0.030576	1.320197
C9	-1.006619	0.704936	0.360260	-1.012350	0.703237	0.354533
C10	-0.188953	1.800108	0.979270	-0.198346	1.787327	0.998817
C11	1.148345	1.815951	0.981000	1.139100	1.794551	1.020115
C12	1.918532	0.743167	0.377900	1.910036	0.726884	0.408766
C13	3.310731	0.691802	0.393270	3.301567	0.661372	0.456256
C14	3.965603	-0.384383	-0.192120	3.965647	-0.402315	-0.156788
C15	3.260466	-1.425577	-0.797390	3.252403	-1.419569	-0.807681
C16	1.876498	-1.384919	-0.816690	1.870382	-1.356300	-0.855140
C17	1.201311	-0.303421	-0.237350	1.193896	-0.288984	-0.253531
O18	-0.140828	-0.303552	-0.307310	-0.152208	-0.267316	-0.357710
C8a	-1.193331	-0.691246	2.443720	-1.158857	-0.760424	2.396191
C1a	-2.684582	2.529267	-0.347540	-2.718100	2.535855	-0.270860
C1b	-1.458241	1.253795	-2.134280	-1.510047	1.325104	-2.113701
N14a	5.432952	-0.426510	-0.170800	5.359112	-0.497455	-0.050886
O14a1	6.023084	0.502198	0.370770	6.129503	0.496029	0.303315
O14a2	5.983863	-1.387682	-0.695390	6.094464	-1.267903	-0.807757
H3	-4.325982	0.197078	-2.337470	-4.370518	0.252009	-2.304731
H4	-5.884748	-1.582944	-1.575860	-5.904749	-1.562375	-1.574669
H5	-5.543804	-2.677157	0.612880	-5.522582	-2.719581	0.574777
H6	-3.649525	-2.033826	2.070780	-3.611676	-2.105613	2.023021
H10	-0.752449	2.587257	1.461640	-0.763275	2.569165	1.487847
H11	1.685957	2.631564	1.453490	1.674545	2.598744	1.514383
H13	3.891582	1.478403	0.856360	3.871504	1.436503	0.953594
H15	3.807263	-2.245531	-1.241320	3.789558	-2.233225	-1.277231
H16	1.296775	-2.174311	-1.277940	1.292965	-2.120409	-1.360086
H8a1	-0.365992	-0.091608	2.823690	-0.333110	-0.165683	2.787096
H8a2	-1.916174	-0.814278	3.252960	-1.868562	-0.922151	3.210305
H8a3	-0.813593	-1.680741	2.157630	-0.771967	-1.734218	2.068356
H1a1	-3.513696	2.744950	-1.024550	-3.561151	2.763101	-0.926645
H1a2	-3.080342	2.520274	0.670400	-3.095661	2.494669	0.753268
H1a3	-1.956558	3.340216	-0.437590	-1.999241	3.356085	-0.350740
H1b1	-2.214187	1.609386	-2.839170	-2.279766	1.696613	-2.795209
H1b2	-0.627805	1.965568	-2.156690	-0.684733	2.042974	-2.126843
H1b3	-1.095881	0.286194	-2.477540	-1.145615	0.371336	-2.491422

**Table 5.2.** Cartesian coordinates (in Å) of 6-nitro-BIPS isomers calculated at B3LYP/6-311G(*d, p*) (continued)

	CTC S <sub>0</sub>			CTC T <sub>1</sub>		
	x	y	x	y	x	y
C1	2.708315	1.193404	2.708315	1.193404	2.708315	1.193404
C2	3.929112	0.296766	3.929112	0.296766	3.929112	0.296766
C3	5.273866	0.593046	5.273866	0.593046	5.273866	0.593046
C4	6.204641	-0.451925	6.204641	-0.451925	6.204641	-0.451925
C5	5.782293	-1.771182	5.782293	-1.771182	5.782293	-1.771182
C6	4.428588	-2.083627	4.428588	-2.083627	4.428588	-2.083627
C7	3.523453	-1.029051	3.523453	-1.029051	3.523453	-1.029051
N8	2.116257	-1.071016	2.116257	-1.071016	2.116257	-1.071016
C9	1.572159	0.171199	1.572159	0.171199	1.572159	0.171199
C10	0.244614	0.571427	0.244614	0.571427	0.244614	0.571427
C11	-0.920605	-0.202441	-0.920605	-0.202441	-0.920605	-0.202441
C12	-2.239423	0.270520	-2.239423	0.270520	-2.239423	0.270520
C13	-3.281174	-0.690727	-3.281174	-0.690727	-3.281174	-0.690727
C14	-4.595158	-0.315961	-4.595158	-0.315961	-4.595158	-0.315961
C15	-4.974817	1.059575	-4.974817	1.059575	-4.974817	1.059575
C16	-4.021604	2.018925	-4.021604	2.018925	-4.021604	2.018925
C17	-2.592351	1.714618	-2.592351	1.714618	-2.592351	1.714618
O18	-1.749541	2.616268	-1.749541	2.616268	-1.749541	2.616268
C8a	1.400504	-2.298182	1.400504	-2.298182	1.400504	-2.298182
C1a	2.739058	2.155811	2.739058	2.155811	2.739058	2.155811
C1b	2.550091	1.990299	2.550091	1.990299	2.550091	1.990299
N14a	-5.629276	-1.337477	-5.629276	-1.337477	-5.629276	-1.337477
O14a1	-6.800243	-0.963751	-6.800243	-0.963751	-6.800243	-0.963751
O14a2	-5.281608	-2.515421	-5.281608	-2.515421	-5.281608	-2.515421
H3	5.606299	1.618003	5.606299	1.618003	5.606299	1.618003
H4	7.259561	-0.234641	7.259561	-0.234641	7.259561	-0.234641
H5	6.511401	-2.572869	6.511401	-2.572869	6.511401	-2.572869
H6	4.114205	-3.114494	4.114205	-3.114494	4.114205	-3.114494
H10	0.080758	1.640567	0.080758	1.640567	0.080758	1.640567
H11	-0.835157	-1.279581	-0.835157	-1.279581	-0.835157	-1.279581
H13	-3.042599	-1.744972	-3.042599	-1.744972	-3.042599	-1.744972
H15	-6.029284	1.300635	-6.029284	1.300635	-6.029284	1.300635
H16	-4.281024	3.068516	-4.281024	3.068516	-4.281024	3.068516
H8a1	2.098774	-3.017331	2.098774	-3.017331	2.098774	-3.017331
H8a2	0.940662	-2.736051	0.940662	-2.736051	0.940662	-2.736051
H8a3	0.627730	-2.091845	0.627730	-2.091845	0.627730	-2.091845
H1a1	3.586904	2.839056	3.586904	2.839056	3.586904	2.839056
H1a2	2.845191	1.607268	2.845191	1.607268	2.845191	1.607268
H1a3	1.823539	2.748703	1.823539	2.748703	1.823539	2.748703
H1b1	3.397017	2.669369	3.397017	2.669369	3.397017	2.669369
H1b2	1.633846	2.583448	1.633846	2.583448	1.633846	2.583448
H1b3	2.515057	1.323939	2.515057	1.323939	2.515057	1.323939

**Table 5.2.** Cartesian coordinates (in Å) of 6-nitro-BIPS isomers calculated at B3LYP/6-311G(*d, p*) (continued)

	CTT S <sub>0</sub>			CTT T <sub>1</sub>		
	x	y		x	y	
C1	2.322820	-1.341186	C1	2.322820	-1.341186	C1
C2	3.722292	-0.760153	C2	3.722292	-0.760153	C2
C3	4.959297	-1.374159	C3	4.959297	-1.374159	C3
C4	6.113321	-0.582923	C4	6.113321	-0.582923	C4
C5	6.015188	0.802537	C5	6.015188	0.802537	C5
C6	4.772793	1.433746	C6	4.772793	1.433746	C6
C7	3.640194	0.627859	C7	3.640194	0.627859	C7
N8	2.281510	1.009242	N8	2.281510	1.009242	N8
C9	1.459396	-0.072216	C9	1.459396	-0.072216	C9
C10	0.075065	-0.128858	C10	0.075065	-0.128858	C10
C11	-0.850302	0.920907	C11	-0.850302	0.920907	C11
C12	-2.241144	0.834995	C12	-2.241144	0.834995	C12
C13	-2.964477	-0.383304	C13	-2.964477	-0.383304	C13
C14	-4.329572	-0.379866	C14	-4.329572	-0.379866	C14
C15	-5.079244	0.837593	C15	-5.079244	0.837593	C15
C16	-4.437437	2.028665	C16	-4.437437	2.028665	C16
C17	-2.978237	2.130018	C17	-2.978237	2.130018	C17
O18	-2.393824	3.214527	O18	-2.393824	3.214527	O18
C8a	1.872488	2.386742	C8a	1.872488	2.386742	C8a
C1a	2.018522	-2.108957	C1a	2.018522	-2.108957	C1a
C1b	2.103591	-2.255819	C1b	2.103591	-2.255819	C1b
N14a	-5.046131	-1.649109	N14a	-5.046131	-1.649109	N14a
O14a1	-6.274060	-1.612485	O14a1	-6.274060	-1.612485	O14a1
O14a2	-4.390307	-2.685895	O14a2	-4.390307	-2.685895	O14a2
H3	5.039084	-2.452029	H3	5.039084	-2.452029	H3
H4	7.087720	-1.049428	H4	7.087720	-1.049428	H4
H5	6.914754	1.406802	H5	6.914754	1.406802	H5
H6	4.714105	2.512220	H6	4.714105	2.512220	H6
H10	-0.318354	-1.139019	H10	-0.318354	-1.139019	H10
H11	-0.506568	1.945180	H11	-0.506568	1.945180	H11
H13	-2.459151	-1.336552	H13	-2.459151	-1.336552	H13
H15	-6.158573	0.768498	H15	-6.158573	0.768498	H15
H16	-4.982473	2.961369	H16	-4.982473	2.961369	H16
H8a1	2.729700	2.951089	H8a1	2.729700	2.951089	H8a1
H8a2	1.095163	2.417520	H8a2	1.095163	2.417520	H8a2
H8a3	1.495133	2.858107	H8a3	1.495133	2.858107	H8a3
H1a1	2.688879	-2.967260	H1a1	2.688879	-2.967260	H1a1
H1a2	2.159779	-1.472146	H1a2	2.159779	-1.472146	H1a2
H1a3	0.991302	-2.479525	H1a3	0.991302	-2.479525	H1a3
H1b1	2.775504	-3.115759	H1b1	2.775504	-3.115759	H1b1
H1b2	1.077723	-2.629345	H1b2	1.077723	-2.629345	H1b2
H1b3	2.306829	-1.723552	H1b3	2.306829	-1.723552	H1b3

**Table 5.2.** Cartesian coordinates (in Å) of 6-nitro-BIPS isomers calculated at B3LYP/6-311G(*d, p*) (continued)

	TTC S <sub>0</sub>			TTC T <sub>1</sub>		
	x	y	x	y	x	y
C1	2.146423	-1.108909	2.146423	-1.108909	2.146423	-1.108909
C2	3.643053	-0.840770	3.643053	-0.840770	3.643053	-0.840770
C3	4.716699	-1.715090	4.716699	-1.715090	4.716699	-1.715090
C4	6.016015	-1.195619	6.016015	-1.195619	6.016015	-1.195619
C5	6.223358	0.182383	6.223358	0.182383	6.223358	0.182383
C6	5.149025	1.075145	5.149025	1.075145	5.149025	1.075145
C7	3.866807	0.537669	3.866807	0.537669	3.866807	0.537669
N8	2.623452	1.200125	2.623452	1.200125	2.623452	1.200125
C9	1.582274	0.321587	1.582274	0.321587	1.582274	0.321587
C10	0.269963	0.768217	0.269963	0.768217	0.269963	0.768217
C11	-0.871072	-0.039838	-0.871072	-0.039838	-0.871072	-0.039838
C12	-2.203532	0.390637	-2.203532	0.390637	-2.203532	0.390637
C13	-3.218205	-0.604632	-3.218205	-0.604632	-3.218205	-0.604632
C14	-4.542383	-0.267289	-4.542383	-0.267289	-4.542383	-0.267289
C15	-4.959685	1.100014	-4.959685	1.100014	-4.959685	1.100014
C16	-4.033103	2.090114	-4.033103	2.090114	-4.033103	2.090114
C17	-2.595883	1.827435	-2.595883	1.827435	-2.595883	1.827435
O18	-1.777134	2.756284	-1.777134	2.756284	-1.777134	2.756284
C8a	2.457990	2.647764	2.457990	2.647764	2.457990	2.647764
C1a	1.739092	-1.882035	1.739092	-1.882035	1.739092	-1.882035
C1b	1.739091	-1.882038	1.739091	-1.882038	1.739091	-1.882038
N14a	-5.549565	-1.321049	-5.549565	-1.321049	-5.549565	-1.321049
O14a1	-5.170491	-2.491130	-5.170491	-2.491130	-5.170491	-2.491130
O14a2	-6.730654	-0.980161	-6.730654	-0.980161	-6.730654	-0.980161
H3	4.560931	-2.788366	4.560931	-2.788366	4.560931	-2.788366
H4	6.865214	-1.868253	6.865214	-1.868253	6.865214	-1.868253
H5	7.233972	0.573562	7.233972	0.573562	7.233972	0.573562
H6	5.327115	2.142763	5.327115	2.142763	5.327115	2.142763
H10	0.083674	1.832930	0.083674	1.832930	0.083674	1.832930
H11	-0.743153	-1.117882	-0.743153	-1.117882	-0.743153	-1.117882
H13	-2.949297	-1.654029	-2.949297	-1.654029	-2.949297	-1.654029
H15	-6.020858	1.309979	-6.020858	1.309979	-6.020858	1.309979
H16	-4.321901	3.134241	-4.321901	3.134241	-4.321901	3.134241
H8a1	3.435734	3.121837	3.435734	3.121837	3.435734	3.121837
H8a2	1.906517	2.968649	1.906517	2.968649	1.906517	2.968649
H8a3	1.906518	2.968650	1.906518	2.968650	1.906518	2.968650
H1a1	2.247755	-2.848777	2.247755	-2.848777	2.247755	-2.848777
H1a2	2.022367	-1.331005	2.022367	-1.331005	2.022367	-1.331005
H1a3	0.664376	-2.063226	0.664376	-2.063226	0.664376	-2.063226
H1b1	2.247754	-2.848779	2.247754	-2.848779	2.247754	-2.848779
H1b2	0.664375	-2.063230	0.664375	-2.063230	0.664375	-2.063230
H1b3	2.022365	-1.331009	2.022365	-1.331009	2.022365	-1.331009

**Table 5.2.** Cartesian coordinates (in Å) of 6-nitro-BIPS isomers calculated at B3LYP/6-311G(*d, p*) (continued)

	TTT S <sub>0</sub>			TTT T <sub>1</sub>		
	x	y		x	y	
C1	-2.329798	1.017514	C1	-2.329798	1.017514	C1
C2	-3.721556	0.405017	C2	-3.721556	0.405017	C2
C3	-4.969351	1.005287	C3	-4.969351	1.005287	C3
C4	-6.112465	0.198375	C4	-6.112465	0.198375	C4
C5	-5.993798	-1.189865	C5	-5.993798	-1.189865	C5
C6	-4.740981	-1.808076	C6	-4.740981	-1.808076	C6
C7	-3.619210	-0.987059	C7	-3.619210	-0.987059	C7
N8	-2.255128	-1.342490	N8	-2.255128	-1.342490	N8
C9	-1.446989	-0.243246	C9	-1.446989	-0.243246	C9
C10	-0.066476	-0.346440	C10	-0.066476	-0.346440	C10
C11	0.819701	0.737162	C11	0.819701	0.737162	C11
C12	2.211878	0.710751	C12	2.211878	0.710751	C12
C13	2.980962	-0.481599	C13	2.980962	-0.481599	C13
C14	4.345084	-0.425259	C14	4.345084	-0.425259	C14
C15	5.048871	0.824198	C15	5.048871	0.824198	C15
C16	4.362667	1.992179	C16	4.362667	1.992179	C16
C17	2.899730	2.037030	C17	2.899730	2.037030	C17
O18	2.275033	3.099669	O18	2.275033	3.099669	O18
C8a	-1.763924	-2.711941	C8a	-1.763924	-2.711941	C8a
C1a	-2.116681	1.866628	C1a	-2.116681	1.866628	C1a
C1b	-2.116688	1.866634	C1b	-2.116688	1.866634	C1b
N14a	5.107922	-1.669112	N14a	5.107922	-1.669112	N14a
O14a1	6.333883	-1.585567	O14a1	6.333883	-1.585567	O14a1
O14a2	4.490534	-2.733400	O14a2	4.490534	-2.733400	O14a2
H3	-5.066415	2.085404	H3	-5.066415	2.085404	H3
H4	-7.094704	0.655250	H4	-7.094704	0.655250	H4
H5	-6.885485	-1.805732	H5	-6.885485	-1.805732	H5
H6	-4.667180	-2.888013	H6	-4.667180	-2.888013	H6
H10	0.352285	-1.345628	H10	0.352285	-1.345628	H10
H11	0.423260	1.746017	H11	0.423260	1.746017	H11
H13	2.511275	-1.456493	H13	2.511275	-1.456493	H13
H15	6.130303	0.797274	H15	6.130303	0.797274	H15
H16	4.872422	2.947992	H16	4.872422	2.947992	H16
H8a1	-2.606423	-3.398066	H8a1	-2.606423	-3.398066	H8a1
H8a2	-1.158152	-2.903064	H8a2	-1.158152	-2.903064	H8a2
H8a3	-1.158138	-2.903065	H8a3	-1.158138	-2.903065	H8a3
H1a1	-2.850023	2.676164	H1a1	-2.850023	2.676164	H1a1
H1a2	-2.250244	1.262191	H1a2	-2.250244	1.262191	H1a2
H1a3	-1.121754	2.311629	H1a3	-1.121754	2.311629	H1a3
H1b1	-2.850030	2.676169	H1b1	-2.850030	2.676169	H1b1
H1b2	-1.121761	2.311635	H1b2	-1.121761	2.311635	H1b2
H1b3	-2.250254	1.262201	H1b3	-2.250254	1.262201	H1b3

**Table 5.2.** Cartesian coordinates (in Å) of 6-nitro-BIPS isomers calculated at B3LYP/6-311G(*d, p*) (continued)

	CCC S <sub>0</sub>			CCC T <sub>1</sub>		
	x	y	x	y	x	y
C1	-2.684759	1.377758	-2.684759	1.377758	-2.684759	1.377758
C2	-3.479089	0.098730	-3.479089	0.098730	-3.479089	0.098730
C3	-4.748056	-0.258289	-4.748056	-0.258289	-4.748056	-0.258289
C4	-5.226831	-1.537640	-5.226831	-1.537640	-5.226831	-1.537640
C5	-4.441135	-2.438330	-4.441135	-2.438330	-4.441135	-2.438330
C6	-3.162114	-2.088158	-3.162114	-2.088158	-3.162114	-2.088158
C7	-2.712087	-0.812356	-2.712087	-0.812356	-2.712087	-0.812356
N8	-1.481818	-0.204806	-1.481818	-0.204806	-1.481818	-0.204806
C9	-1.379958	1.021435	-1.379958	1.021435	-1.379958	1.021435
C10	-0.304238	1.919139	-0.304238	1.919139	-0.304238	1.919139
C11	1.063888	1.706557	1.063888	1.706557	1.063888	1.706557
C12	1.866118	0.641902	1.866118	0.641902	1.866118	0.641902
C13	3.248572	0.678384	3.248572	0.678384	3.248572	0.678384
C14	4.115304	-0.252966	4.115304	-0.252966	4.115304	-0.252966
C15	3.662393	-1.259176	3.662393	-1.259176	3.662393	-1.259176
C16	2.350474	-1.302525	2.350474	-1.302525	2.350474	-1.302525
C17	1.357498	-0.381691	1.357498	-0.381691	1.357498	-0.381691
O18	0.160311	-0.457608	0.160311	-0.457608	0.160311	-0.457608
C8a	-0.510874	-0.849679	-0.510874	-0.849679	-0.510874	-0.849679
C1a	-2.383961	1.668794	-2.383961	1.668794	-2.383961	1.668794
C1b	-3.391057	2.581704	-3.391057	2.581704	-3.391057	2.581704
N14a	5.524908	-0.195494	5.524908	-0.195494	5.524908	-0.195494
O14a1	5.895419	0.687680	5.895419	0.687680	5.895419	0.687680
O14a2	6.274606	-1.039084	6.274606	-1.039084	6.274606	-1.039084
H3	-5.362912	0.434354	-5.362912	0.434354	-5.362912	0.434354
H4	-6.214457	-1.834128	-6.214457	-1.834128	-6.214457	-1.834128
H5	-4.822709	-3.428806	-4.822709	-3.428806	-4.822709	-3.428806
H6	-2.549956	-2.797240	-2.549956	-2.797240	-2.549956	-2.797240
H10	-0.613307	2.958678	-0.613307	2.958678	-0.613307	2.958678
H11	1.637715	2.561282	1.637715	2.561282	1.637715	2.561282
H13	3.643372	1.442836	3.643372	1.442836	3.643372	1.442836
H15	4.384191	-1.964741	4.384191	-1.964741	4.384191	-1.964741
H16	1.980437	-2.048710	1.980437	-2.048710	1.980437	-2.048710
H8a1	-1.047133	-1.417788	-1.047133	-1.417788	-1.047133	-1.417788
H8a2	0.095718	-0.084892	0.095718	-0.084892	0.095718	-0.084892
H8a3	0.139027	-1.514479	0.139027	-1.514479	0.139027	-1.514479
H1a1	-1.831713	0.842475	-1.831713	0.842475	-1.831713	0.842475
H1a2	-3.320259	1.819240	-3.320259	1.819240	-3.320259	1.819240
H1a3	-1.778498	2.573466	-1.778498	2.573466	-1.778498	2.573466
H1b1	-4.345090	2.765818	-4.345090	2.765818	-4.345090	2.765818
H1b2	-2.788732	3.488558	-2.788732	3.488558	-2.788732	3.488558
H1b3	-3.590534	2.396709	-3.590534	2.396709	-3.590534	2.396709

**Table 5.2.** Cartesian coordinates (in Å) of 6-nitro-BIPS isomers calculated at B3LYP/6-311G(*d, p*) (continued)

	CCT S <sub>0</sub>			CCT T <sub>1</sub>		
	x	y		x	y	
C1	2.495521	-1.309118	C1	2.495521	-1.309118	C1
C2	3.196136	-0.063776	C2	3.196136	-0.063776	C2
C3	4.440940	0.467442	C3	4.440940	0.467442	C3
C4	4.836696	1.653265	C4	4.836696	1.653265	C4
C5	3.992345	2.288077	C5	3.992345	2.288077	C5
C6	2.736595	1.759710	C6	2.736595	1.759710	C6
C7	2.368277	0.580501	C7	2.368277	0.580501	C7
N8	1.170947	-0.157218	N8	1.170947	-0.157218	N8
C9	1.148282	-1.229234	C9	1.148282	-1.229234	C9
C10	0.150718	-2.181381	C10	0.150718	-2.181381	C10
C11	-1.238220	-2.187094	C11	-1.238220	-2.187094	C11
C12	-2.202705	-1.176613	C12	-2.202705	-1.176613	C12
C13	-1.962789	0.164401	C13	-1.962789	0.164401	C13
C14	-2.985221	1.072303	C14	-2.985221	1.072303	C14
C15	-4.333260	0.707789	C15	-4.333260	0.707789	C15
C16	-4.621729	-0.563397	C16	-4.621729	-0.563397	C16
C17	-3.595142	-1.602392	C17	-3.595142	-1.602392	C17
O18	-3.860036	-2.751216	O18	-3.860036	-2.751216	O18
C8a	0.233615	0.110650	C8a	0.233615	0.110650	C8a
C1a	2.274476	-1.259030	C1a	2.274476	-1.259030	C1a
C1b	3.272908	-2.586334	C1b	3.272908	-2.586334	C1b
N14a	-2.693490	2.439025	N14a	-2.693490	2.439025	N14a
O14a1	-1.513740	2.761501	O14a1	-1.513740	2.761501	O14a1
O14a2	-3.640358	3.207593	O14a2	-3.640358	3.207593	O14a2
H3	5.101479	-0.019802	H3	5.101479	-0.019802	H3
H4	5.804069	2.085115	H4	5.804069	2.085115	H4
H5	4.307630	3.211130	H5	4.307630	3.211130	H5
H6	2.078512	2.267632	H6	2.078512	2.267632	H6
H10	0.525598	-3.116028	H10	0.525598	-3.116028	H10
H11	-1.683735	-3.177350	H11	-1.683735	-3.177350	H11
H13	-0.978514	0.487127	H13	-0.978514	0.487127	H13
H15	-5.097475	1.470181	H15	-5.097475	1.470181	H15
H16	-5.633187	-0.866915	H16	-5.633187	-0.866915	H16
H8a1	0.798569	0.436874	H8a1	0.798569	0.436874	H8a1
H8a2	-0.307219	-0.801644	H8a2	-0.307219	-0.801644	H8a2
H8a3	-0.484875	0.885759	H8a3	-0.484875	0.885759	H8a3
H1a1	1.729709	-0.358719	H1a1	1.729709	-0.358719	H1a1
H1a2	3.237889	-1.256108	H1a2	3.237889	-1.256108	H1a2
H1a3	1.706618	-2.128849	H1a3	1.706618	-2.128849	H1a3
H1b1	4.257844	-2.576259	H1b1	4.257844	-2.576259	H1b1
H1b2	2.748710	-3.484696	H1b2	2.748710	-3.484696	H1b2
H1b3	3.414608	-2.647741	H1b3	3.414608	-2.647741	H1b3

**Table 5.2.** Cartesian coordinates (in Å) of 6-nitro-BIPS isomers calculated at B3LYP/6-311G(*d, p*) (continued)

	TCC S <sub>0</sub>			TCC T <sub>1</sub>		
	x	y	x	y	x	y
C1				-1.481998	-0.725788	-0.438909
C2				-2.961073	-0.936222	-0.142181
C3				-3.690358	-2.102781	0.008399
C4				-5.060523	-2.021956	0.287863
C5				-5.680894	-0.780343	0.417134
C6				-4.958275	0.405591	0.272409
C7				-3.596935	0.301832	-0.004374
N8				-2.659504	1.320612	-0.185994
C9				-1.407512	0.815301	-0.480816
C10				-0.414459	1.659438	-0.991152
C11				0.968844	1.505791	-1.116932
C12				1.907532	0.852014	-0.252032
C13				3.142326	0.404456	-0.729908
C14				4.077941	-0.161112	0.133642
C15				3.851692	-0.313610	1.514939
C16				2.661100	0.125369	2.031175
C17				1.658185	0.772906	1.209868
O18				0.641254	1.276853	1.726896
C8a				-2.971678	2.729879	-0.035627
C1a		Not available		-1.110222	-1.304216	-1.826172
C1b				-0.627037	-1.411733	0.648813
N14a				5.354412	-0.633935	-0.423724
O14a1				5.539014	-0.495671	-1.628552
O14a2				6.161264	-1.139573	0.350591
H3				-3.213671	-3.072048	-0.089709
H4				-5.641263	-2.929353	0.402824
H5				-6.742454	-0.729813	0.630319
H6				-5.451953	1.364909	0.363794
H10				-0.803875	2.565601	-1.456184
H11				1.425279	2.063076	-1.931848
H13				3.387072	0.475474	-1.781013
H15				4.618301	-0.766912	2.126968
H16				2.444253	0.062035	3.090583
H8a1				-3.758536	2.846446	0.710822
H8a2				-2.085226	3.258313	0.313359
H8a3				-3.312518	3.176590	-0.976447
H1a1				-1.748161	-0.892209	-2.610848
H1a2				-1.231601	-2.390487	-1.821464
H1a3				-0.070953	-1.074410	-2.069354
H1b1				-0.910564	-2.465566	0.712604
H1b2				0.433389	-1.371041	0.400831
H1b3				-0.774067	-0.949111	1.624476

**Table 5.2.** Cartesian coordinates (in Å) of 6-nitro-BIPS isomers calculated at B3LYP/6-311G(*d, p*) (continued)

	TCT S <sub>0</sub>			TCT T <sub>1</sub>		
	x	y		x	y	
C1	-2.329798	1.017514	C1	-2.329798	1.017514	C1
C2	-3.721556	0.405017	C2	-3.721556	0.405017	C2
C3	-4.969351	1.005287	C3	-4.969351	1.005287	C3
C4	-6.112465	0.198375	C4	-6.112465	0.198375	C4
C5	-5.993798	-1.189865	C5	-5.993798	-1.189865	C5
C6	-4.740981	-1.808076	C6	-4.740981	-1.808076	C6
C7	-3.619210	-0.987059	C7	-3.619210	-0.987059	C7
N8	-2.255128	-1.342490	N8	-2.255128	-1.342490	N8
C9	-1.446989	-0.243246	C9	-1.446989	-0.243246	C9
C10	-0.066476	-0.346440	C10	-0.066476	-0.346440	C10
C11	0.819701	0.737162	C11	0.819701	0.737162	C11
C12	2.211878	0.710751	C12	2.211878	0.710751	C12
C13	2.980962	-0.481599	C13	2.980962	-0.481599	C13
C14	4.345084	-0.425259	C14	4.345084	-0.425259	C14
C15	5.048871	0.824198	C15	5.048871	0.824198	C15
C16	4.362667	1.992179	C16	4.362667	1.992179	C16
C17	2.899730	2.037030	C17	2.899730	2.037030	C17
O18	2.275033	3.099669	O18	2.275033	3.099669	O18
C8a	-1.763924	-2.711941	C8a	-1.763924	-2.711941	C8a
C1a	-2.116681	1.866628	C1a	-2.116681	1.866628	C1a
C1b	-2.116688	1.866634	C1b	-2.116688	1.866634	C1b
N14a	5.107922	-1.669112	N14a	5.107922	-1.669112	N14a
O14a1	6.333883	-1.585567	O14a1	6.333883	-1.585567	O14a1
O14a2	4.490534	-2.733400	O14a2	4.490534	-2.733400	O14a2
H3	-5.066415	2.085404	H3	-5.066415	2.085404	H3
H4	-7.094704	0.655250	H4	-7.094704	0.655250	H4
H5	-6.885485	-1.805732	H5	-6.885485	-1.805732	H5
H6	-4.667180	-2.888013	H6	-4.667180	-2.888013	H6
H10	0.352285	-1.345628	H10	0.352285	-1.345628	H10
H11	0.423260	1.746017	H11	0.423260	1.746017	H11
H13	2.511275	-1.456493	H13	2.511275	-1.456493	H13
H15	6.130303	0.797274	H15	6.130303	0.797274	H15
H16	4.872422	2.947992	H16	4.872422	2.947992	H16
H8a1	-2.606423	-3.398066	H8a1	-2.606423	-3.398066	H8a1
H8a2	-1.158152	-2.903064	H8a2	-1.158152	-2.903064	H8a2
H8a3	-1.158138	-2.903065	H8a3	-1.158138	-2.903065	H8a3
H1a1	-2.850023	2.676164	H1a1	-2.850023	2.676164	H1a1
H1a2	-2.250244	1.262191	H1a2	-2.250244	1.262191	H1a2
H1a3	-1.121754	2.311629	H1a3	-1.121754	2.311629	H1a3
H1b1	-2.850030	2.676169	H1b1	-2.850030	2.676169	H1b1
H1b2	-1.121761	2.311635	H1b2	-1.121761	2.311635	H1b2
H1b3	-2.250254	1.262201	H1b3	-2.250254	1.262201	H1b3

**Table 5.3.** Energy and vibrational frequencies of 6-nitro-BIPS isomers calculated at B3LYP/6-311G(*d, p*)

Energy <sup>[a]</sup> /Hartree	SP S <sub>0</sub>			SP T <sub>1</sub>		
	-1069.868271			-1069.777772		
	12.02	39.59	51.04	10.44	39.28	54.14
	89.31	104.37	112.90	85.07	98.95	112.67
	121.95	156.27	175.69	122.26	139.88	172.43
	197.18	218.02	230.17	193.56	207.23	221.16
	234.81	261.66	263.67	228.85	240.30	251.05
	284.04	303.87	319.74	281.05	289.46	305.34
	323.20	339.53	367.97	310.44	336.93	356.12
	402.62	418.30	424.26	377.37	395.62	413.04
	456.21	485.85	504.25	420.64	451.69	482.54
	528.07	543.73	552.92	500.81	522.70	535.14
	556.54	570.54	576.66	553.81	566.40	570.41
	585.42	636.03	642.92	577.45	581.48	588.12
	693.42	726.15	744.25	641.50	652.22	721.85
	752.05	755.87	775.02	726.12	754.58	755.99
	778.10	790.64	817.75	775.33	780.45	789.78
	829.32	852.78	858.42	823.46	835.61	843.81
	863.14	925.38	933.90	862.26	891.96	914.84
	938.04	939.80	954.82	930.38	937.87	953.78
	964.97	974.60	982.90	958.64	964.49	973.74
	999.07	1005.62	1031.44	976.65	998.58	1004.03
	1046.08	1083.58	1103.78	1030.93	1046.01	1082.84
	1119.06	1139.09	1142.23	1089.33	1117.40	1138.97
	1144.82	1160.04	1179.94	1142.27	1145.92	1159.88
	1183.24	1201.97	1205.55	1179.97	1183.06	1200.65
	1243.45	1261.39	1277.56	1205.43	1238.28	1259.79
	1288.09	1300.27	1323.33	1281.89	1287.17	1293.79
	1329.28	1369.30	1376.55	1321.73	1329.38	1358.10
	1387.84	1397.23	1405.85	1387.36	1389.20	1396.79
	1419.85	1457.74	1476.42	1410.39	1419.28	1456.93
	1488.11	1491.05	1491.90	1478.64	1487.57	1490.85
	1495.60	1503.77	1506.44	1491.44	1495.36	1503.88
	1513.57	1514.67	1518.36	1508.06	1513.16	1514.08
	1584.86	1620.28	1638.78	1518.15	1596.28	1631.70
	1647.89	1651.51	1699.33	1638.43	1647.73	1696.67
	2996.06	3029.05	3035.94	2994.91	3028.28	3035.56
	3077.72	3089.71	3098.47	3077.00	3088.99	3097.48
	3108.00	3121.39	3135.32	3106.78	3121.13	3135.52
	3160.96	3166.18	3168.90	3160.57	3164.21	3168.47
	3184.68	3192.83	3199.48	3184.42	3192.65	3192.92
	3207.32	3211.89	3225.87	3195.65	3208.03	3209.02

<sup>[a]</sup> Sum of electronic and zero-point energies.

**Table 5.3.** Energy and vibrational frequencies of 6-nitro-BIPS isomers calculated at B3LYP/6-311G(*d, p*) (continued)

Energy <sup>[a]</sup> /Hartree	CTC S <sub>0</sub>			CTC T <sub>1</sub>		
	-1069.859855			-1069.809488		
	18.70	30.65	18.70	30.65	18.70	30.65
	56.59	76.73	56.59	76.73	56.59	76.73
	106.11	130.33	106.11	130.33	106.11	130.33
	155.05	170.50	155.05	170.50	155.05	170.50
	234.96	249.48	234.96	249.48	234.96	249.48
	263.92	277.71	263.92	277.71	263.92	277.71
	310.08	319.51	310.08	319.51	310.08	319.51
	356.23	357.35	356.23	357.35	356.23	357.35
	399.56	464.57	399.56	464.57	399.56	464.57
	480.19	508.13	480.19	508.13	480.19	508.13
	550.95	552.79	550.95	552.79	550.95	552.79
	579.29	631.66	579.29	631.66	579.29	631.66
	664.38	705.51	664.38	705.51	664.38	705.51
	741.91	754.40	741.91	754.40	741.91	754.40
	760.77	774.72	760.77	774.72	760.77	774.72
	846.55	860.84	846.55	860.84	846.55	860.84
	910.01	914.59	910.01	914.59	910.01	914.59
	947.14	949.55	947.14	949.55	947.14	949.55
	956.33	988.61	956.33	988.61	956.33	988.61
	1011.09	1030.59	1011.09	1030.59	1011.09	1030.59
	1048.52	1092.71	1048.52	1092.71	1048.52	1092.71
	1136.82	1137.44	1136.82	1137.44	1136.82	1137.44
	1149.03	1152.38	1149.03	1152.38	1149.03	1152.38
	1198.39	1207.73	1198.39	1207.73	1198.39	1207.73
	1246.35	1266.13	1246.35	1266.13	1246.35	1266.13
	1314.28	1325.57	1314.28	1325.57	1314.28	1325.57
	1360.19	1382.45	1360.19	1382.45	1360.19	1382.45
	1402.30	1412.84	1402.30	1412.84	1402.30	1412.84
	1447.48	1470.26	1447.48	1470.26	1447.48	1470.26
	1488.67	1491.88	1488.67	1491.88	1488.67	1491.88
	1503.47	1505.51	1503.47	1505.51	1503.47	1505.51
	1517.70	1534.38	1517.70	1534.38	1517.70	1534.38
	1593.65	1608.78	1593.65	1608.78	1593.65	1608.78
	1647.12	1657.62	1647.12	1657.62	1647.12	1657.62
	3034.75	3034.84	3034.75	3034.84	3034.75	3034.84
	3103.88	3107.21	3103.88	3107.21	3103.88	3107.21
	3114.20	3117.52	3114.20	3117.52	3114.20	3117.52
	3169.05	3171.01	3169.05	3171.01	3169.05	3171.01
	3189.13	3191.73	3189.13	3191.73	3189.13	3191.73
	3198.91	3200.23	3198.91	3200.23	3198.91	3200.23

<sup>[a]</sup> Sum of electronic and zero-point energies.

**Table 5.3.** Energy and vibrational frequencies of 6-nitro-BIPS isomers calculated at B3LYP/6-311G(*d, p*) (continued)

Energy <sup>[a]</sup> /Hartree	CTT S <sub>0</sub>			CTT T <sub>1</sub>		
	-1069.858749			-1069.811818		
	19.91	26.68	19.91	26.68	19.91	26.68
	51.43	75.55	51.43	75.55	51.43	75.55
	107.54	129.35	107.54	129.35	107.54	129.35
	162.44	185.77	162.44	185.77	162.44	185.77
	233.11	241.69	233.11	241.69	233.11	241.69
	263.60	270.81	263.60	270.81	263.60	270.81
	305.60	316.29	305.60	316.29	305.60	316.29
	353.53	357.52	353.53	357.52	353.53	357.52
	409.72	473.45	409.72	473.45	409.72	473.45
	481.39	501.33	481.39	501.33	481.39	501.33
	551.74	557.46	551.74	557.46	551.74	557.46
	585.34	595.83	585.34	595.83	585.34	595.83
	652.51	700.90	652.51	700.90	652.51	700.90
	737.17	756.45	737.17	756.45	737.17	756.45
	774.19	786.97	774.19	786.97	774.19	786.97
	838.93	857.27	838.93	857.27	838.93	857.27
	881.91	914.60	881.91	914.60	881.91	914.60
	944.91	948.26	944.91	948.26	944.91	948.26
	973.40	988.19	973.40	988.19	973.40	988.19
	1019.89	1029.99	1019.89	1029.99	1019.89	1029.99
	1049.22	1084.60	1049.22	1084.60	1049.22	1084.60
	1133.37	1136.52	1133.37	1136.52	1133.37	1136.52
	1150.74	1154.15	1150.74	1154.15	1150.74	1154.15
	1186.76	1211.51	1186.76	1211.51	1186.76	1211.51
	1257.04	1267.53	1257.04	1267.53	1257.04	1267.53
	1303.80	1325.23	1303.80	1325.23	1303.80	1325.23
	1352.32	1382.15	1352.32	1382.15	1352.32	1382.15
	1413.68	1420.73	1413.68	1420.73	1413.68	1420.73
	1462.64	1477.11	1462.64	1477.11	1462.64	1477.11
	1488.04	1492.30	1488.04	1492.30	1488.04	1492.30
	1504.14	1504.39	1504.14	1504.39	1504.14	1504.39
	1518.31	1536.62	1518.31	1536.62	1518.31	1536.62
	1594.03	1608.61	1594.03	1608.61	1594.03	1608.61
	1647.08	1655.67	1647.08	1655.67	1647.08	1655.67
	3034.88	3038.32	3034.88	3038.32	3034.88	3038.32
	3102.96	3107.53	3102.96	3107.53	3102.96	3107.53
	3111.73	3114.39	3111.73	3114.39	3111.73	3114.39
	3169.11	3170.72	3169.11	3170.72	3169.11	3170.72
	3190.61	3192.07	3190.61	3192.07	3190.61	3192.07
	3204.57	3208.76	3204.57	3208.76	3204.57	3208.76

<sup>[a]</sup> Sum of electronic and zero-point energies.

**Table 5.3.** Energy and vibrational frequencies of 6-nitro-BIPS isomers calculated at B3LYP/6-311G(*d, p*) (continued)

Energy <sup>[a]</sup> /Hartree	TTC S <sub>0</sub>			TTC T <sub>1</sub>		
	-1069.863568			-1069.812717		
	29.48	30.43	29.48	30.43	29.48	30.43
	48.84	65.28	48.84	65.28	48.84	65.28
	98.58	116.09	98.58	116.09	98.58	116.09
	149.27	170.21	149.27	170.21	149.27	170.21
	214.77	238.51	214.77	238.51	214.77	238.51
	254.20	271.83	254.20	271.83	254.20	271.83
	302.21	320.02	302.21	320.02	302.21	320.02
	357.12	357.51	357.12	357.51	357.12	357.51
	407.39	465.08	407.39	465.08	407.39	465.08
	478.24	508.83	478.24	508.83	478.24	508.83
	548.28	556.15	548.28	556.15	548.28	556.15
	579.09	631.60	579.09	631.60	579.09	631.60
	667.41	700.07	667.41	700.07	667.41	700.07
	735.99	752.83	735.99	752.83	735.99	752.83
	759.36	774.24	759.36	774.24	759.36	774.24
	837.45	853.16	837.45	853.16	837.45	853.16
	865.39	916.03	865.39	916.03	865.39	916.03
	944.65	950.36	944.65	950.36	944.65	950.36
	960.03	987.39	960.03	987.39	960.03	987.39
	1010.75	1034.63	1010.75	1034.63	1010.75	1034.63
	1063.68	1098.82	1063.68	1098.82	1063.68	1098.82
	1137.80	1138.42	1137.80	1138.42	1137.80	1138.42
	1149.02	1152.50	1149.02	1152.50	1149.02	1152.50
	1194.09	1209.30	1194.09	1209.30	1194.09	1209.30
	1248.28	1285.60	1248.28	1285.60	1248.28	1285.60
	1303.48	1335.63	1303.48	1335.63	1303.48	1335.63
	1369.94	1385.78	1369.94	1385.78	1369.94	1385.78
	1404.27	1407.09	1404.27	1407.09	1404.27	1407.09
	1448.25	1470.60	1448.25	1470.60	1448.25	1470.60
	1486.39	1488.85	1486.39	1488.85	1486.39	1488.85
	1499.21	1502.75	1499.21	1502.75	1499.21	1502.75
	1519.24	1533.48	1519.24	1533.48	1519.24	1533.48
	1592.56	1607.42	1592.56	1607.42	1592.56	1607.42
	1645.01	1658.72	1645.01	1658.72	1645.01	1658.72
	3041.66	3044.02	3041.66	3044.02	3041.66	3044.02
	3100.29	3108.07	3100.29	3108.07	3100.29	3108.07
	3122.98	3123.81	3122.98	3123.81	3122.98	3123.81
	3163.89	3169.16	3163.89	3169.16	3163.89	3169.16
	3188.35	3191.50	3188.35	3191.50	3188.35	3191.50
	3200.96	3209.47	3200.96	3209.47	3200.96	3209.47

<sup>[a]</sup> Sum of electronic and zero-point energies.

**Table 5.3.** Energy and vibrational frequencies of 6-nitro-BIPS isomers calculated at B3LYP/6-311G(*d, p*) (continued)

Energy <sup>[a]</sup> /Hartree	TTT S <sub>0</sub>			TTT T <sub>1</sub>		
	-1069.861331			-1069.813953		
	16.64	33.70	16.64	33.70	16.64	33.70
	51.18	74.16	51.18	74.16	51.18	74.16
	93.06	118.75	93.06	118.75	93.06	118.75
	134.70	169.02	134.70	169.02	134.70	169.02
	217.80	247.12	217.80	247.12	217.80	247.12
	254.57	263.99	254.57	263.99	254.57	263.99
	299.70	308.60	299.70	308.60	299.70	308.60
	353.20	358.22	353.20	358.22	353.20	358.22
	415.74	470.96	415.74	470.96	415.74	470.96
	480.20	501.44	480.20	501.44	480.20	501.44
	550.83	556.62	550.83	556.62	550.83	556.62
	585.76	599.09	585.76	599.09	585.76	599.09
	660.89	691.25	660.89	691.25	660.89	691.25
	737.58	756.00	737.58	756.00	737.58	756.00
	773.25	786.17	773.25	786.17	773.25	786.17
	838.88	844.70	838.88	844.70	838.88	844.70
	864.67	879.44	864.67	879.44	864.67	879.44
	939.06	944.66	939.06	944.66	939.06	944.66
	970.32	987.35	970.32	987.35	970.32	987.35
	1015.73	1037.94	1015.73	1037.94	1015.73	1037.94
	1066.30	1083.34	1066.30	1083.34	1066.30	1083.34
	1132.97	1139.09	1132.97	1139.09	1132.97	1139.09
	1148.92	1150.27	1148.92	1150.27	1148.92	1150.27
	1186.95	1200.19	1186.95	1200.19	1186.95	1200.19
	1249.57	1278.06	1249.57	1278.06	1249.57	1278.06
	1301.12	1321.68	1301.12	1321.68	1301.12	1321.68
	1357.09	1383.58	1357.09	1383.58	1357.09	1383.58
	1407.19	1416.60	1407.19	1416.60	1407.19	1416.60
	1459.30	1472.83	1459.30	1472.83	1459.30	1472.83
	1487.78	1491.43	1487.78	1491.43	1487.78	1491.43
	1501.89	1504.06	1501.89	1504.06	1501.89	1504.06
	1519.38	1535.20	1519.38	1535.20	1519.38	1535.20
	1592.13	1608.03	1592.13	1608.03	1592.13	1608.03
	1646.78	1656.33	1646.78	1656.33	1646.78	1656.33
	3036.24	3040.88	3036.24	3040.88	3036.24	3040.88
	3091.06	3106.69	3091.06	3106.69	3091.06	3106.69
	3124.50	3126.43	3124.50	3126.43	3124.50	3126.43
	3169.63	3174.30	3169.63	3174.30	3169.63	3174.30
	3190.17	3191.07	3190.17	3191.07	3190.17	3191.07
	3199.76	3206.06	3199.76	3206.06	3199.76	3206.06

<sup>[a]</sup> Sum of electronic and zero-point energies.

**Table 5.3.** Energy and vibrational frequencies of 6-nitro-BIPS isomers calculated at B3LYP/6-311G(*d, p*) (continued)

Energy <sup>[a]</sup> /Hartree	CCC S <sub>0</sub>			CCC T <sub>1</sub>		
	-1069.853172			-1069.798257		
	26.86	35.42	26.86	35.42	26.86	35.42
	65.23	88.87	65.23	88.87	65.23	88.87
	116.48	132.10	116.48	132.10	116.48	132.10
	163.10	177.06	163.10	177.06	163.10	177.06
	227.91	250.11	227.91	250.11	227.91	250.11
	265.65	282.90	265.65	282.90	265.65	282.90
	315.23	325.06	315.23	325.06	315.23	325.06
	354.36	373.97	354.36	373.97	354.36	373.97
	434.40	465.27	434.40	465.27	434.40	465.27
	484.73	525.28	484.73	525.28	484.73	525.28
	550.76	552.66	550.76	552.66	550.76	552.66
	581.30	632.34	581.30	632.34	581.30	632.34
	663.56	684.49	663.56	684.49	663.56	684.49
	740.60	753.77	740.60	753.77	740.60	753.77
	763.16	776.83	763.16	776.83	763.16	776.83
	804.99	845.16	804.99	845.16	804.99	845.16
	872.95	894.34	872.95	894.34	872.95	894.34
	942.93	947.26	942.93	947.26	942.93	947.26
	959.27	976.07	959.27	976.07	959.27	976.07
	1004.20	1032.64	1004.20	1032.64	1004.20	1032.64
	1050.64	1092.48	1050.64	1092.48	1050.64	1092.48
	1129.02	1138.53	1129.02	1138.53	1129.02	1138.53
	1148.35	1151.62	1148.35	1151.62	1148.35	1151.62
	1186.44	1205.82	1186.44	1205.82	1186.44	1205.82
	1251.09	1262.26	1251.09	1262.26	1251.09	1262.26
	1321.63	1341.81	1321.63	1341.81	1321.63	1341.81
	1371.28	1382.42	1371.28	1382.42	1371.28	1382.42
	1400.46	1424.64	1400.46	1424.64	1400.46	1424.64
	1455.30	1473.91	1455.30	1473.91	1455.30	1473.91
	1484.43	1489.35	1484.43	1489.35	1484.43	1489.35
	1501.04	1505.52	1501.04	1505.52	1501.04	1505.52
	1513.16	1526.69	1513.16	1526.69	1513.16	1526.69
	1580.02	1596.76	1580.02	1596.76	1580.02	1596.76
	1642.70	1655.26	1642.70	1655.26	1642.70	1655.26
	3034.32	3037.52	3034.32	3037.52	3034.32	3037.52
	3101.68	3106.22	3101.68	3106.22	3101.68	3106.22
	3115.91	3125.85	3115.91	3125.85	3115.91	3125.85
	3143.15	3154.58	3143.15	3154.58	3143.15	3154.58
	3179.73	3184.62	3179.73	3184.62	3179.73	3184.62
	3195.65	3202.46	3195.65	3202.46	3195.65	3202.46

<sup>[a]</sup> Sum of electronic and zero-point energies.

**Table 5.3.** Energy and vibrational frequencies of 6-nitro-BIPS isomers calculated at B3LYP/6-311G(*d, p*) (continued)

Energy <sup>[a]</sup> /Hartree	CCT S <sub>0</sub>			CCT T <sub>1</sub>		
	-1069.847953			-1069.802540		
	18.64	30.52	18.64	30.52	18.64	30.52
	62.06	71.22	62.06	71.22	62.06	71.22
	106.11	134.41	106.11	134.41	106.11	134.41
	168.59	183.91	168.59	183.91	168.59	183.91
	220.66	246.47	220.66	246.47	220.66	246.47
	261.58	279.75	261.58	279.75	261.58	279.75
	312.36	322.64	312.36	322.64	312.36	322.64
	350.96	359.86	350.96	359.86	350.96	359.86
	437.28	474.87	437.28	474.87	437.28	474.87
	493.87	515.88	493.87	515.88	493.87	515.88
	550.22	559.66	550.22	559.66	550.22	559.66
	578.66	598.68	578.66	598.68	578.66	598.68
	665.79	698.00	665.79	698.00	665.79	698.00
	739.33	759.92	739.33	759.92	739.33	759.92
	774.38	780.56	774.38	780.56	774.38	780.56
	824.71	834.53	824.71	834.53	824.71	834.53
	872.96	896.79	872.96	896.79	872.96	896.79
	948.30	954.26	948.30	954.26	948.30	954.26
	968.45	991.21	968.45	991.21	968.45	991.21
	1013.29	1031.27	1013.29	1031.27	1013.29	1031.27
	1047.30	1075.72	1047.30	1075.72	1047.30	1075.72
	1132.73	1140.32	1132.73	1140.32	1132.73	1140.32
	1148.35	1156.19	1148.35	1156.19	1148.35	1156.19
	1186.38	1195.18	1186.38	1195.18	1186.38	1195.18
	1262.88	1265.46	1262.88	1265.46	1262.88	1265.46
	1308.99	1323.90	1308.99	1323.90	1308.99	1323.90
	1345.08	1381.46	1345.08	1381.46	1345.08	1381.46
	1415.25	1426.97	1415.25	1426.97	1415.25	1426.97
	1464.24	1477.13	1464.24	1477.13	1464.24	1477.13
	1489.21	1490.44	1489.21	1490.44	1489.21	1490.44
	1502.86	1505.91	1502.86	1505.91	1502.86	1505.91
	1524.04	1530.20	1524.04	1530.20	1524.04	1530.20
	1591.81	1602.17	1591.81	1602.17	1591.81	1602.17
	1642.68	1653.93	1642.68	1653.93	1642.68	1653.93
	3034.96	3037.97	3034.96	3037.97	3034.96	3037.97
	3103.10	3107.56	3103.10	3107.56	3103.10	3107.56
	3112.80	3113.59	3112.80	3113.59	3112.80	3113.59
	3141.78	3155.62	3141.78	3155.62	3141.78	3155.62
	3179.99	3189.89	3179.99	3189.89	3179.99	3189.89
	3202.40	3213.76	3202.40	3213.76	3202.40	3213.76

<sup>[a]</sup> Sum of electronic and zero-point energies.

**Table 5.3.** Energy and vibrational frequencies of 6-nitro-BIPS isomers calculated at B3LYP/6-311G(*d, p*) (continued)

	TCC S <sub>0</sub>	TCC T <sub>1</sub>		
Energy <sup>[a]</sup> /Hartree	Not available	-1069.792545		
		20.36	28.55	38.63
		49.80	74.71	108.82
		113.91	126.47	131.98
		141.00	144.84	192.02
		216.06	240.23	254.62
		268.62	291.57	308.84
		314.47	319.25	320.51
		333.77	353.28	359.51
		426.88	442.20	464.59
		481.35	510.87	527.66
		541.11	553.50	557.64
		577.09	588.98	624.73
		642.51	668.04	680.91
		713.62	742.75	745.66
		755.51	764.11	772.63
		803.14	829.56	839.13
		856.98	861.89	862.45
		916.67	934.35	940.73
		947.77	952.95	980.42
		982.27	1029.13	1044.56
		1058.28	1079.61	1094.98
		1124.43	1130.79	1135.74
		1138.51	1148.45	1151.03
		1183.78	1190.82	1224.09
		1250.02	1254.48	1287.86
		1321.89	1328.01	1334.43
		1364.72	1370.77	1374.85
		1398.12	1402.33	1422.99
		1439.35	1458.38	1464.47
		1480.65	1489.02	1490.45
		1492.67	1495.42	1502.67
		1508.18	1513.06	1515.09
		1516.83	1566.39	1579.39
		1605.63	1635.97	1642.44
		3014.87	3033.30	3043.05
		3085.87	3091.98	3101.84
		3109.35	3112.40	3126.97
		3133.16	3137.79	3166.36
		3174.45	3188.83	3194.14
		3197.11	3211.56	3226.20
Frequency /cm <sup>-1</sup>	Not available			

<sup>[a]</sup> Sum of electronic and zero-point energies.

**Table 5.3.** Energy and vibrational frequencies of 6-nitro-BIPS isomers calculated at B3LYP/6-311G(*d, p*) (continued)

Energy <sup>[a]</sup> /Hartree	TCT S <sub>0</sub>			TCT T <sub>1</sub>		
	-1069.835128			-1069.789808		
	12.65	34.34	12.65	34.34	12.65	34.34
	61.47	75.78	61.47	75.78	61.47	75.78
	100.79	108.85	100.79	108.85	100.79	108.85
	144.37	175.79	144.37	175.79	144.37	175.79
	202.51	216.34	202.51	216.34	202.51	216.34
	256.49	274.09	256.49	274.09	256.49	274.09
	306.92	321.73	306.92	321.73	306.92	321.73
	358.48	358.68	358.48	358.68	358.48	358.68
	448.96	470.79	448.96	470.79	448.96	470.79
	490.82	531.50	490.82	531.50	490.82	531.50
	549.91	557.98	549.91	557.98	549.91	557.98
	582.88	595.15	582.88	595.15	582.88	595.15
	684.41	687.94	684.41	687.94	684.41	687.94
	735.97	755.42	735.97	755.42	735.97	755.42
	775.78	782.89	775.78	782.89	775.78	782.89
	826.77	839.75	826.77	839.75	826.77	839.75
	862.41	868.49	862.41	868.49	862.41	868.49
	942.90	945.92	942.90	945.92	942.90	945.92
	966.48	988.54	966.48	988.54	966.48	988.54
	1030.15	1042.35	1030.15	1042.35	1030.15	1042.35
	1062.26	1067.01	1062.26	1067.01	1062.26	1067.01
	1126.61	1137.07	1126.61	1137.07	1126.61	1137.07
	1146.05	1151.51	1146.05	1151.51	1146.05	1151.51
	1187.15	1194.36	1187.15	1194.36	1187.15	1194.36
	1257.87	1263.20	1257.87	1263.20	1257.87	1263.20
	1319.83	1334.72	1319.83	1334.72	1319.83	1334.72
	1376.49	1390.05	1376.49	1390.05	1376.49	1390.05
	1420.49	1432.67	1420.49	1432.67	1420.49	1432.67
	1473.01	1486.01	1473.01	1486.01	1473.01	1486.01
	1492.22	1497.91	1492.22	1497.91	1492.22	1497.91
	1505.90	1514.26	1505.90	1514.26	1505.90	1514.26
	1523.08	1534.46	1523.08	1534.46	1523.08	1534.46
	1585.49	1605.79	1585.49	1605.79	1585.49	1605.79
	1646.86	1652.89	1646.86	1652.89	1646.86	1652.89
	3037.17	3048.77	3037.17	3048.77	3037.17	3048.77
	3092.11	3105.20	3092.11	3105.20	3092.11	3105.20
	3112.38	3153.14	3112.38	3153.14	3112.38	3153.14
	3163.82	3171.72	3163.82	3171.72	3163.82	3171.72
	3179.57	3191.29	3179.57	3191.29	3179.57	3191.29
	3199.78	3215.84	3199.78	3215.84	3199.78	3215.84

<sup>[a]</sup> Sum of electronic and zero-point energies.

**Table 5.4.** Refined structures of 6-nitro-BIPS and their abundance<sup>[a]</sup>

# of Products	Quality of Fit $\chi^2$ <sup>[b]</sup>	# of Fitted Parameters $n$	Fractional Abundance of Isomeric Species <sup>[c]</sup>						
			SP (S <sub>0</sub> )	SP (T <sub>1</sub> )	CTC (S <sub>0</sub> )	CTT (S <sub>0</sub> )	CTC (T <sub>1</sub> )	CTT (T <sub>1</sub> )	TCT (S <sub>0</sub> )
3	90	5	0.30	0.39	0.31	-	-	-	-
	120	4	0.39	0.36	-	0.25	-	-	-
	126	4	0.42	0.34	-	-	-	0.24	-
	150	2	0.59	-	0.25	-	-	0.16	-
	164	1	0.39	0.34	-	-	0.27	-	-
4	100	1	0.35	0.37	0.08 <sup>[b]</sup>	0.20	-	-	-
	108	2	0.32	0.33	-	-	0.19	-	0.16
	109	1	0.37	0.33	0.15	-	-	0.15	-
	133	0	0.33	0.35	0.28	-	0.04 <sup>[b]</sup>	-	-
	140	1	0.40	0.33	-	0.13	0.14	-	-

<sup>[a]</sup>It is assumed that the structures and frequencies obtained from the DFT calculations provide a good approximation to the actual structures. If the linear combination is correct, then the structural refinement should only produce geometries, which differ minimally from the theoretically predicted ones, when reaching an  $n$ -dimensional minimum on the  $\chi^2$ -hypersurface.

<sup>[b]</sup> $\chi^2 = \sum_s \{Experiment(s) - Theory(s)\}^2 \cdot w(s)$  is the parameter being minimized in the least-squares fitting routine. Note that it is weighted by the error,  $w(s)$ , associated with the diffraction intensity measured at each pixel. Thus it is a relative measure of the quality of the fit for data collected under the exact same conditions.<sup>2</sup>

<sup>[c]</sup>The error bar ( $3\sigma$ ) for fitted fractions is  $\sim 0.1$ . Thus fractions less than 0.1 are below the detection limit of UED4.

**Table 5.5.** Refined open CTC structure of 6-nitro-BIPS in the ground-state at 1132 K

Bond Lengths	Refined Value		DFT	Bond Angles	Refined Value		DFT
	[a]	[a]	[b]		[a]	[b]	
C1-C2	1.536	± 0.017	1.532	C9-C1-C2	101.9	± 2.9	101.771
C2-C3	1.417	± 0.017	1.400	C1-C2-C7	108.9	± 4.3	109.020
C3-C4	1.420	± 0.018	1.415	C2-C7-N8	109.0	± 3.1	109.198
C4-C5	1.418	± 0.016	1.409	C7-N8-C9	111.2	± 2.7	111.216
C5-C6	1.421	± 0.013	1.413	N8-C9-C1	108.8	± 3.6	108.687
C6-C7	1.412	± 0.014	1.405	C3-C2-C7C1	-11.4	± 1.5	-11.294
C7-N8	1.428	± 0.042	1.431	C6-C7-C2N8	-6.5	± 2.0	-6.558
N8-C9	1.381	± 0.034	1.376	C4-C3-C2	119.0	± 1.9	119.048
C9-C10	1.417	± 0.037	1.402	C5-C4-C3	120.4	± 2.1	120.398
C10-C11	1.431	± 0.034	1.415	C6-C5-C4	121.2	± 0.9	121.129
C11-C12	1.413	± 0.030	1.417	C7-C6-C5	117.5	± 1.0	117.456
C12-C13	1.451	± 0.026	1.437	C10-C9-C1N8	-9.0	± 3.9	-9.026
C13-C14	1.391	± 0.023	1.382	C9-C10-C11	129.6	± 5.2	129.554
C14-C15	1.445	± 0.019	1.446	C10-C11-C12	126.3	± 4.3	126.644
C15-C16	1.378	± 0.020	1.371	C11-C12-C17C13	5.5	± 5.5	5.904
C16-C17	1.474	± 0.014	1.478	O18-C17-C12C16	2.2	± 2.1	2.315
C17-O18	1.229	± 0.055	1.251	C13-C12-C17	119.5	± 4.7	119.121
C9-C1	1.542	± 0.020	1.554	C16-C17-C12	116.0	± 3.4	115.627
C2-C7	1.412	± 0.016	1.411	C12-C13-C14	121.1	± 2.9	121.328
C12-C17	1.481	± 0.032	1.506	C13-C14-C15	120.7	± 6.3	121.248
C1-C1a	1.534	± 0.031	1.565	C14-C15-C16	119.8	± 2.3	119.900
C1-C1b	1.537	± 0.028	1.562	C15-C16-C17	122.9	± 2.8	122.775
N8-C8a	1.469	± 0.008	1.471	C1a-C1-C2	111.5	± 1.3	111.497
C14-N14a	1.495	± 0.042	1.474	C1a-C1-C1b	110.3	± 0.9	110.298
N14a-O14a1	1.215	± 0.046	1.243	C1b-C1-C9	110.8	± 0.6	110.878
N14a-O14a2	1.217	± 0.046	1.244	C1a-C1-C9	110.2	± 0.9	110.277
				C1b-C1-C2	111.9	± 1.4	111.859
				C8a-N8-C7C9	-3.9	± 1.2	-3.845
				N14a-C14-C13-C15	0.1	± 1.3	0.016
				O14a1-N14a-C14	117.8	± 1.8	117.617
				O14a2-N14a-C14- O14a1	-5.5	± 1.8	-5.693

*continued on next page*

<sup>[a]</sup> The error bars reported here are  $3\sigma$ .

<sup>[b]</sup> Theoretical structures were obtained using DFT at B3LYP/6-311G(*d, p*).

<sup>[c]</sup> If four atoms are listed, A1-A2-A3-A4, the angle is defined as

$$(A1-A2-A3)-(A1-A2-A4).$$

**Table 5.5.** Refined open CTC structure of 6-nitro-BIPS in the ground-state at 1132 K (continued)

Dihedral Angles	Refined Value [a]			DFT [b]
C3-C4-C5-C6	0.21	±	0.15	0.478
C4-C5-C6-C7	0.19	±	0.07	-179.347
C2-C3-C4-C5	-0.12	±	0.07	-179.359
C5-C6-C7-C2	-0.71	±	0.14	-2.537
C7-C2-C3-C4	-0.38	±	0.22	1.434
C6-C7-C2-C3	0.81	±	0.05	-2.938
C1-C2-C7-N8	0.49	±	0.20	3.461
C3-C2-C7-N8	-179.34	±	0.71	115.489
C6-C7-C2-C1	-179.36	±	0.62	-116.117
C2-C7-N8-C9	-2.53	±	0.70	-122.051
C7-C2-C1-C9	1.43	±	0.55	119.847
C2-C1-C9-N8	-2.94	±	0.08	173.969
C7-N8-C9-C1	3.47	±	0.29	-172.880
C1a-C1-C9-N8	115.56	±	0.15	177.413
C1a-C1-C2-C7	-116.12	±	0.24	-176.932
C1b-C1-C9-N8	-122.13	±	0.27	-169.891
C1b-C1-C2-C7	119.87	±	0.17	10.544
C8a-N8-C7-C2	173.98	±	0.44	178.952
C8a-N8-C9-C1	-172.87	±	0.04	-178.153
C10-C9-C1-C2	177.42	±	0.02	1.460
C10-C9-N8-C7	-176.93	±	0.04	-179.535
C11-C10-C9-C1	-169.90	±	0.03	179.736
C11-C10-C9-N8	10.55	±	0.01	-0.164
C9-C10-C11-C12	178.97	±	0.02	-0.207
C10-C11-C12-C13	-178.16	±	0.02	0.072
C10-C11-C12-C17	1.46	±	0.01	0.030
C11-C12-C17-C16	-179.54	±	0.01	0.162
C11-C12-C13-C14	179.74	±	0.02	0.106
C12-C13-C14-C15	-0.16	±	0.02	179.953
C12-C17-C16-C15	-0.21	±	0.02	179.909
C13-C12-C17-C16	0.07	±	0.02	179.934
C13-C14-C15-C16	0.03	±	0.01	179.932
C14-C15-C16-C17	0.16	±	0.01	-0.197
C14-C13-C12-C17	0.11	±	0.01	179.709
O18-C17-C12-C13	179.95	±	0.01	179.796
O18-C17-C16-C15	179.91	±	0.01	-0.298
N14a-C14-C15-C16	179.93	±	0.00	0.000
N14a-C14-C13-C12	179.93	±	0.00	0.000
O14a1-N14a-C14-C15	-0.20	±	0.00	0.000
O14a1-N14a-C14-C13	179.71	±	0.00	0.000
O14a2-N14a-C14-C15	179.80	±	0.00	0.000
O14a2-N14a-C14-C13	-0.30	±	0.00	0.000

**Table 5.6.** Refined closed structure of 6-nitro-BIPS in the lowest triplet-state at 843 K

Bond Lengths	Refined Value		DFT	Bond Angles	Refined Value		DFT
	[a]	[a]	[b]		[a]	[a]	[b]
C1-C2	1.551	± 0.016	1.535	C9-C1-C2	100.4	± 2.4	100.446
C2-C3	1.387	± 0.021	1.396	C1-C2-C7	109.1	± 2.8	108.811
C3-C4	1.404	± 0.022	1.416	C2-C7-N8	110.3	± 2.6	110.220
C4-C5	1.395	± 0.014	1.405	C7-N8-C9	108.5	± 2.7	108.682
C5-C6	1.402	± 0.020	1.413	N8-C9-C1	102.9	± 1.2	103.064
C6-C7	1.406	± 0.017	1.405	C3-C2-C7-C1	-10.6	± 1.5	-10.560
C7-N8	1.446	± 0.026	1.416	C6-C7-C2-N8	-7.7	± 2.3	-7.404
N8-C9	1.477	± 0.023	1.464	C4-C3-C2	119.4	± 1.2	119.268
C9-C10	1.508	± 0.013	1.516	C5-C4-C3	120.3	± 2.9	120.022
C10-C11	1.347	± 0.020	1.351	C6-C5-C4	121.3	± 1.6	121.221
C11-C12	1.460	± 0.011	1.466	C7-C6-C5	117.9	± 2.2	118.018
C12-C13	1.404	± 0.021	1.408	C1-C9-C10	115.7	± 0.9	115.668
C13-C14	1.400	± 0.018	1.410	N8-C9-O18	107.9	± 0.8	107.893
C14-C15	1.406	± 0.017	1.416	C10-C9-O18	111.3	± 1.4	111.416
C15-C16	1.393	± 0.019	1.398	C1-C9-O18	106.0	± 0.7	106.015
C16-C17	1.403	± 0.018	1.413	N8-C9-C10	112.3	± 1.5	112.140
C17-O18	1.365	± 0.011	1.364	C9-C10-C11	123.5	± 1.6	123.571
O18-C9	1.482	± 0.018	1.494	C10-C11-C12	121.4	± 1.5	121.348
C9-C1	1.620	± 0.014	1.602	C11-C12-C17	117.3	± 2.0	117.287
C2-C7	1.413	± 0.027	1.414	C12-C17-O18	122.1	± 1.6	122.115
C12-C17	1.407	± 0.019	1.422	C17-O18-C9	123.7	± 1.6	123.567
C1-C1a	1.550	± 0.036	1.561	C13-C12-C17-C11	-4.0	± 1.2	-4.064
C1-C1b	1.544	± 0.035	1.548	C16-C17-C12-O18	3.1	± 2.2	2.980
N8-C8a	1.476	± 0.026	1.467	C12-C13-C14	119.8	± 1.0	119.724
C14-N14a	1.429	± 0.049	1.415	C13-C14-C15	120.8	± 4.8	120.970
N14a-O14a1	1.333	± 0.039	1.319	C14-C15-C16	119.4	± 1.1	119.371
N14a-O14a2	1.331	± 0.038	1.319	C15-C16-C17	120.2	± 2.1	120.178
				C1a-C1-C2	108.5	± 1.6	108.547
				C1a-C1-C1b	109.4	± 1.0	109.505
				C1b-C1-C9	112.5	± 3.0	112.492
				C1a-C1-C9	111.0	± 1.5	110.904
				C1b-C1-C2	114.8	± 1.2	114.637
				C8a-N8-C7-C9	0.6	± 0.6	0.552
				N14a-C14-C13-C15	0.01	± 0.5	0.010
				O14a1-N14a-C14	123.7	± 2.2	123.753
				O14a2-N14a-C14- O14a1	17.8	± 1.8	17.907

*continued on next page*

<sup>[a]</sup> The error bars reported here are  $3\sigma$ .

<sup>[b]</sup> Theoretical structures were obtained using DFT at B3LYP/6-311G(*d, p*).

<sup>[c]</sup> If four atoms are listed, A1-A2-A3-A4, the angle is defined as

$$(A1-A2-A3)-(A1-A2-A4).$$

**Table 5.6.** Refined closed structure of 6-nitro-BIPS in the lowest triplet-state at 843 K (continued)

Dihedral Angles	Refined Value [a]			DFT [b]
C3-C4-C5-C6	-0.24	±	0.04	-0.243
C4-C5-C6-C7	0.395	±	0.06	0.396
C2-C3-C4-C5	0.10	±	0.10	0.098
C5-C6-C7-C2	-0.42	±	0.10	-0.415
C7-C2-C3-C4	-0.12	±	0.07	-0.117
C6-C7-C2-C3	0.3	±	0.07	0.283
C1-C2-C7-N8	-1.9	±	0.42	-1.829
C3-C2-C7-N8	-179.2	±	0.50	-179.238
C6-C7-C2-C1	177.7	±	0.45	177.692
C2-C7-N8-C9	-17.8	±	1.17	-17.855
C7-C2-C1-C9	18.3	±	1.12	18.351
C2-C1-C9-N8	-27.6	±	0.57	-27.651
C7-N8-C9-C1	28.5	±	1.50	28.612
C1a-C1-C9-N8	87.0	±	2.32	86.972
C1a-C1-C2-C7	-98.1	±	1.43	-98.043
C1b-C1-C9-N8	-150.1	±	0.92	-150.004
C1b-C1-C2-C7	139.2	±	1.54	139.183
C8a-N8-C7-C2	-162.9	±	1.13	-162.826
C8a-N8-C9-C1	173.8	±	0.79	173.810
C10-C9-C1-C2	-150.5	±	1.14	-150.387
C10-C9-N8-C7	153.6	±	1.11	153.675
O18-C9-C1-C2	85.6	±	1.49	85.598
O18-C9-N8-C7	-83.3	±	1.07	-83.259
C11-C10-C9-C1	-126.7	±	0.63	-126.750
C11-C10-C9-N8	115.5	±	0.57	115.457
C17-O18-C9-C1	136.6	±	0.84	136.572
C17-O18-C9-N8	-113.7	±	0.87	-113.564
C9-O18-C17-C12	-8.60	±	0.44	-8.558
C9-C10-C11-C12	-0.1	±	0.21	-0.124
C10-C9-O18-C17	10.0	±	0.68	9.942
C10-C11-C12-C17	2.5	±	0.33	2.457
O18-C9-C10-C11	-5.6	±	0.51	-5.600
O18-C17-C12-C11	1.81	±	0.14	1.818
O18-C17-C12-C13	-178.60	±	0.08	-178.594
C11-C12-C17-C16	-179.41	±	0.08	-179.402
C13-C12-C17-C16	0.19	±	0.04	0.186
C13-C14-C15-C16	0.795	±	0.05	0.796
C14-C15-C16-C17	-0.266	±	0.02	-0.265
C14-C13-C12-C17	0.333	±	0.02	0.334
C15-C16-C17-C12	-0.222	±	0.04	-0.220
C15-C14-C13-C12	-0.830	±	0.05	-0.831
N14a-C14-C15-C16	176.912	±	0.12	176.906
N14a-C14-C13-C12	-176.947	±	0.10	-176.941
O14a1-N14a-C14-C15	166.625	±	0.70	166.598
O14a1-N14a-C14-C13	-17.208	±	0.48	-17.232
O14a2-N14a-C14-C15	19.094	±	0.50	19.118
O14a2-N14a-C14-C13	-164.740	±	0.72	-164.712

**Table 5.7.** The refined structure of ground-state nitrobenzene

Parameters	Refined value <sup>[a]</sup>	Domenicano et al. <sup>[b]</sup>	Shishkov et al. <sup>[c]</sup>	Theoretical <sup>[d]</sup>
C1-C2, C6-C1	1.409 ± 0.009	1.3986	1.391	1.391
C2-C3, C5-C6	1.388 ± 0.024 <sup>[e]</sup>	1.3991		1.391
C3-C4, C4-C5	1.390 ± 0.009	1.3991		1.395
C-H	1.083	1.093	1.114	1.083
C1-N7	1.492 ± 0.001	1.486	1.478	1.481
N7-O8, N7-O9	1.219 ± 0.006	1.2234	1.218	1.223
C6-C1-C2	123.4 ± 0.8	123.4	125.1	122.3
C1-C2-C3, C5-C6-C1	117.3 ± 0.7 <sup>[e]</sup>	117.6	115.7	118.5
C2-C3-C4, C4-C5-C6	120.9 ± 0.7 <sup>[e]</sup>	120.6	122.5	120.2
C3-C4-C5	119.8 ± 0.6	120.18	118.3	120.3
C1-N7-O8, C1-N7-O9	116.4 ± 0.2	117.34	118.3	117.6
C2-C1-N7-O8	⟨0⟩ (28.7) <sup>[f]</sup>	⟨13.2⟩ (0) <sup>[f]</sup>	⟨22.7⟩ (0) <sup>[f]</sup>	0
V <sub>0</sub> (kcal mol <sup>-1</sup> ) <sup>[g]</sup>	3.1 ± 0.4	4	1.3	6.5

<sup>[a]</sup> C<sub>2v</sub> symmetry was used during the structural refinement. The error bars reported here are 3σ.

<sup>[b]</sup> Taken from Ref. [180](#).

<sup>[c]</sup> Taken from Ref. [181](#).

<sup>[d]</sup> Theoretical structures were obtained using DFT at B3LYP/6-311G(*d, p*).

<sup>[e]</sup> Dependent variables and *propagated errors*.

<sup>[f]</sup> Brackets denote the center values, while those in parenthesis are the population-weighted standard deviation. See text for detail.

<sup>[g]</sup> V<sub>0</sub> denotes rotational barrier along the torsional motion of nitro group.

**Table 5.8.** Refined structures of intermediates

Species	Parameters	Refined value <sup>[a]</sup>	Theoretical <sup>[b]</sup>
nitric oxide	N-O	1.148	1.148
phenoxy	C1-C2, C6-C1	$1.465 \pm 0.018^{[c]}$	1.452
	C2-C3, C5-C6	$1.382 \pm 0.018^{[c]}$	1.375
	C3-C4, C4-C5	$1.420 \pm 0.018^{[c]}$	1.408
	C-H	1.084	1.084
	C1-O7	$1.232 \pm 0.064$	1.251
	C6-C1-C2	116.9	116.9
	C1-C2-C3, C5-C6-C1	121.0	121.0
	C2-C3-C4, C4-C5-C6	120.2	120.2
	C3-C4-C5	120.7	120.7

<sup>[a]</sup>  $C_{2v}$  symmetry was used for the phenoxy radical. The N–O distance of nitric oxide and all structural parameters involving hydrogen atoms were fixed at DFT provided values. Only two structural parameters, the C–O bond length and the mean ring C–C bond distance were refined due to correlation difficulties; the individual ring C–C distances were defined from the mean refined value. The error bars reported here are  $3\sigma$ .

<sup>[b]</sup> Theoretical structures were obtained using DFT at B3LYP/6-311G(*d, p*).

<sup>[c]</sup> Dependent variables and *propagated errors*.

**Table 5.9.** Structural parameters of indole in the  $S_0$  state

	UED <sup>[a]</sup>	DFT
C1-C2	1.404 ± 0.004	1.397
C2-C3	1.392 ± 0.004	1.387
C3-C4	1.414 ± 0.004	1.408
C4-C5	1.391 ± 0.004	1.386
C5-C6	1.406 ± 0.006	1.404
C6-C1	1.428 ± 0.004	1.422
C6-C7	1.438 ± 0.006	1.436
C7-C8	1.376 ± 0.004	1.367
C8-N9	1.389 ± 0.001	1.382
N9-C1	1.388 ± 0.005	1.379
C6-C1-C2	122.3 ± 0.1	122.3
C1-C2-C3	117.4 ± 0.2	117.5
C2-C3-C4	121.2 ± 0.1	121.2
C3-C4-C5	121.2 ± 0.1	121.1
C4-C5-C6	119.0 ± 0.2	119.1
C5-C6-C1	118.8 ± 0.1	118.7
C1-C6-C7	107.0 ± 0.2	106.9
C6-C7-C8	107.2 ± 0.1	107.1
C7-C8-N9	109.5 ± 0.2	109.5
C8-N9-C1	109.2 ± 0.1	109.3
N9-C1-C6	107.1 ± 0.1	107.2
H2-C2		1.085
H3-C3		1.084
H4-C4		1.084
H5-C5		1.085
H7-C7		1.079
H8-C8		1.079
H9-N9		1.005
H2-C2-C1 – H2-C2-C3		0.3
H3-C3-C2 – H3-C3-C4		0.0
H4-C4-C3 – H4-C4-C5		-0.5
H5-C5-C4 – H5-C5-C3		0.2
H7-C7-C6 – H7-C7-C8		1.2
H8-C8-C7 – H8-C8-N9		9.6
H9-N9-C1 – H9-N9-C8		0.3

<sup>[a]</sup> Five general coordinates out of 10 bond lengths and 11 bending angles were fitted.

**Table 5.9.** Structural parameters of indole in the S0 state (continued)

UED	DFT
C6-C1-C2-C3	0.0
C1-C2-C3-C4	0.0
C2-C3-C4-C5	0.0
C3-C4-C5-C6	0.0
C4-C5-C6-C1	0.0
C5-C6-C1-C2	0.0
C6-C7-C8-N9	0.0
C7-C8-N9-C1	0.0
C8-N9-C1-C6	0.0
N9-C1-C6-C7	0.0
C1-C6-C7-C8	0.0
C4-C5-C6-C7	180.0
C5-C6-C7-C8	180.0
N9-C1-C2-C3	180.0
C8-N9-C1-C2	180.0
C2-C1-C6-C7	180.0
C5-C6-C1-N9	180.0
H2-C2-C1-C3	180.0
H3-C3-C2-C4	180.0
H4-C4-C3-C5	180.0
H5-C5-C4-C3	180.0
H7-C7-C6-C8	180.0
H8-C8-C7-N9	180.0
H9-N9-C1-C8	180.0

**Table 5.10.** Structural parameters of indole in the T<sub>1</sub> state

	UED <sup>[a]</sup>	DFT
C1-C2	1.377 ± 0.039	1.376
C2-C3	1.488 ± 0.036	1.483
C3-C4	1.353 ± 0.032	1.371
C4-C5	1.405 ± 0.044	1.417
C5-C6	1.469 ± 0.034	1.457
C6-C1	1.439 ± 0.040	1.432
C6-C7	1.389 ± 0.021	1.382
C7-C8	1.450 ± 0.015	1.440
C8-N9	1.368 ± 0.013	1.372
N9-C1	1.405 ± 0.024	1.391
C6-C1-C2	122.8 ± 1.3	123.4
C1-C2-C3	116.6 ± 2.1	116.5
C2-C3-C4	121.9 ± 1.7	121.5
C3-C4-C5	122.1 ± 2.0	121.8
C4-C5-C6	118.2 ± 0.9	118.1
C5-C6-C1	118.5 ± 0.6	118.7
C1-C6-C7	107.7 ± 0.7	107.8
C6-C7-C8	108.5 ± 0.5	108.5
C7-C8-N9	106.3 ± 0.9	106.2
C8-N9-C1	111.2 ± 0.5	111.0
N9-C1-C6	106.2 ± 1.7	106.4
H2-C2		1.082
H3-C3		1.083
H4-C4		1.085
H5-C5		1.082
H7-C7		1.080
H8-C8		1.075
H9-N9		1.007
H2-C2-C1 – H2-C2-C3		2.4
H3-C3-C2 – H3-C3-C4		-1.9
H4-C4-C3 – H4-C4-C5		0.4
H5-C5-C4 – H5-C5-C3		0.9
H7-C7-C6 – H7-C7-C8		2.4
H8-C8-C7 – H8-C8-N9		8.7
H9-N9-C1 – H9-N9-C8		-0.6

<sup>[a]</sup> Four general coordinates out of 10 bond lengths and 11 bending angles were fitted.

**Table 5.10.** Structural parameters of indole in the T1 state (continued)

	UED	DFT
	C6-C1-C2-C3	0.0
	C1-C2-C3-C4	0.0
	C2-C3-C4-C5	0.0
	C3-C4-C5-C6	0.0
	C4-C5-C6-C1	0.0
	C5-C6-C1-C2	0.0
	C6-C7-C8-N9	0.0
	C7-C8-N9-C1	0.0
	C8-N9-C1-C6	0.0
	N9-C1-C6-C7	0.0
	C1-C6-C7-C8	0.0
	C4-C5-C6-C7	180.0
	C5-C6-C7-C8	180.0
	N9-C1-C2-C3	180.0
	C8-N9-C1-C2	180.0
	C2-C1-C6-C7	180.0
	C5-C6-C1-N9	180.0
	H2-C2-C1-C3	180.0
	H3-C3-C2-C4	180.0
	H4-C4-C3-C5	180.0
	H5-C5-C4-C3	180.0
	H7-C7-C6-C8	180.0
	H8-C8-C7-N9	180.0
	H9-N9-C1-C8	180.0

**Table 5.11.** Refined structure of ground-state L-tryptophan at 1000 K

	Structural Coordinate <sup>[a]</sup>	Refined Value <sup>[b]</sup>	DFT <sup>[c]</sup>	
			(80°,58°,229°) Conformer	Ensemble Average <sup>[d]</sup>
Bond Lengths	C1-C2	1.419 ± 0.002	1.401	1.401
	C2-C3	1.409 ± 0.002	1.395	1.395
	C3-C4	1.430 ± 0.002	1.414	1.414
	C4-C5	1.408 ± 0.001	1.394	1.394
	C1-C6	1.440 ± 0.001	1.428	1.428
	C5-C6	1.425 ± 0.002	1.408	1.408
	C6-C7	1.464 ± 0.003	1.450	1.451
	C7-C8	1.389 ± 0.003	1.378	1.379
	C1-N9	1.402 ± 0.002	1.390	1.389
	C8-N9	1.404 ± 0.002	1.394	1.394
	C7-C71	1.530 ± 0.001	1.502	1.504
	C71-C72	1.580 ± 0.001	1.549	1.552
	C72-N73a	1.487 ± 0.001	1.465	1.460
	C72-C73	1.558 ± 0.001	1.526	1.529
	C73-O73a	1.244 ± 0.002	1.233	1.235
	C73-O73b	1.400 ± 0.001	1.390	1.384
Bond Angles <sup>[e]</sup>	C6-C1-C2	122.25 ± 0.71	122.22	122.24
	C3-C2-C1	117.53 ± 0.62	117.56	117.58
	C4-C3-C2	121.18 ± 0.91	121.19	121.16
	C5-C4-C3	121.05 ± 0.51	121.05	121.10
	C6-C5-C4	119.08 ± 0.59	119.08	119.06
	C5-C6-C1	118.91 ± 1.04	118.88	118.86
	C8-C7-C6	106.54 ± 0.89	106.56	106.59
	N9-C8-C7	109.85 ± 0.95	109.81	109.71
	C8-N9-C1	109.27 ± 1.27	109.23	109.35
	C72-C71-C7	113.96 ± 0.97	113.93	114.62
	N73a-C72-C71	110.05 ± 1.00	110.03	110.59
	C73-C72-C71	111.99 ± 0.48	111.99	110.54
	C73-C72-N73a	111.10 ± 0.22	111.10	112.85
	O73a-C73-C72	126.71 ± 0.42	126.60	126.03
	O73b-C73-C72-O73a	-9.66 ± 0.28	-9.71	-9.50
	N9-C1-C2-C6	23.73 ± 0.20	23.69	23.73
	C7-C6-C1-C5	-26.44 ± 0.10	-26.42	-26.45
C71-C7-C6-C8	-0.23 ± 0.26	-0.22	-1.17	

*continued on next page*

**Table 5.11.** Refined structure of ground-state L-tryptophan at 1000 K (continued)

	Structural Coordinate <sup>[a]</sup>	Refined Value <sup>[b]</sup>	DFT <sup>[c]</sup>	
			(80°,58°,229°) Conformer	Ensemble Average <sup>[d]</sup>
Dihedral Angles	C5-C4-C3-C2	-0.19 ± 0.09	-0.190	-0.068
	C5-C6-C1-C2	-0.25 ± 0.27	-0.252	-0.036
	C3-C2-C1-C6	0.08 ± 0.19	0.080	0.016
	C3-C4-C5-C6	0.01 ± 0.11	0.013	0.047
	C1-C6-C5-C4	0.20 ± 0.12	0.199	0.004
	C1-C2-C3-C4	0.14 ± 0.16	0.140	0.036
	C3-C2-C1-N9	180.23 ± 0.14	180.230	180.155
	C7-C6-C5-C4	179.73 ± 0.07	179.734	179.774
	C5-C6-C1-N9	179.63 ± 0.14	179.629	179.853
	C7-C6-C1-C2	180.10 ± 0.16	180.100	180.138
	C8-C7-C6-C1	-0.02 ± 0.22	-0.025	-0.059
	N9-C8-C7-C6	0.06 ± 0.17	0.060	0.068
	C1-N9-C8-C7	-0.07 ± 0.14	-0.074	-0.053
	C8-N9-C1-C6	0.06 ± 0.27	0.056	0.014
	C7-C6-C1-N9	-0.02 ± 0.14	-0.019	0.027
	C8-C7-C6-C5	180.40 ± 0.24	180.401	180.153
	C8-N9-C1-C2	179.92 ± 0.14	179.923	179.891
	C71-C7-C6-C1	181.16 ± 0.42	181.162	180.563
	C71-C7-C6-C5	1.59 ± 0.16	1.588	0.774
	N9-C8-C7-C71	178.87 ± 0.19	178.870	179.426
	C72-C71-C7-C6	-	80.448	174.224
	C72-C71-C7-C8	-	261.869	125.888
	N73a-C72-C71-C7	-	182.336	169.106
	C73-C72-C71-C7	-	58.241	174.281
	O73a-C73-C72-C71	-	228.631	196.562
	O73a-C73-C72-N73a	-	105.137	203.004
	O73b-C73-C72-C71	-	53.103	180.177
	O73b-C73-C72-N73a	-	289.609	186.619

<sup>[a]</sup> The atomic labels are shown in Figure 5.29.

<sup>[b]</sup> The error bars reported here are  $3\sigma$ .

<sup>[c]</sup> Theoretical structures were obtained using DFT at B3LYP/6-311G(*d, p*).

<sup>[d]</sup> Unweighted average of eleven conformers (see Figure 5.26).

<sup>[e]</sup> If four atoms are listed, A1-A2-A3-A4, the angle is defined as

$$(A1-A2-A3)-(A1-A2-A4).$$

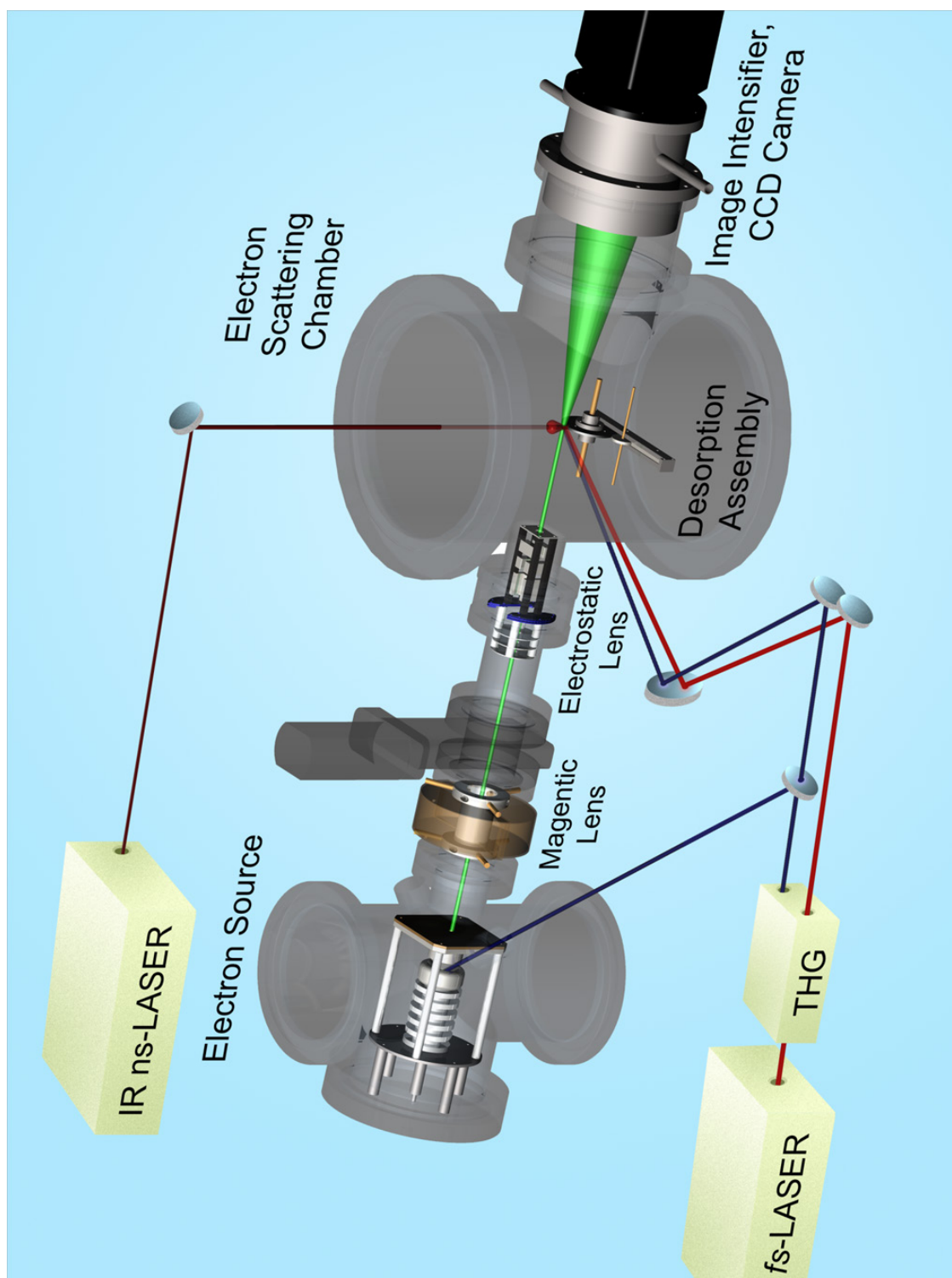


**Figure 5.1.** Schematic illustration of the electron diffraction-laser desorption (UED4) apparatus. We note that besides the two fs lasers used in UED studies,<sup>1,2,5,7</sup> here an additional third laser is used to desorb the molecules into the gas phase. See text for details.

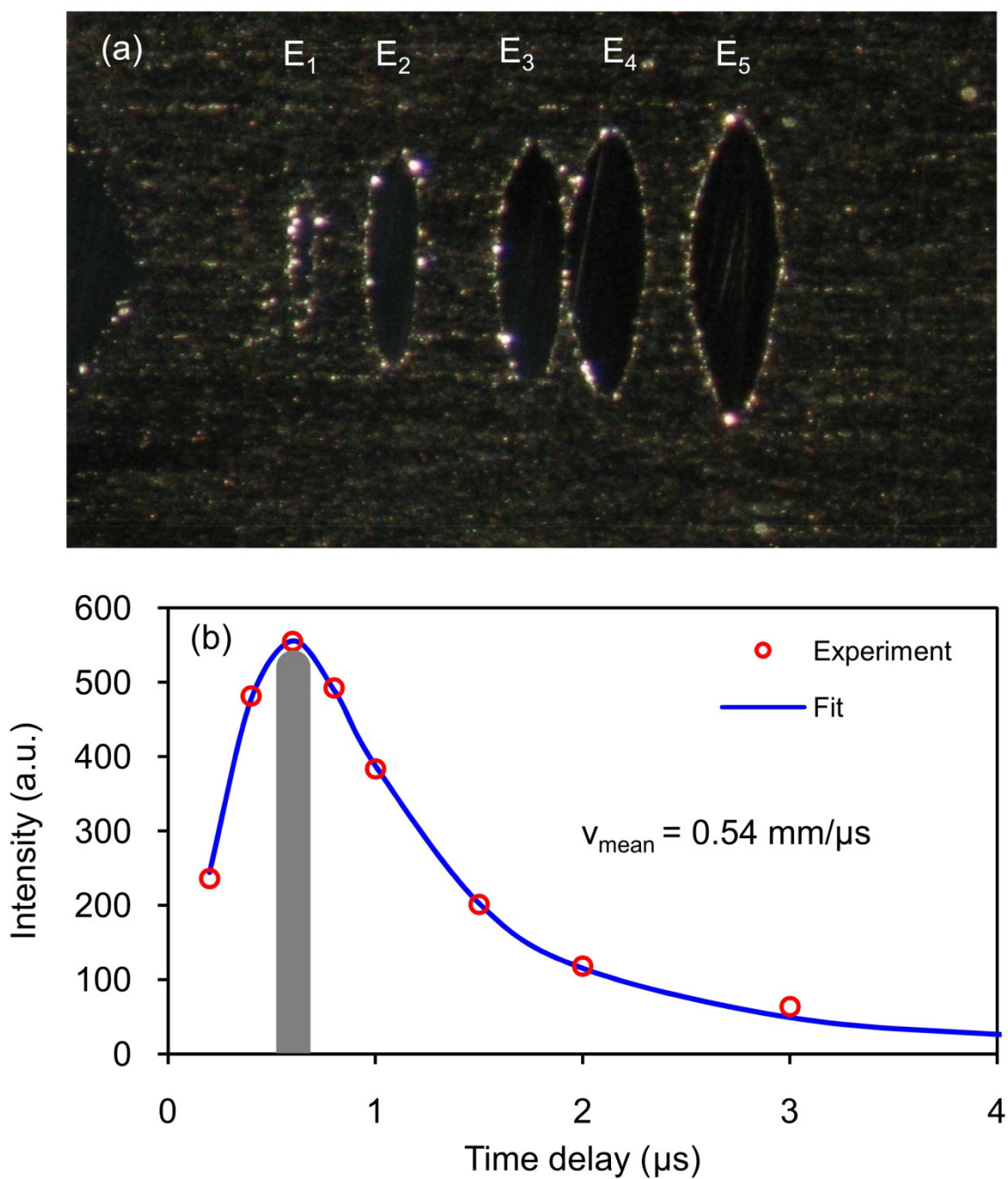


**Figure 5.2.** Image and intensity of the plume. (a) Image of the substrate after single shots of IR laser at different pulse energies:  $E_1=90 \mu\text{J}$ ,  $E_2=170 \mu\text{J}$ ,  $E_3=260 \mu\text{J}$ ,  $E_4=340 \mu\text{J}$ ,  $E_5=420 \mu\text{J}$ ; (b) Scattering intensity as a function of the time delay between the desorption laser and the electron pulse.

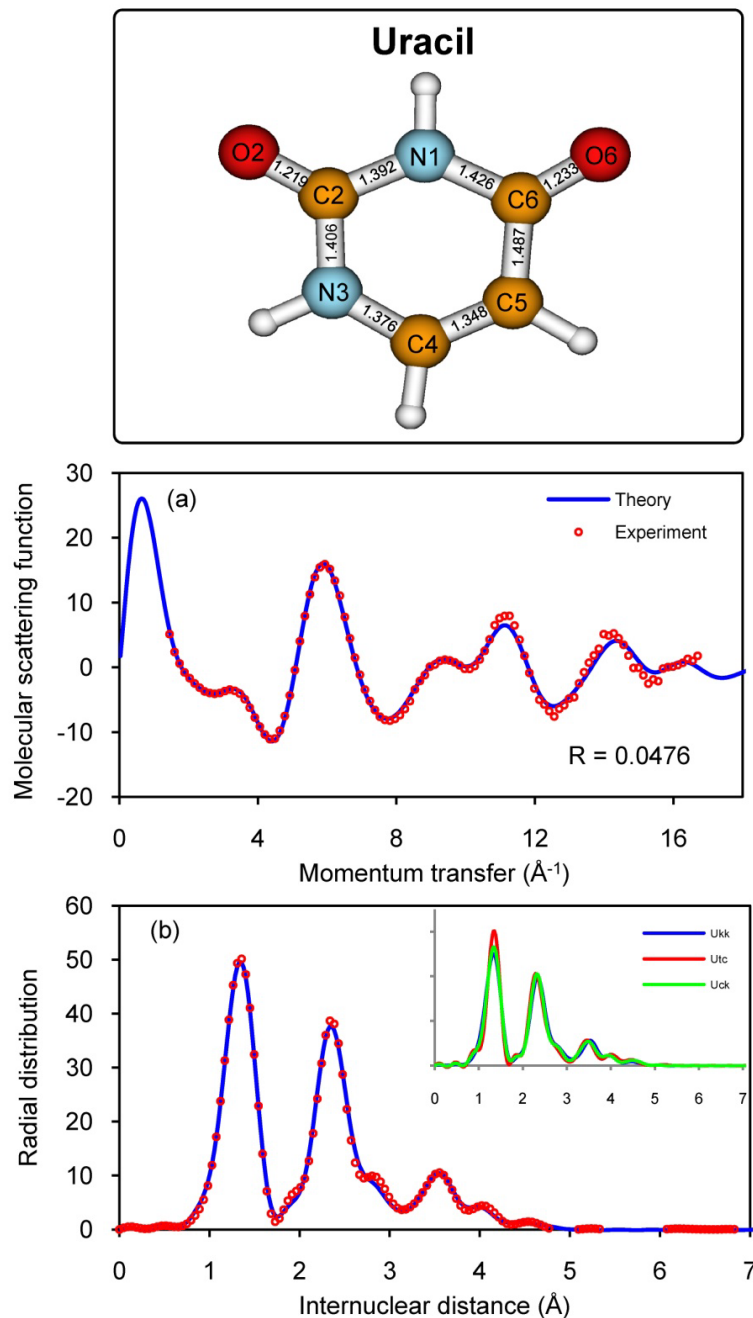


**Figure 5.3.** Diffraction of uracil. Shown are (a) the molecular scattering function,  $sM(s)$ , and (b) the radial distribution,  $f(r)$ , for the experimental (points) and theoretical (line) curves, together with theoretical results for the different tautomers. Also shown are the molecular structure of uracil and the atomic designations. As in a previous study,<sup>5</sup> the number of independent structural parameters included in the refinement was chosen, such that the experimental noise did not affect the determined bond lengths and angles beyond the well-known chemical structural information of, e.g., C-C bonds, etc.; four parameters were used to refine the structure of uracil.

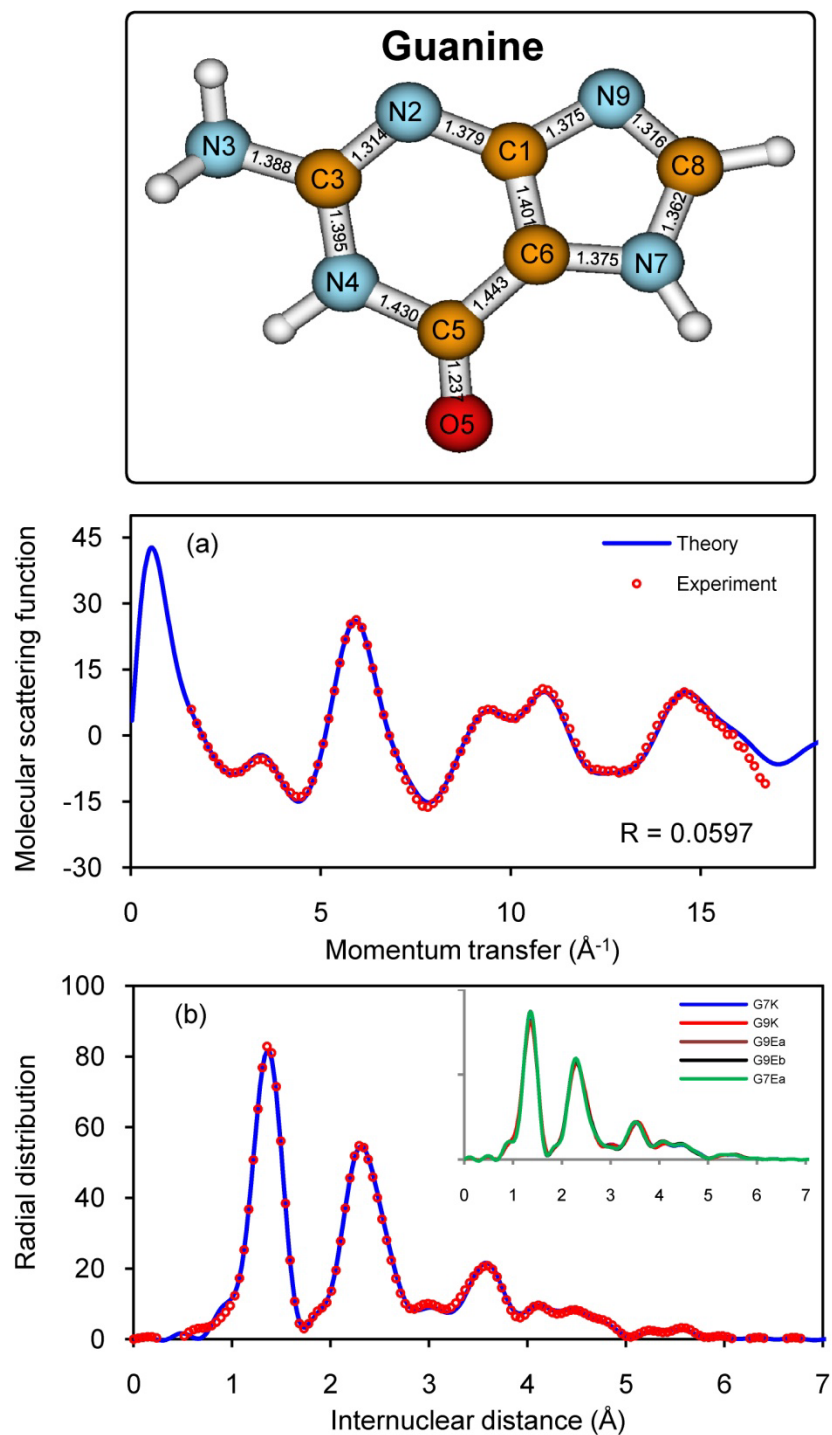


**Figure 5.4.** Diffraction of guanine. Shown are (a) the molecular scattering function,  $sM(s)$ , and (b) the radial distribution,  $f(r)$ , for the experimental (points) and theoretical (line) curves, together with theoretical results for the different tautomers. Also shown are the molecular structure of guanine and the atomic designations. Two independent parameters were used to refine the structure of guanine (see Figure 5.3).

## Photo-switchable Molecular Conformations

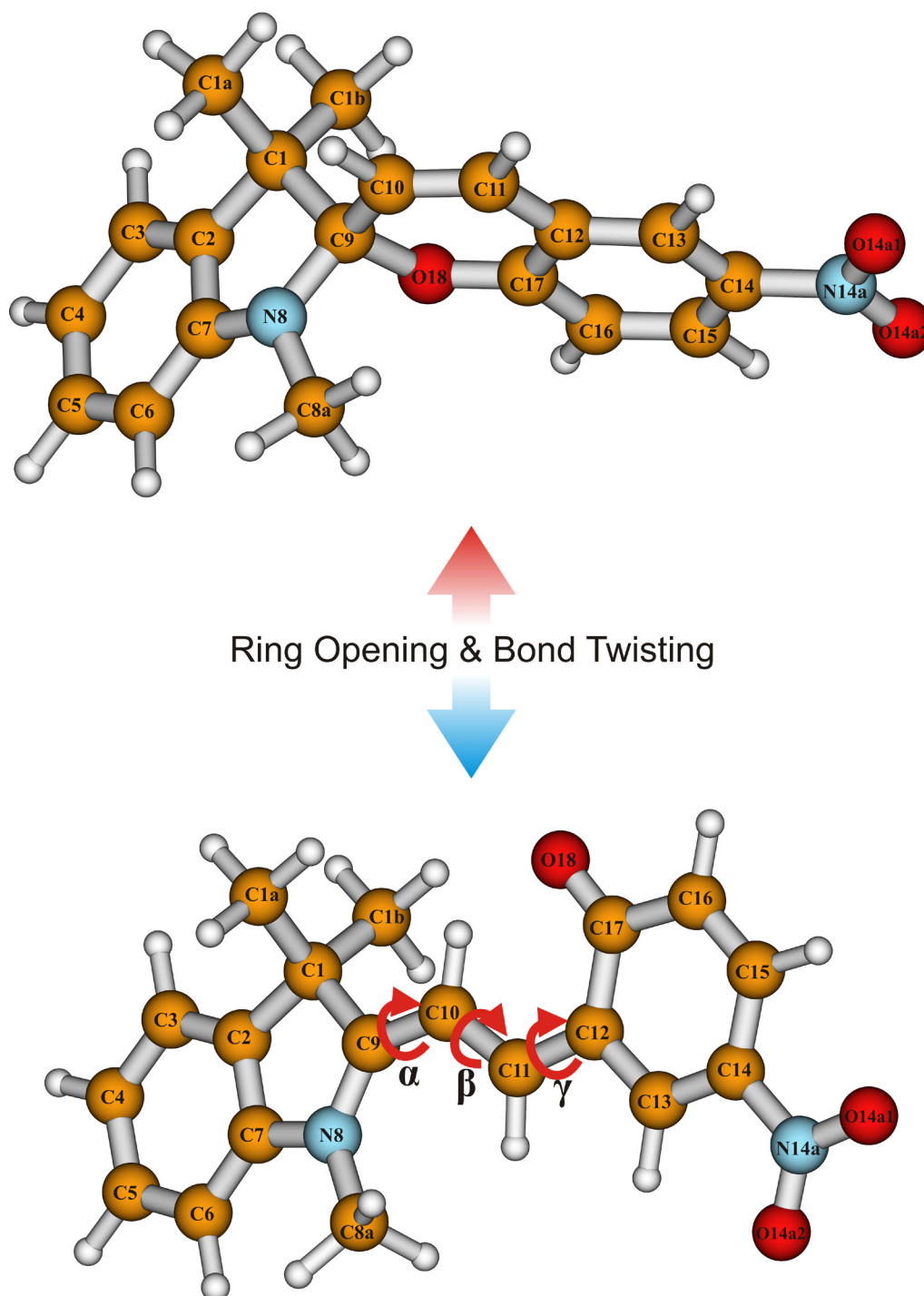


**Figure 5.5.** Structures of the photoswitchable closed and open *cis-trans-cis* form of 6-nitro-BIPS. The open structures, formed after photoexcitation, are labeled by the *cis* (C) or *trans* (T) configuration of the indicated dihedral angles ( $\alpha\beta\gamma$ ) in the bridge segment.

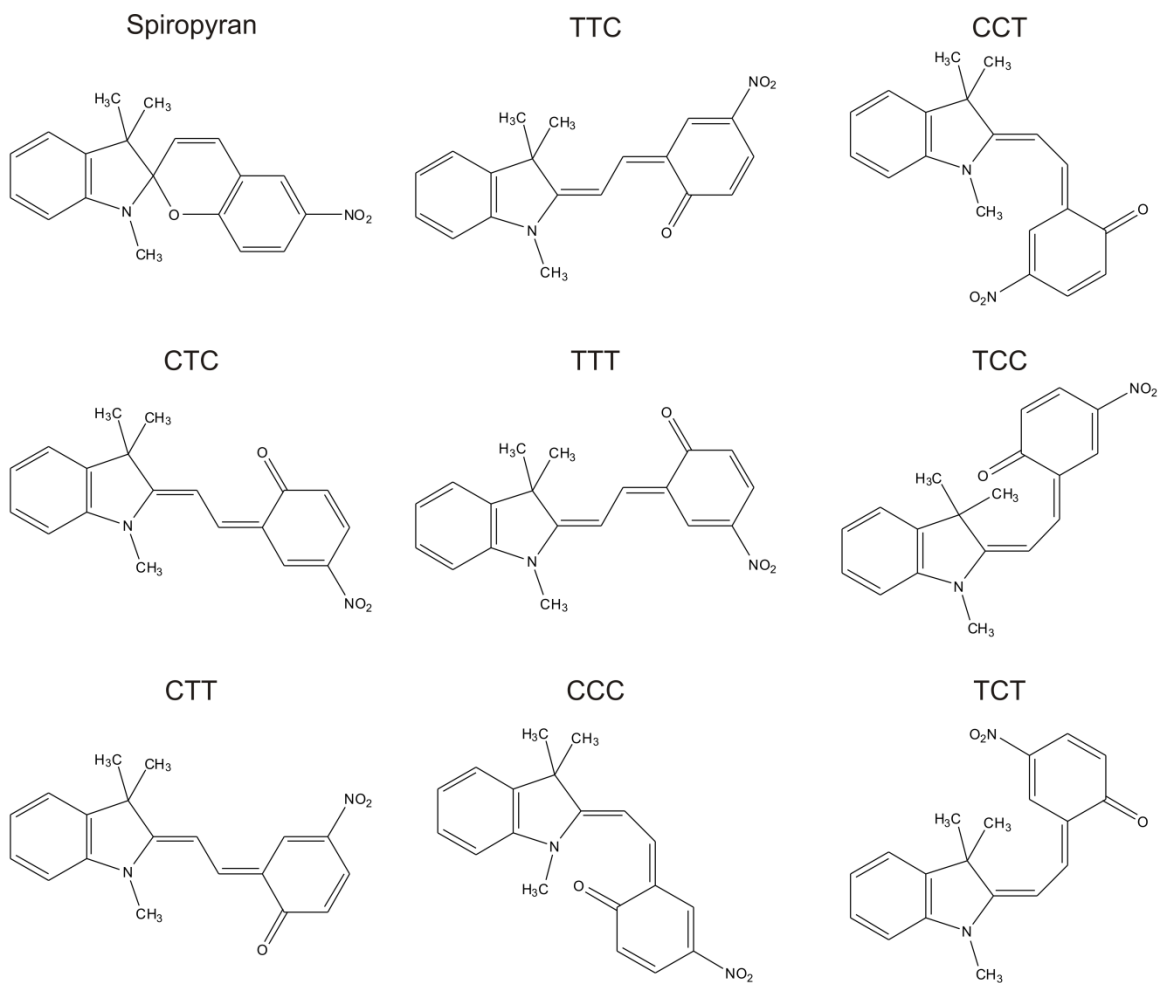


**Figure 5.6.** Chemical structures of the spiropyran and merocyanine forms considered in the analysis of the electron diffraction data of 6-nitro-BIPS. For each structure (except TCC) the lowest singlet and triplet electronic state geometries and vibrational frequencies were calculated.

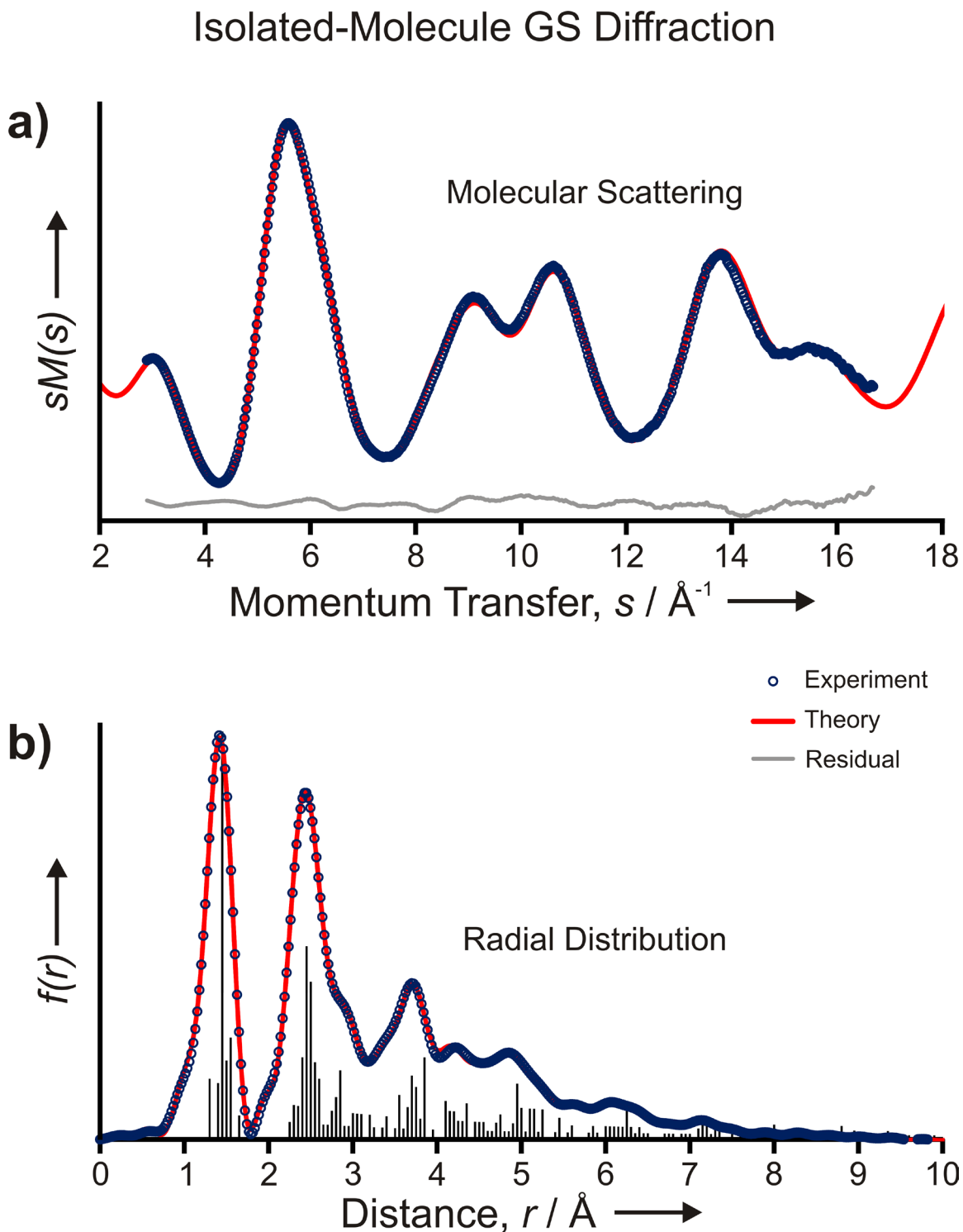


**Figure 5.7.** Diffraction results of the ground-state (GS) structure of 6-nitro-BIPS. Shown are a) the molecular scattering function,  $sM(s)$ , and b) the radial distribution,  $f(r)$ , for the experimental (circles) and theoretical (line) curves. Also shown is a weighted histogram of all the internuclear distances measured in the diffraction experiment.

## Isolated-Molecule ES-products Diffraction

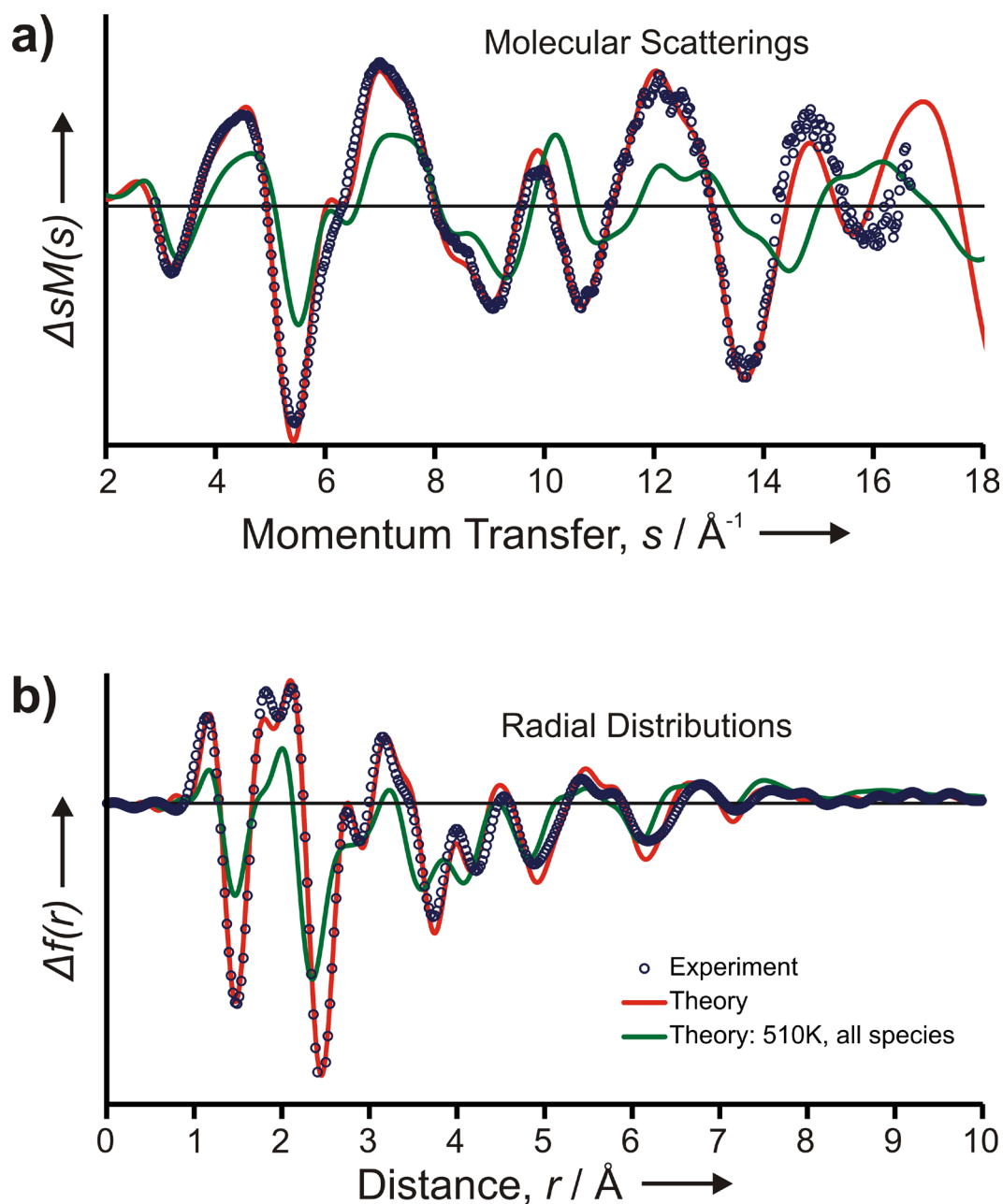


**Figure 5.8.** Diffraction results of the excited state(ES)-products structures of 6-nitro-BIPS, following ultraviolet excitation. Shown are a) frame-referenced molecular scattering function,  $\Delta sM(s; t = +100 \text{ ns}, t_{ref} = -100 \text{ ns})$ , and b) the frame-referenced radial distribution,  $\Delta f(r; t = +100 \text{ ns}, t_{ref} = -100 \text{ ns})$ , for the experimental (circles) and theoretical (line) curves. Also shown in green are the difference curves, where all species are held at the temperature of the ground state (510 K), to highlight the contribution due to structural rearrangement.

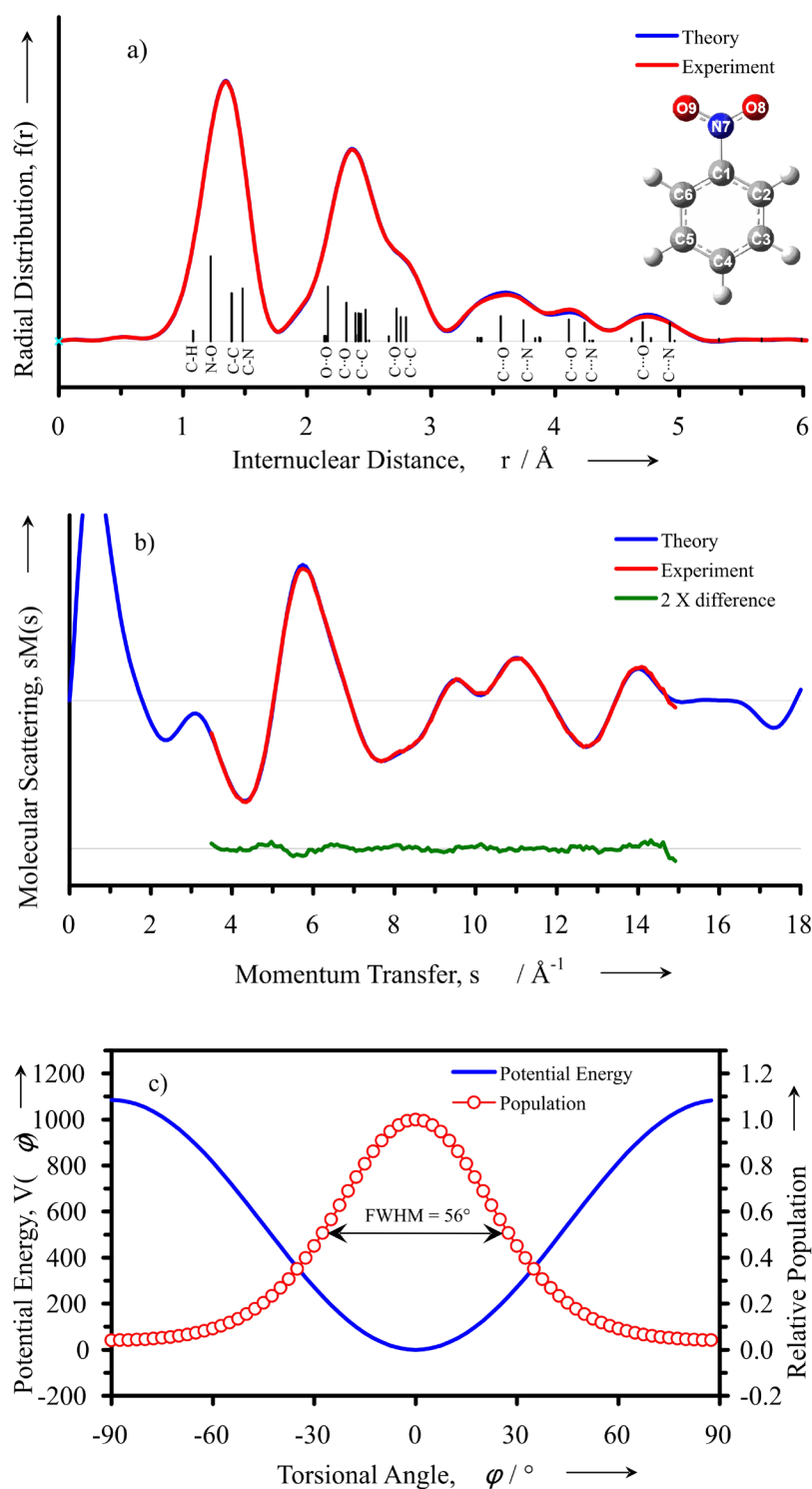


**Figure 5.9.** (a) Radial distribution curve,  $f(r)$ , (b) molecular scattering,  $sM(s)$ , and (c) the rotational population and the potential energy curve along the torsional angle, for ground state nitrobenzene. Theoretical (blue) and experimental (red) curves match with  $R = 0.023$ .

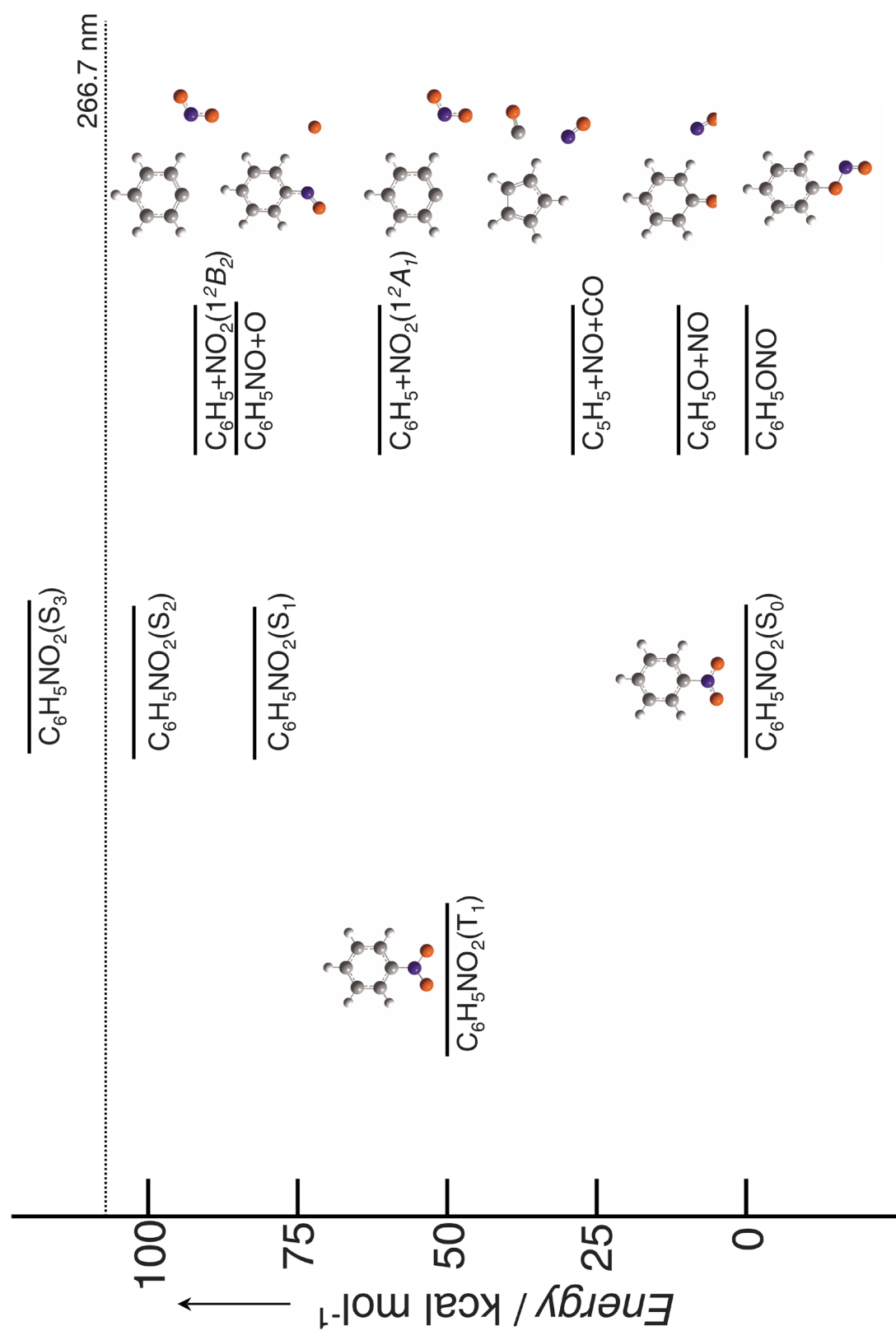


**Figure 5.10.** Energy diagram of excited states and chemical channels of nitrobenzene.

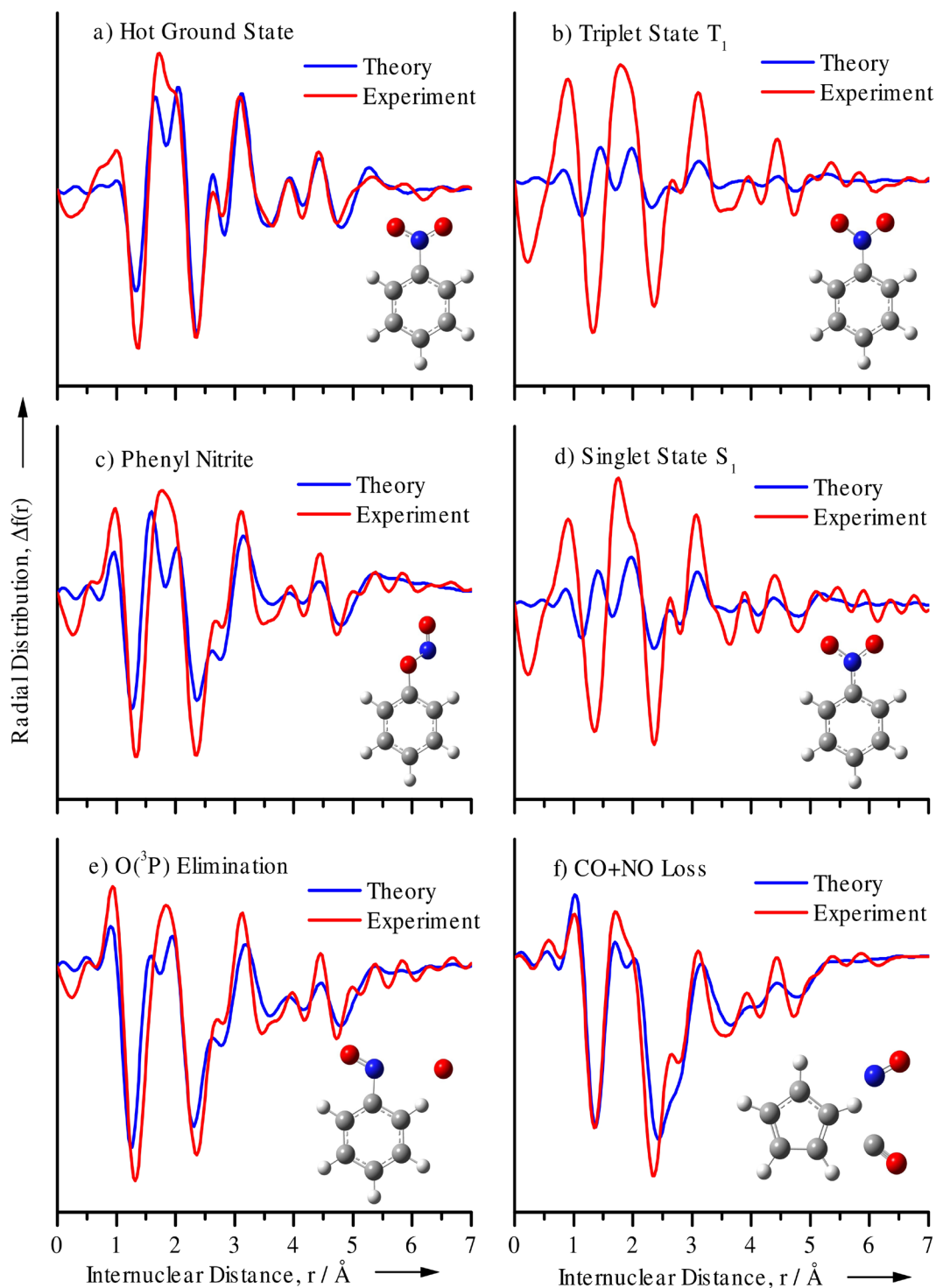


**Figure 5.11.** Radial distribution curves,  $\Delta f(r; t = +1 \text{ ns}, t_{ref} = -100 \text{ ps})$ , for trial fits of different reaction pathways. The product channels are: (a) “hot” ground state C6H5NO2; (b) triplet ( $T_1$ ,  ${}^3\pi\pi^*$ ) C6H5NO2; (c) phenylnitrite (C6H5ONO); (d)  $S_1$  ( ${}^1n\pi^*$ ) C6H5NO2; (e) C6H5NO + O(^3P); and (f) C5H5 + CO + NO.

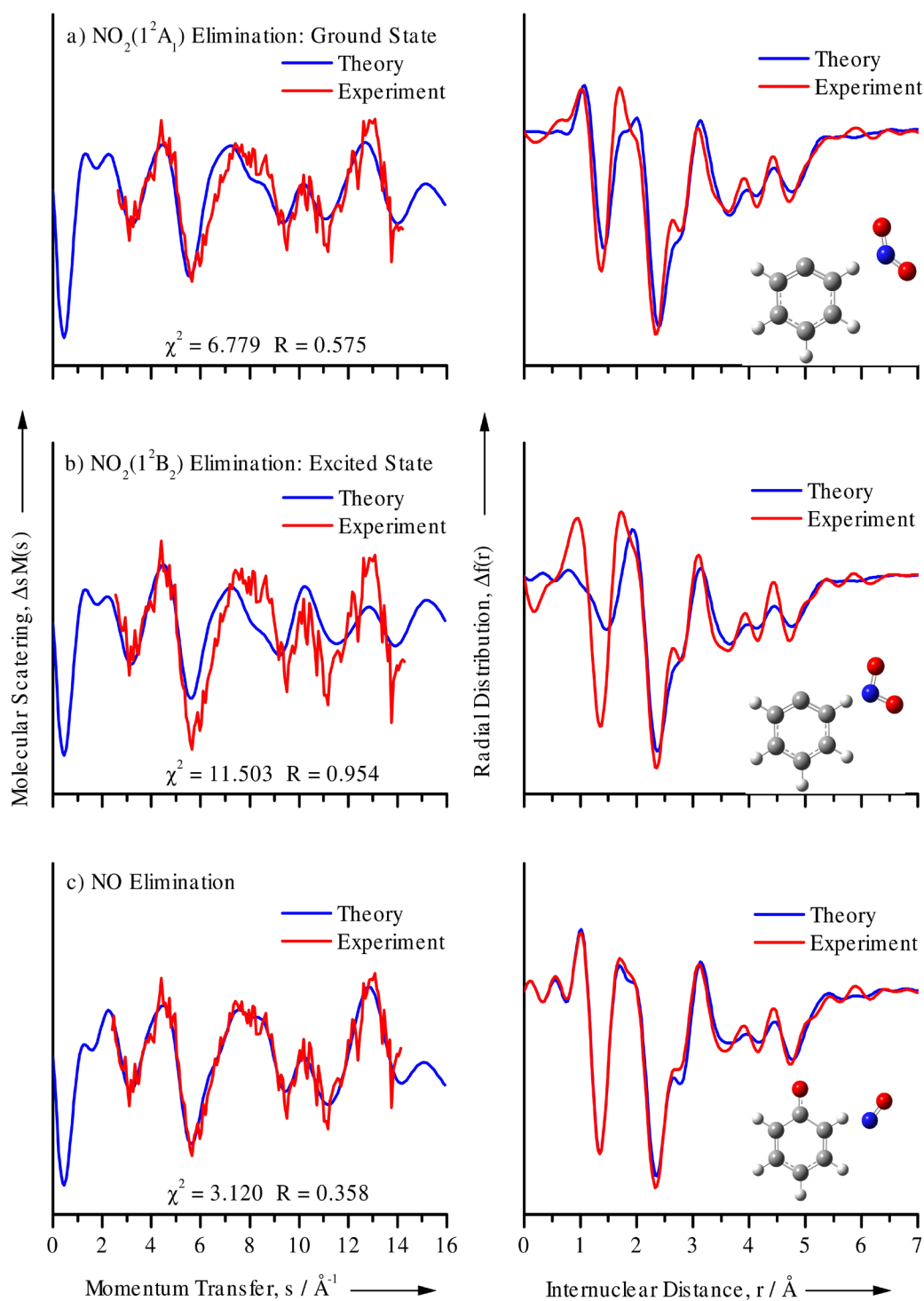


**Figure 5.12.** Molecular scattering curves,  $\Delta sM(s; t = +1 \text{ ns}, t_{ref} = -100 \text{ ps})$ , and radial distribution curves,  $\Delta f(r; t = +1 \text{ ns}, t_{ref} = -100 \text{ ps})$ , for trial fits of  $\text{NO}_2$  and NO elimination reactions: (a)  $\text{C}_6\text{H}_5 + \text{NO}_2(1^2A_1)$ ; (b)  $\text{C}_6\text{H}_5 + \text{NO}_2(1^2B_2)$ ; and (c)  $\text{C}_6\text{H}_5\text{O} + \text{NO}$ .

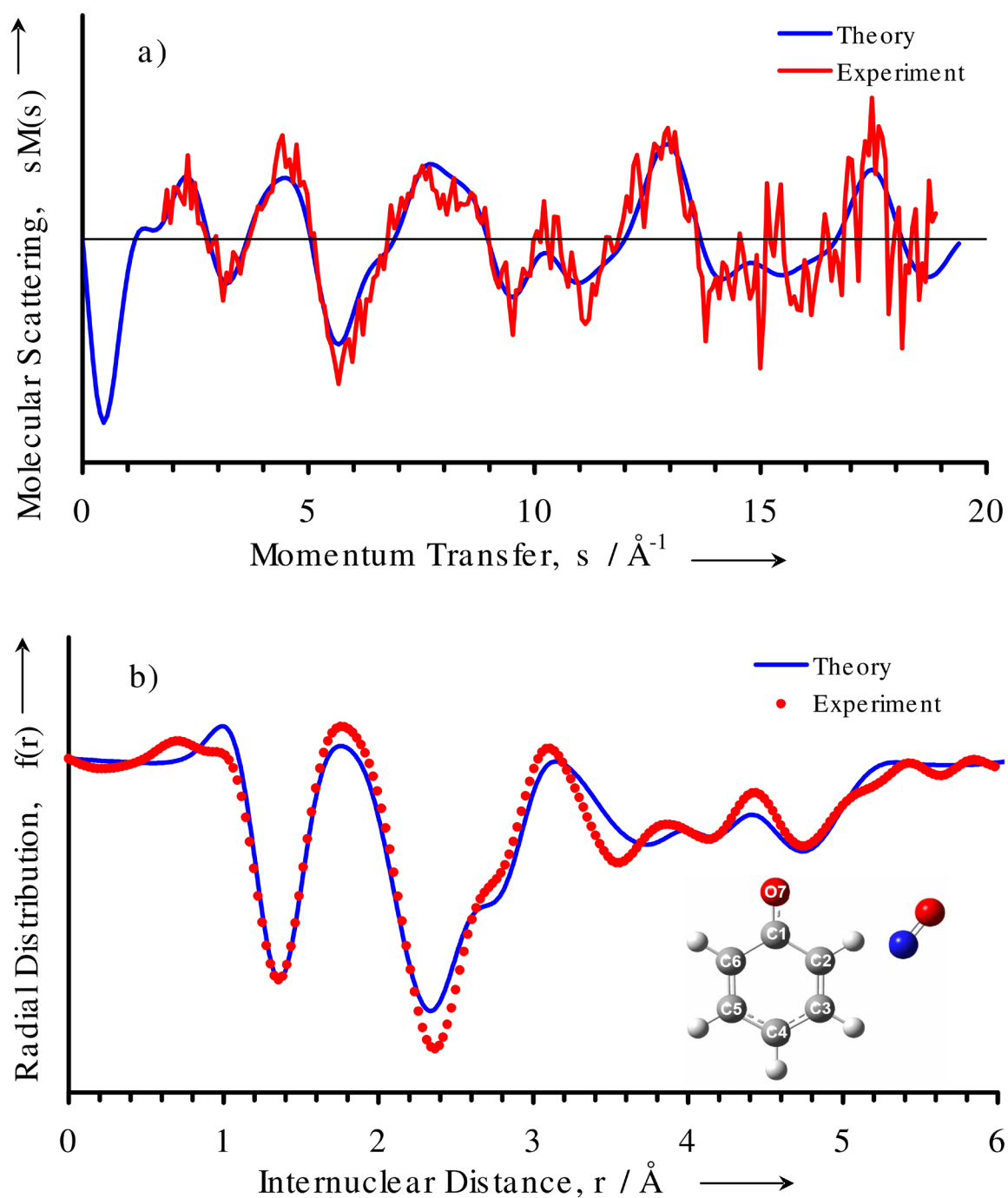


**Figure 5.13.** (a) Frame-referenced modified molecular scattering curves,  $\Delta sM(s;t)$ , and (b) frame-referenced radial distributions,  $\Delta f(r;t)$  for nitrobenzene (266.7 nm excitation) at  $t = +1$  ns ( $t_{ref} = -100$  ps) along with the refined theoretical curves corresponding to the reaction products phenoxyl and NO radicals. The experimental data points are shown as a red line and the refined theory is a blue line.  $R = 0.375$ .

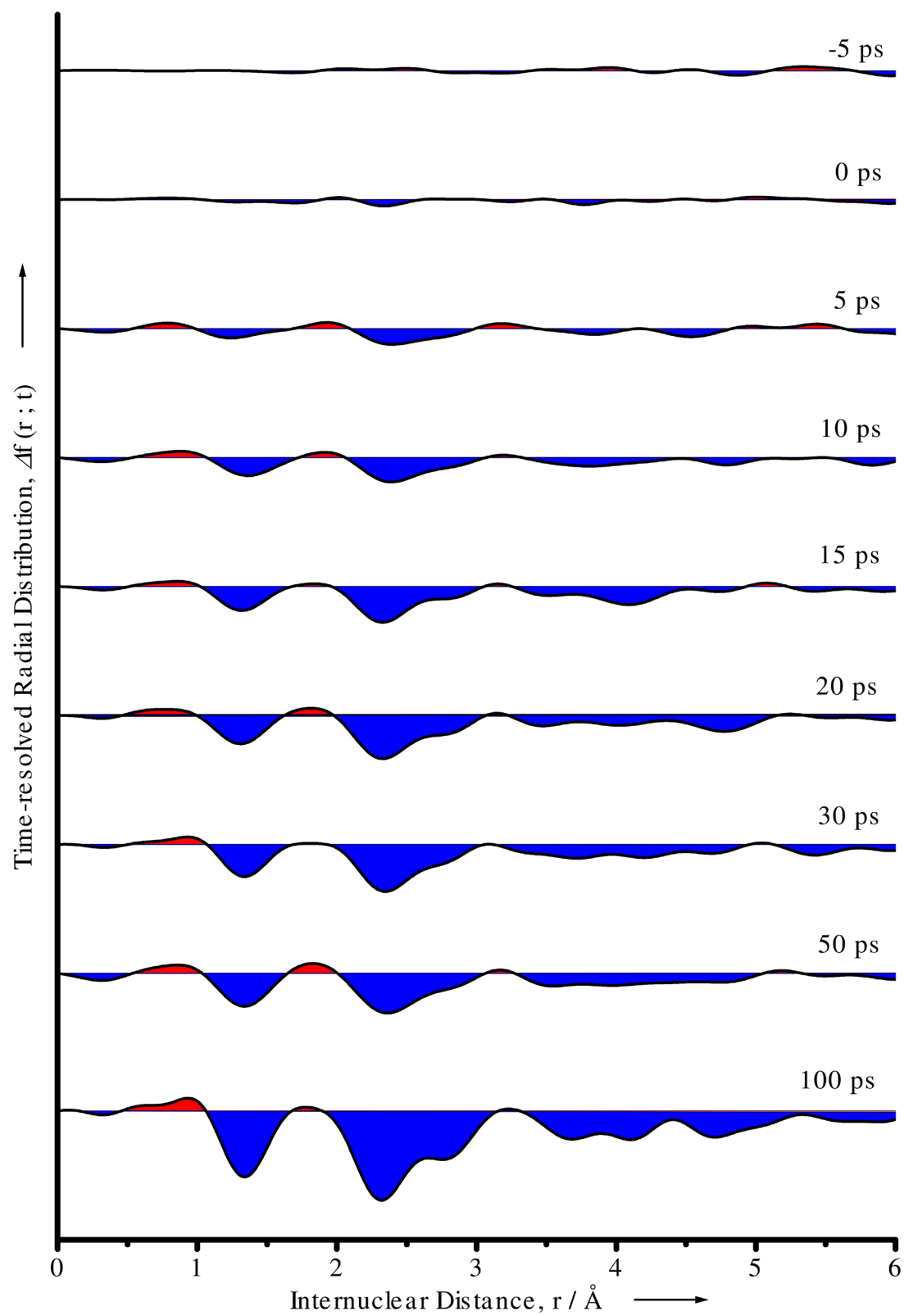


**Figure 5.14.** The experimental  $\Delta f(r;t)$  with the time steps indicated.

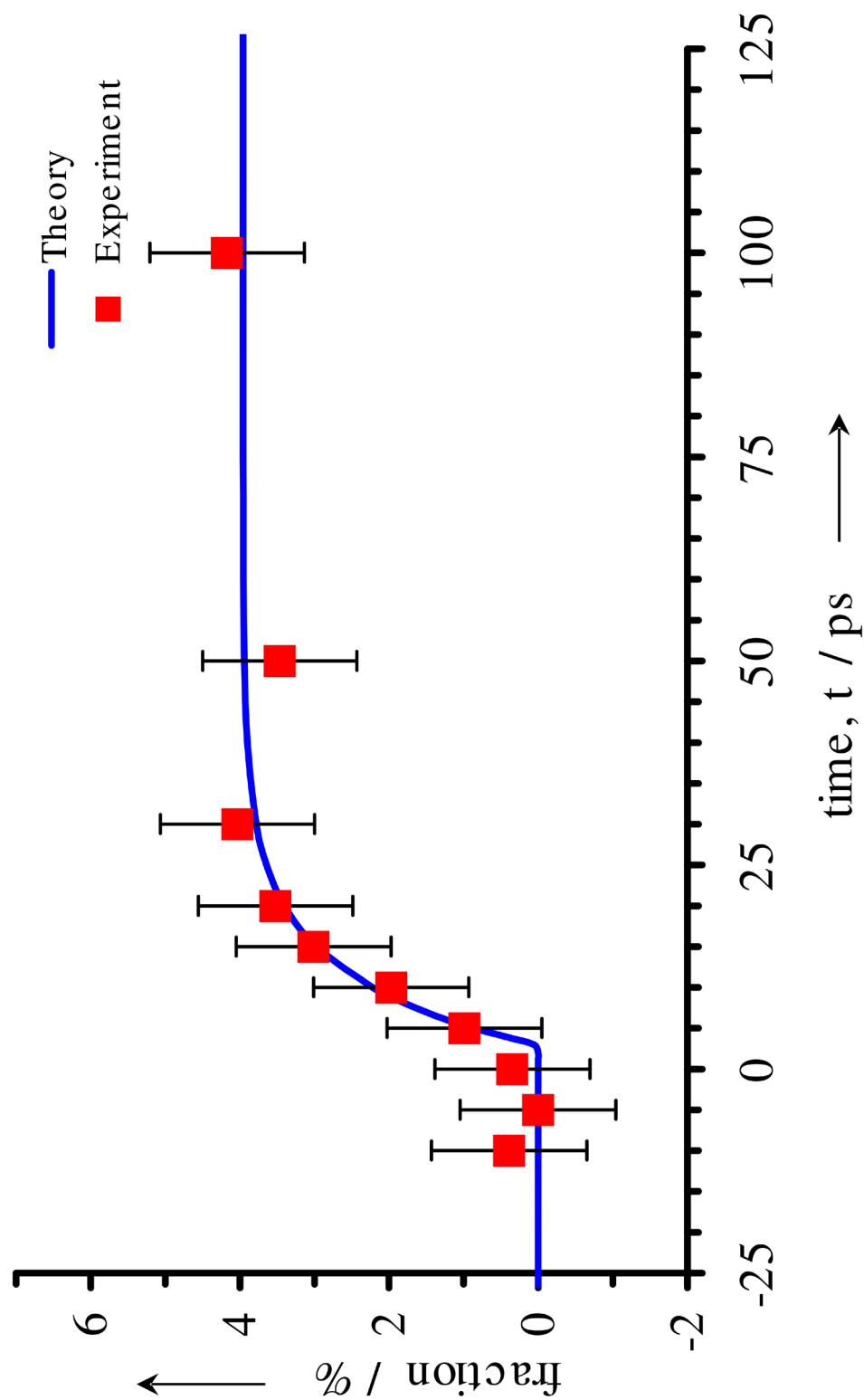


**Figure 5.15.** The temporal dependence of the product fraction in the reaction  $\text{C}_6\text{H}_5\text{NO}_2 \rightarrow \text{C}_6\text{H}_5\text{O} + \text{NO}$ . Nonlinear fitting of a single step reaction yields a time constant of  $8.8 \pm 2.2$  ps.

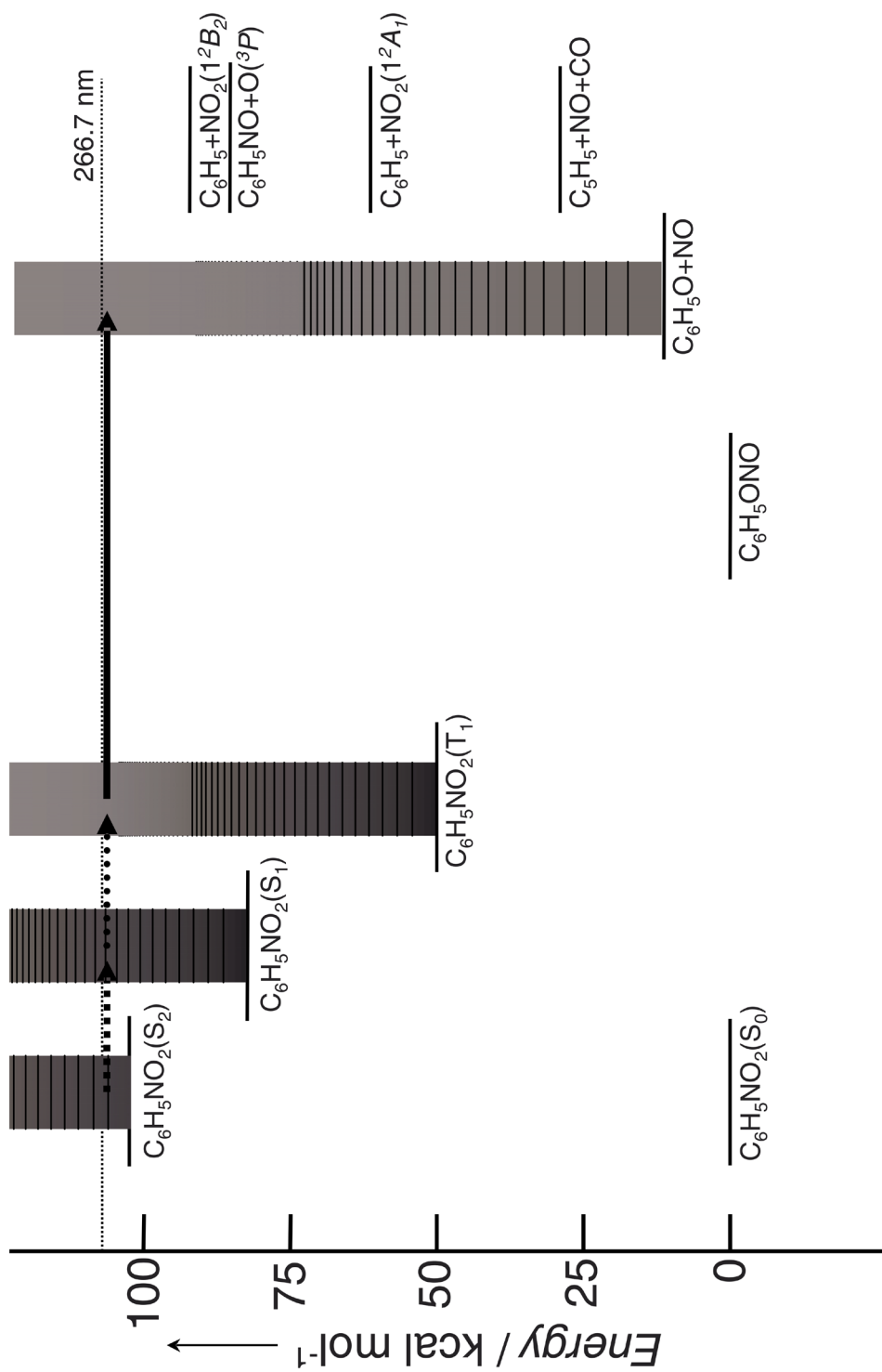


**Figure 5.16.** Possible photophysical and photochemical pathways of nitrobenzene upon 266.7 nm excitation.

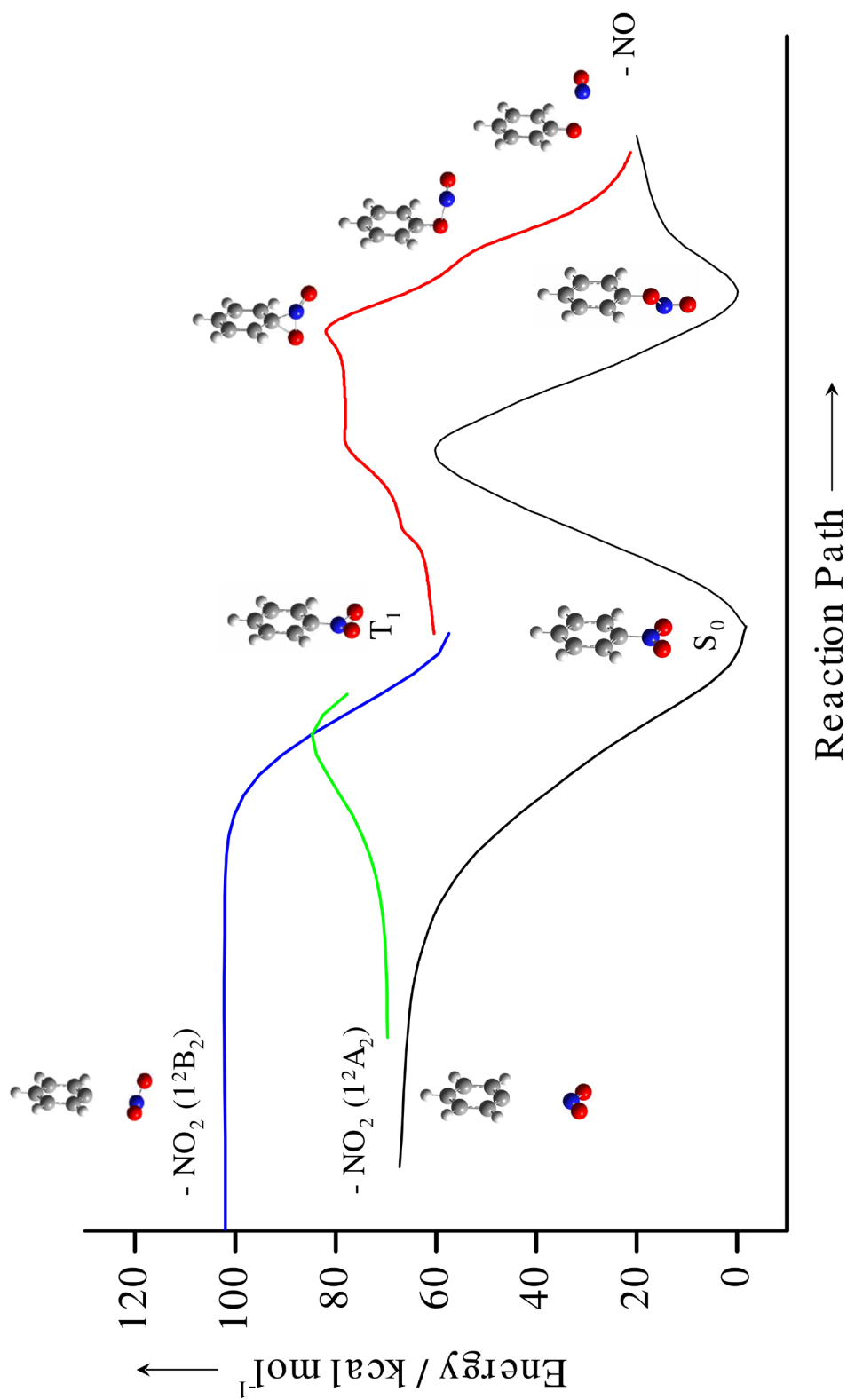


**Figure 5.17.** Theoretical calculations of the S<sub>0</sub> and T<sub>1</sub> surfaces for NO and NO<sub>2</sub> eliminations (see text).

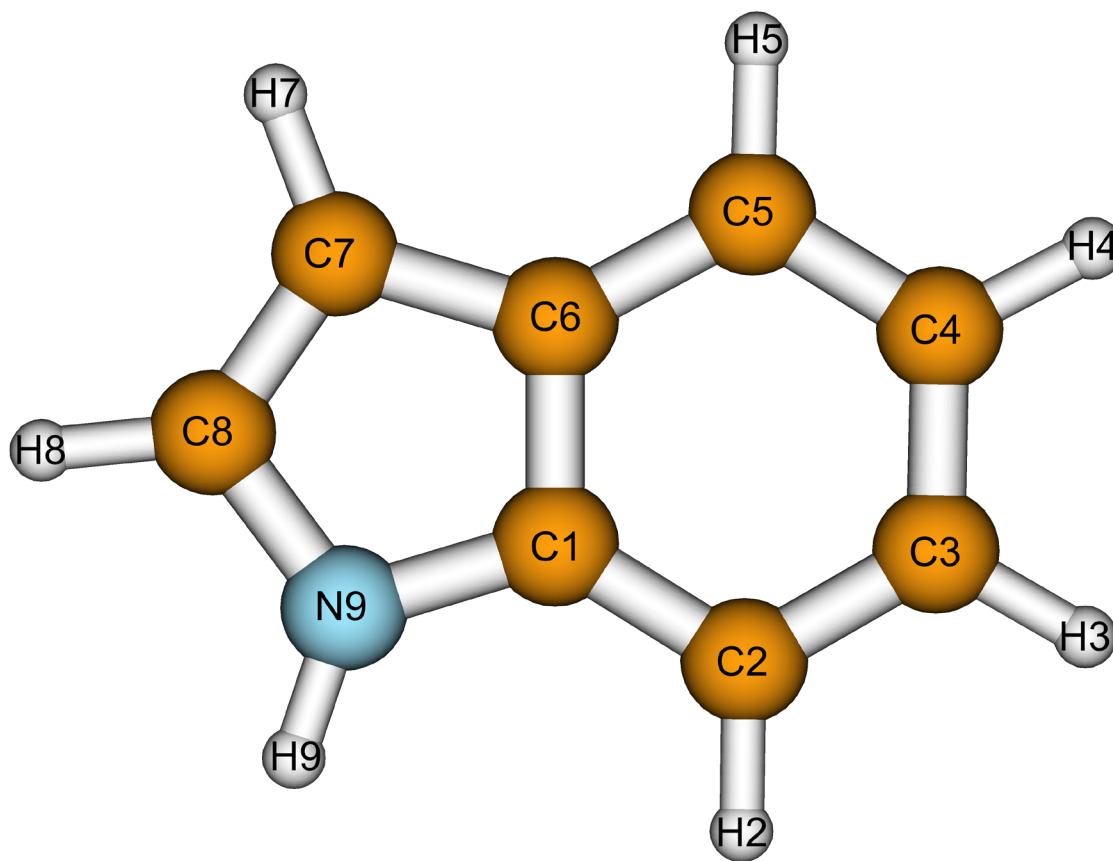


**Figure 5.18.** The geometry and atomic numbering of the indole molecule.

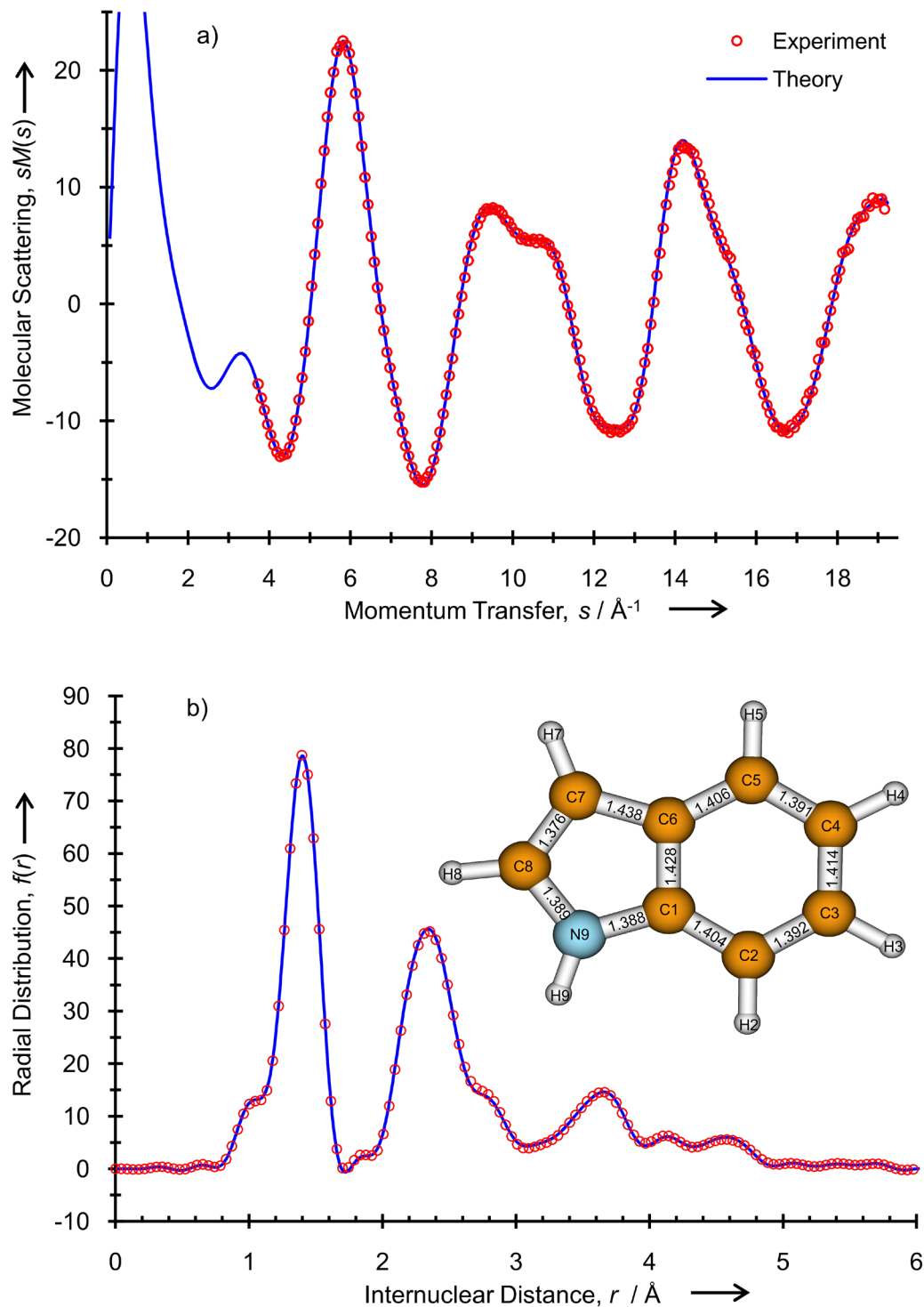


**Figure 5.19.** UED determined molecular structure of indole in the ground-state. Shown are a) the molecular scattering function,  $sM(s)$ , and b) the radial distribution,  $f(r)$ , for the experimental (points) and theoretical (line) curves. The maximum discrepancies are  $0.007 \text{ \AA}$  and  $0.1^\circ$  for bond lengths and angles, respectively.

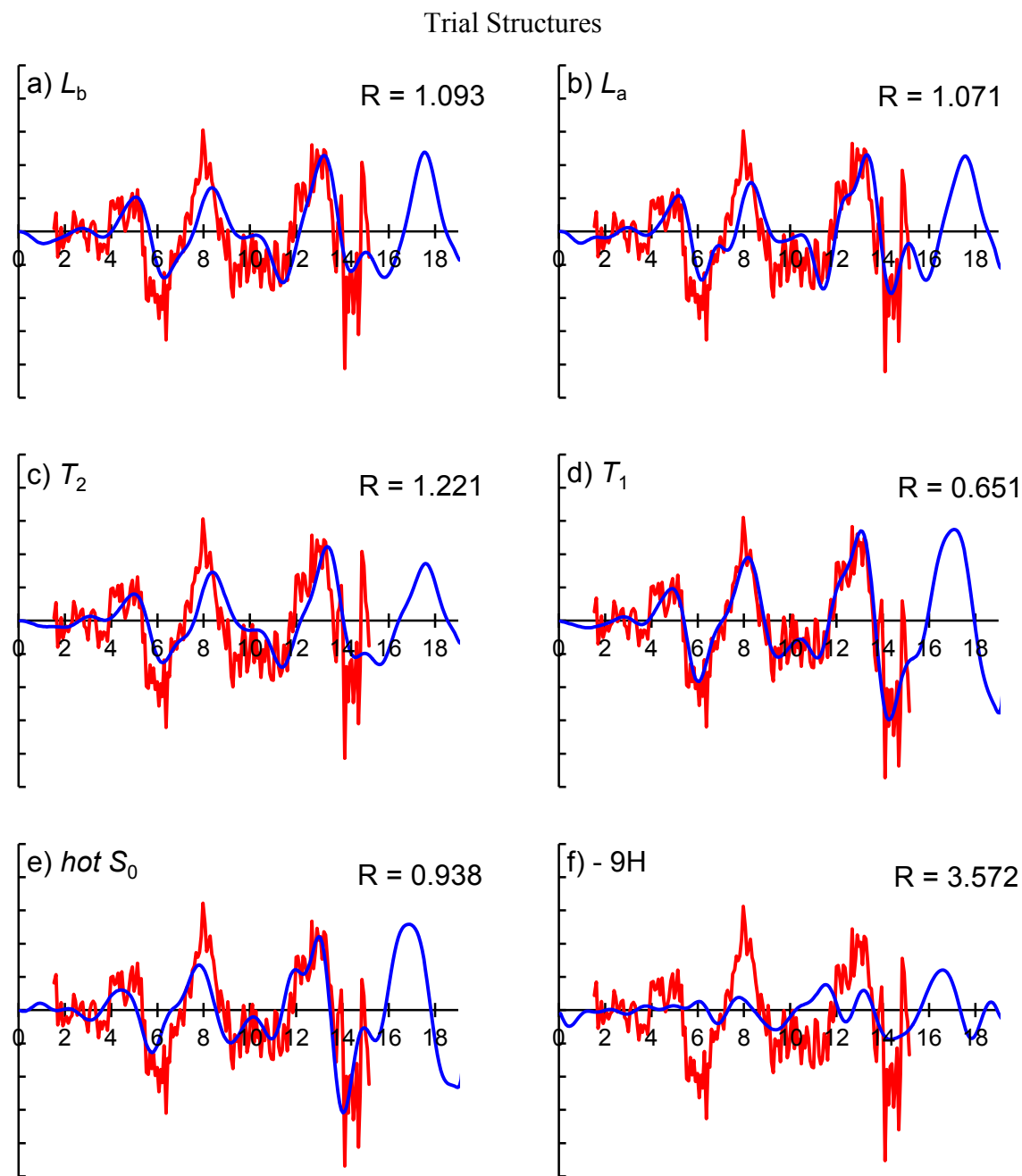


**Figure 5.20.** Temporal frame-referenced molecular scattering function,  $\Delta sM(s; t = +100 \text{ ps}, t_{ref} = -100 \text{ ps})$ , for trial fits of different reaction pathways of indole. The quality of fit ( $R$  value) is also shown for each trial fit. Note that the lower the  $R$  value (approaching zero) the better the fit, and the  $T_1$  value is the lowest.

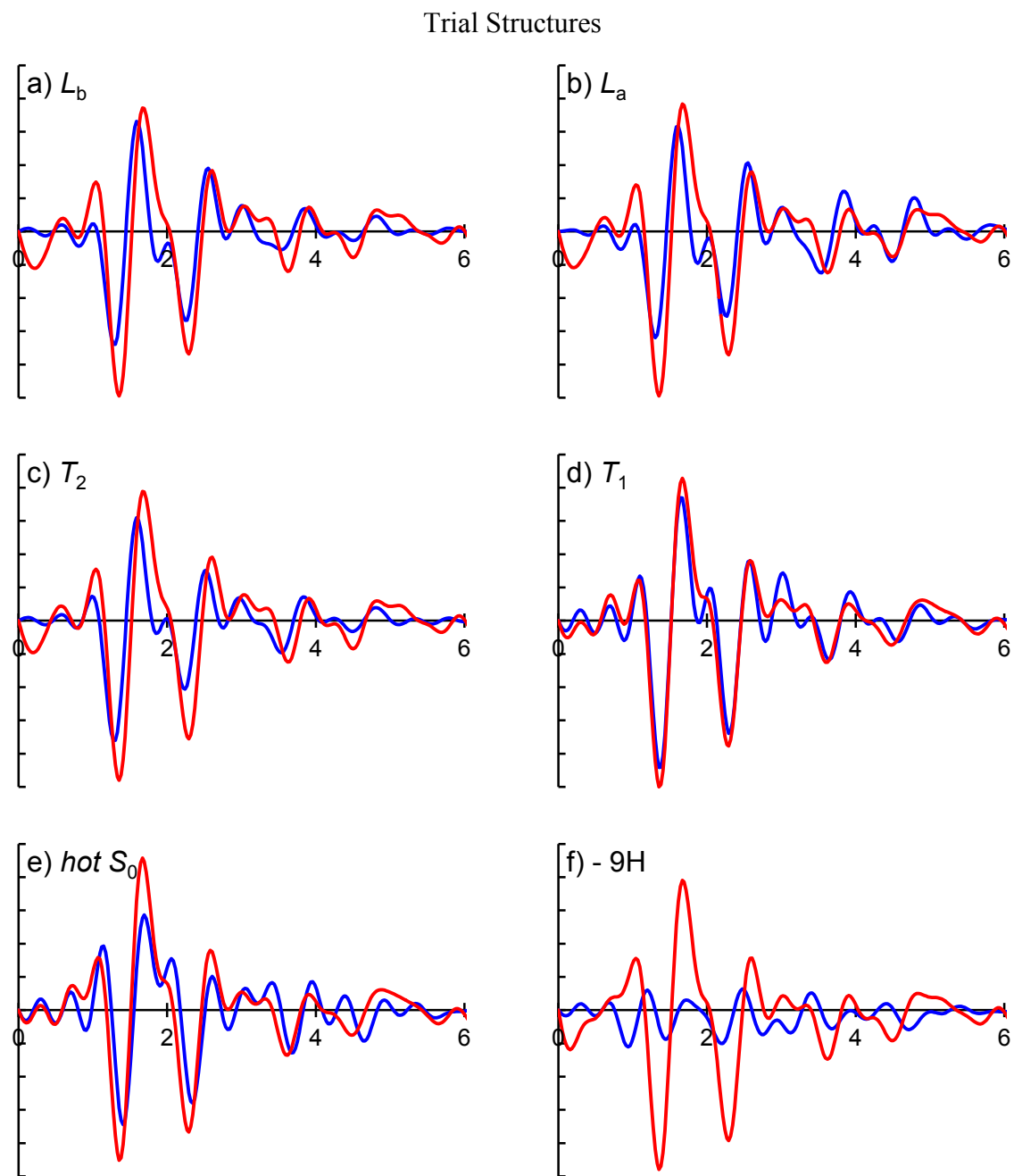


**Figure 5.21.** Temporal frame-referenced radial distribution curves,  $\Delta f(r; t = +100 \text{ ps}, t_{ref} = -100 \text{ ps})$ , for trial fits of different reaction pathways of indole.

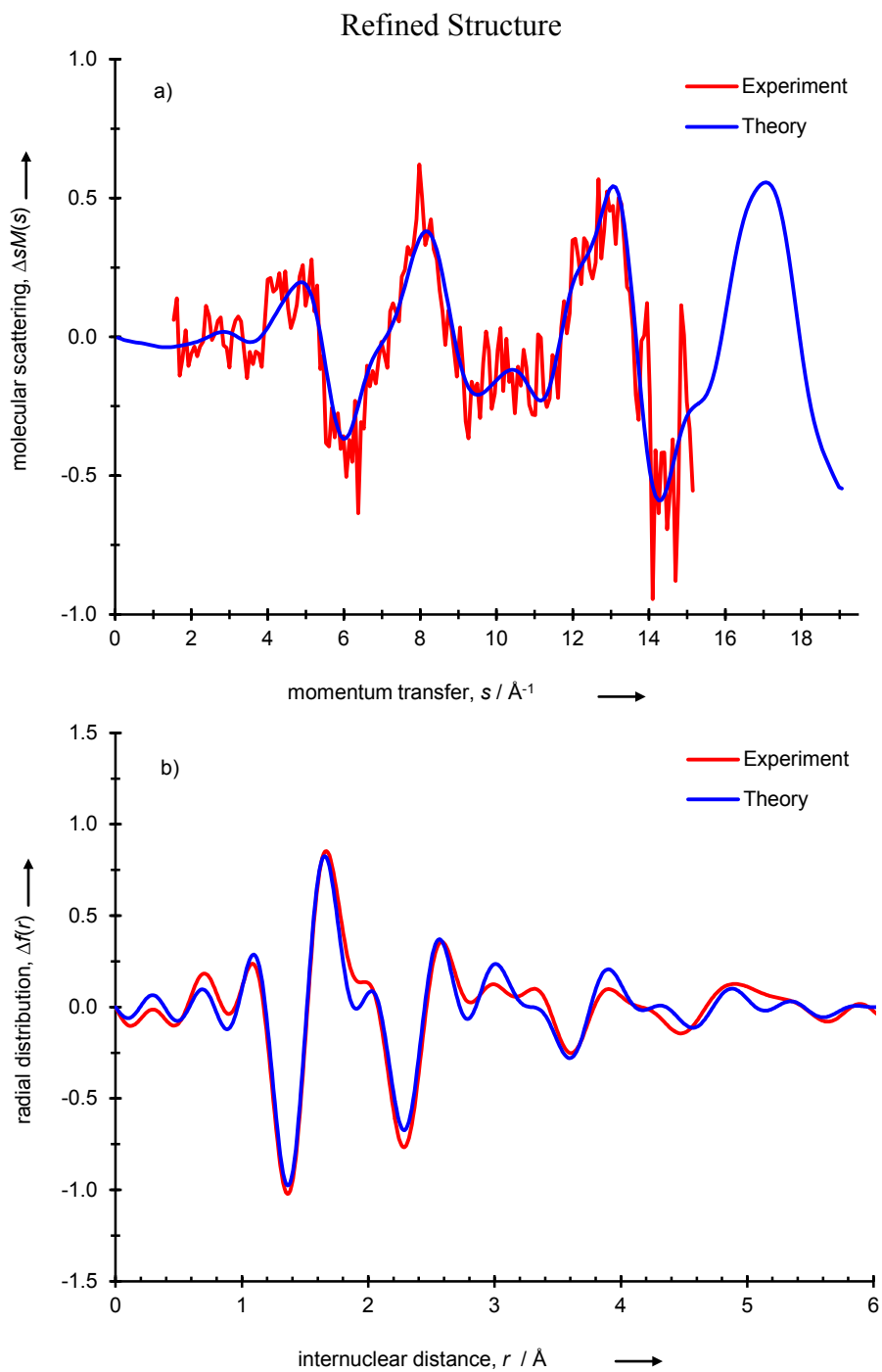


**Figure 5.22.** The frame-referenced molecular scattering function,  $\Delta sM(s)$ , and the frame-referenced radial distribution,  $\Delta f(r)$ , of the indole molecule in the  $T_1$  ( ${}^3\pi\pi^*$ ) state.

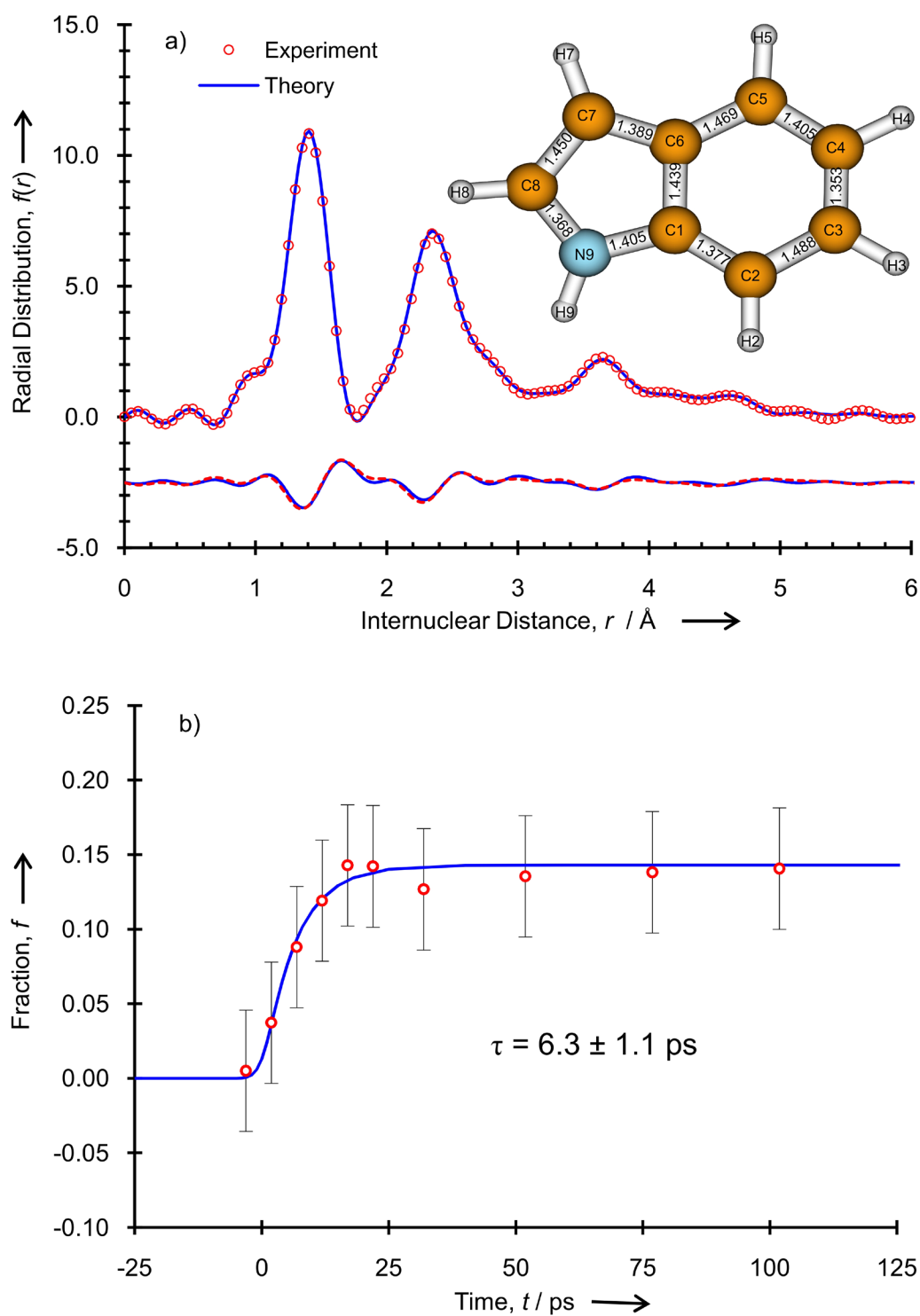


**Figure 5.23.** UED determined excited-state structure following UV excitation. a) Product-only radial distribution curve,  $f(r; t = +100 \text{ ps})$ , for indole with  $T_1$  as a product. Also shown in the lower trace is the frame-referenced radial distribution curve,  $\Delta f(r; t = +100 \text{ ps}, t_{ref} = -100 \text{ ps})$ . b) Temporal evolution of the fraction of the product. The rise gives  $\tau = 6.3 \pm 1.1 \text{ ps}$ .

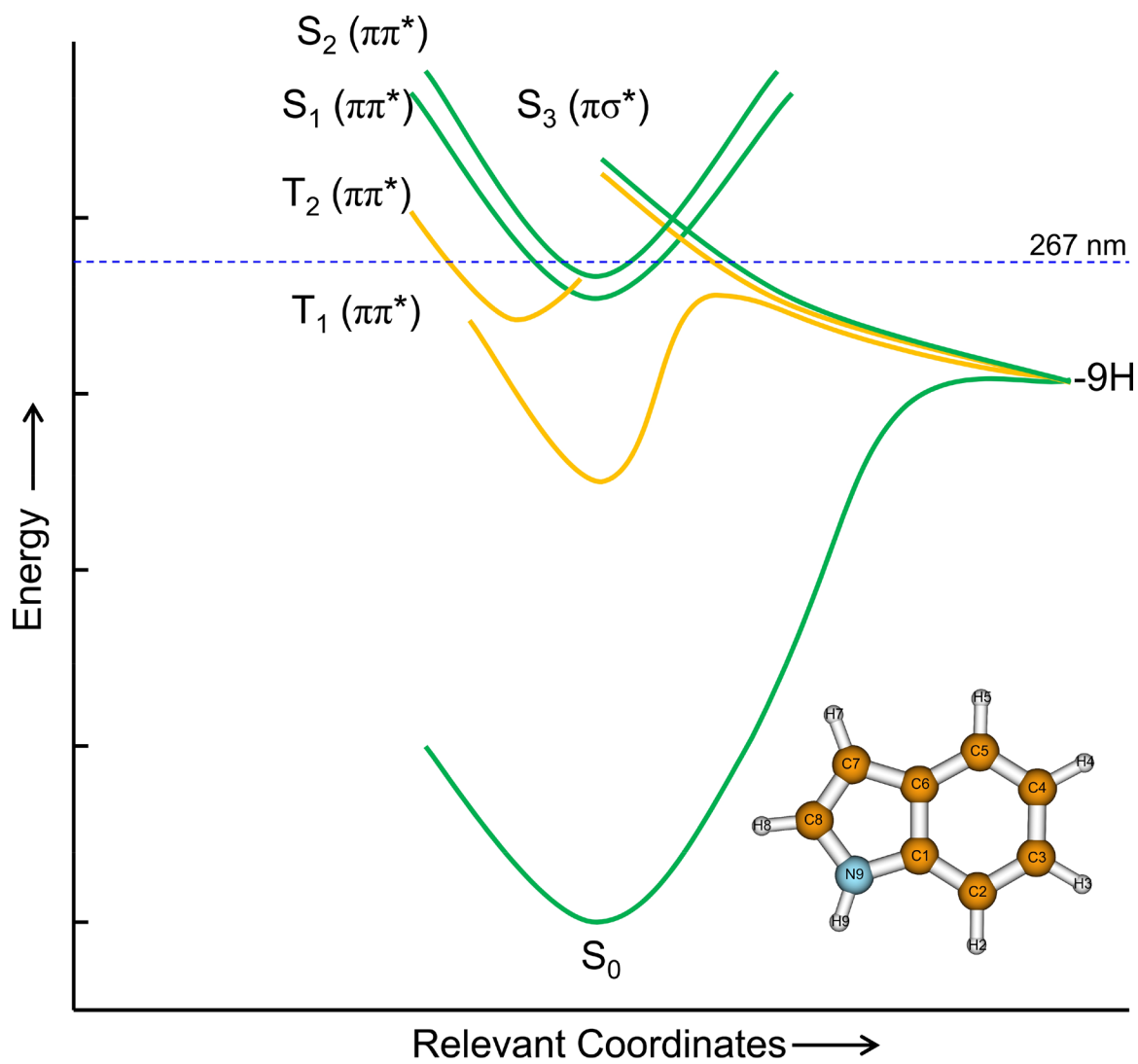


**Figure 5.24.** Potential energy curves of the excited and ground-states of indole along the hydrogen-atom loss and bound effective coordinates. For discussion of the excited states involved, see text.

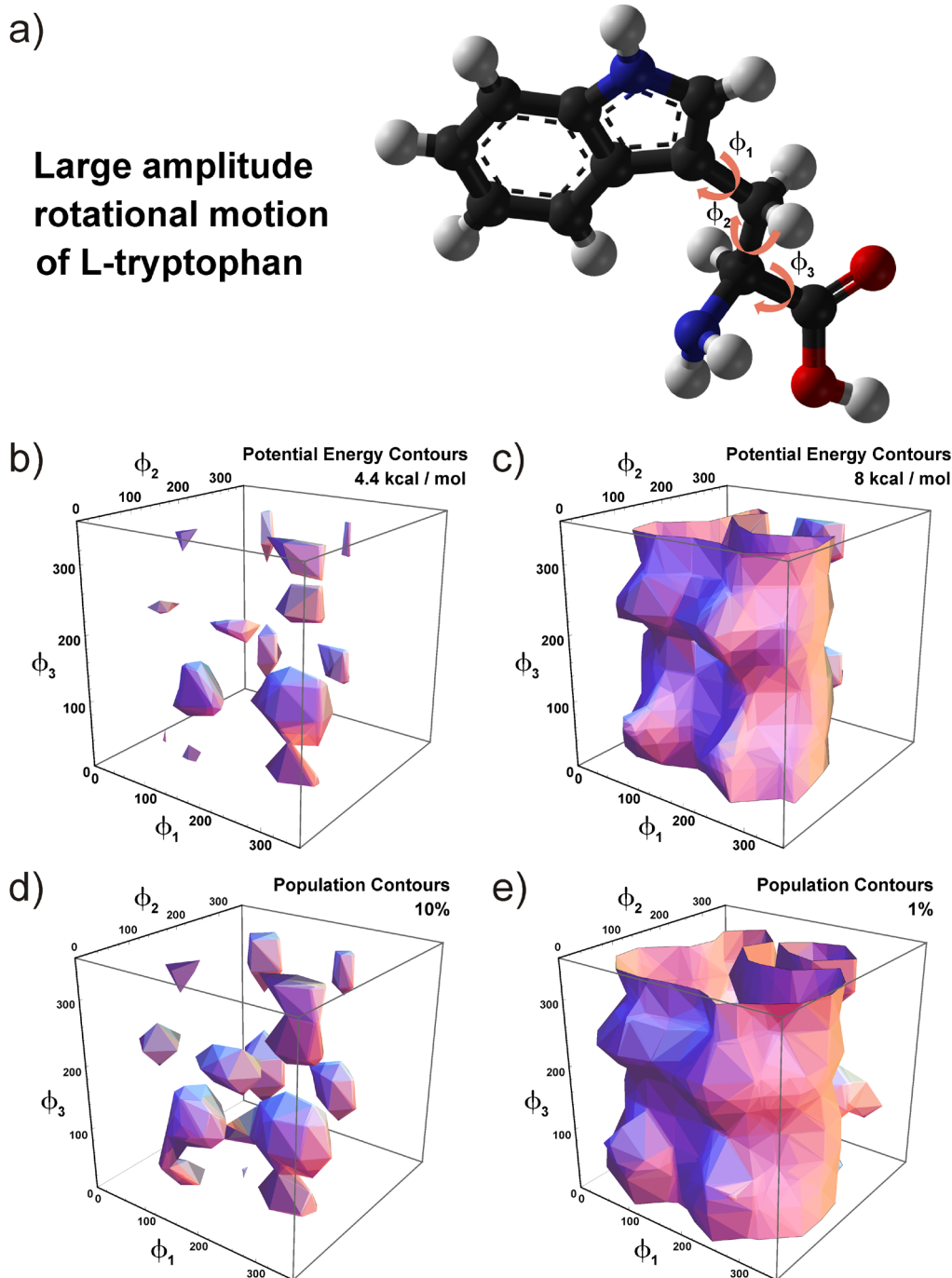


**Figure 5.25.** a) Three dihedral angles of the amino acid group of tryptophan give rise to significant conformational heterogeneity. b)-c) The potential energy hypersurface contours show the presence of numerous local minima connected by barriers of  $<10 \text{ kcal mol}^{-1}$ . The edgy shapes are due to the finite step size used in the scanning the conformational landscape. d)-e) The corresponding Boltzmann-weighted thermal populations are distributed over a large region of the conformational space. Shown are the relative probability contours at 10% and 1% of the most probable conformation.

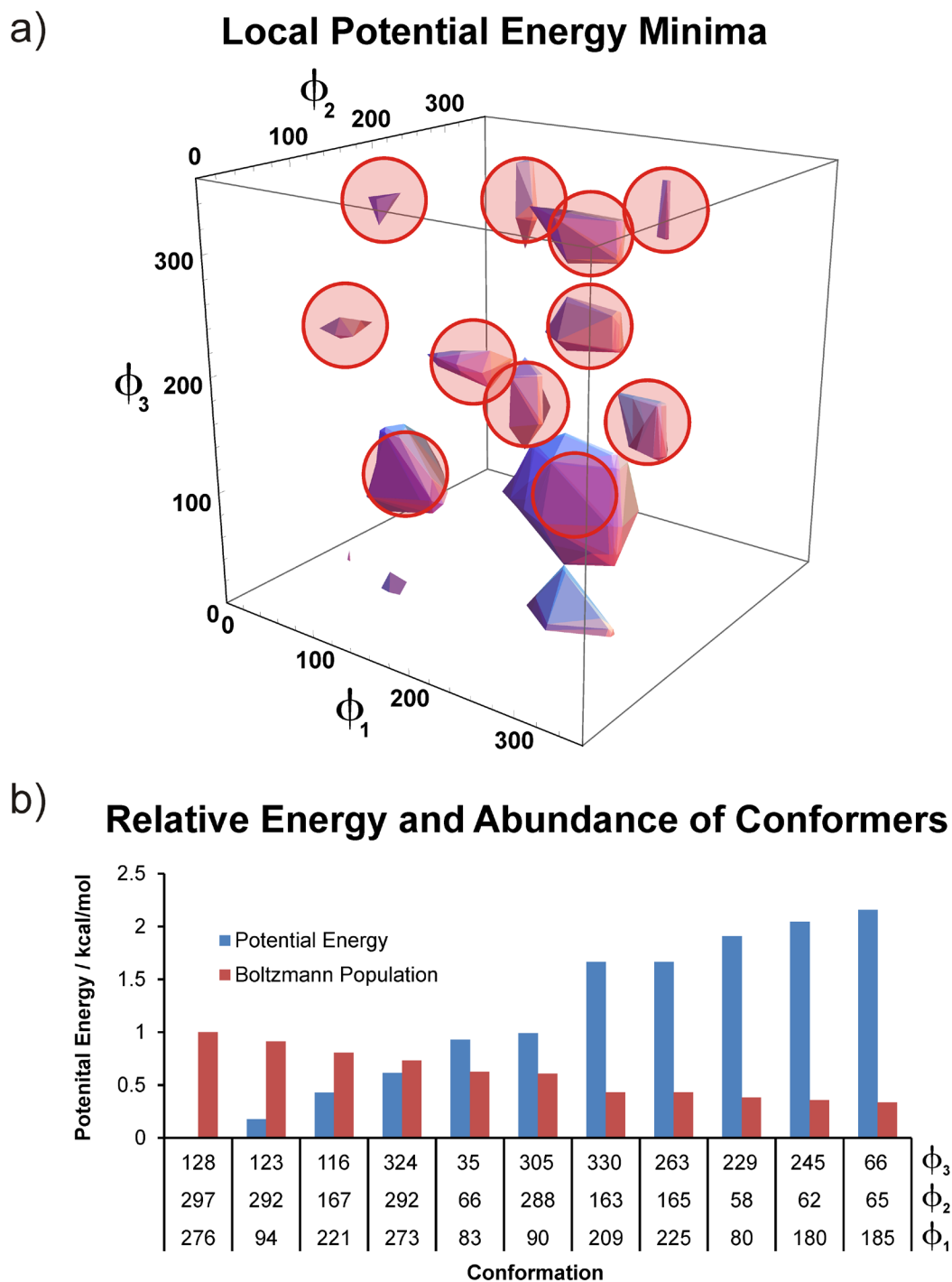


**Figure 5.26.** a) Eleven putative potential energy wells were identified, which were then verified by full geometry optimizations at the B3LYP/6-311G(*d, p*) level of theory. b) The potential energy and corresponding Boltzmann-weighted thermal population of the eleven conformers. Coordinates of the dihedral angles are rounded to whole numbers.

## Internuclear Distance Distributions

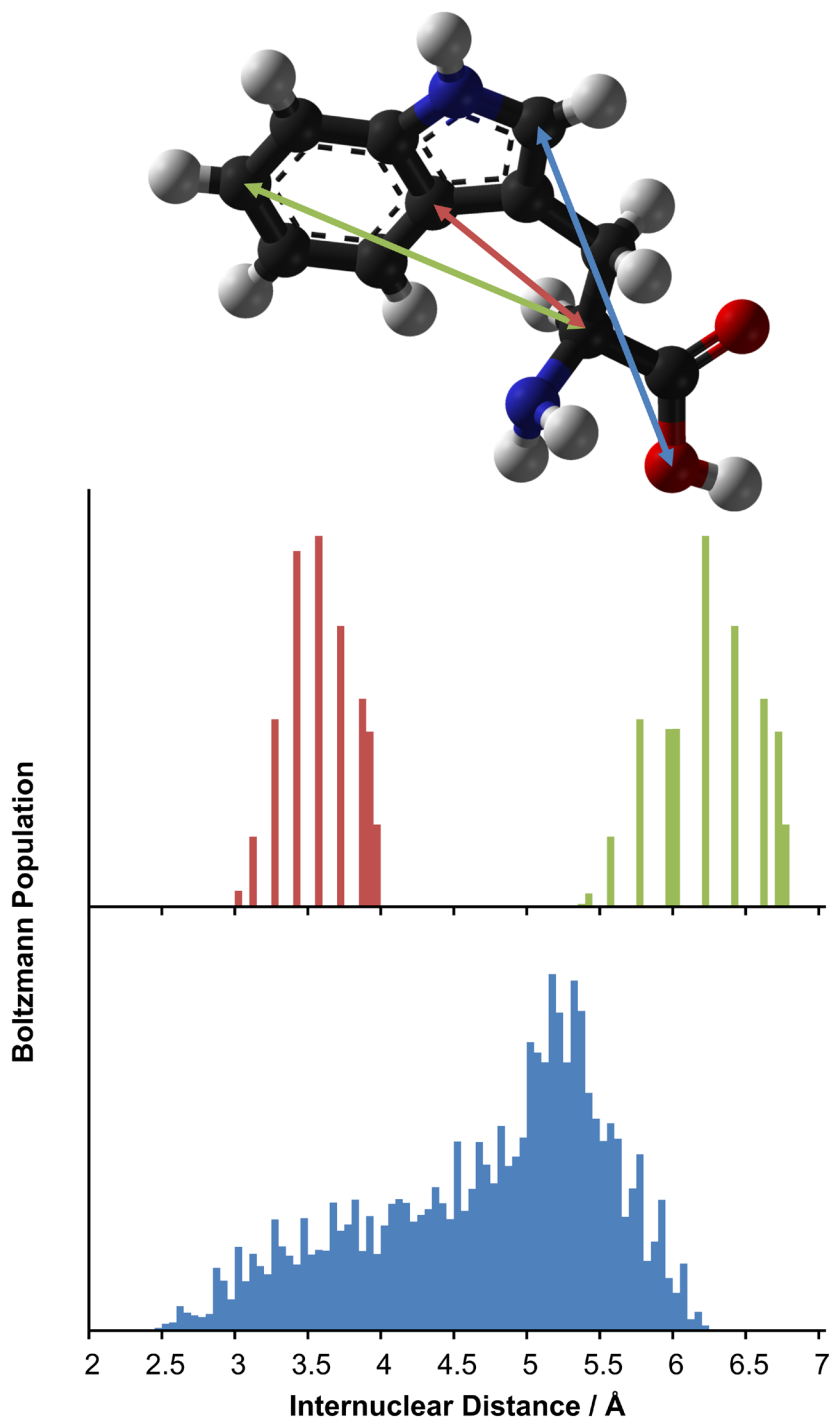


**Figure 5.27.** Large amplitude rotational motions lead to a considerable distance distribution of certain affected distances. Shown are three representative examples. The discreteness of the red and green histogram is due to the finite step size used in the scanning the conformational landscape.

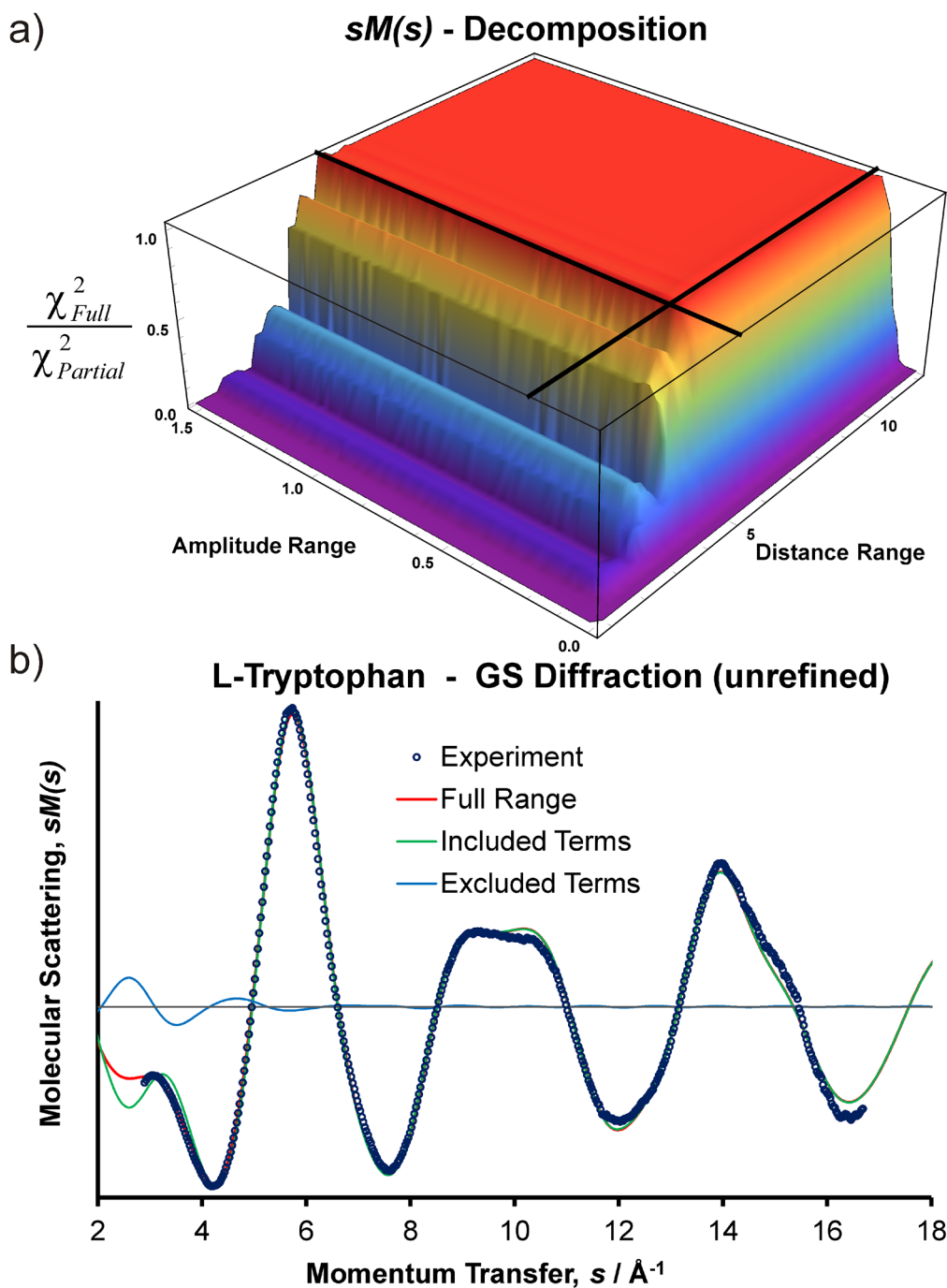


**Figure 5.28.** a) The quality of fit by a reduced model function. The asymptotic value of unity is already achieved, when only terms in the intervals  $r_{ij} \in (0, 4.8)$  and  $l_{ij} \in (0, 0.2)$  are included. b) Quality of fit by the reduced model function  $sM(s)_{Partial}^{Theory}$  (green) only deviates appreciably from the experimental data at  $s < 4 \text{\AA}^{-1}$ . Plotting the excluded terms (blue) shows that the electron diffraction data at  $s > 6 \text{\AA}^{-1}$  carries no information about large and largely distributed internuclear distances.

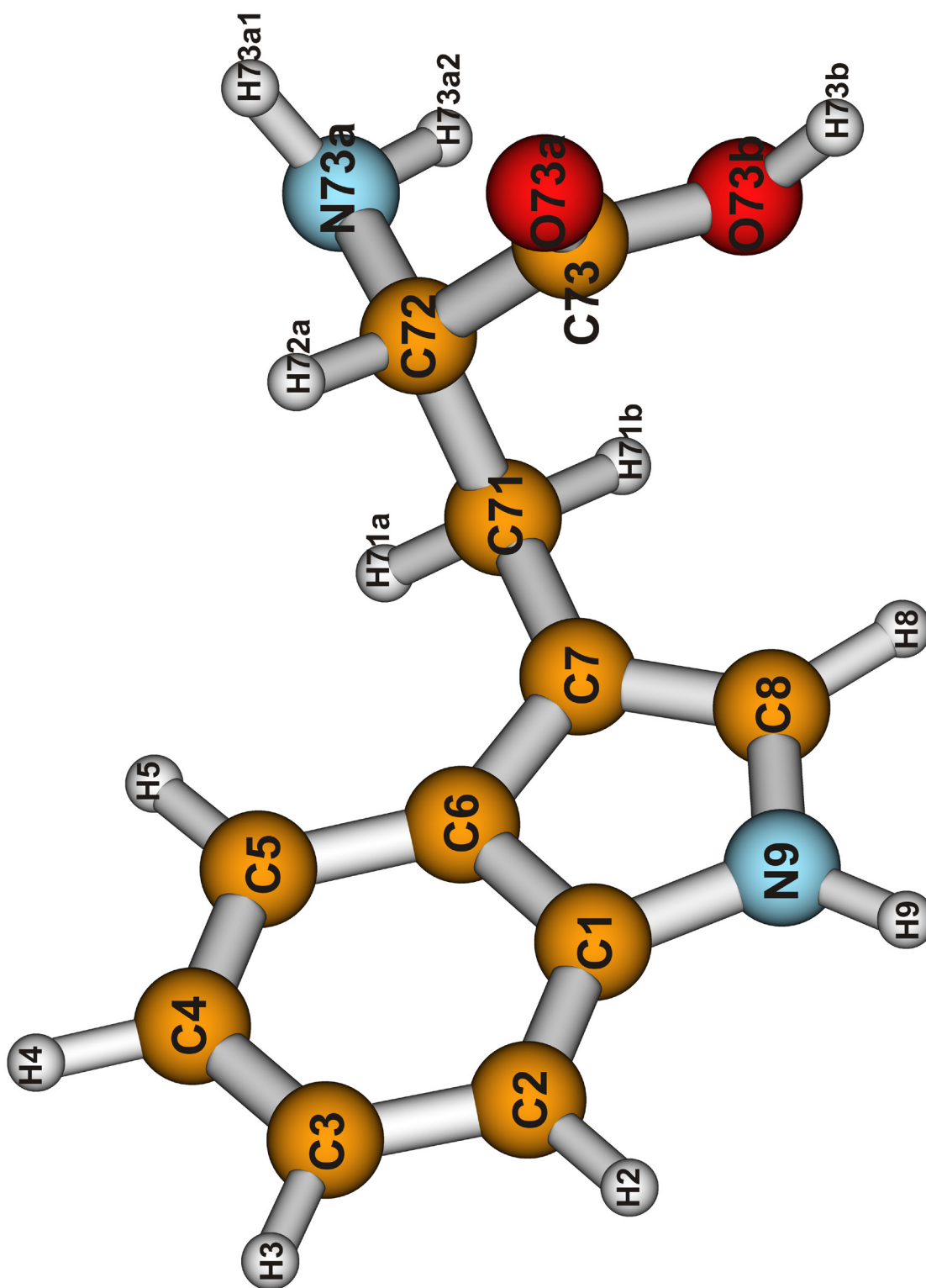


**Figure 5.29.** Tryptophan atomic labels used for structural analysis (see Table 5.11)

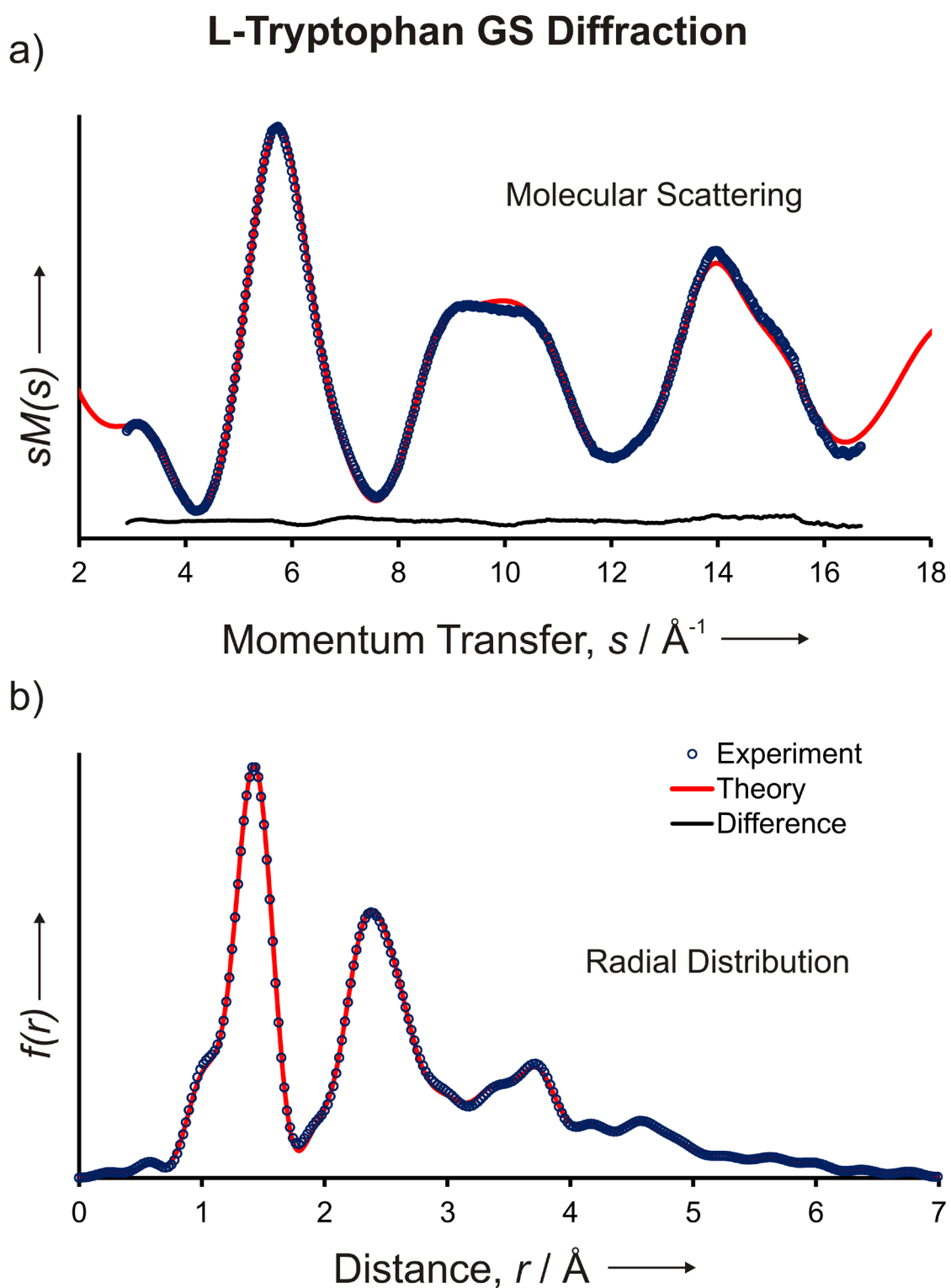


**Figure 5.30.** Diffraction results of the ground-state (GS) structure of L-tryptophan. Shown are a) the molecular scattering function,  $sM(s)$ , and b) the radial distribution,  $f(r)$ , for the experimental (circles) and theoretical (line) curves.

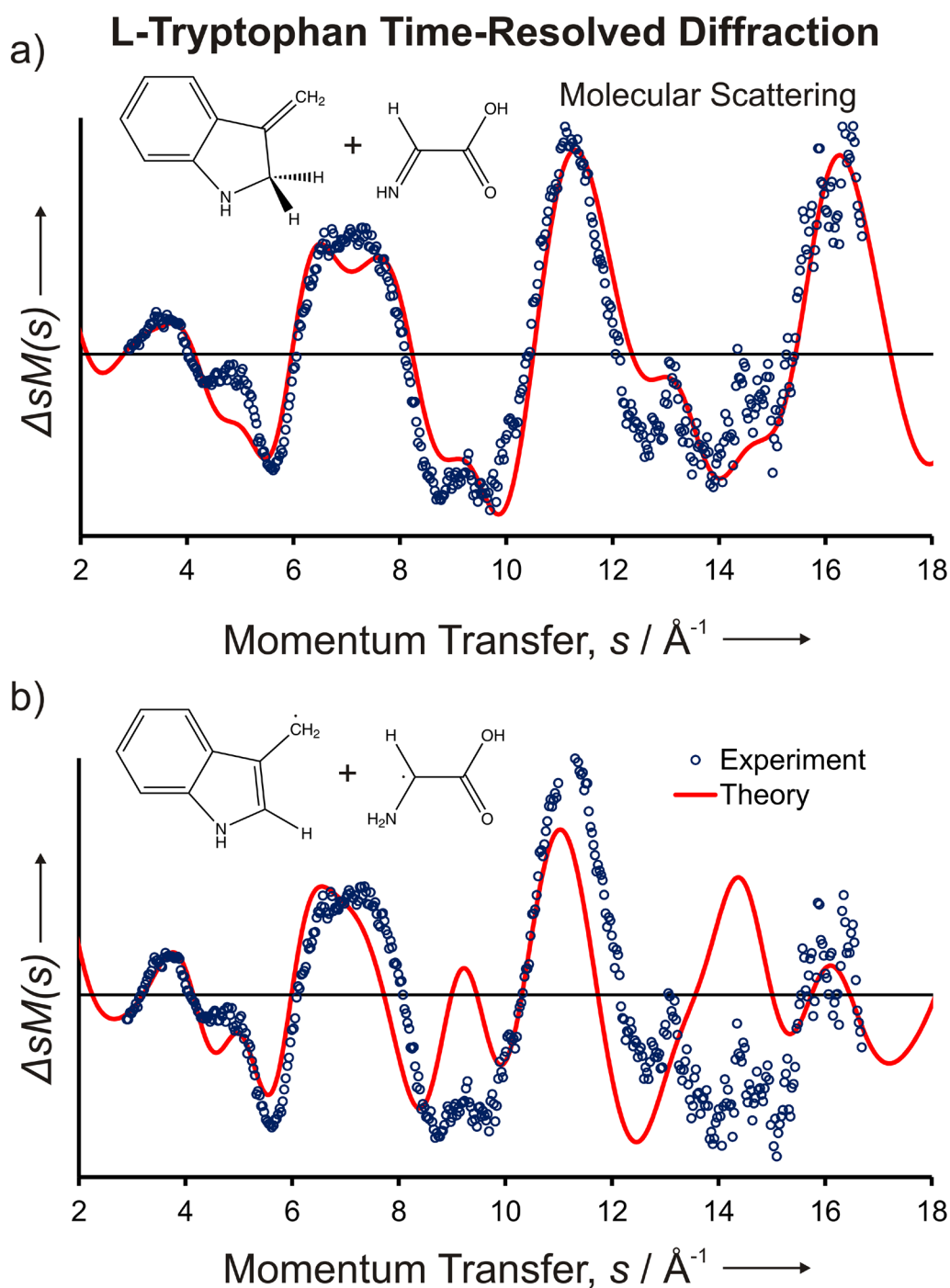


**Figure 5.31.** Time-resolved electron diffraction remains sensitive to the breaking of chemical bonds and the subsequent loss of internuclear distances (blue circles), in spite of the conformational heterogeneity of the parent structure. Shown in a) and b) are two different fragmentation pathways that differ in the position of a single hydrogen atom. The resulting change in bond order, indicated in the chemical structures, leads to a drastically different diffraction signature (red lines).

# **Chapter 6.**

## **Reflections and Future Directions**

## 6.1 Capabilities of Laser Desorption–Electron Diffraction

Laser desorption permits the vaporization of thermally labile compounds independent of their molecular masses and boiling points. During the years of operation of the UED4 desorption source, we have not yet encountered a molecular sample that could not be vaporized. Even powdered sample from an undefined mixture of long chain DNA and carbohydrates produced an interference signal; however, because these preliminary experiments were conducted with an undetermined sample mixture, it was not possible to extract any structural information in this particular case. Nonetheless, the obtained diffraction signal gives reason for optimism that the desorption source of UED4 is capable of vaporizing even biological macromolecules.

The combination of UED with laser desorption has opened the door to structural investigations of thermally labile organic chromophores and their photophysical and photochemical reaction dynamics, as documented in this thesis. Furthermore, the capability of vaporizing biological macromolecules has been highly anticipated in the Zewail group. Consequently, this group has produced several theoretical studies investigating observable signatures in the diffraction patterns that would allow for structural information to be extracted from the ensemble of gas-phase macromolecules.<sup>259-261</sup> The spatial repeats in secondary structural motifs of biological macromolecules, such as the  $\alpha$ -helix of polypeptides<sup>260</sup> or the double helix in DNA,<sup>261</sup> received particular attention as a possible source of spatial resonances, i.e., large peaks, in the radial distribution curve. Given the experimental advancements detailed in in this thesis, future UED experiments might soon be able to realize this ambition.

## 6.2 Inherent Challenges of a Gas-Phase Electron Diffraction Experiment

As stated in Chapter 1, gas-phase electron diffraction (GED) can, in combination with quantum chemical calculations, solve three-dimensional molecular structures to provide the average position of every atom with sub-Ångstrom resolution. Many of the results contained in Chapter 5 demonstrate this ability of both UED3 and UED4 by providing both reactant and product structures. From these results, it is also clear that analysis of the diffraction data becomes increasingly complex, if molecular systems increase in size, as exemplified by spiropyran,<sup>25</sup> or if the structures possess large rotational freedom on a complex potential energy surface, as exemplified by tryptophan.

### 6.2.1 Large Distances

Large distances are challenging to resolve in diffraction for reasons that emerge from the physics of the electron scattering process. From Equation 2.21 it is evident that the interference signal originating from large internuclear distances becomes increasingly confined to lower scattering angles due to the damped nature of the sinc function. The low  $s$  region of the detector is difficult to access experimentally, because of the presence of the physical beam block that is used to capture the very intense beam of unscattered electrons. Even in the absence of such a beam block, the finite width of the unscattered beam directly determines the lower bound of the angular range, in which scattered electrons can be recorded.

Even if these experimental hurdles could be overcome, the low  $s$  range is also the region, where two assumptions made to arrive at Equation 2.18 start to break down. The first assumption is the independent atom model (IAM), which states that molecules can

be assumed to be made up of spherical atoms, i.e., we neglect the aspherical shape of atomic and molecular orbitals. The weaker field due to the electron charge density becomes comparable to the nuclear field at low momentum transfer ( $s < 5 \text{ \AA}^{-1}$ , see Section 2.2 and Figure 2.2) and these effects may measurably perturb the interference signal.<sup>8,28,33</sup> The second assumption was the neglect of the higher-order multiple scattering terms in Equation 2.15. Because the scattering amplitudes decays as  $\frac{1}{s^2}$ , their magnitude is much larger in the low  $s$ -range and these higher-order multiple scattering terms may also have to be accounted for in the theoretical model.<sup>31,32</sup> Although these arguments are presented only qualitatively here, it is clear that it is increasingly challenging to (i) detect and (ii) accurately and quantitatively model the total electron intensity at low scattering angles, where information about large internuclear distances is located. These experimental and theoretical challenges have been successfully circumvented thus far in both GED and UED, where diffraction data is commonly collected in the ranges  $4 \text{ \AA}^{-1} < s < 32 \text{ \AA}^{-1}$  and  $3 \text{ \AA}^{-1} < s < 17 \text{ \AA}^{-1}$ , respectively, and the low  $s$  region remains effectively unexplored.<sup>28,262</sup>

The diffraction data from the spiropyran molecule, 6-nitro-BIPS, obtained with UED4 and presented in Section 5.2,<sup>25</sup> show the formation of an extended MC structure, which contains internuclear distances up to 14 Å. The successful identification of the entirety of this structure demonstrates the ability of electron diffraction to solve a large (nanometer-scale) molecular framework devoid of any symmetry, even though the largest internuclear distances are beyond the instrumental coherence length, which was estimated in Section 3.2, given the different parameters involved in the experiments, to be ~6-7 Å

(88% visibility).<sup>4</sup> In the presence of limited visibility, large internuclear distances remain observable, only if the the overall structure remains sufficiently rigid. This was the case for the CTC structure of ring-opened 6-nitro-BIPS, because the partial double bond character of the extended aromatic structure restricted the rotational motion around the dihedral angles in the bridge segment. The ability of UED4 to distinguish the CTC structure from the many candidates was, therefore, in large part due to the rigidity of the molecule.

### 6.2.2 Molecular Ensemble Averaging

Because UED is an ensemble-averaged measurement,<sup>102,259</sup> there are three separate averages that have to be carried out and incorporated into the model before arriving at the final theoretical molecular scattering function. A rotational average over the isotropic distribution of spatial orientation of the internuclear separation vectors,  $\mathbf{r}_i - \mathbf{r}_j$ , results in the sinc function in the molecular scattering equation (Equation 2.21). A vibrational average over all instantaneous distortions of the molecular frame results in the exponential damping function that contains the harmonic rms amplitude of vibration as its argument. (The calculation of these vibrational rms amplitudes was described in detail in Section 4.3.2.) A third average is over the stable and distinct molecular conformations that are available to the molecule. This type of average is explicitly carried out in the analysis of time-resolved data that contains contributions, according to their mole fractions, of clearly distinguishable molecular species, such as, for example, fragmentation products.

While it is straightforward to incorporate these three averages into the molecular scattering model for small molecules and/or for molecules of high rigidity, the treatment of large amplitude rotational motions about dihedral angles often merits special attention. These rotational motions give rise to distinguishable molecular pseudo-conformations and are usually treated explicitly in what is known as the dynamic model.<sup>120,182,258,259</sup> This type of treatment is straightforward, if the motion can be decoupled from other vibrational modes, and if the potential energy surface can be expressed in simple analytical form, as was done in the case of nitrobenzene.<sup>3</sup>

The diffraction data obtained from tryptophan (see Section 5.5) show that extensive rotations about three dihedral angles in the amino acid moiety significantly broaden the distribution of certain internuclear distances. The cumulative effect of these broad distributions is that the electron interferences are “washed out” and become a contribution to the monotonous background intensity, especially at higher scattering angles. The only interferences that remain observable are those that correspond to rigid portions of the molecular structure and are therefore narrowly defined in space, i.e., the first- and second-order nearest neighbor bond distances. Even if an accurate, in the case of tryptophan three-dimensional, potential energy surface could be calculated and incorporated into the theoretical model to estimate the conformer contributions, the diffraction data would likely not be able to distinguish between the more accurate and the more primitive model, at least at the current signal-to-noise levels of the instrument and high internal temperatures of the gas-phase molecules. In light of these observations, it is appropriate to redefine the concept of structure, which thus far meant solving the position of all atoms in a molecule, and shift the focus toward solving those structural elements,

which have observable signatures in the diffraction pattern. Taking this approach, the structural analysis of the rigid parts of tryptophan, i.e., excluding the dihedral angles in the amino acid moiety, was sufficient to allow for the unambiguous identification of the photochemical reaction products in the time-resolved experiment.

The challenge of conformational heterogeneity has also been recognized in a theoretical account from this group, where molecular dynamics simulations were used to computationally construct a gaseous ensemble of DNA conformations.<sup>261</sup> The authors stated:

*“The size and conformational flexibility of an ensemble of free DNA macromolecules represent a real challenge to both experiment and theory because the amount of individual structures to be considered is far beyond human comprehension.”*

In that paper, the authors additionally demonstrated that abrupt changes in the internal temperatures of the molecules results in changes in the radial distribution function in the range of large internuclear distances (4 – 40 Å). The corresponding changes in the diffraction data are thus largely confined to a region of  $s < 2 \text{ \AA}^{-1}$  on the detector, where damping of the interference signal due to vibrational oscillations is least severe.

### 6.3 Possible Improvements of the UED4 Apparatus

If the low  $s$  region is to be made accessible experimentally, the pulsed electron beam in UED4 must be improved. An optimized design of the electron optical column should be considered, possibly with additional electron optical elements to reduce the transverse FWHM of the electron beam from the current 500 – 750  $\mu\text{m}$  to less than

100  $\mu\text{m}$ . Upon these changes, the size of the beam block could be reduced significantly to probe the diffraction signal further into the low  $s$  region.

Additionally, UED4 has thus far operated in the nanosecond regime, because we were only able to produce the required  $10^7$  electrons per pulse using UV laser pulses of nanosecond duration. With femtosecond laser pulses, we were able to produce  $10^5$  electrons per pulse, but the gun performance in combination with picosecond pulses remains unexplored. It is very well possible that the use of femtosecond or picosecond lasers, together with radio-frequency compression techniques,<sup>93,263</sup> may yield highly coherent electron beams of a few picosecond or even femtosecond duration that contain  $10^6$ - $10^7$  electrons. Any experimental efforts to compress/reduce the lateral and longitudinal extent of the electron pulses should be guided by accurate numerical simulations.<sup>4,264</sup> These alterations would then make the picosecond and, possibly, the femtosecond time scale accessible to UED4.

The operation time of the current desorption source is limited only by the length of the scoop. The current size of the scattering chamber allows for the full translation of a sample length of 3 inches inside the scoop, which allows for  $\sim 60$  h of continuous operation. A slightly enlarged scattering chamber could be installed to accommodate a longer scoop to allow for the long operation times that are necessary for the collection of multiple time points. In addition to the identification of the nanosecond scale product structures that were presented in this thesis, these modification would then make it possible to resolve the early population dynamics on the electronic excited states of, for example, spiropyran and nucleic acid bases.<sup>23,153</sup>

## 6.4 Future Directions

Given the current state of the art of the UED, two avenues can be simultaneously explored for further contributions. Laser desorption electron diffraction works exceptionally well with small, but thermally labile chromophores. Conducting time-resolved measurements on these systems to investigate photoinduced molecular dynamics is the niche, where UED can make the most quantitative and conclusive contribution. Molecular systems that are small enough and therefore amenable to high-level quantum chemical calculations at reasonable computational costs are ideally suited experimental targets for ultrafast electron diffraction, because (i) the data analysis techniques are well-established and (ii) necessary instrumental improvements are well within reach.

Alternatively, the diffraction signatures for more complex molecules can be assessed in more detail. The experimental results in this thesis have demonstrated that diffraction data analysis is made more challenging, if the molecular sample is (i) large, (ii) floppy, (iii) devoid of any symmetry. The question that needs to be answered conclusively by the field is the following: What type of structural information can be extracted, quantitatively or qualitatively, from an ensemble of molecules that satisfy all of the above criteria? Because a priori estimation of the molecular conformations in a gaseous ensemble of macromolecules is only possible through molecular dynamics simulations, this challenge is mainly a theoretical one. A theoretical analysis should fully take into account the presence of instrumental noise, instrumental considerations, such as the limited access to the low  $s$ -range of the diffraction signal and the instrumental coherence length (see Section 3.2), as well as the internal temperature of the molecular sample. In particular, it would be interesting to assess, whether an externally imposed

order through, e.g., a photoswitchable peptide staple,<sup>265,266</sup> would stabilize the secondary biological motif and thus enhance the resonances in the radial distribution function. Photoinduced alteration of the used staple could then be used to disrupt or enhance the formation of an  $\alpha$ -helix in the gas phase, which might lead to a measureable time-dependent diffraction signature.

## 6.5 Conclusion

UED4 is the latest instrument in a long line of electron diffraction instruments constructed at Caltech and it builds on the capabilities and the expertise that was accumulated over nearly two decades in the Zewail laboratory. The successful combination of laser desorption and time-resolved electron diffraction in the same instrument has given the field a radically new direction: After decades of experiments with thermal evaporation, surface-assisted laser desorption has been proven to be a soft yet extremely efficient and universal method of vaporizing thermally labile compounds for UED experiments. The door is now open to utilize these capabilities and elucidate the photophysical and photochemical structural dynamics of a number of yet unexplored molecular systems.

# References

1. Srinivasan, R., Lobastov, V. A., Ruan, C.-Y. & Zewail, A. H. Ultrafast electron diffraction (UED) - A new development for the 4D determination of transient molecular structures. *Helv. Chim. Acta* **86**, 1763-1838 (2003).
2. Park, S. T., Feenstra, J. S. & Zewail, A. H. Ultrafast electron diffraction: Excited state structures and chemistries of aromatic carbonyls. *J. Chem. Phys.* **124**, 174707 (2006).
3. He, Y. G., Gahlmann, A., Feenstra, J. S., Park, S. T. & Zewail, A. H. Ultrafast electron diffraction: Structural dynamics of molecular rearrangement in the NO release from nitrobenzene. *Chem. Asian J.* **1**, 56-63 (2006).
4. Gahlmann, A., Park, S. T. & Zewail, A. H. Ultrashort electron pulses for diffraction, crystallography and microscopy: Theoretical and experimental resolutions. *Phys. Chem. Chem. Phys.* **10**, 2894-2909 (2008).
5. Park, S. T., Gahlmann, A., He, Y., Feenstra, J. S. & Zewail, A. H. Ultrafast electron diffraction reveals dark structures of the biological chromophore indole. *Angew. Chem. Int. Ed.* **47**, 9496-9499 (2008).
6. Xu, S. J., Park, S. T., Feenstra, J. S., Srinivasan, R. & Zewail, A. H. Ultrafast electron diffraction: Structural dynamics of the elimination reaction of acetylacetone. *J. Phys. Chem. A* **108**, 6650-6655 (2004).
7. Srinivasan, R., Feenstra, J. S., Park, S. T., Xu, S. J. & Zewail, A. H. Dark structures in molecular radiationless transitions determined by ultrafast diffraction. *Science* **307**, 558-563 (2005).
8. Williamson, J. C. Ultrafast gas-phase electron diffraction. *PhD Dissertation*, California Institute of Technology (1997).
9. Srinivasan, R. Structural dynamics of complex molecules by ultrafast electron diffraction: Concepts, methodology and applications. *PhD Dissertation*, California Institute of Technology (2004).
10. Zewail, A. H. 4D ultrafast electron diffraction, crystallography, and microscopy. *Annu. Rev. Phys. Chem.* **57**, 65-103 (2006).
11. Ewbank, J. D., Schäfer, L., Paul, D. W., Benston, O. J. & Lennox, J. C. Real-time data acquisition for gas electron diffraction. *Rev. Sci. Instrum.* **55**, 1598-1603 (1984).
12. Ewbank, J. D., *et al.* Time-resolved gas electron-diffraction study of the 193 nm photolysis of 1,2-dichloroethenes. *J. Phys. Chem.* **97**, 8745-8751 (1993).
13. Ewbank, J. D., *et al.* Instrumentation for gas electron diffraction employing a pulsed electron beam synchronous with photoexcitation. *Rev. Sci. Instrum.* **63**, 3352-3358 (1992).
14. Lobastov, V. A., Ewbank, J. D., Schafer, L. & Ischenko, A. A. Instrumentation for time-resolved electron diffraction spanning the time domain from microseconds to picoseconds. *Rev. Sci. Instrum.* **69**, 2633-2643 (1998).
15. Williamson, J. C. & Zewail, A. H. Structural femtochemistry: Experimental methodology. *Proc. Natl. Acad. Sci. USA* **88**, 5021-5025 (1991).

16. Williamson, J. C., Cao, J. M., Ihee, H., Frey, H. & Zewail, A. H. Clocking transient chemical changes by ultrafast electron diffraction. *Nature* **386**, 159-162 (1997).
17. Williamson, J. C., Dantus, M., Kim, S. B. & Zewail, A. H. Ultrafast diffraction and molecular structure. *Chem. Phys. Lett.* **196**, 529-534 (1992).
18. Feenstra, J. S. Ultrafast electron diffraction: Direct determination of structural dynamics of molecular excited states. *PhD Dissertation*, California Institute of Technology (2006).
19. Sipachev, V. A. Calculation of shrinkage corrections in harmonic approximation. *Theochem - J. Mol. Struct.* **22**, 143-151 (1985).
20. Sipachev, V. A. Anharmonic corrections to structural experiment data. *Struct. Chem.* **11**, 167-172 (2000).
21. Sipachev, V. A. Local centrifugal distortions caused by internal motions of molecules. *J. Mol. Struct.* **567**, 67-72 (2001).
22. Sipachev, V. A. The use of quantum-mechanical third-order force constants in structural studies. *J. Mol. Struct.* **693**, 235-240 (2004).
23. Middleton, C. T., *et al.* DNA excited-state dynamics: From single bases to the double helix. *Annu. Rev. Phys. Chem.* **60**, 217-239 (2009).
24. Gahlmann, A., Park, S. T. & Zewail, A. H. Structure of isolated biomolecules by electron diffraction-laser desorption: Uracil and guanine. *J. Am. Chem. Soc.* **131**, 2806-2808 (2009).
25. Gahlmann, A., Lee, I. R. & Zewail, A. H. Direct structural determination of conformations of photoswitchable molecules by laser desorption-electron diffraction. *Angew. Chem. Int. Ed.* **49**, 6524-6527 (2010).
26. Sakurai, J. J. *Modern quantum mechanics*, (Addison Wesley Publishing Company, New York, 1994).
27. Shankar, R. *Principles of quantum mechanics*, (Springer, New York, 1994).
28. Hargittai, I. & Hargittai, M. *Stereochemical applications of gas-phase electron diffraction*, (VCH Publishers, New York, 1988).
29. Cowley, J. C. *Diffraction physics*, (Elsevier, Amsterdam, 1995).
30. Ross, A. W., Fink, M., Hilderbrandt, R., Wang, J. & Smith Jr., V. H. Complex scattering factors for the diffraction of electrons by gases. In *International Tables for Crystallography*, vol. C 262-387 (Kluwer Academic Publishers, Boston, 1999).
31. McCaffrey, P. D., Dewhurst, J. K., Rankin, D. W. H., Mawhorter, R. J. & Sharma, S. Interatomic contributions to high-energy electron-molecule scattering. *J. Chem. Phys.* **128**(2008).
32. Meier, C., Volkmer, M., Lieschke, J., Fink, M. & Bowering, N. Intramolecular multiple scattering in electron diffraction from fluoro-methyl halides. *Z. Phys. D-Atoms Mol. Clusters* **30**, 183-187 (1994).
33. Nagashima, M., Konaka, S. & Kimura, M. A reinvestigation of small-angle electron scattering by CS<sub>2</sub> and CCl<sub>4</sub> molecules. *Bull. Chem. Soc. Jpn.* **55**, 28-32 (1982).
34. Kohl, D. A. & Arvedson, M. M. Elastic electron scattering. 1. Scattering from diatomic potentials. *J. Chem. Phys.* **72**, 1915-1921 (1980).

35. Kohl, D. A. & Arvedson, M. M. Elastic electron scattering. 2. Scattering from polyatomic potentials. *J. Chem. Phys.* **72**, 1922-1927 (1980).
36. Miller, B. R. & Bartell, L. S. Extension of Glauber theory to account for intra-target diffraction in multicenter scattering. *J. Chem. Phys.* **72**, 800-807 (1980).
37. Iga, I., Lee, M. T. & Bonham, R. A. Role of the intramolecular multiple scattering on electron diffraction from nitrogen molecule in the intermediate energy range. *Theochem - J. Mol. Struct.* **468**, 241-251 (1999).
38. Liu, J. W. & Bonham, R. A. Multiple intramolecular scattering effects on electron-diffraction patterns for Re<sub>6</sub> molecule. *J. Mol. Struct.* **11**, 297-& (1972).
39. Nation, J., *et al.* Advances in cold cathode physics and technology. *Proc. IEEE* **87**, 865-889 (1999).
40. Malacara, D. & Cornejo, A. Testing of aspherical surfaces with newton fringes. *Appl. Opt.* **9**, 837-839 (1970).
41. Berger, M. J., Coursey, J. S., Zucker, M. A. & Chang, J. Stopping-power and range tables for electrons, protons, and helium ions. (NIST, 2009).
42. <http://resolver.caltech.edu/CaltechTHESIS:04042011-112659805>.
43. <http://rsbweb.nih.gov/ij/>.
44. Dreisewerd, K. The desorption process in MALDI. *Chem. Rev.* **103**, 395-425 (2003).
45. Levis, R. J. Laser-desorption and ejection of biomolecules from the condensed-phase into the gas-phase. *Annu. Rev. Phys. Chem.* **45**, 483-518 (1994).
46. Handschuh, M., Nettesheim, S. & Zenobi, R. Is infrared laser-induced desorption a thermal process? The case of aniline. *J. Phys. Chem. B* **103**, 1719-1726 (1999).
47. Zare, R. N. & Levine, R. D. Mechanism for bond-selective processes in laser desorption. *Chem. Phys. Lett.* **136**, 593-599 (1987).
48. Holme, T. A. & Levine, R. D. Computational studies of rapid laser-induced desorption - A microscopic mechanism for selectivity. *Surf. Sci.* **216**, 587-614 (1989).
49. Maechling, C. R., Clemett, S. J., Engelke, F. & Zare, R. N. Evidence for thermalization of surface-desorbed molecules at heating rates of 10<sup>8</sup> K/s. *J. Chem. Phys.* **104**, 8768-8776 (1996).
50. Kozlov, B. & Pilyyugin, I. Particle number density and velocity distributions in laser plumes. *Mikrochim. Acta* **120**, 111-119 (1995).
51. Kelly, R. & Dreyfus, R. W. On the effect of knudsen-layer formation on studies of vaporization, sputtering, and desorption. *Surf. Sci.* **198**, 263-276 (1988).
52. Knochenmuss, R. & Zenobi, R. MALDI ionization: The role of in-plume processes. *Chem. Rev.* **103**, 441-452 (2003).
53. Noorbacha, I., Lucchese, R. R. & Zeiri, Y. Monte-Carlo simulations of gas-phase collisions in rapid desorption of molecules from surfaces. *J. Chem. Phys.* **86**, 5816-5824 (1987).
54. Kinsel, G. R., Lindner, J., Grottemeyer, J. & Schlag, E. W. Absorption effects in laser desorption of neutral organic molecules. *J. Phys. Chem.* **95**, 7824-7830 (1991).

55. Sibold, D. & Urbassek, H. M. Effect of gas-phase collisions in pulsed-laser desorption - A 3-dimensional Monte-Carlo simulation study. *J. Appl. Phys.* **73**, 8544-8551 (1993).
56. Urbassek, H. M. & Sibold, D. Gas-phase segregation effects in pulsed laser desorption from binary targets. *Phys. Rev. Lett.* **70**, 1886-1889 (1993).
57. Elam, J. W. & Levy, D. H. Ultraviolet laser desorption of indole. *J. Chem. Phys.* **106**, 10368-10378 (1997).
58. Pajasová, L., Soukup, L., Jastrabík, L. & Chvostová, D. Optical properties of glassy carbon. *Surf. Rev. Lett.* **9**, 473-477 (2002).
59. Takahashi, Y. & Edgar F. Westrum, J. Glassy carbon low temperature thermodynamic properties. *J. Chem. Thermodyn.* **2**, 847-854 (1970).
60. Ihee, H., *et al.* Direct imaging of transient molecular structures with ultrafast diffraction. *Science* **291**, 458-462 (2001).
61. Ruan, C. Y., Vigliotti, F., Lobastov, V. A., Chen, S. Y. & Zewail, A. H. Ultrafast electron crystallography: Transient structures of molecules, surfaces, and phase transitions. *Proc. Natl. Acad. Sci. USA* **101**, 1123-1128 (2004).
62. Ruan, C. Y., Lobastov, V. A., Vigliotti, F., Chen, S. Y. & Zewail, A. H. Ultrafast electron crystallography of interfacial water. *Science* **304**, 80-84 (2004).
63. Lobastov, V. A., Srinivasan, R. & Zewail, A. H. Four-dimensional ultrafast electron microscopy. *Proc. Natl. Acad. Sci. USA* **102**, 7069-7073 (2005).
64. Williamson, J. C. & Zewail, A. H. Ultrafast electron diffraction - Velocity mismatch and temporal resolution in crossed-beam experiments. *Chem. Phys. Lett.* **209**, 10-16 (1993).
65. Dantus, M., Kim, S. B., Williamson, J. C. & Zewail, A. H. Ultrafast electron diffraction. 5. Experimental time resolution and applications. *J. Phys. Chem.* **98**, 2782-2796 (1994).
66. Reed, B. W. Femtosecond electron pulse propagation for ultrafast electron diffraction. *J. Appl. Phys.* **100**, 034916 (2006).
67. Collin, S., *et al.* Transverse and longitudinal space-charge-induced broadenings of ultrafast electron packets. *J. Appl. Phys.* **98**, 094910 (2005).
68. Merano, M., *et al.* High brightness picosecond electron gun. *Rev. Sci. Instrum.* **76**, 085108 (2005).
69. Qian, B. L. & Elsayed-Ali, H. E. Comment on "Ultrafast electron optics: Propagation dynamics of femtosecond electron packets". *J. Appl. Phys.* **94**, 803-806 (2003).
70. Siwick, B. J., Dwyer, J. R., Jordan, R. E. & Miller, R. J. D. Ultrafast electron optics: Propagation dynamics of femtosecond electron packets. *J. Appl. Phys.* **92**, 1643-1648 (2002).
71. Orloff, J. *Handbook of charged particle optics*, (CRC Press, New York, 1997).
72. Jansen, G. H. *Coulomb interaction in particle beams*, (Academic Press, San Diego, 1990).
73. Luiten, O. J., van der Geer, S. B., de Loos, M. J., Kiewiet, F. B. & van der Wiel, M. J. How to realize uniform three-dimensional ellipsoidal electron bunches. *Phys. Rev. Lett.* **93**, 094802 (2004).

74. King, W. E., *et al.* Ultrafast electron microscopy in materials science, biology, and chemistry. *J. Appl. Phys.* **97**, 111101 (2005).
75. Michalik, A. M. & Sipe, J. E. Analytic model of electron pulse propagation in ultrafast electron diffraction experiments. *J. Appl. Phys.* **99**, 054908 (2006).
76. Barwick, B., *et al.* Laser-induced ultrafast electron emission from a field emission tip. *New J. Phys.* **9**, 142 (2007).
77. Endriz, J. G. & Spicer, W. E. Experimental evidence for surface photoelectric effect in aluminum. *Phys. Rev. Lett.* **27**, 570-573 (1971).
78. Janzen, A., *et al.* A pulsed electron gun for ultrafast electron diffraction at surfaces. *Rev. Sci. Instrum.* **78**, 013906 (2007).
79. Dwyer, J. R., *et al.* Experimental basics for femtosecond electron diffraction studies. *J. Mod. Opt.* **54**, 923-942 (2007).
80. Born, M. & Wolf, E. *Principles of optics*, (Pergamon Press, Oxford, 1975).
81. Rosenzweig, J., Travish, G. & Serafini, L. *The physics and applications of high brightness electron beams*, (World Scientific, Singapore, 2003).
82. Yang, D. S., Gedik, N. & Zewail, A. H. Ultrafast electron crystallography. 1. Nonequilibrium dynamics of nanometer-scale structures. *Journal of Physical Chemistry C* **111**, 4889-4919 (2007).
83. Reimer, L. *Transmission electron microscopy*, (Springer, Berlin, 1997).
84. Tonomura, A. *Electron holography*, (Springer, Berlin, 1999).
85. Armstrong, M. R., *et al.* Practical considerations for high spatial and temporal resolution dynamic transmission electron microscopy. *Ultramicroscopy* **107**, 356-367 (2007).
86. Armstrong, M. R., Reed, B. W., Torralva, B. R. & Browning, N. D. Prospects for electron imaging with ultrafast time resolution. *Appl. Phys. Lett.* **90**, 114101 (2007).
87. Aeschlimann, M., *et al.* A picosecond electron gun for surface analysis. *Rev. Sci. Instrum.* **66**, 1000-1009 (1995).
88. Park, H. S., Baskin, J. S., Kwon, O. H. & Zewail, A. H. Atomic-scale imaging in real and energy space developed in ultrafast electron microscopy. *Nano Lett.* **7**, 2545-2551 (2007).
89. Baum, P., Yang, D. S. & Zewail, A. H. 4D visualization of transitional structures in phase transformations by electron diffraction. *Science* **318**, 788-792 (2007).
90. Baum, P. & Zewail, A. H. Breaking resolution limits in ultrafast electron diffraction and microscopy. *Proc. Natl. Acad. Sci. USA* **103**, 16105-16110 (2006).
91. Hastings, J. B., *et al.* Ultrafast time-resolved electron diffraction with megavolt electron beams. *Appl. Phys. Lett.* **89**, 184109 (2006).
92. Wang, X. J., Xiang, D., Kim, T. K. & Ihee, H. Potential of femtosecond electron diffraction using near-relativistic electrons from a photocathode RF electron gun. *J. Korean Phys. Soc.* **48**, 390-396 (2006).
93. van Oudheusden, T., *et al.* Electron source concept for single-shot sub-100 fs electron diffraction in the 100 keV range. *J. Appl. Phys.* **102**, 093501 (2007).
94. Veisz, L., *et al.* Hybrid dc-ac electron gun for fs-electron pulse generation. *New J. Phys.* **9**, 451 (2007).

95. Salvat, F. & Jablonski, A. NIST electron elastic scattering cross section database: Version 3.1. (National Institute for Standards and Technology, 2002).
96. Berger, M. J., *et al.* XCOM: Photon cross section database: Version 1.3. (National Institute for Standards and Technology, 2005).
97. Lobastov, V. A., Weissenrieder, J., Tang, J. & Zewail, A. H. Ultrafast electron microscopy (UEM): Four-dimensional imaging and diffraction of nanostructures during phase transitions. *Nano Lett.* **7**, 2552-2558 (2007).
98. Bevington, P. R. & Robinson, D. K. *Data reduction and error analysis for the physical sciences*, (McGraw-Hill, New York, 1992).
99. Taylor, J. R. *An introduction to error analysis: The study of uncertainties in physical measurements*, (University Science Books, Sausalito, 1997).
100. Cardoza, J. D., Dudek, R. C., Mawhorter, R. J. & Weber, P. M. Centering of ultrafast time-resolved pump-probe electron diffraction patterns. *Chem. Phys.* **299**, 307-312 (2004).
101. Press, W. H., Teukolsky, S. A., Vetterling, W. T. & Flannery, B. P. *Numerical recipes in C: The art of scientific computing*, (Cambridge University Press, Cambridge, 1999).
102. Shorokhov, D., Park, S. T. & Zewail, A. H. Ultrafast electron diffraction: Dynamical structures on complex energy landscapes. *Chem. Phys. Chem.* **6**, 2228-2250 (2005).
103. Pulay, P. & Fogarasi, G. Geometry optimization in redundant internal coordinates. *J. Chem. Phys.* **96**, 2856-2860 (1992).
104. Peng, C. Y., Ayala, P. Y., Schlegel, H. B. & Frisch, M. J. Using redundant internal coordinates to optimize equilibrium geometries and transition states. *J. Comput. Chem.* **17**, 49-56 (1996).
105. Wilson, W. B., Jr., Decius, J. C. & Cross, P. C. *Molecular vibrations*, (McGraw-Hill, New York, 1955).
106. Califano, S. *Vibrational states*, (John Wiley & Sons, London, 1976).
107. Axler, S. J. *Linear algebra done right*, (Springer, New York, 1997).
108. Kim, K. & Jordan, K. D. Comparison of density functional and MP2 calculations on the water monomer and dimer. *J. Phys. Chem.* **98**, 10089-10094 (1994).
109. Stephens, P. J., Devlin, F. J., Chabalowski, C. F. & Frisch, M. J. Ab initio calculation of vibrational absorption and circular dichroism spectra using density functional force fields. *J. Phys. Chem.* **98**, 11623-11627 (1994).
110. Martell, J. M., Yu, H. & Goddard, J. D. Molecular decompositions of acetaldehyde and formamide: Theoretical studies using Hartree-Fock, Moller-Plesset and density functional theories. *Mol. Phys.* **92**, 497-502 (1997).
111. Frisch, M. J., *et al.* Gaussian 98. (Gaussian, Pittsburgh, PA, 1998).
112. Schmidt, M. W., *et al.* General atomic and molecular electronic structure system. *J. Comput. Chem.* **14**, 1347-1363 (1993).
113. Mastryukov, V. S. & Dorofeeva, O. V. Relationship between vibrational amplitudes and internuclear distances. 7. Amplitudes calculated from spectroscopic data. *J. Struct. Chem.* **20**, 504-508 (1979).

114. Mastryukov, V. S. & Cyvin, S. J. Relations between mean amplitudes of vibration and corresponding internuclear distances I. Bonded and nonbonded carbon-carbon distances. *J. Mol. Struct.* **29**, 15-25 (1975).
115. Mastryukov, V. S., Osina, E. L., Vilkov, L. V. & Cyvin, S. J. The relationship between vibrational amplitudes and internuclear distances. *Zhu. Strukt. Khim.* **17**, 80-85 (1976).
116. Hedberg, L. & Mills, I. M. ASYM20 - A program for force-constant and normal-coordinate calculations, with a critical review of the theory involved. *J. Mol. Spectrosc.* **160**, 117-142 (1993).
117. Novikov, V. P., Sipachev, V. A., Kulikova, E. I. & Vilkov, L. V. A comparison of amplitudes and shrinkage corrections for  $C_6Cl_3(NO_2)_3$  calculated using conventional and new procedures. *J. Mol. Struct.* **301**, 29-36 (1993).
118. Mawhorter, R. J., Fink, M. & Archer, B. T. The vibrationally averaged, temperature-dependent structure of polyatomic-molecules. 1.  $CO_2$ . *J. Chem. Phys.* **79**, 170-174 (1983).
119. Ferenczy, G., Harsányi, L., Rozsondai, B. & Hargittai, I. The molecular structure of uracil - An electron diffraction study. *J. Mol. Struct.* **140**, 71-77 (1986).
120. Shorokhov, D. Molecular structures and conformational preferences studied by quantum chemical calculations and gas electron diffraction using different recording media. *PhD Dissertation*, University of Oslo (2000).
121. Vogt, N., Khaikin, L. S., Grikina, O. E., Rykov, A. N. & Vogt, J. Study of the thymine molecule: Equilibrium structure from joint analysis of gas-phase electron diffraction and microwave data and assignment of vibrational spectra using results of ab initio calculations. *J. Phys. Chem. A* **112**, 7662-7670 (2008).
122. Speir, J. P. & Amster, I. J. Substrate-assisted laser desorption of neutral peptide molecules. *Anal. Chem.* **64**, 1041-1045 (1992).
123. Vaquero, V., Sanz, M. E., López, J. C. & Alonso, J. L. The structure of uracil: A laser ablation rotational study. *J. Phys. Chem. A* **111**, 3443-3445 (2007).
124. Choi, M. Y. & Miller, R. E. Infrared laser spectroscopy of uracil and thymine in helium nanodroplets: Vibrational transition moment angle study. *J. Phys. Chem. A* **111**, 2475-2479 (2007).
125. Pitoňák, M., Riley, K. E., Neogrady, P. & Hobza, P. Highly accurate CCSD(T) and DFT-SAPT stabilization energies of H-bonded and stacked structures of uracil dimer. *Chem. Phys. Chem.* **9**, 1636-1644 (2008).
126. Ha, T.-K., Keller, H.-J., Gunde, R. & Gunthard, H.-H. Energy increment method based on quantum chemical results: A general recipe for approximative prediction of isomerization and tautomerization energies of pyrimidine and purine nucleic acid bases and related compounds. *J. Phys. Chem. A* **103**, 6612-6623 (1999).
127. Hanus, M., *et al.* Correlated ab Initio study of nucleic acid bases and their tautomers in the gas phase, in a microhydrated environment and in aqueous solution. Guanine: Surprising stabilization of rare tautomers in aqueous solution. *J. Am. Chem. Soc.* **125**, 7678-7688 (2003).
128. Choi, M. Y. & Miller, R. E. Four tautomers of isolated guanine from infrared laser spectroscopy in helium nanodroplets. *J. Am. Chem. Soc.* **128**, 7320-7328 (2006).

129. Berkovic, G., Krongauz, V. & Weiss, V. Spiropyran and spirooxazines for memories and switches. *Chem. Rev.* **100**, 1741-1753 (2000).
130. Willner, I. Photoswitchable biomaterials: En route to optobioelectronic systems. *Acc. Chem. Res.* **30**, 347-356 (1997).
131. Bercovici, T. & Fischer, E. Photosensitized coloration of photochromic spiropyran. *J. Am. Chem. Soc.* **86**, 5687-5688 (1964).
132. Reeves, D. A. & Wilkinson, F. Photochromism of spiropyran. 1. Mechanism of photocolouration. *J. Chem. Soc., Faraday Trans. 2* **69**, 1381-1390 (1973).
133. Krysanov, S. A. & Alfimov, M. V. Ultrafast formation of transients in spiropyran photochromism. *Chem. Phys. Lett.* **91**, 77-80 (1982).
134. Lenoble, C. & Becker, R. S. Photophysics, photochemistry, kinetics, and mechanism of the photochromism of 6'-nitroindolinospiropyran. *J. Phys. Chem.* **90**, 62-65 (1986).
135. Yuzawa, T., Shimojima, A. & Takahashi, H. Photochromic reaction of 6-nitro-1',3',3'-trimethylspiro[2H-1-benzopyran-2,2'-indoline]: Time-resolved resonance Raman and absorption study. *J. Mol. Struct.* **352**, 497-507 (1995).
136. Görner, H., Atabekyan, L. S. & Chibisov, A. K. Photoprocesses in spiropyran-derived merocyanines: Singlet versus triplet pathway. *Chem. Phys. Lett.* **260**, 59-64 (1996).
137. Görner, H. Photochromism of nitrospiropyran: Effects of structure, solvent and temperature. *Phys. Chem. Chem. Phys.* **3**, 416-423 (2001).
138. Futami, Y., Chin, M. L. S., Kudoh, S., Takayanagi, M. & Nakata, M. Conformations of nitro-substituted spiropyran and merocyanine studied by low-temperature matrix-isolation infrared spectroscopy and density functional theory calculation. *Chem. Phys. Lett.* **370**, 460-468 (2003).
139. Cottone, G., Noto, R. & La Manna, G. Theoretical study of spiropyran-merocyanine thermal isomerization. *Chem. Phys. Lett.* **388**, 218-222 (2004).
140. Sheng, Y., *et al.* Comprehensive theoretical study of the conversion reactions of spiropyran: Substituent and solvent effects. *J. Phys. Chem. B* **108**, 16233-16243 (2004).
141. Ernsting, N. P. & Arthen-Engeland, T. Photochemical ring-opening reaction of indolinospiryran studied by subpicosecond transient absorption. *J. Phys. Chem.* **95**, 5502-5509 (1991).
142. Zhang, J. Z., Schwartz, B. J., King, J. C. & Harris, C. B. Ultrafast studies of photochromic spiropyran in solution. *J. Am. Chem. Soc.* **114**, 10921-10927 (1992).
143. Alfimov, M. V., *et al.* Femtosecond spectrochronography of the reverse photochromic transition in derivatives of spiro compounds. *Russ. J. Phys. Chem.* **73**, 1685-1694 (1999).
144. Holm, A.-K., Rini, M., Nibbering, E. T. J. & Fidler, H. Femtosecond UV/mid-IR study of photochromism of the spiropyran 1',3'-dihydro-1',3',3'-trimethyl-6-nitrospiro[2H-1-benzopyran-2,2'-(2H)-indole] in solution. *Chem. Phys. Lett.* **376**, 214-219 (2003).

145. Rini, M., Holm, A.-K., Nibbering, E. T. J. & Fidler, H. Ultrafast UV-mid-IR investigation of the ring opening reaction of a photochromic spiropyran. *J. Am. Chem. Soc.* **125**, 3028-3034 (2003).
146. Fidler, H., Rini, M. & Nibbering, E. T. J. The role of large conformational changes in efficient ultrafast internal conversion: Deviations from the energy gap law. *J. Am. Chem. Soc.* **126**, 3789-3794 (2004).
147. Heiligman-Rim, R., Hirshberg, Y. & Fischer, E. Photochromism in spiropyrans. Part 4. Evidence for existence of several forms of colored modification. *J. Phys. Chem.* **66**, 2465-2470 (1962).
148. Yoshida, T., Morinaka, A. & Funakoshi, N. Photochromism of a vacuum-deposited 1',3',3'-trimethyl-6-hydroxyspiro[2H-1-benzopyran-2,2'-indoline] film. *J. Chem. Soc., Chem. Commun.*, 437-438 (1986).
149. Holm, A.-K., *et al.* Sequential merocyanine product isomerization following femtosecond UV excitation of a spiropyran. *J. Phys. Chem. A* **109**, 8962-8968 (2005).
150. Hobley, J., Malatesta, V., Millini, R., Montanari, L. & Parker, W. O. N. Proton exchange and isomerisation reactions of photochromic and reverse photochromic spiropyrans and their merocyanine forms. *Phys. Chem. Chem. Phys.* **1**, 3259-3267 (1999).
151. Delbaere, S., Bochu, C., Azaroual, N., Buntinx, G. & Vermeersch, G. NMR studies of the structure of the photoinduced forms of photochromic spironaphthoxazines. *J. Chem. Soc., Perkin Trans. 2*, 1499-1501 (1997).
152. Aldoshin, S. M. & Atovmyan, L. O. The structure of open merocyanine forms of photochromic indoline spiropyrans and the mechanism of their structural conversions. *Mol. Cryst. Liq. Cryst.* **149**, 251-290 (1987).
153. Poisson, L., Raffael, K. D., Soep, B., Mestdagh, J.-M. & Buntinx, G. Gas-phase dynamics of spiropyran and spirooxazine molecules. *J. Am. Chem. Soc.* **128**, 3169-3178 (2006).
154. Schackelford, W. M., Cline, D. M., Faas, L. & Kurth, G. An evaluation of automated spectrum matching for survey identification of wastewater components by gas chromatography-mass spectrometry. *Anal. Chim. Acta* **146**, 15-27 (1983).
155. Mark, H. F., Othmer, D. F., Overberger, C. G. & Seaburg, G. T. *Kirk-Othmer encyclopedia of chemical technology*, (Wiley/Interscience, New York, 1992).
156. Hayward, K. Drinking water contaminant hitlist for U.S. EPA. *Water* **21**, 4 (1999).
157. Atkinson, R., *et al.* Atmospheric chemistry of aniline, N,N-dimethylaniline, pyridine, 1,3,5-triazine, and nitrobenzene. *Environ. Sci. Technol.* **21**, 64-72 (1987).
158. Brill, T. B. & James, K. J. Kinetics and mechanisms of thermal decomposition of nitroaromatic explosives. *Chem. Rev.* **93**, 2667-2692 (1993).
159. Fukuhara, K., Kurihara, M. & Miyata, N. Photochemical generation of nitric oxide from 6-nitrobenzo[*a*]pyrene. *J. Am. Chem. Soc.* **123**, 8662-8666 (2001).
160. Suzuki, T., *et al.* Photoinduced nitric oxide release from nitrobenzene derivatives. *J. Am. Chem. Soc.* **127**, 11720-11726 (2005).

161. Murad, F. Discovery of some of the biological effects of nitric oxide and its role in cell signaling. *Angew. Chem. Int. Ed.* **38**, 1856-1868 (1999).
162. Furchgott, R. F. Endothelium-derived relaxing factor: Discovery, early studies, and identification as nitric oxide. *Angew. Chem. Int. Ed.* **38**, 1870-1880 (1999).
163. Ignarro, L. J. Nitric oxide: A unique endogenous signaling molecule in vascular biology. *Angew. Chem. Int. Ed.* **38**, 1882-1892 (1999).
164. Wang, P. G., *et al.* Nitric oxide donors: Chemical activities and biological applications. *Chem. Rev.* **102**, 1091-1134 (2002).
165. Tonokura, K., Ogura, T. & Koshi, M. Near-UV absorption spectrum of the phenoxyl radical and kinetics of its reaction with CH<sub>3</sub>. *J. Phys. Chem. A* **108**, 7801-7805 (2004).
166. Spanget-Larsen, J., *et al.* Vibrations of the phenoxyl radical. *J. Am. Chem. Soc.* **123**, 11253-11261 (2001).
167. Porter, G. & Wright, F. J. Primary photochemical processes in aromatic molecules. 3. Absorption spectra of benzyl, anilino, phenoxy and related free radicals. *Trans. Faraday Soc.* **51**, 1469-1474 (1955).
168. Land, E. J., Porter, G. & Strachan, E. Primary photochemical processes in aromatic molecules. 6. Absorption spectra and acidity constants of phenoxyl radicals. *Trans. Faraday Soc.* **57**, 1885-1893 (1961).
169. Roebber, J. L. Photolysis of the phenoxy radical in a nitrogen matrix. *J. Chem. Phys.* **37**, 1974-1981 (1962).
170. Beck, S. M. & Brus, L. E. The resonance Raman spectra of aqueous phenoxy and phenoxy-*d*<sub>5</sub> radicals. *J. Chem. Phys.* **76**, 4700-4704 (1982).
171. Tripathi, G. N. R. & Schuler, R. H. The resonance Raman spectrum of phenoxyl radical. *J. Chem. Phys.* **81**, 113-121 (1984).
172. Mukherjee, A., McGlashen, M. L. & Spiro, T. G. Ultraviolet resonance Raman spectroscopy and general valence force field analysis of phenolate and phenoxyl radical. *J. Phys. Chem.* **99**, 4912-4917 (1995).
173. Radziszewski, J. G., *et al.* Electronic states of the phenoxyl radical. *J. Chem. Phys.* **115**, 9733-9738 (2001).
174. Yang, R., Jin, X., Wang, W., Fan, K. & Zhou, M. Infrared spectra of phenyl nitrite and phenoxyl radical-nitric oxide complex in solid argon. *J. Phys. Chem. A* **109**, 4261-4266 (2005).
175. Dixon, W. T. & Norman, R. O. C. Electron spin resonance studies of oxidation. Part IV. Some benzenoid compounds. *J. Chem. Soc.*, 4857-4860 (1964).
176. Stone, T. J. & Waters, W. A. Aryloxy-radicals. Part I. Electron spin resonance spectra of radicals from some substituted monohydric phenols. *J. Chem. Soc.*, 213-218 (1964).
177. Dixon, W. T. & Murphy, D. Determination of the acidity constants of some phenol radical cations by means of electron spin resonance. *J. Chem. Soc., Faraday Trans.* **72**, 1221-1230 (1976).
178. Chipman, D. M., Liu, R., Zhou, X. & Pulay, P. Structure and fundamental vibrations of phenoxyl radical. *J. Chem. Phys.* **100**, 5023-5035 (1994).

179. Qin, Y. & Wheeler, R. A. Density functional methods give accurate vibrational frequencies and spin-densities for phenoxyl radical. *J. Chem. Phys.* **102**, 1689-1698 (1995).
180. Domenicano, A., *et al.* Planar and orthogonal conformations - A concerted study by electron diffraction, X-ray crystallography, and molecular orbital calculations. *Struct. Chem.* **1**, 107-122 (1990).
181. Shishkov, I. F., Sadova, N. I., Novikov, V. P. & Vilkov, L. V. An electron diffraction study of the molecular structure of nitrobenzene in the vapor state. *Zh. Strukt. Khim.* **25**, 98 (1984).
182. Tsuji, T., Takashima, H., Takeuchi, H., Egawa, T. & Konaka, S. Molecular structure and torsional potential of trans-azobenzene. A gas electron diffraction study. *J. Phys. Chem. A* **105**, 9347-9353 (2001).
183. Høg, J. H. A study of nitrobenzene. *PhD Dissertation*, University of Copenhagen (1971).
184. Carreira, L. A. & Towns, T. G. Raman spectra and barriers to internal rotation - Biphenyl and nitrobenzene. *J. Mol. Struct.* **41**, 1 (1977).
185. Galloway, D. B., Glenewinkel-Meyer, T., Bartz, J. A., Huey, L. G. & Crim, F. F. The kinetic and internal energy of NO from the photodissociation of nitrobenzene. *J. Chem. Phys.* **100**, 1946-1952 (1994).
186. Nagakura, S., Kojima, M. & Maruyama, Y. Electronic spectra and electronic structures of nitrobenzene and nitromesitylene. *J. Mol. Spectrosc.* **13**, 174-192 (1964).
187. Galloway, D. B., Bartz, J. A., Huey, L. G. & Crim, F. F. Pathways and kinetic energy disposal in the photodissociation of nitrobenzene. *J. Chem. Phys.* **98**, 2107-2114 (1993).
188. Castle, K. J., Abbott, J., Peng, X. & Kong, W. Direction of the transition dipole moment of nitrobenzene determined from oriented molecules in a uniform electric field. *J. Chem. Phys.* **113**, 1415-1419 (2000).
189. Abbott, J. E., Peng, X. & Kong, W. Symmetry properties of electronically excited states of nitroaromatic compounds. *J. Chem. Phys.* **117**, 8670-8675 (2002).
190. Vidal, B. & Murrell, J. N. Effect of solvent on position of first absorption band of nitrobenzene. *Chem. Phys. Lett.* **31**, 46-47 (1975).
191. Robin, M. B. *Higher excited states of polyatomic molecules*, (Academic Press, New York, 1975).
192. Kröhl, O., Malsch, K. & Swiderek, P. The electronic states of nitrobenzene: Electron-energy-loss spectroscopy and CASPT2 calculations. *Phys. Chem. Chem. Phys.* **2**, 947-953 (2000).
193. Yip, R. W., Sharma, D. K., Giasson, R. & Gravel, D. Picosecond excited-state absorption of alkyl nitrobenzenes in solution. *J. Phys. Chem.* **88**, 5770-5772 (1984).
194. Hurley, R. & Testa, A. C. Triplet-state yield of aromatic nitro compounds. *J. Am. Chem. Soc.* **90**, 1949-1952 (1968).
195. Takezaki, M., Hirota, N. & Terazima, M. Nonradiative relaxation processes and electronically excited states of nitrobenzene studied by picosecond time-resolved transient grating method. *J. Phys. Chem. A* **101**, 3443-3448 (1997).

196. Takezaki, M., *et al.* Geometries and energies of nitrobenzene studied by CAS-SCF calculations. *J. Phys. Chem. A* **101**, 5190-5195 (1997).
197. Takezaki, M., Hirota, N. & Terazima, M. Relaxation of nitrobenzene from the excited singlet state. *J. Chem. Phys.* **108**, 4685-4686 (1998).
198. Schuler, V. H. & Woeldike, A. Ein weiterer beitrag zur unterschiedlichen anregung von molekülen durch light und elektronenstoß durch die beobachtung eines emissionspektrums des NO<sub>2</sub>. *Phys. Z.* **45**, 171 (1944).
199. Hastings, S. H. & Matsen, F. A. The photodecomposition of nitrobenzene. *J. Am. Chem. Soc.* **70**, 3514-3515 (1948).
200. Porter, G. & Ward, B. The photolytic preparation of cyclopentadienyl and phenyl nitrene from benzene derivatives. *Proc. R. Soc. London, Ser. A* **303**, 139-156 (1968).
201. Gonzalez, A. C., Larson, C. W., McMillen, D. F. & Golden, D. M. Mechanism of decomposition of nitroaromatics - Laser-powered homogeneous pyrolysis of substituted nitrobenzenes. *J. Phys. Chem.* **89**, 4809-4814 (1985).
202. Apel, E. C. & Nogar, N. S. Multiphoton photoionization mass spectra of nitrobenzene and 2,4,6-trinitrotoluene. *Int. J. Mass Spectrom. Ion Processes* **70**, 243-246 (1986).
203. Tsang, W., Robaugh, D. & Mallard, W. G. Single-pulse shock-tube studies on C-NO<sub>2</sub> bond cleavage during the decomposition of some nitro aromatic compounds. *J. Phys. Chem.* **90**, 5968-5973 (1986).
204. Marshall, A., *et al.* Laser-induced dissociation, ionization and fragmentation processes in nitroaromatic molecules. *Int. J. Mass Spectrom. Ion Processes* **116**, 143-156 (1992).
205. Marshall, A., Clark, A., Jennings, R., Ledingham, K. W. D. & Singhal, R. P. Wavelength-dependent laser-induced fragmentation of nitrobenzene. *Int. J. Mass Spectrom. Ion Processes* **112**, 273-283 (1992).
206. Kosmidis, C., *et al.* On the dissociation pathways of nitrobenzene. *Int. J. Mass Spectrom. Ion Processes* **135**, 229-242 (1994).
207. Zhu, X.-M., Zhang, S.-Q., Zheng, X. & Phillips, D. L. Resonance Raman study of short-time photodissociation dynamics of the charge-transfer band absorption of nitrobenzene in cyclohexane solution. *J. Phys. Chem. A* **109**, 3086-3093 (2005).
208. Nwobi, O., Higgins, J., Zhou, X. & Liu, R. Density functional calculation of phenoxyl radical and phenolate anion: An examination of the performance of DFT methods. *Chem. Phys. Lett.* **272**, 155-161 (1997).
209. Adamo, C., Subra, R., Di Matteo, A. & Barone, V. Structure and magnetic properties of benzyl, anilino, and phenoxyl radicals by density functional computations. *J. Chem. Phys.* **109**, 10244-10254 (1998).
210. Schnepf, R., *et al.* Resonance Raman spectroscopic study of phenoxyl radical complexes. *J. Am. Chem. Soc.* **120**, 2352-2364 (1998).
211. Feenstra, J. S., Park, S. T. & Zewail, A. H. Excited state molecular structures and reactions directly determined by ultrafast electron diffraction. *J. Chem. Phys.* **123**, 221104 (2005).
212. Kasha, M. Paths of molecular excitation. *Radiation Res. Suppl.* **2**, 243-275 (1960).

213. Takezaki, M., Hirota, N. & Terazima, M. Excited state dynamics of nitrobenzene studied by the time-resolved transient grating method. *Prog. Nat. Sci.* **6**, S453-S456 (1996).
214. Lim, E. C. Proximity effect in molecular photophysics - Dynamic consequences of pseudo-Jahn-Teller interaction. *J. Phys. Chem.* **90**, 6770-6777 (1986).
215. El-Sayed, M. A. Spin-orbit coupling and the radiationless processes in nitrogen heterocyclics. *J. Chem. Phys.* **38**, 2834-2838 (1963).
216. Glenewinkel-Meyer, T. & Crim, F. F. The isomerization of nitrobenzene to phenylnitrite. *Theochem - J. Mol. Struct.* **337**, 209-224 (1995).
217. Li, Y.-M., Sun, J.-L., Yin, H.-M., Han, K.-L. & He, G.-Z. Photodissociation of nitrobenzene at 266 nm: Experimental and theoretical approach. *J. Chem. Phys.* **118**, 6244-6249 (2003).
218. Xu, S. & Lin, M. C. Computational study on the kinetics and mechanism for the unimolecular decomposition of  $C_6H_5NO_2$  and the related  $C_6H_5+NO_2$  and  $C_6H_5O+NO$  reactions. *J. Phys. Chem. B* **109**, 8367-8373 (2005).
219. Butler, L. J., Krajnovich, D., Lee, Y. T., Ondrey, G. & Bersohn, R. The photodissociation of nitromethane at 193 nm. *J. Chem. Phys.* **79**, 1708-1722 (1983).
220. Lao, K. Q., Jensen, E., Kash, P. W. & Butler, L. J. Polarized emission spectroscopy of photodissociating nitromethane at 200 and 218 nm. *J. Chem. Phys.* **93**, 3958-3969 (1990).
221. Daugey, N., Shu, J., Bar, I. & Rosenwaks, S. Nitrobenzene detection by one-color laser-photolysis/laser-induced fluorescence of NO ( $v''=0-3$ ). *Appl. Spectrosc.* **53**, 57-64 (1999).
222. Sobolewski, A. L. & Domcke, W. Computational studies of the photophysics of hydrogen-bonded molecular systems. *J. Phys. Chem. A* **111**, 11725-11735 (2007).
223. Martinez, T. J. Insights for light-driven molecular devices from ab initio multiple spawning excited-state dynamics of organic and biological chromophores. *Acc. Chem. Res.* **39**, 119-126 (2006).
224. Hudock, H. R., *et al.* Ab initio molecular dynamics and time-resolved photoelectron spectroscopy of electronically excited uracil and thymine. *J. Phys. Chem. A* **111**, 8500-8508 (2007).
225. Kohler, B. DNA photodynamics. *Photochem. Photobiol.* **83**, 592-594 (2007).
226. Crespo-Hernández, C. E., Cohen, B., Hare, P. M. & Kohler, B. Ultrafast excited-state dynamics in nucleic acids. *Chem. Rev.* **104**, 1977-2019 (2004).
227. Hare, P. M., Crespo-Hernández, C. E. & Kohler, B. Solvent-dependent photophysics of 1-cyclohexyluracil: Ultrafast branching in the initial bright state leads nonradiatively to the electronic ground state and a long-lived  $^1n\pi^*$  state. *J. Phys. Chem. B* **110**, 18641-18650 (2006).
228. Callis, P. R. Electronic states and luminescence of nucleic acid systems. *Annu. Rev. Phys. Chem.* **34**, 329-357 (1983).
229. Creed, D. The photophysics and photochemistry of the near-UV absorbing amino acids. 1. Tryptophan and its simple derivatives. *Photochem. Photobiol.* **39**, 537-562 (1984).

230. Creed, D. The photophysics and photochemistry of the near-UV absorbing amino acids. 2. Tyrosine and its simple derivatives. *Photochem. Photobiol.* **39**, 563-575 (1984).
231. Creed, D. The photophysics and photochemistry of the near-UV absorbing amino acids. 3. Cystine and its simple derivatives. *Photochem. Photobiol.* **39**, 577-583 (1984).
232. Peon, J. & Zewail, A. H. DNA/RNA nucleotides and nucleosides: Direct measurement of excited-state lifetimes by femtosecond fluorescence up-conversion. *Chem. Phys. Lett.* **348**, 255-262 (2001).
233. Pal, S. K., Peon, J. & Zewail, A. H. Ultrafast decay and hydration dynamics of DNA bases and mimics. *Chem. Phys. Lett.* **363**, 57-63 (2002).
234. Michl, J. & Bonačić-Koutecký, V. *Electronic aspects of organic photochemistry*, (Wiley, New York, 1990).
235. Lakowicz, J. R. *Principles of fluorescence spectroscopy*, (Plenum, New York, 1999).
236. Lipert, R. J., Bermudez, G. & Colson, S. D. Pathways of S<sub>1</sub> decay in phenol, indoles, and water complexes of phenol and indole in a free jet expansion *J. Phys. Chem.* **92**, 3801-3805 (1988).
237. Bersohn, R., Even, U. & Jortner, J. Fluorescence excitation-spectra of indole, 3-methyl indole, and 3-indole acetic-acid in supersonic jets. *J. Chem. Phys.* **80**, 1050-1058 (1984).
238. Hays, T. R., Henke, W. E., Selzle, H. L. & Schlag, E. W. Fluorescence excitation and multiphoton ionization spectroscopy of 3-methylindole in a supersonic jet *Chem. Phys. Lett.* **97**, 347-351 (1983).
239. Hager, J. & Wallace, S. C. Laser spectroscopy and photodynamics of indole and indole-van der Waals molecules in a supersonic beam. *J. Phys. Chem.* **87**, 2121-2127 (1983).
240. Hager, J. W., Demmer, D. R. & Wallace, S. C. Electronic spectra of jet-cooled indoles: Evidence for the <sup>1</sup>L<sub>a</sub> state. *J. Phys. Chem.* **91**, 1375-1382 (1987).
241. Sammeth, D. M., Yan, S., Spangler, L. H. & Callis, P. R. Two-photon fluorescence excitation spectra of indole in vapor and jet: <sup>1</sup>L<sub>a</sub> states. *J. Phys. Chem.* **94**, 7340-7342 (1990).
242. Short, K. W. & Callis, P. R. One- and two-photon spectra of jet-cooled 2,3-dimethylindole: <sup>1</sup>L<sub>b</sub> and <sup>1</sup>L<sub>a</sub> assignments. *Chem. Phys.* **283**, 269-278 (2002).
243. Lippert, H., Ritze, H.-H., Hertel, I. V. & Radloff, W. Femtosecond time-resolved analysis of the photophysics of the indole molecule. *Chem. Phys. Lett.* **398**, 526-531 (2004).
244. Lin, M.-F., Tseng, C.-M., Lee, Y. T. & Ni, C.-K. Photodissociation dynamics of indole in a molecular beam. *J. Chem. Phys.* **123**, 124303 (2005).
245. Nix, M. G. D., Devine, A. L., Cronin, B. & Ashfold, M. N. R. High-resolution photofragment translational spectroscopy of the near UV photolysis of indole: Dissociation via the <sup>1</sup>πσ\* state. *Phys. Chem. Chem. Phys.* **8**, 2610-2618 (2006).
246. Sobolewski, A. L. & Domcke, W. Ab initio investigations on the photophysics of indole. *Chem. Phys. Lett.* **315**, 293-298 (1999).

247. Sobolewski, A. L., Domcke, W., Dedonder-Lardeux, C. & Jouvét, C. Excited-state hydrogen detachment and hydrogen transfer driven by repulsive  $1\pi\sigma^*$  states: A new paradigm for nonradiative decay in aromatic biomolecules. *Phys. Chem. Chem. Phys.* **4**, 1093-1100 (2002).
248. Dedonder-Lardeux, C., Jouvét, C., Perun, S. & Sobolewski, A. L. External electric field effect on the lowest excited states of indole: Ab initio and molecular dynamics study. *Phys. Chem. Chem. Phys.* **5**, 5118-5126 (2003).
249. Dian, B. C., Longarte, A. & Zwier, T. S. Hydride stretch infrared spectra in the excited electronic states of indole and its derivatives: Direct evidence for the  $1\pi\sigma^*$  state. *J. Chem. Phys.* **118**, 2696-2706 (2003).
250. Lim, E. C. & Yu, J. M. H. Vibronic spin-orbit interactions in heteroaromatic molecules. I. Polycyclic monoazines. *J. Chem. Phys.* **47**, 3270-3275 (1967).
251. Merchán, M., Serrano-Andrés, L., Robb, M. A. & Blancafort, L. Triplet-state formation along the ultrafast decay of excited singlet cytosine. *J. Am. Chem. Soc.* **127**, 1820-1825 (2005).
252. Matsunaga, N., Koseki, S. & Gordon, M. S. Relativistic potential energy surfaces of  $XH_2$  ( $X=C, Si, Ge, Sn, \text{ and } Pb$ ) molecules: Coupling of  $^1A_1$  and  $^3B_1$  states. *J. Chem. Phys.* **104**, 7988-7996 (1996).
253. Marian, C. M. Spin-orbit coupling in molecules. In *Rev. Comput. Chem.*, vol. 17 99-204 (Wiley-VCH, Weinheim, 2001).
254. Jalviste, E. & Ohta, N. Stark absorption spectroscopy of indole and 3-methylindole. *J. Chem. Phys.* **121**, 4730-4739 (2004).
255. Albinsson, B. & Nordén, B. Excited-state properties of the indole chromophore. Electronic transition moment directions from linear dichroism measurements: Effect of methyl and methoxy substituents. *J. Phys. Chem.* **96**, 6204-6212 (1992).
256. Baskin, J. S. & Zewail, A. H. Ultrafast electron diffraction: Oriented molecular structures in space and time. *Chem. Phys. Chem.* **6**, 2261-2276 (2005).
257. Baskin, J. S. & Zewail, A. H. Oriented ensembles in ultrafast electron diffraction. *Chem. Phys. Chem.* **7**, 1562-1574 (2006).
258. Morino, Y. & Hirota, E. Molecular structure and internal rotation of hexachloroethane, hexachlorodisilane, and trichloromethyl-trichlorosilane. *J. Chem. Phys.* **28**, 185-197 (1958).
259. Lin, M. M., Shorokhov, D. & Zewail, A. H. Conformations and coherences in structure determination by ultrafast electron diffraction. *J. Phys. Chem. A* **113**, 4075-4093 (2009).
260. Lin, M. M., Shorokhov, D. & Zewail, A. H. Helix-to-coil transitions in proteins: Helicity resonance in ultrafast electron diffraction. *Chem. Phys. Lett.* **420**, 1-7 (2006).
261. Lin, M. M., Shorokhov, D. & Zewail, A. H. Structural ultrafast dynamics of macromolecules: Diffraction of free DNA and effect of hydration. *Phys. Chem. Chem. Phys.* **11**, 10619-10632 (2009).
262. Vogt, N., Dorofeeva, O. V., Sipachev, V. A. & Rykov, A. N. Molecular structure of 9H-adenine tautomer: Gas-phase electron diffraction and quantum chemical studies. *J. Phys. Chem. A* **113**, 13816-13823 (2009).

- 
263. van Oudheusden, T., *et al.* Compression of subrelativistic space-charge-dominated electron bunches for single-shot femtosecond electron diffraction. *Phys. Rev. Lett.* **105**(2010).
264. <http://www.pulsar.nl/gpt/>.
265. Kneissl, S., Loveridge, E. J., Williams, C., Crump, M. P. & Allemann, R. K. Photocontrollable peptide-based switches target the anti-apoptotic protein Bcl-x<sub>L</sub>. *Chem. Bio. Chem.* **9**, 3046-3054 (2008).
266. Zhang, Z. H., Burns, D. C., Kumita, J. R., Smart, O. S. & Woolley, G. A. A water-soluble azobenzene cross-linker for photocontrol of peptide conformation. *Bioconj. Chem.* **14**, 824-829 (2003).